Characterization of Propylene Glycol *n*-Propyl Ether

Measuring and Modeling of Important Thermodynamic Parameters

Dissertation
zur Erlangung des Grades
Doktor der Naturwissenschaften
(Dr. rer. nat.)

der
Naturwissenschaftlichen Fakultät IV
Chemie und Pharmazie
der Universität Regensburg

von
Bernhard Ramsauer
REGENSBURG
2010

Promotionsgesuch eingereicht am:	30.11.2009
Tag des Kolloquiums	12.01.2010
Die Arbeit wurde angeleitet von:	Prof. Dr. W. Kunz
Prüfungsausschuß:	Prof. em. Dr. Dr. h.c. J. Barthel, Vorsitzender Prof. Dr. W. Kunz Prof. Dr. G. Schmeer Prof. Dr. J. Daub

Acknowledgement

The work of the present dissertation took place between February 2006 and September 2009 at the Department of Chemistry and Pharmacy, Institute of Physical and Theoretical Chemistry, at the University of Regensburg under the leadership of Prof. Dr. Werner Kunz.
First, I would like to thank **Prof. Dr. Werner Kunz** for giving me the opportunity to do my Ph.D. in his labs, his constructive support in different ways and for setting up the funding of the work.

I want to express my special gratitude to my *little* supervisor **Dr. Roland Neueder**, with whom I spent many moments in discussing many theoretical as well as experimental aspects. He not only gave me the opportunity to work with the vapor pressure apparatuses built by himself, but let me participate from his impressive theoretical, methodological and experimental knowledge on numerous aspects of physical chemistry. Furthermore he provided me with stimulating and helpful ideas for the every-day lab work. My hope is that we will climb the *Passo dello Stelvio* with road bikes in the near future together.
Dr. Andreas Klamt, COSMOlogic GmbH & Co. KG, Leverkusen, broadended my perspective of the COSMO-RS model simulation during his course held at the University of Regensburg and during his kind support when preparing and writting a publication manuscript. Connected to this is the indispensable help of **Dr. Sven Hartmann**, LTP GmbH, Oldenburg, who I met first in Cannes. He made it possible to include UNIFAC calculation within this thesis.
I am grateful for the experience of being part of the institute's research team. I want to thank in general all members of the faculty and especially the fellow workers of the mechanical and electronic workshops for their quick and conscientious settlement of various kinds of work.
Five student assistants devoted themselves to different study goals: **Markus Karl** and **Andrea Hoffmann** did a lot of work on the VLE investigations, **Hermann Nuss** and **Julian Kaiser** supported me with experimental help on vapor pressure and heat capacity measurements and finally **Monika M. Meier**, who spent so much time and effort on the conductivity study.
More personally, I would like to thank **Dr. Stefan „Steve" Thomaier** and **Dr. Christian „Schreini" Schreiner** for their endless motivation, encouragement and sharing all the ups and downs.
Please let me not forget the *workhorse* of the institute, **Wolfgang „Wolfi" Simon**. His never ending effort to get things running and his special kind of humor made this time a special one.

It is very important to emphasis my great time I had in the *Oberpfalz* students' hostel, where I have been living for almost seven years and during which time I got to know so many wonderful people. I want to thank them for their affectionate support in all these things that seem to be not directly related to the performance of a Ph.D. thesis.
Of course I would also like to thank my family for their endless assistance and generous support, without which I would never have become what I am today and my sister **Doris** for her help in editing the pictures.

Abbreviations and Physical Constants

Abbreviations

1-HeOH	1-Hexanol
2-BuOH	2-Butanol
COSMO-RS	Conductor like screening model - for real solvent
EOS	Equation of State
EtOH	Ethanol
FID	Flame Ionization detector
lcCM	low concentration Chemical Model
LCST	Lower critical solution temperature
MeOH	Methanol
MHC	minimum hydrotrope concentration
mod-UNIFAC (Do)	modified UNIFAC model (Dortmund)
MSA	Mean Spherical Approximation
PM	1-Methoxy-2-propanol
PnP	1-Propoxy-2-propanol
RMS	Root mean square
TCD	Thermal conductivity detector
VLE	Vapor-Liquid Equilibria

Physical Constants

Avogadro's constant	N_A	$= 6.022\,52 \times 10^{23}\,\mathrm{mol}^{-1}$
Boltzmann's constant	k	$= 1.380\,54 \times 10^{-23}\,\mathrm{J\,K}^{-1}$
Electron charge	e_0	$= 1.602\,10 \times 10^{-19}\,\mathrm{C}$
Vacuum permittivity	ϵ_0	$= 8.854\,185 \times 10^{-12}\,\mathrm{C\,V}^{-1}\,\mathrm{mol}^{-1}$
Gas constant	R	$= 8.314\,33\,\mathrm{J\,K}^{-1}\,\mathrm{mol}^{-1}$

Conversion

$$1\,\mathrm{Torr} = 133.32\,\mathrm{Pa} = 1.3332 \times 10^{-3}\,\mathrm{bar}$$

List of Symbols

α	nonrandomness parameter in NRTL model	
α'	parameter in COSMO	
$\Delta\Lambda_{12}, \Delta\Lambda_{21}$	binary parameters in Wilson equation	
Δu_{ij}, Δu_{ji}	energy parameters in UNIQUAC equation	$\mathrm{J\,mol^{-1}}$
γ	activity coefficient (on a molal basis)	
γ	surface tension	$\mathrm{N\,m^{-1}}$
κ	specific conductivity	$\mathrm{S\,m^{-1}}$
$\Lambda, \Lambda^{\infty}$	molar conductivity, limiting molar conductivity	$\mathrm{S\,cm^2\,mol^{-1}}$
Λ^{∞}	limiting ionic conductivity	$\mathrm{S\,cm^2\,mol^{-1}}$
$\lambda_{ij}, \lambda_{ji}$	energy parameters in Wilson equation	$\mathrm{J\,mol^{-1}}$
μ	chemical potential	$\mathrm{J\,mol^{-1}}$
$\mu_{i,S}$	σ-potential of i in solvent mixture S	$\mathrm{kcal\,mol^{-1}nm^{-2}}$
ν	molar volume	$\mathrm{cm^3\,mol^{-1}}$
ν_+, ν_-	stoichiometric coefficients	
$\overline{S^{\mathrm{ex}}}$	mean molar excess entropy	$\mathrm{J\,K^{-1}\,mol^{-1}}$
$\overline{V^{\mathrm{ex}}}$	mean molar excess volume	$\mathrm{m^3\,mol^{-1}}$
$\overline{G^{\mathrm{ex}}}$	mean molar Gibbs excess energy	$\mathrm{J\,mol^{-1}}$
$\overline{H^{\mathrm{ex}}}$	mean molar excess enthalpy	$\mathrm{J\,mol^{-1}}$
ϕ	fugacity coefficient	
Φ_c	apparent molar heat capacity	$\mathrm{J\,K^{-1}mol^{-1}}$
Φ_v	apparent molar volume	$\mathrm{m^3\,mol^{-1}}$
ρ_N	N-particle distribution function	
σ_{hb}	parameter in COSMO	
σ_i	charge density of surface segment i	$\mathrm{e\,nm^{-2}}$
τ_{ij}, τ_{ji}	binary parameter in NRTL model	
τ_{vdW}	parameter in COSMO	
τ_{ij},τ_{ji}	binary parameters in UNIQUAC equation	
ξ_i	area fraction in GC analysis	
a_{eff}	effective surface area	$\mathrm{nm^2}$
a_{nm}	interaction parameter of mod. UNIFAC	K
B	second virial coefficient	$\mathrm{m^3\,mol^{-1}}$
b_{nm}	interaction parameter of mod. UNIFAC	
c_{hb}	parameter in COSMO	
c_{nm}	interaction parameter of mod-UNIFAC	$\mathrm{K^{-1}}$
d^*, d	pure solvent's and solution's density, respectively	$\mathrm{kg\,m^{-3}}$
f	fugacity	Pa
G_i^R	molar residual Gibbs energy	$\mathrm{J\,mol^{-1}}$
g_{ig}, g_{ji}	energy parameters in NRTL model	$\mathrm{J\,mol^{-1}}$

K_A	association constant	$\mathrm{dm^3\,mol^{-1}}$
p	(vapor) pressure	Pa
$P_i(\sigma)$	σ-profile; distribution function	
p_i^{vap}	pure component's vapor pressure	Pa
$Q(K)$	relative van-der-Waals surface area of subgroup K	
q_i	effective volume of molecule i	
$R(K)$	relative van-der-Waals volume of subgroup K	
r_i	effective size of molecule i	
T	temperature	K
$W_{ij}(\vec{r_1}, \vec{r_2})$	potential of mean force	J
x	liquid-phase mole fraction	
y	vapor-phase mole fraction	
Z	compressibility factor	
O.D.	optical density: $-\log_{10} \frac{I}{I_0}$	

Contents

List of Figures xi

List of Tables xv

1. Introduction 1

2. Materials, Purification and Analysis 5
2.1. Pure Solvents . . . 5
2.1.1. Water . . . 6
2.1.2. Propylene Glycol Ethers . . . 6
2.1.3. Ethanol . . . 7
2.2. Electrolytes . . . 7
2.2.1. Potassium chloride KCl . . . 7
2.2.2. Tetrabutylammonium Salts . . . 7
2.3. Nitrogen Purification . . . 8

3. Properties and characterization of 1-propoxy-2-propanol / water mixtures 9
3.1. Solubilization curve . . . 9
3.2. Surface Tension Measurements . . . 10
3.3. Measurements of Density and Heat Capacity . . . 12
3.3.1. Experimental . . . 13
3.3.2. Results and Conclusion . . . 14

4. Vapor-Liquid Phase Equilibria 19
4.1. Fugacity and Activity . . . 19
4.2. Calculation of Chemical Potentials . . . 21
4.3. Calculation of VLE . . . 21
4.4. Bubble-Point Calculations . . . 23
4.5. Excess Gibbs Energy Models . . . 24
4.5.1. Wilson Model . . . 26
4.5.2. NRTL Model . . . 27
4.5.3. UNIQUAC Model . . . 27
4.6. Data Reduction . . . 29
4.7. Consistency Tests . . . 29
4.8. Data Processing . . . 32
4.9. Measurement Method . . . 32
4.9.1. Experimental Setup . . . 32
4.9.2. Experimental Procedure . . . 35
4.9.3. Temperature Calibration . . . 37
4.10. Analytical Determination of Phase Composition . . . 38
4.10.1. Setup . . . 38
4.10.2. Calibration . . . 39
4.11. Predictive Models . . . 41
4.11.1. UNIFAC . . . 41
4.11.2. COSMO-RS . . . 42

4.11.2.1. Theory . . . 42
4.11.2.2. Calculation of Phase Equilibria . . . 45
4.11.2.3. Parametrization . . . 46
4.12. Discussion of Experimental Results . . . 48
4.12.1. 1-propoxy-2-propanol + methanol . . . 56
4.12.2. 1-propoxy-2-propanol + ethanol . . . 56
4.12.3. 1-propoxy-2-propanol + 2-butanol . . . 57
4.12.4. 1-propoxy-2-propanol + 1-hexanol . . . 57
4.12.5. 1-propoxy-2-propanol + water . . . 58
4.12.6. 1-methoxy-2-propanol + water . . . 59
4.12.7. 1-propoxy-2-propanol + 1-methoxy-2-propanol . . . 59
4.13. Conclusion . . . 60
4.14. Isothermal Vapor-Liquid Equilibria for PnP + ethanol . . . 62
4.14.1. Experimental Procedure . . . 63
4.14.2. Results and Discussion . . . 63

5. Electrical Conductivity in 1-Propoxy-2-propanol 67
5.1. Theoretical Aspects . . . 67
5.1.1. Statistical Mechanical Principles . . . 67
5.1.2. Electrostatic Potentials and Ion-Association . . . 69
5.1.2.1. Debye-Hückel Model . . . 69
5.1.2.2. Chemical Model at Low Concentration . . . 71
5.1.2.3. Thermodynamics of Association Process . . . 72
5.1.2.4. Transport Properties . . . 74
5.1.3. Conductance of Concentrated Solutions . . . 75
5.2. Temperature Control . . . 75
5.3. Density Measurements . . . 78
5.3.1. Principle of Density Measurements . . . 78
5.3.2. Measuring Unit . . . 78
5.3.3. Execution of Measurements . . . 80
5.3.4. Calibration . . . 81
5.3.5. Results . . . 82
5.3.6. Comparative Study of Literature . . . 83
5.3.7. Density Coefficients of four Tetrabutylammonium Salts . . . 84
5.4. Relative Permittivity . . . 85
5.4.1. Experimental Set-up . . . 85
5.4.2. Measuring Method . . . 85
5.4.2.1. General Procedure . . . 85
5.4.2.2. Calibration and Evaluation . . . 87
5.4.2.3. Possible Sources of Errors . . . 88
5.4.2.4. Results . . . 89
5.5. Viscosity Measurements . . . 90
5.5.1. Principle of Measurement . . . 90
5.5.2. Instrumentation . . . 91
5.5.3. Measuring Unit . . . 92
5.5.4. Measurement Procedure . . . 92
5.5.5. Calibration . . . 92
5.5.5.1. Possible Sources of Errors . . . 93
5.5.5.2. Results . . . 93
5.5.6. Comparative Study of Literature . . . 95
5.6. Conductance of Dilute Electrolyte Solutions . . . 95
5.6.1. Three-electrode Measuring Cell . . . 96

5.6.2. Alternating Current Conductance Bridge . . . 96
5.6.3. Measuring Principle . . . 99
5.6.3.1. Experimental Procedure . . . 99
5.6.3.2. Frequency Extrapolation . . . 100
5.6.3.3. Molar Conductivities Λ . . . 101
5.6.3.4. Cell Calibration . . . 101
5.6.4. Results . . . 103
5.6.5. Data Analysis . . . 110
5.6.6. Discussion . . . 111
5.6.6.1. Limiting Molar Conductivity . . . 111
5.6.6.2. Association Constants . . . 114
5.6.6.3. FJ2–re-Evaluation . . . 115
5.6.6.4. Thermodynamics of the Ion-Pair Process . . . 116
5.7. Conductance of Concentrated Electrolyte Solutions . . . 118
5.7.1. Conductivity Cells . . . 119
5.7.2. Experimental Procedure . . . 120
5.7.3. Data Analysis . . . 121
5.7.4. Results and Discussion . . . 122
5.7.4.1. Low permittivity Solvent PnP . . . 130
5.7.4.2. Temperature Dependence of μ . . . 131
5.8. Equivalent Conductance from Infinite Dilution to Saturation . . . 132

6. Vapor Pressure of Pure PnP and its Solutions of Electrolytes 137
6.1. Activity Coefficients and Osmotic Coefficients . . . 138
6.2. Experimental Osmotic Coefficients . . . 139
6.3. Experimental Section . . . 140
6.3.1. Measuring Device for Elevated Temperatures . . . 140
6.3.2. Measuring Device for Room Temperatures . . . 145
6.4. Results and Discussion . . . 146
6.4.1. Vapor Pressure of Pure PnP . . . 146
6.4.2. Vapor Pressure Depression on Electrolyte Solutions . . . 148
6.4.2.1. Experimental Osmotic Coefficients . . . 150
6.4.2.2. Correlation of Activity and Osmotic Coefficients . . . 155

7. Summary 163

A. Binary Solution Data of PnP + Water 167
A.1. Apparent Molar Volumes at 298.15 K . . . 167
A.2. Apparent Molar Heat Capacities . . . 167

B. GC Analysis of Binary Mixtures 169

C. Experimental VLE Data 171
C.1. Measurements at 20.0 kPa . . . 171
C.2. Measurements at 101.3 kPa . . . 173
C.3. Vapor Pressure of Binary System PnP(1) + EtOH(2) . . . 176

D. Properties of pure PnP 177
D.1. Experimental Densities . . . 177
D.2. Experimental Dynamic Viscosities and Permittivities . . . 177

E. Conductivity Measurements 179
E.1. Conductivity of Dilute Salt Solutions . . . 179
E.2. Specific Conductivity at High Concentrations . . . 180

F. Results on Vapor Pressure Measurements **183**
F.1. Vapor Pressure of Pure PnP 183
F.2. Solution's Vapor Pressure of Bu_4NBr 184
F.3. Solution's Vapor Pressure of Bu_4NNO_3 185
F.4. Solution's Vapor Pressure of Bu_4NOAc 186
F.5. Solution's Vapor Pressure of Bu_4NSCN 188

G. Extended Correlation Results for Osmotic Coefficients **191**
G.1. Extended Pitzer Model of Archer 191
G.2. Clegg-Pitzer Model 193

Bibliography **195**

List of Figures

1.1. Chemical formula of glycol ethers . . . 2

2.1. Vacuum-tight solvent vessel for long-time storage . . . 5
2.2. Glass vessels for storage and preparation of electrolyte solutions . . . 5
2.3. Gaschromatographic analysis of PnP . . . 6

3.1. The optical density (O.D.) as function of x_{PnP} . . . 10
3.2. Surface tension γ as function of $\ln x$ of different compounds: (▲) 2-butoxyethanol, (○) PnP, (●) 1-propanol and (□) methanol . . . 11
3.3. Apparent and partial molar volume of PnP in water at 25 °C . . . 15
3.4. Apparent molar heat capacity of PnP in water at 25 °C . . . 16

4.1. Block Diagram for the bubble-temperature calculation . . . 25
4.2. Integral Test (area test) for the system 1-Methoxy-2-propanol/water . . . 30
4.3. Block Diagram for processing the VLE data . . . 33
4.4. Schematic diagram of VLE apparatus . . . 34
4.5. Photograph of the VLE apparatus . . . 35
4.6. Calibration of the Pt-100 thermometer of the VLE apparatus . . . 37
4.7. General design of a GC as used in this study . . . 38
4.8. Plot of x_1 vs. ξ_1 of PnP in the binary mixture with methanol . . . 40
4.9. Plot of x_1 vs. ξ_1 of PnP in the binary mixture with ethanol . . . 40
4.10. Plot of x_1 vs. ξ_1 of PnP in the binary mixture with 2-butanol . . . 40
4.11. Plot of x_1 vs. ξ_1 of PnP in the binary mixture with 1-hexanol . . . 40
4.12. Plot of x_1 vs. ξ_1 of PnP in the binary mixture with water . . . 40
4.13. Plot of x_1 vs. ξ_1 of PnP in the binary mixture with PM . . . 40
4.14. Plot of x_1 vs. ξ_1 of PM in the binary mixture with water . . . 41
4.15. Input data for mod-UNIFAC (Do) for the binary system PnP - 1-hexanol . . . 42
4.16. Interaction of molecules described by an ensemble of pairwise interacting surface segments σ 43
4.17. $P(\sigma)$ of PnP . . . 44
4.18. $\mu_{\mathrm{PnP,S}}(\sigma)$ of PnP . . . 44
4.19. Approach to the prediction of VLE diagrams with the COSMO-RS model . . . 47
4.20. Excess molar volume for 1-propoxy-2-propanol in selected mixtures . . . 48
4.21. Temperature-composition diagram for the PnP + methanol system at two different pressures 50
4.22. Temperature-composition diagram for the PnP + ethanol system at two different pressures 51
4.23. Temperature-composition diagram for the PnP + 2-butanol system at two different pressures 52
4.24. Temperature-composition diagram for the PnP + 1-hexanol system at two different pressures 53
4.25. Temperature-composition diagram for the PnP + water system at two different pressures 54
4.26. Temperature-composition diagram for the PM + water system at 101.3 kPa . . . 55
4.27. Temperature-composition diagram for the PnP + PM system at 101.3 kPa . . . 55
4.28. Block Diagram for the calculation of vapor pressure p . . . 63
4.29. Isothermal VLE data for PnP + ethanol . . . 65
4.30. Isothermal VLE data for PnP + ethanol . . . 66

5.1. Cold bath in connection with the main thermostat for conductivity and permittivity measurements in the range between −25 °C and 40 °C . . . 76

5.2. Calibration curve of the Pt-resistance thermometer in the main thermostat 77
5.3. Measured resistance values of two NTC's as a function of temperature 79
5.4. Setup for density measurements under protective gas 80
5.5. Temperature dependency of density d of 1-propoxy-2-propanol and its molar volume ν^*_{PnP} 82
5.6. Solution densities of tetrabutylammonium salts in PnP 84
5.7. Detailed engineering drawing of capacitance measuring unit 86
5.8. Vacuum capacity $C_0(T)$ of the capacitor for measuring permittivity as function of temperature 88
5.9. Relative permittivity ϵ_{PnP} as function of temperature 89
5.10. Ubbelohde Viscometer 90
5.11. Automatically controlled viscosity equipment 92
5.12. Dynamic viscosity η_{PnP} as function of temperature 94
5.13. Three-electrode conductivity measuring cell 97
5.14. Three-electrode cell assembly for low A, medium B, high C concentrations 98
5.15. Schematic diagram of the serial-to-parallel transformation 98
5.16. Molar Conductivity $\Lambda(\sqrt{c}, T)$ of Bu_4NBr in 1-propoxy-2-propanol 104
5.17. Molar Conductivity $\Lambda(\sqrt{c}, T)$ of Bu_4NNO_3 in 1-propoxy-2-propanol 105
5.18. Molar Conductivity $\Lambda(\sqrt{c}, T)$ of Bu_4NOAc in 1-propoxy-2-propanol 106
5.19. Molar Conductivity $\Lambda(\sqrt{c}, T)$ of Bu_4NSCN in 1-propoxy-2-propanol 107
5.20. Plot of the limiting molar conductivities Λ^∞ vs. temperature for Bu_4NNO_3 (●), Bu_4NSCN (▽), Bu_4NBr (■) and Bu_4NOAc (△) in the temperature range from 248.15 to 313.15 K . 112
5.21. Plot of $\log K_A$ vs. $(\epsilon T)^{-1}$ for Bu_4NNO_3 (●), Bu_4NSCN (▽), Bu_4NBr (■) and Bu_4NOAc (△) in the temperature range from 248.15 to 313.15 K 115
5.22. Temperature dependence of thermodynamic functions of association. (□) ΔG^0_A, (△) $T\Delta S^0_A$, (▲) ΔH^0_A 117
5.23. Capillary cells with three electrode assembly 119
5.24. Absolute deviations between κ as obtained from Eq. (5.106) and with different initial concentrations m^1, exemplary presented with Bu_4NBr at 298.15 K 123
5.25. Specific conductivity κ of Bu_4NBr in 1-propoxy-2-propanol at temperatures from -25 °C to 40 °C 124
5.26. Specific conductivity κ of Bu_4NNO_3 in 1-propoxy-2-propanol at temperatures from -25 °C to 40 °C 125
5.27. Specific conductivity κ of Bu_4NOAc in 1-propoxy-2-propanol at temperatures from -25 °C to 40 °C 126
5.28. Specific conductivity κ of Bu_4NSCN in 1-propoxy-2-propanol at temperatures from -25 °C to 40 °C 127
5.29. 3-dimensional illustration of $\kappa(\mathrm{m}, T)$ of Bu_4NOAc in PnP 128
5.30. Residual plot $(\kappa^{\mathrm{calc}} - \kappa^{\mathrm{exp}})/\kappa^{\mathrm{exp}} \cdot 100\,\%$ 130
5.31. Positions μ of the conductance maxima for Bu_4NNO_3 (●), Bu_4NSCN (▽), Bu_4NBr (■) and Bu_4NOAc (△) 132
5.32. Positions μ of the conductance maxima at various temperatures 132
5.33. Molar conductance of Bu_4NNO_3 solutions in PnP at different temperatures 133

6.1. Scheme of the vapor pressure apparatus 142
6.2. Photograph of vapor pressure apparatus 142
6.3. Degassing unit for liquids 143
6.4. $p = f(t)$ at 373.15 K 145
6.5. $\Delta p = f(t)$ at 298.15 K 145
6.6. Time-dependent temperature within the air thermostat 146
6.7. Plot of $\ln(p)$ against T^{-1} for PnP 149
6.8. The concentration dependence of the vapor pressure for Bu_4NSCN solutions at different temperatures. 150

6.9. The concentration dependence of osmotic coefficient for Bu_4NBr in 1-propoxy-2-propanol as function of molality at different temperatures 151
6.10. The concentration dependence of osmotic coefficient for Bu_4NNO_3 in 1-propoxy-2-propanol as function of molality at different temperatures 151
6.11. The concentration dependence of osmotic coefficient for Bu_4NOAc in 1-propoxy-2-propanol as function of molality at different temperatures 152
6.12. The concentration dependence of osmotic coefficient for Bu_4NSCN in 1-propoxy-2-propanol as function of molality at different temperatures 152
6.13. Osmotic coefficients for Bu_4NBr in different solvents 154
6.14. x, f, a, ϕ^{id} and ϕ of PnP 161

List of Tables

4.1. Effect of pressure on the fugacity of a pure, condensed and incompressible substance; $\nu_i = 100\,\mathrm{cm^3\,mol^{-1}}$ at $T = 300\,K$ . . . 22
4.2. Thermodynamic consistency tests . . . 32
4.3. Summary of binary systems under investigation . . . 34
4.4. Description of the apparatus components . . . 36
4.5. Important parameters of the GC throughout the measurements . . . 39
4.6. Partial molar volumes of alkoxypropanols and aliphatic alcohols/water at infinite dilution 49
4.7. Correlation parameters and the absolute deviations in boiling points and vapor-phase mole fractions for the binary systems . . . 61
4.8. The correlation results for binary system composed of PnP + ethanol . . . 64
4.9. Infinite dilution activity coefficients γ_i^{∞} at different temperatures . . . 65

5.1. Parameters of Eq. (5.46), $\sigma = 2.6 \times 10^{-4}$ . . . 77
5.2. Parameters obtained by using the Steinhart equation . . . 79
5.3. Values of the coefficients of the polynomial equation for density . . . 82
5.4. Experimental densities (d_{PnP}) of PnP at different temperatures T . . . 82
5.5. Comparison between literature and experimental density data of PnP . . . 83
5.6. Density coefficients D as slope of the function $d = f(\tilde{m})$ . . . 84
5.7. Calibration results for capacitor filled with argon in the temperature range between $-25\,^{\circ}\mathrm{C}$ and $+40\,^{\circ}\mathrm{C}$ . . . 87
5.8. Coefficients of least-square regression for vacuum capacity of the cell $C_0(T)$ . . . 88
5.9. Coefficients for polynomial equation (5.59) . . . 89
5.10. ${\epsilon_{\mathrm{PnP}}}^{\mathrm{exp}}$ as a function of temperature . . . 89
5.11. Constants for capillary viscometer . . . 93
5.12. Polynomial coefficients for calculation of viscosity . . . 94
5.13. Calculated viscosities (η_{PnP}) of PnP . . . 94
5.14. Comparison between experimental and literature viscosity data of PnP . . . 95
5.15. Coefficients of polynomial expression for molar conductivity of KCl . . . 102
5.16. Cell constants C at 298.15 K . . . 102
5.17. Cell constants C at different temperatures . . . 103
5.18. Results of FJ3-analysis Bu_4NBr in PnP . . . 108
5.19. Results of FJ3-analysis Bu_4NNO_3 in PnP . . . 108
5.20. Results of FJ3-analysis Bu_4NOAc in PnP . . . 109
5.21. Results of FJ3-analysis Bu_4NSCN in PnP . . . 109
5.22. Ionic radii and diameter of solvent PnP . . . 110
5.23. Enthalpy of activation of the charge transport, $\Delta H^{\ddagger}$, in the temperature range from 248.15 to 313.15 K. . . . 112
5.24. Limiting ionic conductivities λ_i and Stoke's radii r_i in PnP . . . 113
5.25. Limiting molar conductivities and association constants of Bu_4NBr in PnP . . . 116
5.26. Coefficients of equation $\Delta G_A^0(T) = A_0 + A_1(298.15 - T)$ and $\Delta H_A^0(298.15K)$ for the systems under investigation. . . . 117
5.27. Cell constants C of capillary cells for concentrated electrolyte solutions at 298.15 K . . . 120
5.28. Casteel-Amis: Regression results for Bu_4NBr . . . 124
5.29. Casteel-Amis: Regression results for Bu_4NNO_3 . . . 125

5.30. Casteel-Amis: Regression results for Bu_4NOAc . . . 126
5.31. Casteel-Amis: Regression results for Bu_4NSCN . . . 127
5.32. Coefficiens of multiple regression $\kappa(mT)$ for Bu_4NBr . . . 129
5.33. Coefficiens of multiple regression $\kappa(mT)$ for Bu_4NNO_3 . . . 129
5.34. Coefficiens of multiple regression $\kappa(mT)$ for Bu_4NSCN . . . 129
5.35. Coefficiens of multiple regression $\kappa(mT)$ for Bu_4NOAc . . . 129
5.36. The minimum of molar conductance, Λ_{min}^{exp} ($S\,cm^2\,mol^{-1}$), and its position, c_{min}^{exp} ($mol\,dm^{-3}$) 134
5.37. Ion-pair and triple-ion formation constants . . . 135

6.1. Second virial coefficient, B_S, molar volume, $v^{*(l)}$ and vapor pressure, p^*, of pure PnP at different temperatures. . . . 141
6.2. Coefficients of the different vapor-pressure equations for PnP . . . 147
6.3. Density, d^*, relative permittivity, ϵ and Debye-Hückel constant for the osmotic coefficient in molality, A_ϕ, and mole fraction scale, A_x. . . . 157
6.4. The parameters for the Pitzer Model for PnP solutions of Bu_4NBr . . . 158
6.5. The parameters for the Pitzer Model for PnP solutions of Bu_4NNO_3 . . . 158
6.6. The parameters for the Pitzer Model for PnP solutions of Bu_4NOAc . . . 159
6.7. The parameters for the Pitzer Model for PnP solutions of Bu_4NSCN . . . 159

B.1. Calibration results of GC for binary mixtures . . . 169

C.1. Experimental VLE data for the binary mixtures of 1-Propoxy-2-propanol with some aliphatic alcohols and water at 20.0 kPa . . . 171
C.2. Experimental VLE data for the binary mixtures of 1-Propoxy-2-propanol with some aliphatic alcohols and water at 101.3 kPa . . . 173
C.3. Values of the composition y_i, vapor pressure p, partial pressure p_1, and activity coefficients γ_i . . . 176

D.1. Experimental densities d_{PnP} at different temperatures . . . 177
D.2. Experimental dynamic viscosities η_{PnP} at different temperatures . . . 177
D.3. Experimental relative permittivity ϵ_{PnP} at different temperatures . . . 177

F.1. Experimental vapor pressure data of 1-propoxy-2-propanol . . . 183
F.2. Vapor pressure lowering, Δp, and osmotic coefficients, ϕ, for Bu_4NBr . . . 184
F.3. Vapor pressure lowering, Δp, and osmotic coefficients, ϕ, for Bu_4NNO_3 . . . 185
F.4. Vapor pressure lowering, Δp, and osmotic coefficients, ϕ, for Bu_4NOAc . . . 186
F.5. Vapor pressure lowering, Δp, and osmotic coefficients, ϕ, for Bu_4NSCN . . . 188

G.1. Parameters for PnP solutions of Bu_4NBr . . . 191
G.2. Parameters for PnP solutions of Bu_4NNO_3 . . . 191
G.3. Parameters PnP solutions of Bu_4NOAc . . . 192
G.4. Parameters for PnP solutions of Bu_4NSCN . . . 192
G.5. Model of Clegg et al. parameters for PnP solutions of Bu_4NBr . . . 193
G.6. Model of Clegg et al. parameters for PnP solutions of Bu_4NNO_3 . . . 193
G.7. Model of Clegg et al. parameters for PnP solutions of Bu_4NOAc . . . 194
G.8. Model of Clegg et al. parameters for PnP solutions of Bu_4NSCN . . . 194

1. Introduction

A continuing growing awareness of the toxicological and environmental concerns of certain chemicals has aimed at restricting the massive use of chlorinated solvents and certain „volatile organic compounds" (VOC) and „volatile organic material" (VOM). As early as in the 1970s for instance, the US Environmental Protection Agency (EPA) named as criteria or „hazardous pollutants" sulfur dioxide, carbon monoxide, nitrogen monoxide, ozone, lead and nonmethane hydrocarbons, known as VOC nowadays. The EPA has identified many volatile organic compounds present in consumer products among which are such common solvents as ethanol, isopropyl alcohol, kerosene, and propylene glycol; and common hydrocarbon solvents such as isobutane, butane and propane, which are often employed as propellants in various aerosol sprays. The search for suitable replacements of the chemicals mentioned is arising from the environmental concern. And only a few of the problems are faced by the chemical and industrial sectors in finding substitute materials. Specifically the growing demand of ethers derived from propylene glycol is an impressive example of a new class of chemical compounds, the industry was obliged to find as substitute for the widely used ethylene glycol based ethers in degreasing processes and cleaning formulations.

Classic glycol ethers are oxygenated hydrocarbons having a primary or secondary hydroxyl group at one end, an alkyl (R^1) ether bond at the other and in between up to three oxyalkylene repeating units with the formulae $R^1 - O - [CH_2 - CH(R) - O]_n - H$ [1]. For the well-known and widely used oligo ethylene glycol ethers, R = H. The short-chain ethylene glycol alkyl ethers are also referred to as ethoxylated alcohols (C_iEO_j, $i \leq 4$, $j \leq 2$). Compounds with $n > 3$ are called polyglycols.

Solvents derived from ethylene glycol ethers have been used in a large scale on the market, firstly introduced in 1930 as a solvent of cellulose polymers and later also used in degreasing and cleaning processes. However, since the 1980s toxicological studies proved them to be hazardous to health and may present genotoxic activity [2]. The need for a less harmful alternative resulted in the growing interest in ethers based on propylene glycol ($R = CH_3$). As final synthetical products of propylene glycol alkyl ethers (PGAE)[1] are often a mixture of constitutional isomers, metabolism can differ significantly, leading to varying toxicological metabolites. Primary alcohols are excellent substrates for alcohol dehydrogenase, yielding relatively harmful alkoxy acids. Recent teratology studies, however, strengthen the assertion that the merely contaminant quantities of those isomers does not increase the toxicological profile of commercial PGAE [3].

For practical reasons the terminology based on the abbreviation of the alcohol component and the propylene glycol, the constituents making up the chemical compound, is used throughout this thesis; i. e. C_3PO_1 = PnP = 1-propoxy-2-propanol. The first letter „P" designates the oxide from which the glycol ether is produced. The letters „nP" designates the alcohol from which the glycol ether is produced, in this case *n*-propanol.

Chemical structures for a typical example of both C_iPO_j and C_iEO_j are given in Fig. 1.1. No fewer than 40 industrial produced solvents are attributed to this denomination, although these are often used in different ways. A first address to turn to for detailed information on the solvents synthesis, industrial use, general properties, metabolism and physical properties is given elsewhere [4, 5].

There is now a great number of patents dealing with PGAE's and their widespread usage in different industrial applications. The fact that these substances possess both hydrophilic and hydrophobic functional groups accounts for their frequent use as cosolvents in organic/water product formulations, cleaning solutions, paints, coatings and inks. Bauduin [5] investigated the properties of aqueous mixtures of propylene glycol ethers in terms of their ability in deinking and degreasing mechanical and electronic parts. Their fast evaporation rate and excellent ability to solubilize organic soils is another argument for commer-

[1] According to the terminology given above for ethylene oxide-based glycol ethers, propylene oxide-based ethers are often referred to as C_iPO_j also.

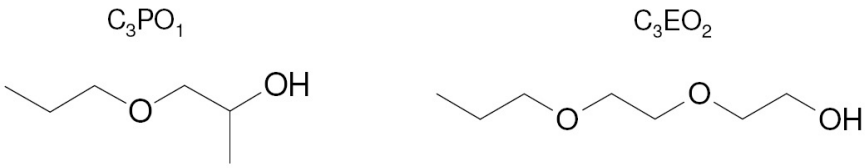

Figure 1.1.: Chemical formula of glycol ethers based on propylene oxide (left: propylene glycol *n*-propyl ether (PnP), 1-propoxy-2-propanol) and based on ethylene oxide (right: Di(ethylene glycol) *n*-propyl ether (DEnP))

cial products utilization (windows, floor or kitchen cleaning) [6], in which respect a very good example is given in patent [7]. The invention provides new binary organic solvent cleaning solutions which are nonflammable, have a mild odor and a low toxicity. Optimized evaporation rate to dry from the surface is accounted for by using PnP in a concentration range of 25-75 % in a mixture with methyl or ethyl lactate. New binary homogeneous azeotropes of octamethyltrisiloxane ($(CH_3)_3Si0(CH_3)_2SiOSi(CH_3)_3$, OMSi) with PnP used as environmentally friendly cleaning agents are enclosed in Ref. [8]. An especially significant and unexpected result flowing from the use of the azeotropes is that it possesses an enhanced solvency power in comparison to the use of OMSi alone, together with advantage and benefit of being more easily recovered and recirculated. In most cases similar cleaning efficiency can be achieved with different propylene glycol ethers.
They also find use as special-purpose fluids including automotive brake fluids and industrial process solvents. From a more scientific point of view an alternative use of propylene glycol alkyl ethers instead of toxic and highly flammable methanol in the determination of traces of water (Karl-Fischer reaction), large amounts of solvent MeOH can be abolished regardless the type of measuring technique (coulometric/volumetric, single-stage/two-stage titration) [9]. Recent developments in biochemistry show their potential to facilitate selective release of intracellular proteins from bacterial fermentation broth [10, 11] and to extract hydrophilic carboxylic acids and polyhydroxy compounds from aqueous solutions [12].

Propylene glycol ethers are commercially prepared by reacting propylene oxide with an alcohol of choice in the presence of a catalyst. Unlike ethylene glycol ethers, which react ethylene oxide to various alcohols, the use of propylene oxide results in the formation of distinct isomers within the specific propylene glycol ether product [6]. The major isomer, typically present in greatest amount, is a secondary alcohol referred to as the α-isomer (left image in Fig. 1.1). The minor isomer, present in small amounts, is a primary alcohol commonly referred to as the β-isomer. The commercial product PnP used within this work contains about 95 % α, the remainder (< 4.9 %) being β-isomer. Ratios of isomeric composition are obtained from gas chromatographic analysis (see Chap. 2). There is one asymmetrical carbon atom in the molecule, hence configurational isomers may also exist.
Since the final product contains an alcohol group, it can be reacted further with additional propylene oxide to yield dipropylene glycol propyl ether (comparative to right image in Fig. 1.1), increasing the number of possible constitutional isomers up to 4. In the same manner extensional additions of propylene oxide units yield products with longer propylene glycol units.

Compared to the abundant literature about C_iEO_j only few experimental data are published about short PGAE. Some investigations cover the volumetric properties of glycol ethers, both with experimental results and calculations [13, 14], the thermophysical and health-related characteristics like cytotoxicity, eye-irritancy and biodegradability [15] or microscopic structures of binary water/PGAE mixtures [16]. Upon the feature that PGAE as well as C_iEO_j are amphiphilic molecules, combining characteristic properties of organic solvents (volatility and solubilization of organics) with those of surfactants (surface activity, formation of emulsions, microemulsions and similar structures), they are considered as hydrotropes or solvo-surfactants. Bauduin et al. [17] gave an attempt for a general classification of cosolvents and hydrotropes by dissolution of an hydrophobic dye in water in the presence of different organic solvents and propylene glycol monoalkyl ethers. In this context the minimum hydrotropic concentration (MHC) is

introduced, a concentration at which the increase in the amount of dissolved hydrophobic compound becomes significant. Surface tension measurements on PnP and DPnP have been thoroughly probed by Bauduin et al. [4] and Lunkenheimer et al. [18], the latter pointing out that inherent, also surface-active contaminants in commercially available ethers may significantly alter their properties.
Studies of the solubility behaviour of several C_iEO_j and PGAE in water exhibit that these mixtures have lower critical solution temperatures (LCST) [4, 19]. The appearance of a LCST is characteristic for systems, in which hydrogen bonds are the dominating interactions. For PGAE the molecules become more hydrophobic (lowering the LCST) as the number of repeating oxypropylene units increases. For 1-propoxy-2-propanol (PnP), studied in the present paper as an exemplary short-chain PGAE, Bauduin [4] determined a LCST of about 32 °C.
Despite the wide range of applications of short-chain propylene glycol monoalkyl ethers in industrial as well as commercial areas, thermodynamic data are either constraint to a relatively small temperature range or not known at all (unless calculated).
This thesis aims specifically at the thermodynamic characterization of propylene glycol n-propyl ether in its pure liquid state, investigating its solution behavior in binary mixtures with different hydroxylic solvents and a comprehensive exploration of the ionic interactions and solvent's activity in electrolyte systems with 1:1 salts.
This dissertation, comprising different studies, is organized in different parts, each of which focuses on a distinct aspect of some different chemical and physical properties.
Chap. 2 presents an overview of the cleaning and purification procedures applied for all salts, solvents and gases, which are involved in the experimental parts. This chapter is apart from all following in that it provides no novel relevant thermodynamic information and is placed at the beginning of the work therefore. It comprises exact information on quantities and equipment required for a relying replication of all purification steps.
Chap. 3 describes four different techniques aiming at a better understanding of the relation between the hydrotropic properties addressed to PnP, and „critical" phenomena in solution. In the present study extensional techniques expand the findings of Bauduin [5] on the solubility behavior in water-PnP mixtures. To this purpose precise surface tension measurements are established along with precise density and heat capacity measurements of aqueous PnP mixtures at 25 °C. Interestingly it could be shown that the maximum in the apparent molar heat capacity and the minimum in the apparent molar volume closely coincide with the onset of increased solubility and the concentration at which the slope of the surface tension significantly changes. It is proposed that this region comes along with the formation of microheterogeneous structures in solution.
In **Chap. 4** is presented the phase equilibria in the binary systems containing PnP and (methanol, ethanol, 2-butanol, 1-hexanol and water, respectively) at 20 kPa and atmospheric pressure. Data of the binaries PnP + water and PnP + PM are obtained at atmospheric pressure only. The data are analyzed in terms of the Wilson, NRTL and UNIQUAC equations and compared to the predictive results of the COSMO-RS and modified UNIFAC (Dortmund) models. The present work aims at contributing to the development of a data base for thermodynamic properties of mixtures containing PGAE, starting with PnP. For that purpose a `Maple` based program script has been developed, incorporating all necessary input information, enabling an automated data progression and processing the output of characteristical numerical results for graphical data presentation, the plots of which are shown in this part of work.
Comprehensive investigations on the electrical conductivity in dilute solutions of PnP enable statements on the association behavior of the ions, their mobility and solvation within the continuous liquid phase. **Chap. 5** is devoted to precise measurement on electrical conductivity of Bu_4NX ($X = Br^-$, NO_3^-, SCN^- and OAc^-) in PnP for the first time. Pure solvent's properties like liquid density, relative permittivity and viscosity in the temperature range between 248.15 K and 313.15 K are also performed on that occasion. Results from low concentrations enter the interpretation of conductivity behavior up to concentrations as high as 1 mol dm^{-1} and more. All systems exhibit a considerable formation of ion pairs and higher aggregates, respectively, upon data analysis with the help of the Chemical Model.
Apart from methods regarding the transport properties (e. g. electrical conductance), precise vapor pressure techniques, developed and designed at the institute, allow for a comparable study of interactions

occurring in solution. **Chap. 6** describes the measurements of electrolyte solutions' vapor pressure of the four electrolytes already presented. Knowledge of the vapor pressure lowering between pure solvent and solutions directly result in the activity and activity coefficient of the solvent, respectively. The Gibbs-Duhem equation allows for a conversion into the mean activity coefficient of the electrolyte. The highly associated systems are subject to different regression models. Experimental vapor pressures of 1-propoxy-2-propanol over a wide temperature range also contribute a very important part of this chapter, as this fundamental property plays an important role not only for experimentalist. It is required for a variety of thermodynamic calculations and simulations (see Chap. 4) and is also a key parameter in the field of quantum and statistical mechanics [20].

Due to the solvent's inherent importance for industrial as well as commercial applications, results from this dissertation can be regarded as being not only of academic interest. Many chemical process steps, involving the propylene glycol propyl ether in different forms of application, may be best planned, controlled and optimized with reliable, basic thermodynamic property data. It is very useful to have phase equilibrium data in the process design for recovery of PnP from the spent aqueous or non-aqueous solutions, which are often encountered in special cleaning fluids (see above). Furthermore such data sets are a sound fundament for the development and validation of theoretical models as well as that such results supplement existing database entries for scientific and economical use (e. g. DECHEMA). Binary interaction parameters obtained in this work may turn out to be used for the prediction of properties of similar systems. The presence of electrolytes in industrial processes requires knowledge of the non-ideality of these solutions in terms of the activity and osmotic coefficient. Only few osmotic coefficient measurements, however, have been made for salts in non-aqueous electrolyte solutions, the thermodynamic properties of which are important for many practical applications. In this connection the salt-depending change of the phase behavior in aqueous mixtures with PnP is a representative example [21].

2. Materials, Purification and Analysis

This chapter is devoted to the detailed explanation of the chemicals used, either as calibration substance or for the corresponding measuring technique. All solvents and salts are used throughout this thesis as result of these purification procedures. They were usually stored in specially designed flask and under a protective atmosphere of nitrogen.

2.1. Pure Solvents

For a proper handling of pure solvents or solvent mixtures under a permanent atmosphere of inert gas, different types of glass flask have delivered an optimal performance in practice. Freshly distilled solvents are directly transferred into flasks of the model shown in Fig. 2.1 (taken from [22]). A long-time stability without a detectable change of quality is maintained within several month. These vessels are equipped with a 14/23 NS cone joint, facilitating the close connection to the distillation apparatus. Rotaflo- or Young stopcocks ensure gas-tight sealing to the atmosphere without the need for glass grease. Stock

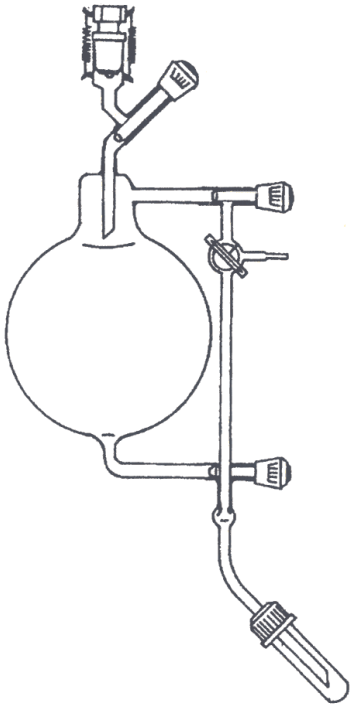

Figure 2.1.: Vacuum-tight solvent vessel for long-time storage

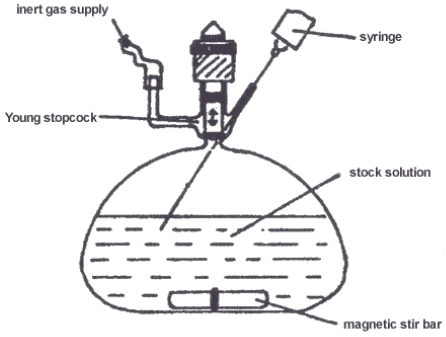

Figure 2.2.: Glass vessels for storage and preparation of electrolyte solutions

solutions of electrolytes may be prepared and handled within glass vessels, specially designed and of low weight as displayed in Fig. 2.2 ([22]). Accurate concentration determination is possible and solutions can be stored for the time period of general conductance measurements. Both flasks are used in the experiments on electrical conductivity, whilst 2.1 serves as container for the regularly used solvents PnP, water, and ethanol also.

2.1.1. Water

The water for the heat capacity measurements, the vapor-liquid equilibria measurements, calibration of the conductivity cell and for all vapor pressure experiments is directly withdrawn from the `Millipore` purification station under a continuous atmosphere of nitrogen. Each aliquot has a specific conductivity of less than $2 \times 10^{-7}\,\mathrm{S\,cm^{-1}}$. It was furthermore double distilled for calibrating the Ubbelohde viscometer and the vibrational tube densitymeter and for the surface tension measurements. An all-quartz column is employed with two independently working heating devices. It allows for the collection of up to 500 mL within 3-4 hours by directly distilling of the water into a flask permitting storage and transference of the solvent into the measuring device under an atmosphere of inert gas.

2.1.2. Propylene Glycol Ethers

1-propoxy-2-propanol (CAS 1569-01-3) is purchased from Sigma-Aldrich with a stated purity of 99 %. Because of small amounts of the isomeric form 2-propoxy-1-propanol (referring to the synthetical route, this by-product emerges from a nucleophilic attack of 1-propanol on position 2 of (±)-propylene oxide [1]), relatively large amounts of this commercial product are purchased, collected and used from the beginning of this work for every experimental investigation. As a changing composition may influence the experimental results and parameters to a certain extent, this precaution helps to minimize any parasitic effect of chemical nature.
Prior to the purification procedure by distillation, 1-propoxy-2-propanol is stored over molecular sieve (3 Å) for at least two weeks. The commercially available solvent is fractionally distilled over a small Vigreux column under reduced pressure ($p < 0.1$ mbar). The distillate is collected in specially designed glass flasks (see Fig. 2.1), allowing for the storage and handling of the liquid samples.
Gaschromatographic analysis (HP-5 column (30 m), FID detector) of the raw solvent reveals impurities with a maximum amount of 0.5 %. Upon distillation the final product shows a purity of better than 99.96 % in the gaschromatogram (neglecting the response factor). A typical GC run gives the following gaschromatogram of PnP in Fig. 2.3. The first two peaks at around 2 min are coming from traces of acetone, used for automatic cleaning of the injection needle and not considered for quantification. The

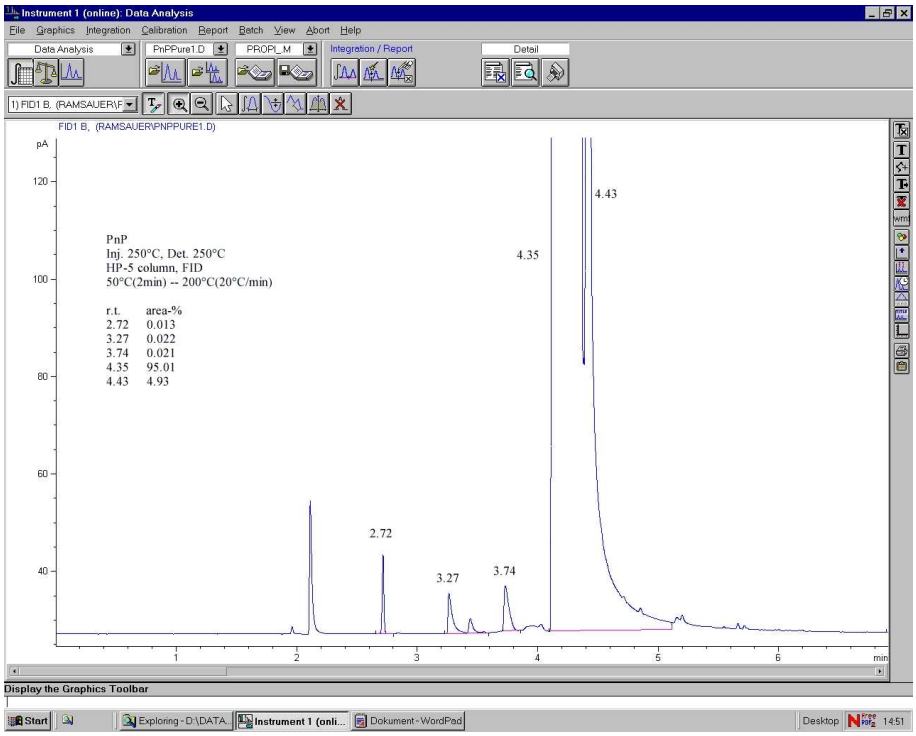

Figure 2.3.: Gaschromatographic analysis of PnP (Sigma-Aldrich)

two constitutional isomers elute at different retention times (r.t.$_1$ = 4.35, r.t.$_2$ = 4.43 min), the ratio of

which, however, does not change in any further GC quality assurances. As even minute impurities of high volatility can have a dramatic influence on such a property like vapor pressure, additional head-space analysis are undertaken to quantify the amounts of impurities in the gas phase. Fortunately, the distillative procedure described reduces these impurities to an extent of less 300 ppm. There is no change detectable between the isomeric composition of liquid injections and analysis of the gaseous sample in head-space analysis. The water content of any sample taken does not exceed a value of 90 ppm, as measured by Karl-Fischer titration (mci, model CA-02), and the specific conductance accounts for less than $6 \times 10^{-7}\,\mathrm{S\,m^{-1}}$.

1-methoxy-2-propanol (CAS 107-98-2) is purchased from Sigma-Aldrich with a stated purity of $\geq 99\,\%$. An equal purification as well as drying procedure is applied and results in a final product of purity $\geq 99.6\,\%$ and a water content of less than 110 ppm. The distribution of two constitutional isomers, also based on the area ratios in GC measurements, reveals a content of 96 % of 1-methoxy-2-propanol.

2.1.3. Ethanol

Ethanol (p.a. Merck) with an initial water content of about 0.15 % is dried with amalgamated aluminium shot [23][1]. Subsequent distillation over a Vigreux column reduced the water content to less than 30 ppm and detectable organic impurities to less than 200 ppm.

2.2. Electrolytes

2.2.1. Potassium chloride KCl

Potassium chloride, KCl (Merck, p.a.), is recrystallized from bidistilled water twice and dried for several days at 200 °C in vacuo ($p < 10^{-2}$ mbar). The drying device is permanently supplied with P_2O_5. KCl is stored under an atmosphere of dry nitrogen.
$M(\mathrm{KCl}) = 74.555\,\mathrm{g\,mol^{-1}}$; $\rho(\mathrm{KCl}) = 1.984\,\mathrm{g\,cm^{-3}}$ [24]

2.2.2. Tetrabutylammonium Salts

All four salts used are purified according to the same procedure.
Bu_4NBr (puriss), Bu_4NSCN (purum) and Bu_4NOAc are purchased from Sigma-Aldrich, Bu_4NNO_3 (puriss) is purchased from Merck. All salts are dried under reduced pressure ($\mathrm{p} < 10^{-1}$ mbar) in the presence of P_2O_5 prior to the preceding purification: all salts are heated in diethylether to reflux and acetone is successively added until complete dissolution. The warm solution is filtered to remove any insoluble constituents. The recrystallization procedure is repeated several times until the mother liquor is colorless. The crystallized salts are dried over P_2O_5 under vacuum. Temperature does not exceed 50 °C. The more or less hygroscopic products are stored in a glove box under nitrogen atmosphere until further use.

$M(Bu_4NBr)$	$= 322.38\,\mathrm{g\,mol^{-1}}$	$\rho(Bu_4NBr)$	$= 1.13\,\mathrm{g\,cm^{-3}}$ [25]
$M(Bu_4NNO_3)$	$= 304.48\,\mathrm{g\,mol^{-1}}$	$\rho(Bu_4NNO_3)$	$= 0.909\,\mathrm{g\,cm^{-3}}$ [26]
$M(Bu_4NOAc)$	$= 301.51\,\mathrm{g\,mol^{-1}}$	$\rho(Bu_4NOAc)$	$= 1.0\,\mathrm{g\,cm^{-3}}$
$M(Bu_4NSCN)$	$= 300.55\,\mathrm{g\,mol^{-1}}$	$\rho(Bu_4NSCN)$	$= 1.0\,\mathrm{g\,cm^{-3}}$

The formerly not available Bu_4NOAc is attempted to be synthesized via ion-exchange on a basic ion exchange resin (ion exchanger III, Merck). In a first preparation step the ion exchanger is loaded with aqueous solution of sodium acetate. A four-fold excess of NaOAc (840 mmol, 69 g) is dissolved in 4.2 $\mathrm{dm^3}$ water. For a successful anion exchange, 210 mmol (63.3 g) Bu_4NBr in 1.6 $\mathrm{dm^3}$ water is slowly columned over the exchanger resin. Progression of reaction is followed by the pH-value of the eluting electrolyte

[1] I´m very grateful to M. Kellermeier, who kindly supplied me with a charge of dried ethanol

solution (basic solution in the presence of OAc^-). Obtained aqueous solutions are freeze-dried and the viscous, brown residual is further dehydrated by repeated azeotropic distillation with toluene. The raw product is dried under vacuum and recrystallized as described above. Due to the small yield of only a few grams related to the amount of Bu_4NBr and the expenditure of time turn this synthetical route into an inappropriate way for the preparation of Bu_4NOAc. Fortunately the salt can be obtained commercially in the meantime.

2.3. Nitrogen Purification

The high accuracy and precision either of conductance, dielectric permittivity, density, viscosity, and vapor pressure measurements makes it necessary to ensure a well defined, pure and inert atmosphere of dry gas. For that reason precautions are taken to avoid any contact between solvent, solvent mixtures and electrolyte solutions with air by applying the technique according to Schlenk. Most of the time nitrogen is used as inert gas, exceptionally argon is implied in the permittivity measurements. Handling of hygroscopic solid materials is performed in a glove box flushed with nitrogen.
The commonly used N_2 is taken from the in-house pipeline, Ar is available in gas cylinders (99.9996 %). The inert gases are purified in a three-step process: first residual traces of oxygen are chemically bound on a BTS-catalyst (operational temperature of 140 °C, Merck), soda-lime subsequently removes carbon dioxide and the concluding blue gel (Merck) and P_2O_5 is responsible for a successful removal of humidity.

3. Properties and characterization of 1-propoxy-2-propanol / water mixtures

In the present chapter a comparative study on four different experimental techniques investigating the binary liquid system of PnP + water is presented. The aim of this is to support and extend already existing observations and results with respect to the hydrotropic nature of PnP and possible phase-transitions in aqueous mixtures.
In this work a systematic evaluation of the effects of 1-propoxy-2-propanol on different properties is presented: the solubility behavior of a hydrophobic dye in aqueous solutions of PnP [17], surface tension measurements ([4], this work), apparent molar volumes of binary mixtures containing PnP and water (this work), and apparent molar heat capacities (this work). The examination of different solution properties aims at verifying the generality of the hydrotrope behavior, as well as at providing some insight on their mechanism of action. More specifically, these results will be analysed in terms of the variations of the measured effects as function of the hydrotrope concentration, in order to verify the existence of proposed critical aggregation region [27].
All results hint to the point of a certain threshold concentration of PnP, at which a significant change in the slope or the course of the plots for O.D. (optical density), γ (surface tension), Φ_c (apparent molar heat capacity), and Φ_v (apparent molar volume) occurs. At this point the onset for the formation of aggregates (whatever the exact geometry or structure is) composed of the hydrotropic molecule PnP, alongside with an increased solubility of the hydrophobic dye, is believed to come into play.

3.1. Solubilization curve

While most compounds when dissolved in water decrease the solubility of a second component, some present opposite behavior, leading to considerable solubility increase. Compounds that cause increase in aqueous solubility are sometimes called hydrotropes, or chaotropes [28]. Over 90 years ago, Neugerg [29] described the large increase in the solubility in water of a variety of hydrophobic compounds brought about by the addition of certain, hydrotropic compounds. Many different compounds have been used as hydrotropes, including urea, guanidinium chloride, nicotinamide, tetraalkyl ammonium halides, aromatic sulfonates, sodium thiocyanate [30–33]. There have been various theoretical and experimental efforts aiming at an explanation for the effects of precipitation of proteins [34], increase of cloud points of detergent solutions [35], and changes in reaction rates [36, 27]. Despite continuous attempts over the years, there is still no consensus on the mechanism behind hydrotropy. Whilst at the beginning hydrotrope molecules were assumed to aggregate by a stacking mechanism of the planar aromatic ring present in their chemical structure [37, 38], this explanation has been reviewed in case of aliphatic compounds such as short sodium alkanoates [39] or alkyl sulfates, which also show hydrotropic behavior [40].
From a systematic investigation on the solubility behavior of a hydrophobic dye, i. e. disperse red 13[1] in water by means of some additives, Bauduin [17] and Makowski [41] classified the additives according to their hydrophobic efficienies, i. e. their abilities to solubilize a water-insoluble hydrophobic compound. The general and similar physico-chemical behavior of the additives studied, formerly classified as co-solvents, hydrotropes, and solvo-surfactant, shows no need to distinguish between these different types and that these synonyms can be used equivalently. The authors present a correlation of the hydrotropic efficiencies with the hydrotropic hydrophobicity, proven by some simple quantum mechanical calculations. Within this work only the results for aqueous solutions of PnP are considered and a plot of the optical density vs. the mole fraction of PnP is shown in Fig. 3.1. Note that the ordinate is given in logarithmic scale. The results are taken from [41]. The profile exhibits a sudden solubility increase of the dye when

[1] 2-[4-(2-chloro-4-nitro-phenylazo)-N-ethylphenylamino]ethanol

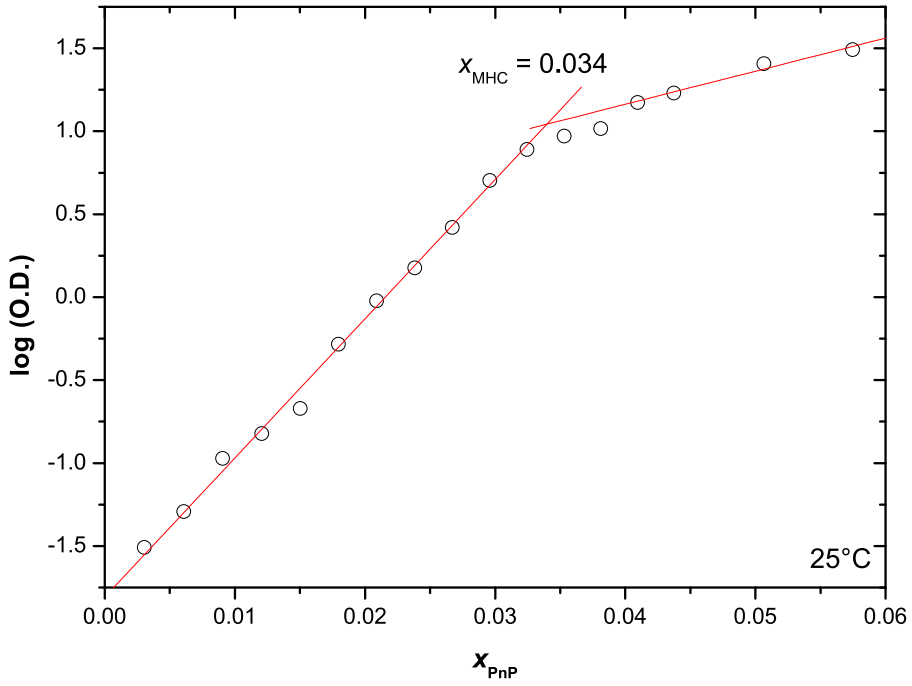

Figure 3.1.: The optical density (O.D.) as function of x_{PnP}; (O.D.) is proportional to the amount of dissolved dye

the additive concentration exceeds a certain threshold, namely the minimum hydrotropic concentration (MHC). Above the MHC the solubilization effected by the dye is increasing linearly. For a more generalized solubility behavior of various additives, refer to [42]. This sudden increase is rationalized in terms of hydrotrope cooperative self-aggregation, although different mechanism schemes are discussed in the literature [43]. This aggregation behavior is often compared to the cooperative process such as micellization, though somewhat less dramatic and efficient. Noteworthy to mention that Balasubramanian explicitly pointed to significant differences between hydrotrope molecules and surfactants, as well. Still the ongoing debate about the detailed interaction pattern accompanying these phase transitions has not ended.
Another statement commonly connected with hydrotropes is their chemical behavior of being surface active [27] and that the change of the slope of the surface tension as function of the hydrotrope concentration often coincides with the MHC. This surface activity is typical for cooperative aggregation such as micellization, but will occur at much higher concentrations ($\approx 1\,\mathrm{M}$) for usual hydrotropes.

3.2. Surface Tension Measurements

In order to infer this surface tension course of aqueous mixtures containing PnP and an onset of hydrotropic association, the mixture's surface tension is determined at increasing concentration of the hydrotrope PnP at 298.15 K. These experimental data points for PnP, as shown in Fig. 3.2, are a replicate of Bauduin's x_{PnP} - γ - measurements [4], but with the improving quality of recording far more data points over the whole composition range.
The surface tension measurements are performed on a KRÜSS tensiometer K100 MK2 with the help of a standard ring suspended from a precision balance[2]. The platinum ring used has an diameter of 19.09 mm and a thickness of 0.37 mm. A direct force procedure is applied and the corrections according to Harkins & Jordan are exerted for the ring method. Collection of all data points over the whole composition range is performed within one single run with the help of an automatically operating dosing device, supplied with the apparatus. The software is provided with the pure components' density in order to convert concentration scales. Results for 2-butoxyethanol, 1-propanol, and methanol are also presented for comparison of the occurrence of these special structural phenomena. It is seen that the

[2] http://www.kruss.info/

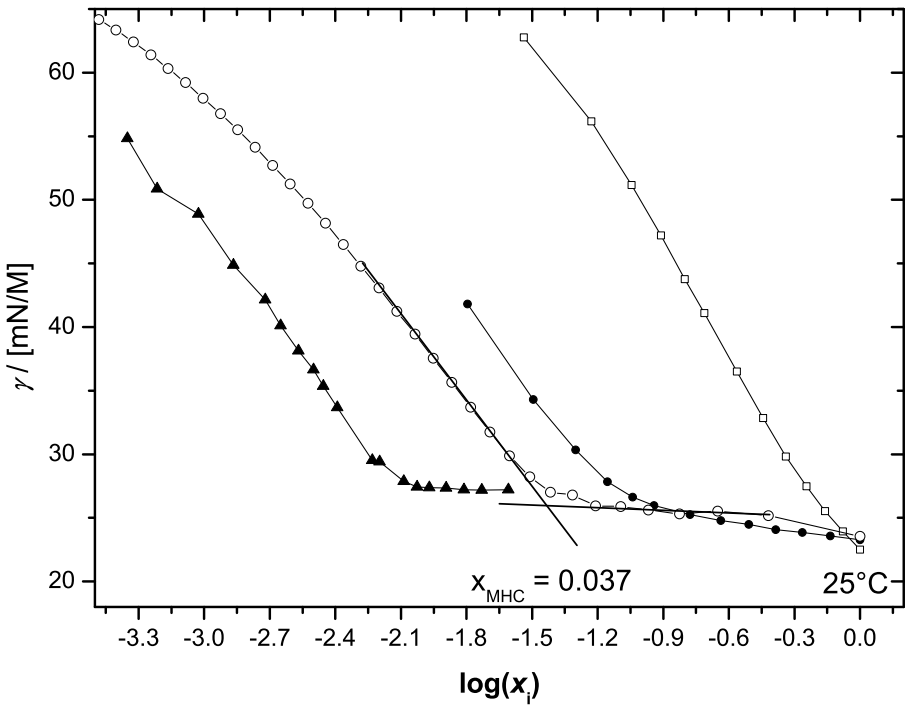

Figure 3.2.: Surface tension γ as function of $\ln x$ of different compounds: (▲) 2-butoxyethanol, (○) PnP, (●) 1-propanol and (□) methanol

surface tension γ decreases from approximately 70 mN/m for the water rich region to a limiting value of around 26 mN/m for PnP. The concentration-dependent reduction in the surface tension is more gradual with hydrotropes compared to the sharper decay encountered with micellar surfactants. The decrease in γ is sharper, however, as is the case for the corresponding n-alcohol (1-propanol) displayed in Fig. 3.2. As the surface tension remains nearly constant at higher PnP concentrations beyond a mole fraction of approximately 0.05, the surface is supposed to be widely saturated with PnP. This change in the slope is in excellent agreement to the results of Bauduin [4], who determined this onset as $x_{\mathrm{PnP}} = 0.037$. At a temperature of 25 °C the intermolecular interactions are strong enough to overcome a miscibility gap. The data in Fig. 3.2 suggest that PnP exhibits self-aggregation beyond a mole fraction of 0.037 in water to produce non-covalent assemblies. This value is remarkable close to the independently determined *minimum hydrotrope concentration* values from the solubilization experiments ($x_{\mathrm{MHC}} = 0.034$) and lend support for the assumption that both variations of the measured effects at a similar concentration point reflect the onset of the same process, namely self-aggregation. In other words, self-aggregation would be regarded as prerequisite for hydrotropic solubilization and probably for other processes being effected by addition of a hydrotropic compound.

In order to avoid a misinterpretation of the exponential decrease of the surface tension for solutions where the solute presents a positive surface excess as a sign of critical aggregation, Speight and Andersen [44] suggested a plot of γ versus the logarithm of concentration. Only than the existence of a c.m.c. (or MHC) is supported by a break in the curve. Moreover, the need for using activities a_i instead of mole fractions x_i in the Gibbs equation for analyzing surface tension curves of amphiphilic association was introduced by Strey et. al. [45]. Based on vapor pressure measurements of binary aqueous solutions of different alcohols both activity coefficients of water and organic component were derived and implied in the evaluation of surface tension data by the authors. If this is done, the break in the surface tension curves, supposed to be the onset of aggregation, disappears or is shifted to much higher values.

This fact can be, at least approximately, be proven by conversion of the mole fraction into activity considering the results of a COSMO-RS calculation for PnP + water at 298.15 K. According to the findings of vapor-liquid equilibria measurements and correlation in Sec. 4.12, the aqueous system of PnP is believed to exhibit large deviations from ideality even at the moderately low temperature of 25°C. As can be expected, the use of activity coefficients obtained in this way changes the findings. The break in the

surface tension curve is changed into a smooth sigmoidal variation.
In most of the cases, however, this fact is not been considered in the studies of hydrotropes, but it is essential for inferring correct MHC values. Corresponding experimental values for the activity coefficients of water and PnP, as obtained for the binary system of PnP + ethanol (see Sec. 4.14) by vapor pressure measurements, are missing. The coincidence of the onset concentrations of surface tension as well as solubility investigations, however, encourage us to continue on the experimental verification of the existence of proposed critical aggregation region [46].
A structural very similar compound to PnP is the molecule 2-butoxyethanol (BE), the properties of its aqueous mixtures have been devoted great attention. Both the bulk and the surface properties undergo dramatic changes in a narrow interval around a critical BE-mole fraction $x \approx 0.02$ [47, 48]. Evidence for micellar-like phase transitions in this system has been collected from infrared absorption [49], compressibility [50] and dielectric measurements [51].
Independent to these investigations, enormous work done by Koga et. al. was published on the same binary system. Studies on vapor pressures [52], partial molar volumes [53], and heat capacities [54] were published at the same time. Three composition regions in the single-phase domains exist, in each of which the mixing scheme between BE and water molecules is qualitatively different. The transition between different regions is associated with peak anomalies in quantities that are proportional to the third derivatives of Gibbs energy [52]. Most interestingly to note, that the collection of all those experimental techniques lead to the conclusion of a mole fraction $x_{\mathrm{BE}} \simeq 0.014$ being the onset for the crossover of region I to region II (see references for detailed description).
Amongst the possible techniques, the next two chapters are devoted for the volumetric and heat capacity measurements on the binary system containing PnP and water at a constant temperature of 298.15 K, because of these accurate and reliable methods being available at our institute. Comparable to the results from literature, these techniques supplement the findings of solubility as well as surface tension measurements. It is very well known that specific heat measurements are a sensitive indicator for microstructuring, resulting in informative thermodynamic characteristics that reflect hydration of organic compounds.

3.3. Measurements of Density and Heat Capacity

Systematic studies carried out by Desnoyers et. al. of the thermodynamic properties of nonelectrolytes in water have suggested the existence of transitions in aqueous solutions of certain hydrophobic organic molecules: *tert*-butanol [55], piperidine [56], and *n*-alkoxyethanols [47]. Different to many other aqueous solutions, spectacular changes in the water-rich region of the apparent molar volumes as well as in the apparent molar heat capacities are taking place, indicating important structural changes: the apparent molal heat capacity, for example, goes through a maximum and then decrease sharply towards the water-rich region. These abnormalities (termed *peak anomaly* by Koga [54]) are compared to that associated with micellization in the case of surfactants and serve as supporting evidence for microheterogeneity in binary systems [57]. Structural factors such as the hydrophobic character of the molecule, the tendency for the system to unmix, the geometry of the molecule and the nature of the polar group can contribute to the microheterogeneity. A relationship between the presence of microheterogeneity and the possibility to act as a cosurfactant for the formation of microemulsions was proven in the aqueous system with 2-butoxyethanol: BE was shown to solubilize large amounts of decane even without the addition of surfactants [58]. Bauduin et. al. gave similar results on the stability increase of micellar systems by addition of 1-propoxy-2-propanol [59, 60]. This similar kinds of action of these alkoxy-compounds encouraged the continuous work on the corresponding aqueous binaries.
In general, thermodynamic properties of binary liquid mixtures are discussed in terms of molar excess functions (see also Figure 4.20). Besides a pronounced asymmetry these curves do not normally show any anomalous behavior. However, these functions are known to reflect the characteristic intermolecular interactions not properly [55]. Partial and apparent molal quantities do not suffer from this drawback and reflect more obvious the characteristic change of interactions and structure in solution.

3.3.1. Experimental

Density The procedure for the density measurements is the same as described in detail in Sec. 5.3.3. However, binary sample solutions are prepared gravimetrically with degassed solvents prior to each data acquisition. The temperature is kept at 298.15 K throughout the investigation. The apparent molar volumes Φ_v of 1-propoxy-2-propanol (1) in water (2) are calculated from the experimental density data d with the relation

$$\Phi_{v,1} = \frac{M_1}{d} + \frac{x_2}{x_1} M_2 \left(\frac{1}{d} - \frac{1}{d_2^*} \right) \tag{3.1}$$

where M_1 is the molar mass of PnP, x the mole fraction. The density of pure water d_2^* is taken as that of Herington [61]. The experimental data x_{PnP}, d, and $\Phi_{v,\mathrm{PnP}}$ are given in Table A.1 (see Sec. A.1).

Heat Capacity The specific heat capacities of aqueous solutions of 1-propoxy-2-propanol, $\tilde{c}$, are measured using a `Setaram Micro DSC III` heat-flux calorimeter, covering the whole range of composition. New vessels with a volume of almost 1 mL equipped with an rigorously improved sealing are employed[3]. A hermetic seal has been obtained by means of a stainless steel sphere set made tight by closing the upper part of the lid. In this type of calorimeter, the output signal recorded is proportional to the total heat flow rate $\dot{Q}$. The proportionality coefficient between signal and heat flow is taken as given by the manufacturer's original calibration polynomial. In order to minimize the vapor space, the level of the liquid in the cell is always filled to a maximum extent. All samples are prepared gravimetrically. The uncertainty in the mole fraction is estimated to be less than 0.001. Conversion into molarity scale is based on the molecular weights. The exact amount of liquid solution filled in the cell is determined on a precise balance with a resolution of 1 μg.
In this work the scanning method to determine the saturated heat capacities is used. The scanning method principle is based on the relation between the heat flow rate (which is proportional to the measured calorimetric signal), the overall heat capacity of the sample (liquid and vapor) inside the cell, C, and the scanning rate β:

$$\dot{Q} = C(T)\beta = m_{\mathrm{s}} \tilde{c}(T) \beta \tag{3.2}$$

The method consists of three steps in which the reference cell is always kept empty during this work.

(a) The heat flow rate of the baseline with an empty sample cell, which is termed $\dot{Q}_{\mathrm{blank}}$, is determined. This experiment defines the asymmetry of the measuring system.

(b) The calibration substance of a recognized heat capacity is put into the sample cell. The corresponding heat flow rate $\dot{Q}_{\mathrm{ref}}$ is determined. α-Al_2O_3 is chosen on account of its very well-known heat capacity and its practical convenience. Coefficients for the fitting polynomials of the heat flow rate calibration substance are taken from [62].

(c) The calibration substance is replaced by the sample liquid and the heat flow rate obtained is termed $\dot{Q}_{\mathrm{s}}$.

In each experiment, the temperature T and the differential heat flow rate $\dot{Q}$ are recorded against time t. By successively applying Eq. (3.2) to each of the above steps, the following ratio for the overall specific heat capacity of the sample is obtained:

$$\tilde{c}(T) = \frac{m_{\mathrm{ref}}}{m_{\mathrm{s}}} \cdot \tilde{c}_{\mathrm{ref}} \cdot \frac{\dot{Q}_{\mathrm{s}} - \dot{Q}_{\mathrm{blank}}}{\dot{Q}_{\mathrm{ref}} - \dot{Q}_{\mathrm{blank}}} \tag{3.3}$$

where m_{ref} and m_{s} denote the reference and sample mass, respectively, and $\tilde{c}_{\mathrm{ref}}$ denotes the specific heat capacity of α-Al_2O_3.
The scanning rate does not appear in Eq. (3.3), but in practice the one chosen must be fast enough to avoid very long experiments and slow enough to prevent excessive thermal delay between the programmed and the real heating or cooling rates, with the consequent disturbance of the quasi-steady-state condition

[3] see engineering drawings at the institute

in the cells. A scanning rate of $0.3\,\mathrm{K\,min^{-1}}$ has been selected in all the experiments. Noteworthy to hint at the necessity to use an identical temperature program for every single measurement run.
Due to the very low amount of gas phase inside the cell, corrections for the vapor-phase heat capacity can be neglected. Therefore the experimentally detectable overall specific heat capacity $\tilde{c}$ is regarded as the saturation heat capacity $\tilde{c}_{\mathrm{sat}}$ [63]. Additionally it is not necessary to make any distinction between the isobaric heat capacity at the saturation curve, $\tilde{c}_{\mathrm{sat}} = \tilde{c}_p$, as the differences are known to be less than the experimental uncertainty. The term $\tilde{c}_p$ will be used in the following equation and in Table A.1 for that reason.
With the aim of checking the experimental technique, the saturated heat capacity of pure toluene has been measured in the temperature range $(10 - 70)\,^{\circ}\mathrm{C}$. The results are found to be in excellent agreement with those of Shulga [64] and Casanova [65].
For the mixtures a temperature program covering a range between $0\,^{\circ}\mathrm{C}$ and $40\,^{\circ}\mathrm{C}$ is selected and the reported values in Table A.1 are the average of two consecutive temperature programs. The temperature is changed at a constant rate by heating an cooling in order to minimize the effect of convection currents. Heat flow signals for blank and reference are used as average of three independent experimental runs within the period of heat capacity measurements. For each mixture and each method of measurements, a polynomial function of order 5 is used to correlate the experimental values of $\dot{Q}$ with temperature using the method of least-squares. Data points given in the appendix are based on Eq. (3.3) together with calculated values of $\dot{Q}$ from these polynomials at temperatures 278.15, 288.15, 298.15, and 308.15 K.
The apparent molar heat capacities $\Phi_{c,1}$ for PnP (1) in water (2) are calculated from the experimental data $\tilde{c}_p$ by means of

$$\Phi_{c,1} = M_1 \tilde{c}_p + 1000 \frac{\tilde{c}_p - \tilde{c}^*_{p,2}}{\mathrm{m}}, \tag{3.4}$$

the results of which are listed in Table A.1. Here $\tilde{c}^*_{p,2}$ is the specific heat capacity of pure water taken from [24]. Note that the last entry of $\Phi_{c,\mathrm{PnP}}$ at every temperature is equivalent to the molar heat capacity of the pure PnP, calculated as $M\tilde{c}^*_p$.

3.3.2. Results and Conclusion

The concentration dependence of the apparent molar volume of PnP is shown over the whole composition range in Fig. 3.3. The partial molar volume v_1 can readily be calculated from $v_1 = \Phi_{v,1} + x_1 x_2\, \mathrm{d}\Phi_{v,1} / \mathrm{d}x_1$ and is displayed as solid line in the plot, also. It is simply obtained by numerical derivation of a polynomial function fit to the values of $\Phi_{v,1}$. The results are typical for most aqueous-organic mixtures [66]: the standard partial molar volume $v_1^{\ominus}$, as obtained from a linear extrapolation to infinite dilution, is smaller than the molar volume v_1 and both apparent and partial molar volumes go through a minimum in the water-rich region and levels off to v_1. The concentration dependence of the molar volume is much more pronounced for v_1, as usual.
Contrary to this the concentration dependence of $\Phi_{c,1}$, as shown in Fig. 3.4, goes through a maximum before decreasing rapidly to the molar heat capacity $\tilde{c}^*_{p,1}$. Increasing temperature shifts the position of the peak maximum to lower concentrations of PnP. The position of the peak with values of the apparent molar heat capacity being much higher than any of the constituting pure species is indicated in the plot. No partial molar heat capacities are derived due to the spare number of data points, but a very similar enhancement of the effect in $\tilde{c}_{p,1}$ might be supposed in this case also. Normally Φ_c decreases in a regular way from infinite dilution to the pure liquid state [47].
Prior to any physical interpretation of the structural effects, a concordance of all four experimental observation with regard to the position of their appearance or maximum extent is clearly seen. It can be assumed that the same molecular organization and subsequent structural changes occurring in the binary mixture are responsible for each effect exemplified in the Figs. 3.1-3.4.
As shown by investigations on ionic surfactants, similar concentration dependence for Φ_c are found [67]: there is a sharp increase just before the critical micellar concentration, followed by a very large decrease during micellization, and a nearly constant value in the postmicellar region. Besides many alcohols, amines, and carboxylic acids also 1-propoxy-2-propanol in water most obvious exhibits such a micellar-

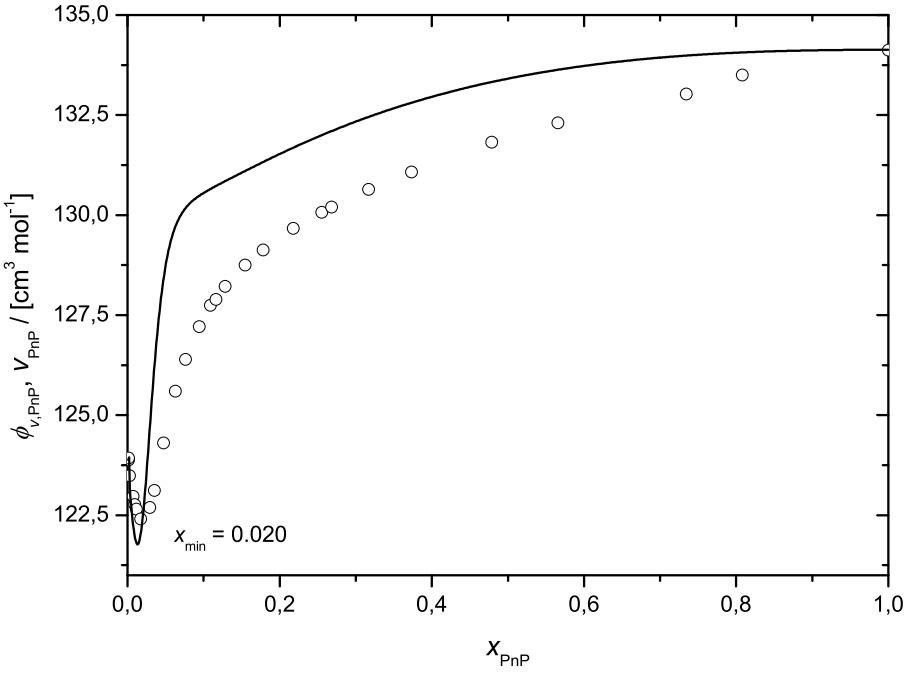

Figure 3.3.: Apparent(○) and partial(—) molar volume of PnP(1) in water at 25 °C

like phase-transition. According to the concentration scale where this transition occurs this molecule behaves like a short-chain surfactant with $n = 4 - 7$.

The observations can be rationalized by assuming hydrophobic hydration of PnP in water at very low concentration. Whilst long-chain hydrophobic molecules generally tend to aggregate, so minimizing their surface contact and associated surface energy with water, smaller hydrophobic materials (or solvo-surfactants) do, however, dissolve as water can rearrange around this molecules without breaking hydrogen bonds or losing much energy. The hydrophobic part of the organic solute can interact with these water molecules with multiple van-der-Waals interactions. Following the conclusion by Roux [68] the basic nature of the hydroxyl group in PnP will reinforce the hydrophobic hydration of the alkyl chain. At this stage the small size and the flexibility of water molecules in their spatial arrangement allows the organic to occupy the natural void space present in liquid water. The hydrophobic hydration, therefore, decreases the partial (and apparent) molar volume, as the molecules fits into cavities in the water network. One possible description for this solvation is the formation of clathrate structures [69, 70], which maximizes the van-der-Waals contacts between the hydrophobic part of the organic solute and the water but without reducing the amount of hydrogen bonding. Hydrophobic hydration is accompanied by a negative entropy change due to the increased order in the surrounding water and a positive heat capacity change (see Fig. 3.4) due to the stronger hydrogen bonds in water at the solute-solvent interface.

As the concentration of PnP is increased, hydrophobic interactions between the solute molecules will tend to decrease the hydrophobic hydration. As the structure around the solutes collapses the solutes will rearrange themselves in a way such as to minimize the contact of their hydrophobic parts with water. The molar quantities of the solute are then similar to those of micellar solutes since the polar group still interacts with water while the hydrophobic part sees only other non-polar chains (strong decrease in $\Phi_{c,1}$, $\tilde{c}_{p,1}$ and increase in $\Phi_{v,1}$, v_1).

As further solutes are added, they dissolve preferentially with their hydrophobic chains in the microphases and the partial (and apparent) molar quantities remain approximately constant. In other words: at high concentration the hydrophobic part of PnP is seeing only other hydrophobic groups and not water, equivalent to a microphase or aggregates beyond the transition region.

The anomalous effect of PnP - water mixtures on the apparent molar volume and heat capacity of the organic compound correlates well with the surface tension measurements and the efficiency to dissolve hydrophobic particles in water. Investigations on these four different experimental procedures indicate a

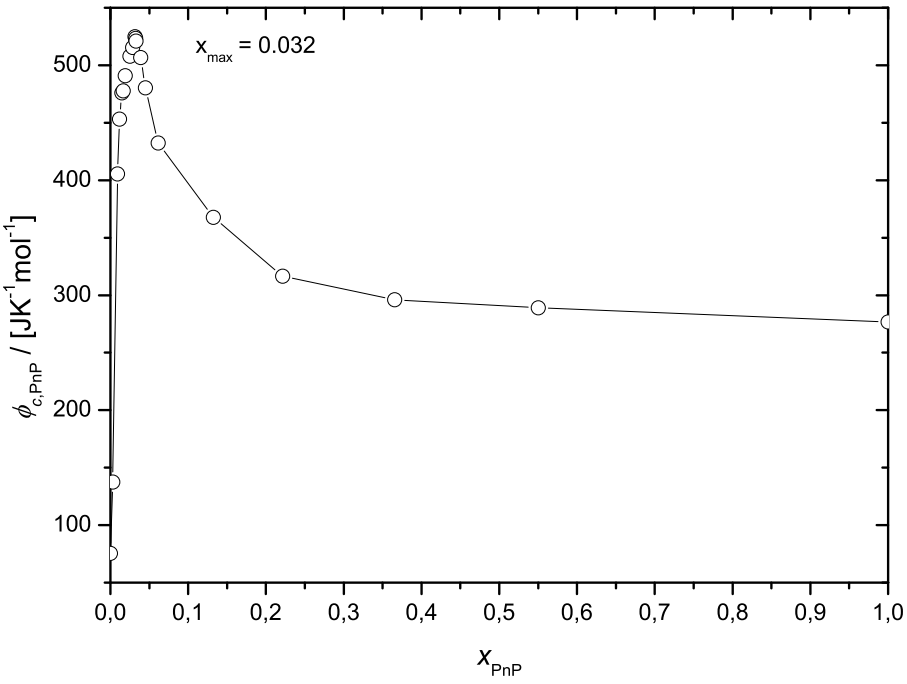

Figure 3.4.: Apparent molar heat capacity of PnP in water at 25 °C

conforming region of phase-transition. The related aggregates appear at relatively high concentrations ($x_{\mathrm{PnP}} = 0.03; \mathrm{m} = 1.7\,\mathrm{mol\,kg^{-1}}$). At such high concentrations and hence short intermolecular distances, only small hydrophobic association effects are sufficient to initiate aggregate formation into a loose non-covalent assembly (characteristic lowering of the surface tension). This microheterogenous structures offering an environment of lower polarity, within which the solubilization of hydrophobic solutes is promoted.

Reported increases in the chemical potential of the solute (and hence activity coefficient), indicative of the organic solute's low solubility in water, can also be expected for PnP/water at 25 °C as inferred from isobaric VLE data (Sec. 4.12.5). Despite the complete miscibility below the critical solution temperature, this unfavorable mixing behavior at higher temperatures is certainly already implied in γ - values beyond unity for room-temperature investigations.

Many more examples of binary mixtures with a relatively non-polar component and a second compound with a spatial H-bond network can be found in the literature. In order to explain the phenomena in diluted aqueous solutions of non-electrolytes similar to those in the vicinity of critical immiscibility point (anomalous light scattering maximum, increase of concentration fluctuations, narrowing the Rayleigh line wine, anomalous absorption and dispersion of sound), Rodnikova first introduced an elasticity parameter of spatial hydrogen bonds network [71, 72] for analysis of liquid structure upon dissolution. The relation between solvophobic (hydrophobic) effects (hydrophobic interactions, microstratification, microheterogeneity, etc.) and these critical phenomena is explained from the point of view of this elasticity parameter: elasticity is the tendency of the network to preserve its primary configuration. In [72], the isothermal bulk modulus $K_T = 1/\beta_T$, where $\beta_T = -\frac{1}{V}\left(\frac{\partial V}{\partial P}\right)_T$ is the isothermal compressibility, was proposed as a measure of elasticity and was used to estimate the elasticity of the spatial H-bond network of diamines, diols and amino alcohols at 298 K [73]. It was demonstrated that the elasticity of liquids with spatial H-bond network is four times that of alkanes and two times that of aliphatic alcohols. Under normal conditions, suitable molecules containing H-bond acceptor as well as donor centers, are mixed with water (or any other H-bond network forming solvent) to form a united network of H-bonds themselves. As the concentration dependent isothermal bulk moduli pass through a maximum (a point at which the network is most elastic), an interplay of two opposite processes in the systems are assumed: on the one hand, the network becomes stronger due to the water-nonelectrolyte interaction, a hydrophobic effect in dilute solutions, which strengthen the spatial network of water H-bonds. H-bonds push nonelectrolyte

molecules out and make them unite. On the other hand, the number of network defects (hydrocarbon backbones) increases with the nonelectrolyte concentration at a threshold concentration, beyond which the network is disturb and hydrophobic effects considerably decreases [74, 75]. Recently the appearance of the maximum of the heat capacity in aqueous and non-aqueous systems confirmed the assumption of a microimmiscibility on the network of H-bonds, which falls into the same concentration range as a minimum in the partial molar volume and immiscibility in the phase diagrams of these binary mixtures [76]. The analysis shows very close similarities to aqueous mixtures of PnP investigated in this work. In order to extend the understanding of microheterogenity in aqueous mixtures of 1-propoxy-2-propanol, extended spectroscopical studies aiming at the structure of the proposed aggregates, like light-scattering, NMR, IR, and dielectric relaxation spectroscopy [77], are believed to provide valuable information.

4. Vapor-Liquid Phase Equilibria

A number of industrially important processes, such as distillation, absorption, and extraction, bring two phases into contact. When the phases are not in equilibrium, mass transfer occurs between them. The rate of transfer of each species depends on the departure of the system from equilibrium. Quantitative treatment of mass-transfer rates require knowledge of the equilibrium states (T, p, and composition) of the system.
Amongst all possible phase equilibria, vapor-liquid-equilibria (VLE) are of particular importance for technical applications. The calculation and prediction of such equilibria forms the basis for the design or simulation of equipment for separation or distillation or for testing the predictive power of existing models.
The criteria for equilibrium is the uniformity of temperature, pressure and chemical potential throughout the entire heterogeneous, closed system. Internal equilibrium with respect to the three processes (heat transfer, boundary displacement and mass transfer) along the phase interface is assumed. Within this chapter the proper application of fundamental thermodynamic relations for the calculation of temperatures, pressures, and phase compositions for systems in vapor/liquid equilibrium at low to moderate pressures are presented. For the description of the real behavior of mixtures or solutions, dimensionless variables simplifying the equation of chemical equilibrium are introduced. Those variables are the fugacity coefficient, ϕ_i , and the activity coefficient, $\gamma_i(x)$.
A dynamic recirculation apparatus has been used to determine the isobaric phase equilibria of binary 1-propoxy-2-propanol mixtures with water and different alcohols (methanol, ethanol, 2-butanol and 1-hexanol). The systems exhibit both positive and negative deviations from Raoult's law. No azeotropic mixture is found in any of the systems under investigation. The binary diagram of water/1-Propoxy-2-propanol (PnP) shows the well-known liquid-liquid-separation. The experimental results are correlated with the Wilson, NRTL and UNIQUAC model and also compared to the COSMO-RS predictive model and the modified UNIFAC group-contribution method.
The present work aims at contributing to the development of a data base for thermodynamic properties of mixtures containing PGAE, starting with PnP.

4.1. Fugacity and Activity

The starting point of all further considerations is the chemical potential, μ. As a function of temperature, pressure and composition it is one of the most important term in physical thermodynamics, allowing for the derivation of all other state functions. It's pressure dependence can be expressed by

$$\mathrm{d}\mu = \nu \mathrm{d}p \quad (T, x_k = \text{const.}). \tag{4.1}$$

Assuming ideal gas behavior $\nu^{\mathrm{ig}} = \mathrm{R}T/p$ it follows:

$$\mathrm{d}\mu^{\mathrm{ig}} = \frac{\mathrm{R}T}{p}\mathrm{d}p = \mathrm{R}T\mathrm{dln}p \tag{4.2}$$

or

$$\mathrm{d}\mu_i^{\mathrm{ig}} = \frac{\mathrm{R}T}{p_i}\mathrm{d}p_i = \mathrm{R}T\mathrm{dln}p_i \tag{4.3}$$

for component i in the mixture. Integration at constant temperature leads to

$$\mu_i - \mu_i^0 = \mathrm{R}T\mathrm{ln}\frac{p_i}{p_i^0}. \tag{4.4}$$

The essential value of Eq. (4.4) is that it simply relates the chemical potential to a common, intensive property p of the real world. To generalize it, G. N. Lewis defined a function f, called fugacity, with which Eq. (4.4) for an isothermal change for any component i is valid in any system, solid, liquid or gas, pure or mixed, ideal or real.

$$\mu_i - \mu_i^0 = \mathrm{R}T\ln\frac{f_i}{f_i^0}. \tag{4.5}$$

Comparing Eq. (4.5) with Eq. (4.4) indicates that the fugacity f_i is equal to the ideal system's pressure or partial pressure p_i, respectively. In other words the fugacity is a corrected pressure and is related to the effective physical pressure in such a way as to fulfill Eq. (4.5). The reference state (c.f. f_i^0) can be chosen arbitrarily. If one takes the ideal gas as a reference at temperature T and pressure p the chemical potential of component i in the mixture can be written as

$$\begin{aligned}\mu_i(T,p,x_k) - \mu_i^{ig}(T,p,x_k) &= \mathrm{R}T\ln\left[\frac{f_i(T,p,x_k)}{f_i^{ig}(T,p,x_k)}\right] \\ &= \mathrm{R}T\ln\phi_i(T,p,x_k)\end{aligned} \tag{4.6}$$

In Eq. (4.6) the fugacity coefficient ϕ_i is introduced, which describes the deviation of ideal gas behavior, e.g. $\phi_i^{ig}(T,p,x_k) = 1$. In terms of fugacity of a component the equation is as follows:

$$f_i = \phi_i f_i^{ig} = \phi_i p_i = x_i\phi_i p. \tag{4.7}$$

If, however, one choses the pure chemical substance as reference state at the same aggregation state, the potential can be written as:

$$\begin{aligned}\mu_i(T,p,x_k) - \mu_i^{*}(T,p,x_k) &= \mathrm{R}T\ln\left[\frac{f_i(T,p,x_k)}{f_i^{*}(T,p,x_k)}\right] \\ &= \mathrm{R}T\ln a_i^{*}(T,p,x_k)\end{aligned} \tag{4.8}$$

Note that this definition of the activity a_i is only valid in case that the state of aggregation of component i currently is the same as in the reference state with $a_i^*(T,p,x_i=1) = 1$.
For ideal solutions the definition $f_i^{iL}(T,p,x_i) = x_i f_i^*(T,p)$ applies (known as the *Lewis/Randall rule*). The activity of component i in an ideal solution can be expressed therefore as:

$$a_i^{iL} = \frac{x_i f_i^{iL}}{f_i^*} = x_i. \tag{4.9}$$

The activity of one component in any mixtures obviously is a measure of the mole fraction corrected for the behavior in real systems. For that reason the activity is split into the mole fraction x and the activity coefficient γ: $a_i(T,p,x_k) = x_i\gamma_i(T,p,x_k)$ (superscript "0", indicating the pure substance as reference state, is omitted here and in the following treatment). The activity coefficient comprises the departure of a mixture from ideal behavior.
Similar conclusions for the fugacity of component i, as shown in Eq. 4.7, can be drawn here:

$$f_i = a_i f_i^* = x_i\gamma_i f_i^* = \gamma_i f_i^{iL} \tag{4.10}$$

for a certain temperature, pressure and mixture composition. Thus the activity coefficient of a species in solution is simply the ratio of its actual fugacity to the value given by the Lewis/Randall rule. A comparison of Eq. (4.9) with Eq. (4.10) shows that the activity coefficient in an ideal solution is unity. The same holds for γ of the pure compound.

4.2. Calculation of Chemical Potentials

The calculation of phase equilibria requires the knowledge of the chemical potential of each constituent of the system in every phase.
If one takes as reference of the gas phase the pure component at its ideal state at standard pressure p^0, the combination of Eq. (4.6) and (4.7) for the chemical potential of solute i in the mixture gives:

$$\begin{aligned}\mu_i(T,p,x_k) &= \mu_i^{*,ig}(T,p^0) + \mathrm{R}T\ln\left[\frac{f_i(T,p,x_k)}{f_i^{*,ig}(T,p^0)}\right] \\ &= \mu_i^{*,ig}(T,p^0) + \mathrm{R}T\ln\left[\frac{x_i\phi_i p}{p^0}\right]\end{aligned} \tag{4.11}$$

The liquid phase is described with the help of Eq. (4.8) with the reference state of the pure component in the liquid form.

$$\begin{aligned}\mu_i^l(T,p,x_k) &= \mu_i^{*,l}(T,p) + \mathrm{R}T\ln\left[\frac{f_i^l(T,p,x_k)}{f_i^{*,l}(T,p)}\right] \\ &= \mu_i^{*,l}(T,p) + \mathrm{R}T\ln a_i(T,p,x_k) \\ &= \mu_i^{*,l}(T,p) + \mathrm{R}T\ln\left(x_i\gamma_i(T,p,x_k)\right)\end{aligned} \tag{4.12}$$

For a convenient description of VLE data the use of pure component vapor pressures is reasonable since p_i^{vap} is easily determined experimentally (see Sec. 6.3) and already known for most of the relevant substances [78–81]. Therefore the chemical potential in the liquid phase is expressed in terms of the pure component at its own vapor pressure as reference state. The conversion can be obtained by integrating the molar liquid volume $\nu_i^{*,l}$ of the pure component i between the limits of the vapor pressure p_i^{vap} and the system's pressure:

$$\mu_i^{*,l}(T,p) = \mu_i^{*,l}(T,p_i^{\mathrm{vap}}) + \int_{p_i^{\mathrm{vap}}}^{p} \nu_i^{*,l}\mathrm{d}p \tag{4.13}$$

Equilibrium of both phases requires

$$\begin{aligned}\mu_i^{*,l}(T,p_i^{\mathrm{vap}}) &= \mu_i^{*,g}(T,p_i^{\mathrm{vap}}) \\ &= \mu_i^{*,ig}(T,p^0) + \mathrm{R}T\ln\left[\frac{\phi_i^{\mathrm{vap}}p_i^{\mathrm{vap}}}{p^0}\right]\end{aligned} \tag{4.14}$$

with $x_i = 1$ and $p = p_i^{\mathrm{vap}}$ for the pure component (cf. Eq. (4.11)). Inserting Eqs. (4.13)(4.14) in Eq. (4.12) finally yields the following expression for practical use:

$$\mu_i^l(T,p,x_k) = \mu_i^{*,ig}(T,p^0) + \mathrm{R}T\ln\left(\frac{\phi_i^{\mathrm{vap}}p_i^{\mathrm{vap}}}{p^0}\right) + \mathrm{R}T\ln\left(x_i\gamma_i(T,p,x_k)\right) + \int_{p^*}^{p}\nu_i^{*,l}\mathrm{d}p \tag{4.15}$$

4.3. Calculation of VLE

If a liquid phase is in thermal equilibrium with its vapor phase, the chemical potential of one species i in both phases has to be identical:

$$\mu_i^v(T,p) = \mu_i^l(T,p) \tag{4.16}$$

All further considerations are dealing with both the vapor and liquid phase behaving like real mixtures. According to Eqs. (4.11)(4.15) of the preceding section, the condition for phase equilibria is:

$$y_i \phi_i p = x_i \gamma_i p_i^{\text{vap}} \phi_i^{\text{vap}} \exp\left[\frac{1}{\mathrm{R}T} \int_{p_i^{\text{vap}}}^{p} \nu_i^{*,l} \mathrm{d}p\right] \tag{4.17}$$

with y_i being the mole fraction of the species i in the gas-phase, ϕ_i and ϕ_i^{vap} being the fugacity coefficient of i in the mixture and of the pure component at its own vapor pressure respectively. The exponential term is called *Poynting factor* and takes into account the compressibility of the liquid in the pressure range. In general, the volume of a liquid is a function of both temperature and pressure, but at conditions remote from critical, a condensed phase may often be regarded as incompressible and in that case the Poynting correction takes the simple form

$$\exp\left[\frac{\nu_i^{*,l}(p - p_i^{\text{vap}})}{\mathrm{R}T}\right] \tag{4.18}$$

The correction is often, but not always, small and sometimes it is negligible at low pressures. Table 4.1 gives some numerical values of the Poynting factor for an incompressible component. Based on Eq. (4.17)

Table 4.1.: Effect of pressure on the fugacity of a pure, condensed and incompressible substance; $\nu_i = 100\,\mathrm{cm}^3\,\mathrm{mol}^{-1}$ at $T = 300\,K$

Pressure in excess of saturation pressure (bar)	Poynting correction
1	1.00405
10	1.0405
100	1.499
1000	57.0

the special case of assuming an ideal gas-phase and liquid-mixture, *Raoult's Law* is obtained with the Poynting-correction set to unity:

$$y_i p = x_i p_i^{\text{vap}}. \tag{4.19}$$

With the exception of systems at high pressure or those containing carboxylic acids the approximations that the gas-phase is ideal is acceptable (the ratio between the fugacity coefficients ϕ_i and ϕ_i^{vap} does not deviate much from unity under moderate conditions as well). Corrections for the liquid's deviations from ideality is accounted for by the activity coefficient γ. The description of VLE with ideal gas behavior is accomplished by the extended *Raoult's law*:

$$y_i p = x_i \gamma_i p_i^{\text{vap}}. \tag{4.20}$$

The calculation of all vapor-liquid equilibrium data in this work is based on the equations for real gas-phase behavior. Since the Poynting factor differs from unity by only a few parts per thousand at moderate pressure, its omission is believed to introduce negligible error. Systematic application of Eq. (4.17) depends on the availability of correlations of data from which values may be obtained for the p_i, ϕ_i and γ_i.

The vapor pressure of species i is usually calculated from equations giving the p_i^{vap} as a function of temperature. Most commonly used is the *Antoine* equation, but other functions also exist (see Chap. 4. The expression for ϕ_i, the fugacity coefficient for the species i in a binary mixture is obtained from [82]

$$\phi_i = \exp\frac{p}{\mathrm{R}T}\left[B_{ii} + y_j^2(2B_{ij} - B_{ii} - B_{jj})\right] \tag{4.21}$$

where y represents mole fractions in the gas mixture. B_{ii} represents the virial coefficient of the pure species i; the cross coefficient B_{ij} characterizes a bimolecular interaction between the molecule i and

the molecule j, and therefore $B_{ij} = B_{ji}$. Both are functions of temperature only. The mathematical relationship given in Eq. (4.24) arises from considerations of the *residual* Gibbs energy (a property defined relative to its ideal gas value at the same temperature and pressure is termed a residual property)

$$\frac{G_i^R}{\mathrm{R}T} = \ln\phi_i \tag{4.22a}$$

$$\frac{G_i^R}{\mathrm{R}T} = \int_0^p (Z_i - 1)\frac{\mathrm{d}p}{p} \tag{4.22b}$$

Fugacity coefficients (and therefore fugacities) are evaluated by these equations from PVT data or from any equation of state (*van der Waals*, etc.). For example, when the compressibility factor Z is given by the simplest form of the virial equation

$$Z_i = 1 + \frac{Bp}{\mathrm{R}T} \tag{4.23}$$

Eq. (4.24) is derived with the help of the last three equations.
Values for the pure-species virial coefficients can be determined with the method of Xiang [83]. All cross second virial coefficients B_{ij} are set to be zero in this work.
The fugacity coefficient for pure i as a saturated vapor ϕ_i^{vap} is obtained from

$$\phi_i^{\mathrm{vap}} = \exp\left[\frac{B_{ii}p_i^{\mathrm{vap}}}{\mathrm{R}T}\right] \tag{4.24}$$

Summing up both expressions for the fugacity coefficients in Eq. (4.17) gives

$$\Phi_i = \frac{\phi_i}{\phi_i^{\mathrm{vap}}} = \exp\left[\frac{B_{ii}(p - p_i^{\mathrm{vap}}) - py_i^2(B_{jj} + B_{ii})}{\mathrm{R}T}\right] \tag{4.25}$$

Activity coefficients (γ_i in Eq. (4.17)) are evaluated from models for G^E as discussed in Sec. 4.5.
Up to now the presented equations provide the theoretical basis for the calculation of VLE data. According to *Gibbs Phase Rule*, there are 2 degrees of freedom f in a binary system specifying the system's pressure p and the liquid-phase composition x_i. That is exactly the remaining number of phase-rule variables, namely the temperature T and the gas-phase composition y_i.

4.4. Bubble-Point Calculations

Bubble-Point: calculate T and $\mathbf{y_i}$ for a given p and $\mathbf{x_i}$

The calculation of bubble-point temperatures requires iterative schemes because of the complex functionality in Eq. (4.17). As in the case of isobaric VLE data when solving for T and y_i, we do not necessarily have values for calculating either $p_i^{\mathrm{vap}} = f(T)$ or $\phi_i = \phi_i(T, p, y_1, y_2, \ldots, y_{k-1})$. To overcome this problem, simple iterative procedures are described below to allow an efficient solution.
Eq. (4.17) together with Eq. (4.25) provides the basis for the bubble-point calculation, written as

$$y_i = \frac{x_i\gamma_i p_i^{\mathrm{vap}}}{\Phi_i p} \tag{4.26}$$

Since $\sum_i y_i = 1$, we also have

$$1 = \sum_i \frac{x_i\gamma_i p_i^{\mathrm{vap}}}{\Phi_i p} \tag{4.27}$$

or

$$p = \sum_i \frac{x_i\gamma_i p_i^{\mathrm{vap}}}{\Phi_i} \tag{4.28}$$

In case of bubble-point procedure the temperature is not known initially, but has to be found iteratively. Although the individual vapor pressures are strong functions of temperature, vapor-pressure ratios are weakly dependent on T. Therefore we multiply the right-hand side of Eq. (4.28) by p_j^{vap} (outside the summation) and divide it by p_j^{vap} (inside the summation). Solution for p_j^{vap} outside the summation gives

$$p_j^{\text{vap}}(\text{new}) = \frac{p}{\sum_i (x_i \gamma_i p_i^{\text{vap}} / \Phi_i)} p_j^{\text{vap}}(\text{old}) \tag{4.29}$$

with $p_j^{\text{vap}}(\text{new})$ being the improved value for the vapor-pressure obtained by the initial value $p_j^{\text{vap}}(\text{old})$ in each step of the iteration procedure. In the equation the summation is over all species including j, which is the remaining species from the binary set of components. With the help of the new, corrected vapor pressure, the vapor-pressure equation for component i is solved for the new temperature. With a new value of the temperature, the process of calculating the activity coefficients and partial pressures of the components is continued until

$$\Delta T = T(\text{new}) - T(\text{old}) < \text{tolerance}(0.01\,\text{K}) \tag{4.30}$$

The iterative scheme for this computer-based bubble-point calculation is shown in Fig. 4.1 and explained below.

The given values of p and x_i along with appropriate constants (e.g. for vapor pressure equations, activity coefficient models, EOS, ...) are read. In the absence of T and y_i, values for Φ_i are set to unity. To calculate the initial temperature guess, the pure components' vapor pressure equations (see Sec. 6.4.1) are used. To find the initial guess for T, these equations are solved for T at the total pressure within the system under investigation. The vapor pressure equations cannot be solved analytically since they contain power and log terms, so they have to be solved numerically for each species.

The iteration is controlled by T, and for an initial estimate we use a mole fraction average, that is to say

$$T_{\text{guess}} = \sum_{i=1}^{2} x_i T_i \tag{4.31}$$

With this primary value of T, we find values for p_i^{vap} from vapor pressure equations and values of γ_i from the activity-coefficient correlation. Species j is identified and p_j^{vap} is calculated by Eq. (4.29) subsequently. A new value of T is found from solving the vapor pressure equations for the temperature. The p_i^{vap} are immediately reevaluated, and the y_i are calculated by Eq. (4.26). Values can now be found for both Φ_i and γ_i, allowing a revised value of p_j^{vap} to be calculated by Eq. (4.29) and a better estimate of T to be found from a vapor pressure equation. Iteration then leads to final values of T and y_i describing the complete boiling point diagram at system pressure p.

Note the fundamental importance of the knowledge of precisely determined p^{vap}-curves. They serve as key functions for the correlative description of equilibrium data and are investigated for pure PnP in Sec. 6.4.1.

4.5. Excess Gibbs Energy Models

Liquid solutions are often dealt with through properties that measure their deviations from the behavior of ideal solutions. This deviation is defined by thermodynamic excess properties such as the difference between the actual property value of a solution and the value it would have as an ideal solution at the same temperature, pressure, and composition.

The fundamental excess property relation is the excess Gibbs energy. From the definition of an excess property and Eq. (4.12) together with $\gamma_i = 1$ it follows that

$$\mu_i^{ex} = \mu_i - \mu_i^{iL} = \mathrm{R}T\ln\gamma_i = \left(\frac{\delta(n\overline{G^{\text{ex}}})}{\delta n_i} \right) = G_i^{ex} \tag{4.32}$$

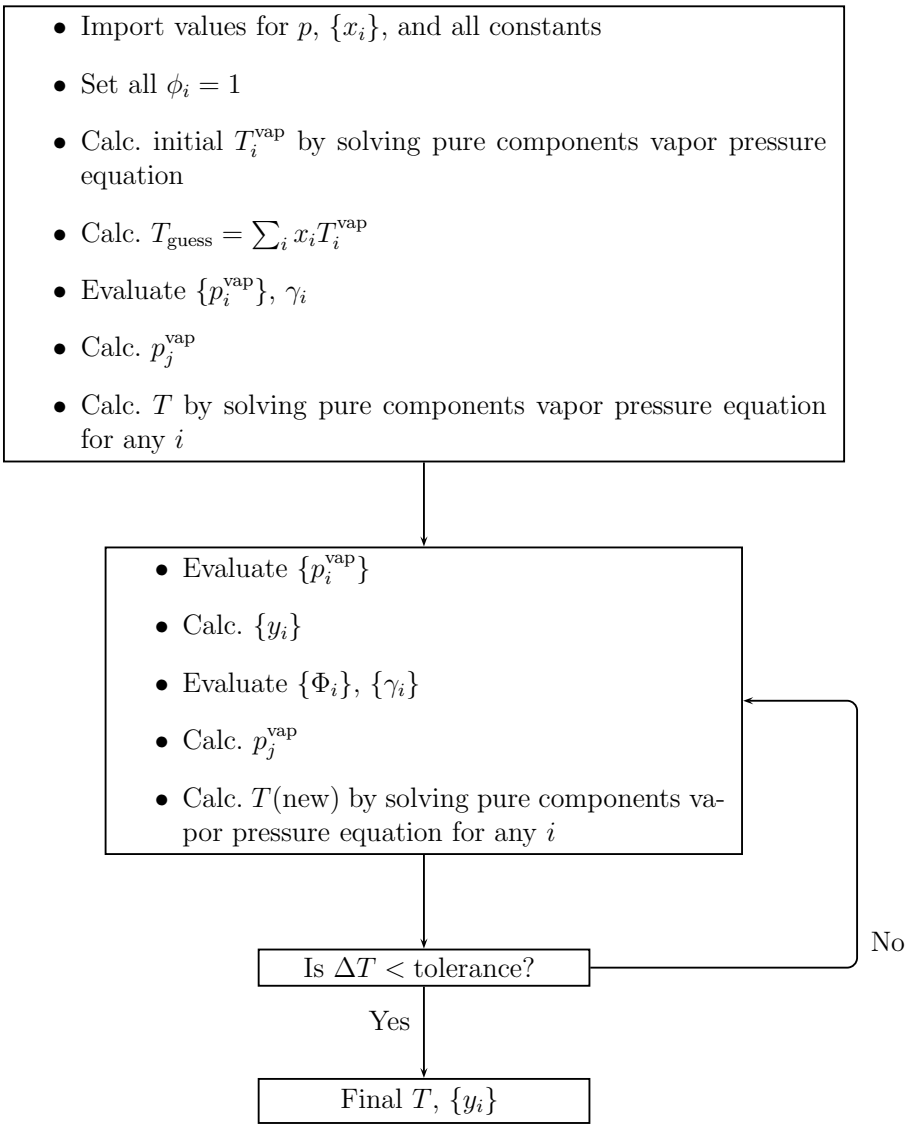

Figure 4.1.: Block Diagram for the bubble-temperature calculation

As the Gibbs energy is a function of temperature, pressure, and composition, another form of its representation is

$$\mathrm{d}\left(n\overline{G^{\mathrm{ex}}}\right) = n\overline{V^{\mathrm{ex}}}\mathrm{d}p - n\overline{S^{\mathrm{ex}}}\mathrm{d}T + \sum_i \frac{\delta(n\overline{G^{\mathrm{ex}}})}{\delta n_i}\mathrm{d}n_i \tag{4.33}$$

Together with Eq. (4.32) if follows that

$$\mathrm{d}\left(\frac{n\overline{G^{\mathrm{ex}}}}{\mathrm{R}T}\right) = \frac{n\overline{V^{\mathrm{ex}}}}{\mathrm{R}T}\mathrm{d}p - \frac{n\overline{S^{\mathrm{ex}}}}{\mathrm{R}T}\mathrm{d}T + \sum_i \ln\gamma_i \mathrm{d}n_i \tag{4.34}$$

Since $\ln\gamma_i$ is a partial property with respect to $\overline{G^{\mathrm{ex}}}/\mathrm{R}T$, we can write:

$$\frac{\overline{G^{\mathrm{ex}}}}{\mathrm{R}T} = \sum_i x_i \ln\gamma_i \tag{4.35}$$

Whereas the fundamental residual property relation Eq. (4.22a) is directly connected to experimental PVT data and equations of state, the excess property formulation has its usefulness from experimentally accessible $\overline{V^{\mathrm{ex}}}$, $\overline{H^{\mathrm{ex}}}$ and γ_i values. Activity coefficients are found from VLE experiments, treated in more detail in Sec. 4.12.

All of the Gibbs excess models used in this study are explained in the following paragraphs. They are all modern theoretical developments in the molecular thermodynamics of solutions based on the concept of *local composition*. Within a liquid solution short-range order and non-random molecular orientation are accounted for by the local compositions different to the overall bulk composition. The main factors determining the local composition are the molecular size and intermolecular forces.

4.5.1. Wilson Model

Based on those molecular considerations, Wilson presented the following expression for the excess Gibbs energy of a binary solution [84]:

$$\frac{\overline{G^{\mathrm{ex}}}}{\mathrm{R}T} = -x_1\ln(x_1 + x_2\Lambda_{12}) - x_2\ln(x_2 + x_1\Lambda 21) \tag{4.36}$$

The activity coefficients derived from this equation according to Eq. (4.35) are

$$\ln\gamma_1 = -\ln\left(x_1 + \Lambda_{12}x_2\right) + x_2\left(\frac{\Lambda_{12}}{x_1 + \Lambda_{12}x_2} - \frac{\Lambda_{21}}{\Lambda_{21}x_1 + x_2}\right) \tag{4.37a}$$

and

$$\ln\gamma_2 = -\ln\left(x_2 + \Lambda_{21}x_1\right) - x_1\left(\frac{\Lambda_{12}}{x_1 + \Lambda_{12}x_2} - \frac{\Lambda_{21}}{\Lambda_{21}x_1 + x_2}\right) \tag{4.37b}$$

Eq. (4.36) obeys the boundary condition that $\overline{G^{\mathrm{ex}}}$ vanishes as x_1 is either zero or unity. The Wilson equation contains two adjustable binary parameters, $\Delta\lambda_{12}$ and $\Delta\lambda_{21}$. These are related to the pure components' molar volume and characteristic interaction energies

$$\Lambda_{12} = \frac{\nu_2}{\nu_1}\exp\left(-\frac{\Delta\lambda_{12}}{\mathrm{R}T}\right) = \frac{\nu_2}{\nu_1}\exp\left(-\frac{\lambda_{12} - \lambda_{11}}{\mathrm{R}T}\right) \tag{4.38a}$$

$$\Lambda_{21} = \frac{\nu_1}{\nu_2}\exp\left(-\frac{\Delta\lambda_{21}}{\mathrm{R}T}\right) = \frac{\nu_1}{\nu_2}\exp\left(-\frac{\lambda_{21} - \lambda_{22}}{\mathrm{R}T}\right) \tag{4.38b}$$

ν_i and ν_j are the liquid molar volumes of the pure components and λ's are the energies of interaction between the molecules designated by the subscripts. To a fair approximation, the differences in the characteristic energies of interactions are independent of temperature, at least over a modest temperature range. In this work, the effect of temperature is effective through the changes of the temperature-

dependent molar volumes in the exponential terms. We note that Λ_{12} and Λ_{21} must always be positive numbers.
The Wilson equation has been shown on many occasions to provide a superior method for the correlation of vapor-liquid equilibria in totally miscible systems [85–88], a condition which constrains the wide application of this correlation. Therefore it should be used only for liquid systems that are completely miscible or else for those limited regions in the phase diagram of partially miscible systems where only one liquid phase is present.

4.5.2. NRTL Model

The concept of local composition was also used by Renon [89] in his derivation of the NRTL (***n**on-**r**andom, **t**wo-**l**iquid*) equation. It is, however, applicable to partially miscible as well as completely miscible systems. The NRTL equation for the excess Gibbs enery is

$$\frac{\overline{G^{\mathrm{ex}}}}{\mathrm{R}T} = x_1 x_2 \left(\frac{\tau_{21} G_{21}}{x_1 + x_2 G_{21}} + \frac{\tau_{12} G_{12}}{x_2 + x_1 G_{12}} \right) \tag{4.39}$$

where

$$\tau_{12} = \frac{g_{12} - g_{22}}{\mathrm{R}T}; \qquad \tau_{21} = \frac{g_{21} - g_{11}}{\mathrm{R}T} \tag{4.40a}$$

and

$$G_{12} = \exp(-\alpha_{12}\tau_{12}); \qquad G_{21} = \exp(-\alpha_{12}\tau_{21}) \tag{4.40b}$$

The significance of g_{ij} is similar to that of λ_{ij}: it is an energy parameter characteristic of the $i - j$ interaction. Parameter α_{12} is related to the nonrandomness in the mixture caused by the interactions: in case α_{12} is zero, the mixture behaves like completely random. The NRTL equation contains three parameters, but the reduction of experimental data for a large set of binary systems indicates that α_{12} varies from about 0.20 to 0.47, maintaining its original physical meaning [90–92]. Correlation results with values of α_{12} from 0.01 to 100 can also be found in the literature as well as results obtained when the non-randomness parameter is largely an empirical one [93], correlating strongly nonideal binary systems. Recently a novel method to increase the flexibility of the composition dependence of $\overline{G^{\mathrm{ex}}}$ models was proposed by Rarey [94]. The formalism can be applied to any mixture model and does not require and re-deriving of the NRTL model equation. It turns out to be a powerful extension for the description of non-ideal systems showing partial miscibility and is therefore applied successfully for the aqueous system in this study, which could not be described very well with the expression in Eq. (4.39).
The activity coefficients are

$$\ln\gamma_1 = x_2^2 \left[\tau_{21} \left(\frac{G_{21}}{x_1 + x_2 G_{21}} \right)^2 + \frac{\tau_{12} G_{12}}{(x_2 + x_1 G_{12})^2} \right] \tag{4.41a}$$

and

$$\ln\gamma_2 = x_1^2 \left[\tau_{12} \left(\frac{G_{12}}{x_2 + x_1 G_{12}} \right)^2 + \frac{\tau_{21} G_{21}}{(x_1 + x_2 G_{21})^2} \right] \tag{4.41b}$$

The NRTL equation often provides a good representation of VLE data and is often superior to Wilson's expression for strongly nonideal mixtures, especially for partially immiscible systems [88, 95–98].

4.5.3. UNIQUAC Model

Further attempt was made to derive a two-parameter expression for $\overline{G^{\mathrm{ex}}}$ that retains at least some of the advantages of the equation of Wilson without being restricted to completely miscible systems [99–102]. Abrams developed an equation which refers to the concept of local composition proposed by the quasichemical theory of Guggenheim [103] for nonrandom mixtures containing molecules of different size. Therefore the extension is called ***uni**versal **qua**si-**c**hemical theory* or UNIQUAC. The expression for $\overline{G^{\mathrm{ex}}}$ consists of a combinatorial term that attempts to describe the dominant entropic contribution which

depends on the size and shape of the molecules, and a residual part that is due to the intermolecular forces responsible for the enthalpy of mixing

$$\frac{\overline{G^{\mathrm{ex}}}}{\mathrm{R}T} = \left(\frac{\overline{G^{\mathrm{ex}}}}{\mathrm{R}T}\right)_{\text{combinatorial}} + \left(\frac{\overline{G^{\mathrm{ex}}}}{\mathrm{R}T}\right)_{\text{residual}} \tag{4.42}$$

with

$$\left(\frac{\overline{G^{\mathrm{ex}}}}{\mathrm{R}T}\right)_{\text{combinatorial}} = x_1 \ln\frac{\Phi_1}{x_1} + x_2 \ln\frac{\Phi_2}{x_2} + \frac{z}{2}\left(q_1 x_1 \ln\frac{\theta_1}{\Phi_1} + q_2 x_2 \ln\frac{\theta_2}{\Phi_2}\right) \tag{4.43a}$$

$$\left(\frac{\overline{G^{\mathrm{ex}}}}{\mathrm{R}T}\right)_{\text{residual}} = -x_1 q_1^{'} \ln(\theta_1^{'} + \theta_2^{'}\tau_{21}) - x_2 q_2^{'} \ln(\theta_2^{'} + \theta_1^{'}\tau_{12}) \tag{4.43b}$$

The segment fraction, Φ_i, and area fraction, θ_i, are

$$\Phi_1 = \frac{x_1 r_1}{x_1 r_1 + x_2 r_2} \qquad \Phi_2 = \frac{x_2 r_2}{x_1 r_1 + x_2 r_2} \tag{4.44a}$$

$$\theta_1 = \frac{x_1 q_1}{x_1 q_1 + x_2 q_2} \qquad \theta_2 = \frac{x_2 q_2}{x_1 q_1 + x_2 q_2} \tag{4.44b}$$

$$\theta_1^{'} = \frac{x_1 q_1^{'}}{x_1 q_1^{'} + x_2 q_2^{'}} \qquad \theta_2^{'} = \frac{x_2 q_2^{'}}{x_1 q_1^{'} + x_2 q_2^{'}} \tag{4.44c}$$

The structural parameters r, q, and $q^{'}$ are pure component constants depending on the molecular size and external surface area. The factor z represents the coordination number and is set equal to 10, as proposed originally by Abrams [99].
Every binary mixture is described by two adjustable parameters, τ_{12} and τ_{21}. These in turn give the characteristic energies of interaction Δu_{12} and Δu_{21}:

$$\tau_{12} = \exp\left(-\frac{\Delta u_{12}}{\mathrm{R}T}\right) \tag{4.45a}$$

$$\tau_{21} = \exp\left(-\frac{\Delta u_{21}}{\mathrm{R}T}\right) \tag{4.45b}$$

The temperature effect on the binary parameters τ_{ij} is primarily given by the last equations.
Finally the expressions for the activity coefficients within the UNIQUAC model are

$$\begin{aligned}\ln\gamma_1 =& \ln\frac{\Phi_1}{x_1} + \frac{z}{2} q_1 \ln\frac{\theta_1}{\Phi_1} + \Phi_2\left(l_1 - \frac{r_1}{r_2} l_2\right) \\ & - q_1 \ln(\theta_1^{'} + \theta_2^{'}\tau_{21}) + \theta_2^{'} q_1^{'}\left(\frac{\tau_{21}}{\theta_1^{'} + \theta_2^{'}\tau_{21}} - \frac{\tau_{12}}{\theta_2^{'} + \theta_1^{'}\tau_{12}}\right)\end{aligned} \tag{4.46a}$$

and

$$\begin{aligned}\ln\gamma_2 =& \ln\frac{\Phi_2}{x_2} + \frac{z}{2} q_2 \ln\frac{\theta_2}{\Phi_2} + \Phi_1\left(l_2 - \frac{r_2}{r_1} l_1\right) \\ & - q_2 \ln(\theta_2^{'} + \theta_1^{'}\tau_{12}) + \theta_1^{'} q_2^{'}\left(\frac{\tau_{12}}{\theta_2^{'} + \theta_1^{'}\tau_{12}} - \frac{\tau_{21}}{\theta_1^{'} + \theta_2^{'}\tau_{21}}\right)\end{aligned} \tag{4.46b}$$

where

$$l_1 = \frac{z}{2}(r_1 - q_1) - (r_1 - 1); \qquad l_2 = \frac{z}{2}(r_2 - q_2) - (r_2 - 1) \tag{4.47}$$

The UNIQUAC equation is applicable to a wide variety of nonelectrolyte liquid mixtures containing nonpolar and polar fluids, including partially miscible systems. The two main advantages in using

the UNIQUAC model lies in its relative simplicity (having only 2 adjustable parameters) and its wide applicability.

4.6. Data Reduction

Data reduction is the process of finding a suitable analytic relation for $\overline{G^{\mathrm{ex}}}/\mathrm{R}T$ as a function of its independent variables T and x_i, thus correlating VLE data sets to the model expressions presented above. The weak dependence of $\overline{G^{\mathrm{ex}}}$ from pressure is neglected without introducing considerable error. Evaluation of the model's parameters is best performed by using efficient and powerful optimization strategies incorporated in most of the modern mathematical software. The Nelder-Mead simplex algorithm in the form published by Kuester [104] has been selected for the correlations in this work. The choice of the objective function in general is determined by the type of data sets to be treated. For a complete set of VLE data, e.g. $x-y-T$ at constant pressure, the objective function ζ is the sum of the squared relative deviations of the experimental and calculated activity coefficients with k data points and i components, respectively.

$$\zeta = \sum_{k=1}^{N} \sum_{i=1}^{2} \left[\left(\frac{\gamma_{\mathrm{i}}^{\mathrm{calc}} - \gamma_{\mathrm{i}}^{\mathrm{exp}}}{\gamma_{\mathrm{i}}^{\mathrm{exp}}} \right)^2 \right]_k \tag{4.48}$$

Minimizing the objective function gives the parameters for an over-all representation of experimental results by each model. It is noteworthy to point out that such a combination of parameters obtained from the correlation is usually not unique, but other parameters will also show a similar accuracy. All parameters in this work are the results of a minimized objective function regardless of the overall accuracy with respect to deviations in temperature or vapor phase composition. The equations of the activity coefficient for Wilson and UNIQUAC contain two adjustable parameters ($\lambda_{12}-\lambda_{11}$, $\lambda_{21}-\lambda_{22}$ and $g_{12}-g_{22}$, $g_{21}-g_{11}$), whereas in the NRTL model the third parameter α_{12} is restricted to a range of values between $0.1-0.9$.
The calculation of the activity coefficients from experimental data, γ_i^{exp}, on the basis of Eq. (4.26) accounts for both, gas phase (Φ) and liquid phase (γ) non-idealities as described in Sec. 4.3. The reliability of the calculations is examined by successful reevaluation of numerous binary system parameters [88].
Once the coefficients of the equations are known, the vapor-liquid equilibrium at the assigned pressure is calculated imposing the isofugacity condition. The fitted parameters of the excess Gibbs energy models together with the mean values of the absolute deviations in boiling point, ΔT, and in vapor-phase mole fraction, Δy_i, are shown in Table 4.7. Isobaric boiling diagrams of every systems under investigation together with the results of the numerical calculations are included in the Figs. 4.21-4.27.
Before the detailed description of the experimental set-up and the presentation of the results, some considerations about the thermodynamic consistency of the VLE data will follow.

4.7. Consistency Tests

The basis of argumentation about the internal consistency of a given set of data is governed by one of the most useful equations in thermodynamics, the *Gibbs-Duhem* equation which puts the partial molar properties of the components in relation to each other.
Starting from Euler's theorem for the internal energy U

$$U = V\left(\frac{\mathrm{d}U}{\mathrm{d}V}\right)_{S,n} + S\left(\frac{\mathrm{d}U}{\mathrm{d}S}\right)_{V,n} + \sum_i n_i \left(\frac{\mathrm{d}U}{\mathrm{d}n_i}\right)_{V,S,n_j\neq i} = -Vp + ST + \sum_i n_i\mu_i \tag{4.49}$$

and its derivative form

$$\mathrm{d}U = -V\mathrm{d}p - p\mathrm{d}V + S\mathrm{d}T + T\mathrm{d}S + \sum_i n_i \mathrm{d}\mu_i + \sum_i \mu_i \mathrm{d}n_i \tag{4.50}$$

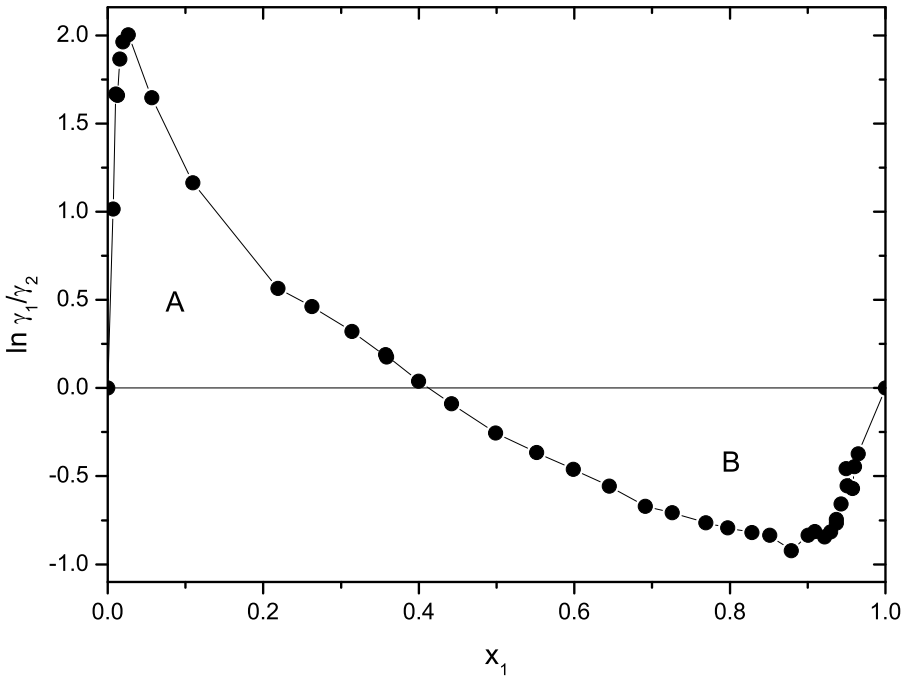

Figure 4.2.: Integral Test (area test) for the system 1-Methoxy-2-propanol/water at atmospheric pressure; $A = 0.3433, B = -0.3396$

the expression for G in terms of its extensive variables (V, S, n_i)

$$\mathrm{d}G = -p\mathrm{d}V + T\mathrm{d}S + \sum_i \mu_i \mathrm{d}n_i \tag{4.51}$$

can be retyped in the form of

$$0 = -V\mathrm{d}p + S\mathrm{d}T + \sum_i n_i \mathrm{d}\mu_i, \tag{4.52}$$

the final form of the Gibbs-Duhem equation.
When applying the equation for experimental systems at constant pressure p and introducing the excess properties similar to Eq. (4.34) an expression is found to show if the experimental data obey the fundamental relations from thermodynamics. The relation $H = TS$ (const.p) was made use of.

$$0 = \frac{\Delta H^{ex}}{\mathrm{R}T^2}\mathrm{d}T + \sum_i n_i \mathrm{dln}\gamma_i \tag{4.53a}$$

and for one mole of mixture it is

$$0 = \frac{\Delta \overline{H^{\mathrm{ex}}}}{\mathrm{R}T^2}\mathrm{d}T + \sum_i x_i \mathrm{dln}\gamma_i \tag{4.53b}$$

Integration of the last equation with the limits of $x_1 = 0$ and $x_1 = 1$, and remembering that $x_2 = 1 - x_1$, the expression for the integral consitency test is derived

$$\int_0^1 \ln\frac{\gamma_1}{\gamma_2}\mathrm{d}x = \int_{x=0}^{x=1} \frac{\overline{H^{\mathrm{ex}}}}{\mathrm{R}T^2}\mathrm{d}T \tag{4.54}$$

This *area test* was first proposed by Herington [105] and Redlich and Kister [106]. In principle the test is performed in such a way that the calculated experimental activity coefficients plotted as $\ln\gamma_1/\gamma_2$ against the mole fraction give a curve, normally the points of which are defining two areas (a positive above the abscissa, A, and a negative below the abscissa, B) as shown in Fig. 4.2. The net area under this curve,

thus called an area test, is equal to the integral on the right-hand side of Eq. (4.54). As the data are expected to have experimental error and due to the assumptions made in the derivation of Eq. (4.54), a certain degree of deviation is defined within which the data are assumed to be thermodynamically consistent.

$$D/\% = 100 \left| \frac{A-B}{A+B} \right| \tag{4.55}$$

Please note that thermodynamic consistency is merely a necessary, but not a sufficient condition for the data to be correct. This is especially true for the integral test, as it treats the data set as a whole. As in the case of isobaric measurements the integral on the right-hand side of Eq. (4.54) is normally not known, it is accounted for by a semiempirical technique for its estimation.

$$J/\% = 150 \frac{|\Delta T_{\max}|}{T_{\min}} \tag{4.56}$$

$\Delta T_{\max}$ is the maximum difference of boiling temperatures in the total composition range, $T_{\min}$ being the lowest boiling temperature.
If $|D-J| \leqslant 10\,\%$, the data set is assumed to be thermodynamical consistent.

A different test regarding the consistency was first introduced by Van Ness [107], a simple direct test of thermodynamic consistency for each point of a VLE data set with respect to the Gibbs-Duhem equation itself [108, 109]. Instead of only one informative value the direct test checks every single data point. The author proved that the residuals of the ratios between experimental and calculated activity coefficients have to be equal to zero for consistent data

$$\ln\frac{\gamma_1^{\mathrm{c}}}{\gamma_2^{\mathrm{c}}} - \ln\frac{\gamma_1^{\mathrm{exp}}}{\gamma_2^{\mathrm{exp}}} = \delta\ln\frac{\gamma_1}{\gamma_2} = 0 \tag{4.57}$$

The closer this residuals are to zero, the better is the consistency of the data points. Being aware that the given condition for the direct test strictly applies only for isothermal data sets, this test is not so stringent in the isobaric case. The appropriate measure is the RMS value of $\delta\ln\frac{\gamma_1}{\gamma_2}$ as determined from the direct test. Van Ness defined a so-called consistency index which starts from 1 for highly consistent data and goes to 10 for data of very poor quality. A maybe more tolerant classification for correlation of isobaric VLE data seems to be adequate as well. Other different approaches can be found in the literature dealing with different functions of measured variables x, T, y, P with and without weighting [110] or a new graphical method to check the consistency [111].
As can be seen from Table 4.2 the consistency area test is satisfied only for PnP + Water, PM + Water at both pressures and PnP + 2-butanol for low-pressure data. For PnP + 1-hexanol this may be due to the fact that this binary mixture is almost ideal and therefore activity coefficients are nearly unary (see Table C.1). Errors in the determined values of γ may drastically change the net area as described by Eq. (4.55). The direct test reveals a somewhat different result with the systems containing ethanol, 2-butanol, 1-hexanol and PM being consistent in a good and satisfactory manner, respectively. However, the aqueous binary systems, having passed the area test, are of only poor quality. The great difference in the activity coefficients of these highly non-ideal systems can cause RMS($\mathrm{d}\ln\gamma_1/\gamma_2$) to become quite large taking into account the uncertainty of the single γ-values. The relatively poor quality of consistency for the system PnP + methanol remains unresolved. It might be due to the inherent approximation in deducing the equations for the consistency tests or the errors of measuring the experimental variables x, y, T, p (being higher than those of high-quality literature data). Also many of the points are measured in the dilute range where only very small errors in the values of T and phase composition give quite large uncertainties in γ. Nevertheless, the good quality of the boiling point diagram defining smooth curves allows for its consideration as a meaningful and correct data set.

Table 4.2.: Thermodynamic consistency tests

	Area test: $D - J$			Direct test: $\mathrm{d}\ln\frac{\gamma_1}{\gamma_2}$		
System	20.0 kPa	101.3 kPa	Results	20.0 kPa	101.3 kPa	Results
PnP + MeOH	31		–	0.16		7
PnP + MeOH		62	–		0.32	10
PnP + EtOH	13		–	0.05		2
PnP + EtOH		70	–		0.10	4
PnP + 2-BuOH	10		+	0.09		4
PnP + 2-BuOH		81	–		0.14	6
PnP + 1-HeOH	42		–	0.04		2
PnP + 1-HeOH		70	–		0.06	3
PnP + Water	8.6		+	0.21		9
PnP + Water		3.6	+		0.24	10
PnP + PM		89	–		0.08	4
PM + Water		7.7	+		0.22	9

4.8. Data Processing

The complete treatment of the measured phase-equilibrium data points was performed on a personal computer running under `Microsoft Windows XP` employing `Maple 10` for the data processing. The flow scheme in Fig. 4.3 shows the principal parts of `Maple` sheet written for the purpose of dealing with just one software. It comprises the input of all required constants, data point values and conversions, both consistency tests, the regression of the model parameters and the preparation of the data collection in terms of boiling point diagrams. The quality of each representation of VLE data sets is given by the standard deviation in the temperature, $\sigma(T)$, and the vapor phase composition, $\sigma(y)$.

4.9. Measurement Method

There exist, in principle, two different techniques for the characterization of vapor-liquid equilibrium for any mixtures: the static as well as the dynamic measurement method. In a dynamic apparatus at least one phase is supposed to recirculate, whilst in the static case the mixture is placed in an enclosed measuring cell. The phase equilibrium is followed by recording the pressure exerted by the liquid phase or the vapor-phase composition at different temperatures. Within the scope of this work the measured VLE data are obtained by the dynamic procedure.
The different binary mixtures containing PnP with alcohols (or water) are chosen so as to have some comparable systems with respect to structure and intermolecular interactions. Solvent 2 always possesses a H-bond network building OH-group and differs in the length of the hydrophobic carbon backbone. An interplay of both, energetic and structural specialities between the mixture's components my be expected. This information will help to expand the concept of possible prevailing interactions existing and described for PnP/H_2O (see Chap. 3).

4.9.1. Experimental Setup

The vapor-liquid equilibria of all mixtures in this study were realized using an all-glass, dynamic recirculating apparatus as described by Walas [91]. The apparatus (Labodest model 602), manufactured by Fischer Labor und Verfahrenstechnik (Germany) allows for the determination of isobaric VLE data.

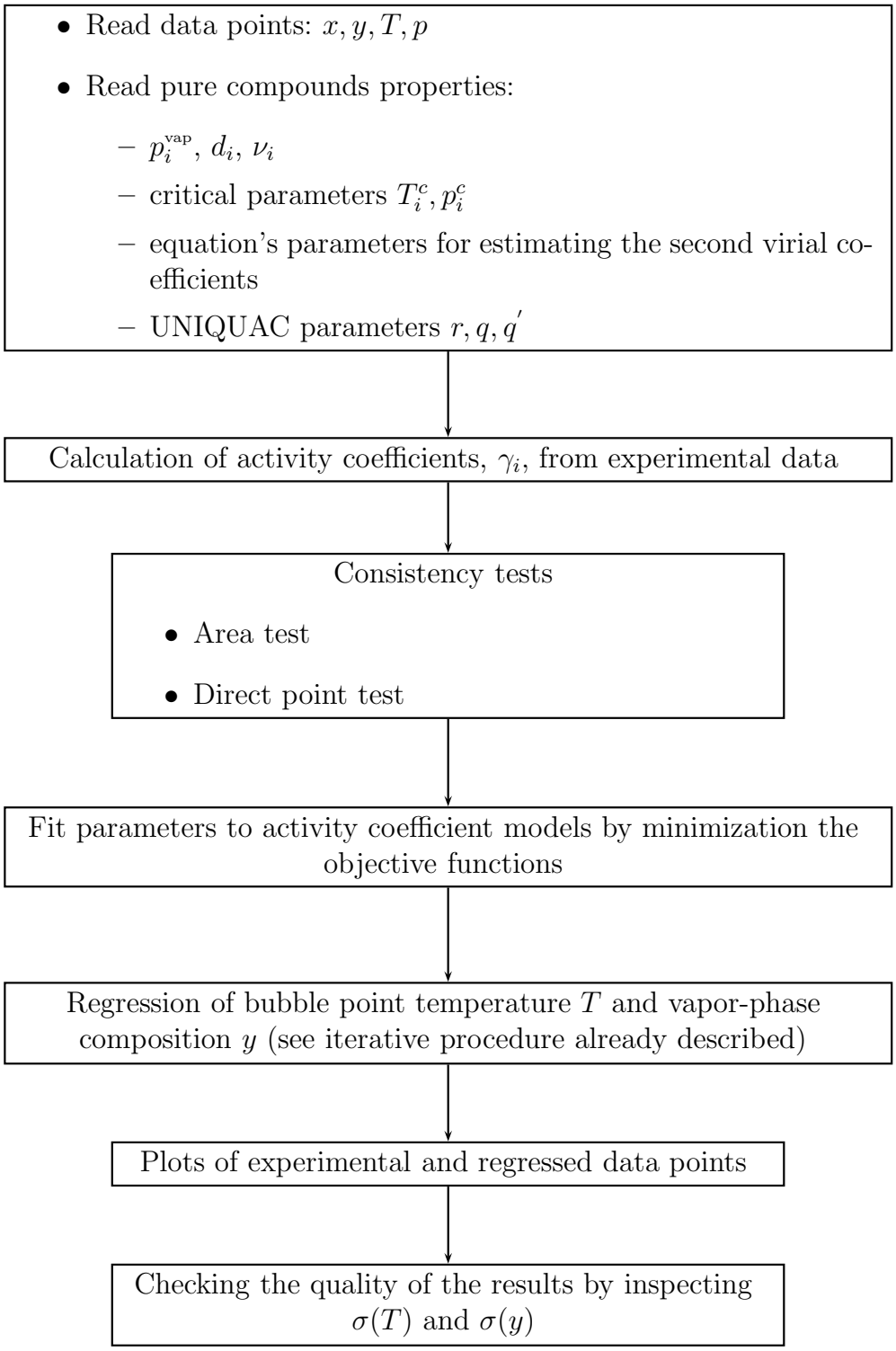

Figure 4.3.: Block Diagram for processing the VLE data

Table 4.3.: Summary of binary systems under investigation

Solvent 1	Solvent 2	$\frac{p}{\text{kPa}}$
PnP	Methanol	101.3, 20.0
PnP	Ethanol	101.3, 20.0
PnP	2-Butanol	101.3, 20.0
PnP	1-Hexanol	101.3, 20.0
PnP	Water	101.3, 20.0
PnP	PM	101.3, 20.0
PM	Water	101.3, 20.0

The measured variables are the boiling temperature and the vapor-phase composition. The apparatus is designed for manual operation at atmospheric pressure, vacuum and overpressure conditions up to 4 bar. The flow chart of the main part of the VLE apparatus is shown in detail in Fig. 4.4. The apparatus consists of one piece of glass body with a total volumetric capacity of about 100 cm^3. The boiling

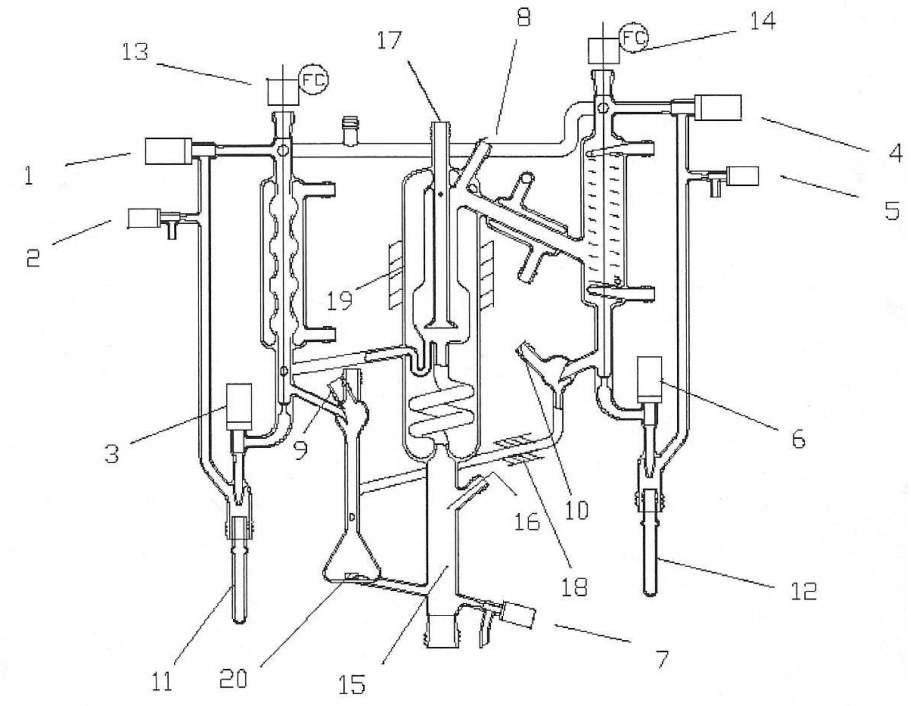

Figure 4.4.: Schematic diagram of the apparatus. Refer to 4.4 for a detailed list of parts.

temperature is measured with a Pt-100 precision resistance (17) connected to a `Kneighley` multimeter with an accuracy of ±0.05 K. The system pressure was controlled at the desired value with an Edwards Barocel digital manometer with a precision of ±0.03 kPa.
The operation procedure is based on the principle of the circulation method as follow: an electrical immersion heater (15) made of quartz glass, which is arranged concentrically in a flow heater, causes evaporation of the liquid. An even circulation of both phases with simultaneous magnetic stirring of the reflowing circulation streams in a special mixing chamber (20) ensures a quick equilibrium adjustment. Before entering the separation chamber, the vapor stream passes a lengthened contact path which guarantees an intimate phase exchange (helical glass element between flow heater and phase separation chamber). Both boiling liquid (drops) as well as rising vapor reach the exchange chamber. This specially designed part of the apparatus is called `Cottrell pump` [112, 113], in which the vapor-liquid mixture is separated in liquid and vapors (4.5). The design of the separation chamber prevents transport of

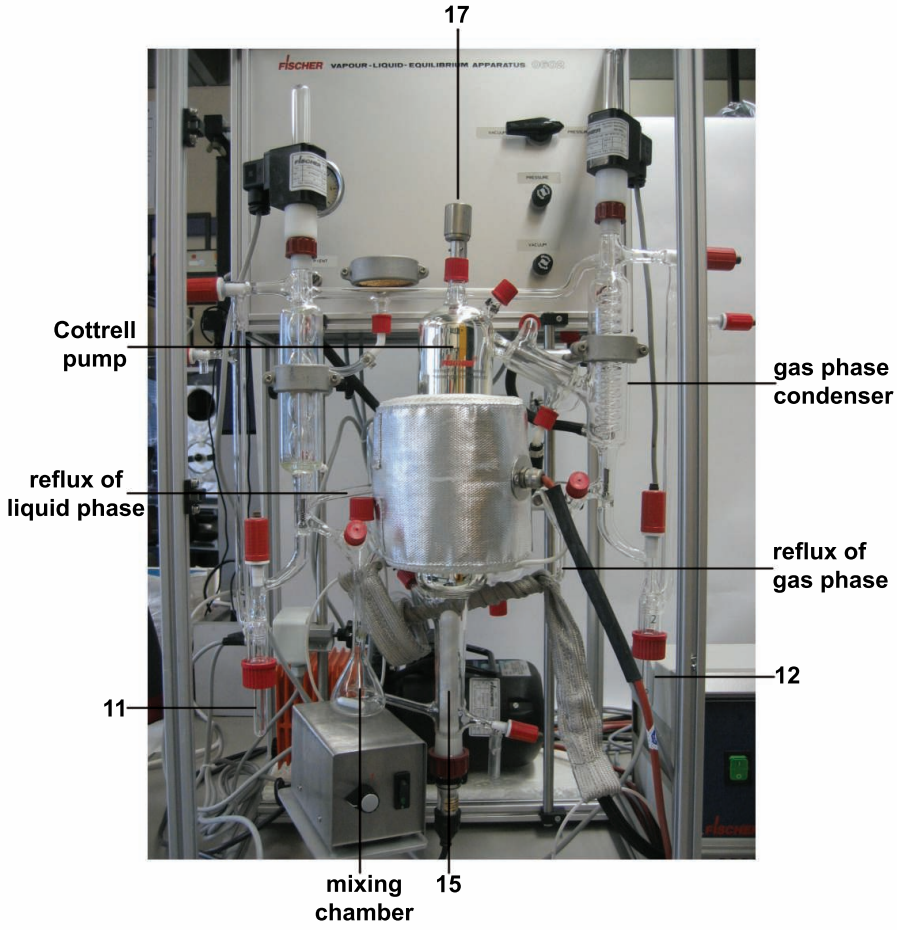

Figure 4.5.: Photograph of the VLE apparatus

liquid drops in the vapor phase, which is condensed in a condenser (gas phase condenser). The status of equilibrium is reached by constant recycling of liquid phase and condensed vapor phase at simultaneous mixing of recirculated flows in the mixing chamber. Equilibrium condition is assumed when constant temperature and pressure are obtained for 20 min or longer. The liquid continuously flows back into the mixing chamber, while the vapor is condensed in a pathway after separation from the liquid.
Sample take-off from the vapor (6) and liquid (3) phases into vacuum and pressure-tight removable receivers (11, 12) is effected by manually controlled solenoid valves (13, 14). Both samples may also be directly extracted from the circulating streams by means of a gas-tight syringe through septa in the apparatus (8, 9, 10).

The control for the apparatus is a Phase Equilibrium Control System M101 by Fischer. It is a control system with micro-processor technology and enables the mantle temperatures (18, 19) and the vacuum/pressure to be controlled, respectively. Actual values to be controlled are displayed in a front display. The measurements can be performed under vacuum, at atmospheric or over-pressure at a temperature of up to approximately 250 °C.

4.9.2. Experimental Procedure

The apparatus is cleaned with water and acetone and flushed with nitrogen overnight until the glass body is dry. Approximately 75 ml of the pure solvent is filled into the mixing chamber so that the liquid level (in the evaporator) is located approximately $2 - 3$ cm above the immersion heater. The immersion heater is set to around 20 % heating power and is adapted properly; it should be neither to low nor to high as to achieve a proper reflux of both phases. The isolation jacket (19) should be preset to 15 °C below

Table 4.4.: Description of the apparatus components

Number	Description
1	valve:pressure equilibrium to sample tube no. 11 (liquid phase sample)
2, 5	ventilation valve
3	outlet valve for the liquid sample
4	valve:pressure equilibrium to sample tube no. 12 (vapor phase sample)
6	outlet valve for the vapor sample
7	discharge valve
8, 10	septum for vapor sample collection
9	septum for liquid sample collection
11	sample tube liquid phase
12	sample tube vapor phase
13	solenoid: liquid sample
14	solenoid: vapor sample
15	electrical immersion heater
16	Pt-100: liquid temperature sensor
17	Pt-100: vapor temperature sensor
18	Pt-100: temperature control of heated tube (condensed vapor reflux)
19	Pt-100: temperature control of heated isolation jacket
20	PTFE stirrer bar

the boiling point of the pure component and has to be adjusted during the measurement. For correct results notice that the mantle temperature must be set lower than the expected vapor temperature. The solvent/mixture is stirred intensively.
When measuring VLE below atmospheric pressure, the whole system loaded with the liquid sample has to be evacuated prior to heating. In this connection both throttle valves are used at vacuum operation (to be operated on the cover plate in Fig 4.5). At the beginning they are closed. The throttle valve `vacuum` has to be opened slowly in order to achieve the desired vacuum and it is used to get an optimal controlling of the pressure when the electrical valve at the vacuum pump is opened. The other valve `pressure` must be opened carefully when the actual value falls below the desired set point. Sample take-out under reduced pressure is best accomplished by means of the septa and a gas-tight syringe with a low distortion of the actual pressure. This procedure is adopted in this work for measurements at 20.0 kPa. Therefore the valves (1, 3, 4, 6) can be left open throughout the operation. Valves (2, 5) are necessarily closed. After each time the equilibrium is established, the temperature is registered, and the samples of both liquid and vapor phase are collected, the second component (between 0.1 mL and 20 mL) is added through port (9). The first additions are small amounts in order to collect enough points to obtain reliable results in the dilute region. In the beginning a small change of the composition could already cause a big change in temperature. The samples withdrawn from the apparatus are filled in GC-vials with 3 μL inlets and subsequently quantitatively analyzed for the composition determination by GC in Sec. 4.10. The process is repeated until the temperature barely changed upon additions of 20 mL and more. To maintain a stable level of the liquid, a volume identical to the next addition step is drained off. When the measurement is finished, the apparatus is cleaned as described above and the measurements are started with the second solvent. This had to be done to obtain the boiling point diagram over the whole composition range ($x_1 = 0 \ldots 1$).

Important notes for operation

A perfect operation of the apparatus depends on the following advices:

1. The volume in the mixing chamber should be constant. Before each new addition the volume of the last addition should be drained off using discharge valve (7).

2. The reflux of the phases has to be steady. The vapor phase should be $60 - 80$ drops per minute, the liquid phase should be a continuously flowing stream. This can be, in part, adjusted by the speed of the stirrer.

3. The heating supply of the immersion heater is adapted properly.

4. The stirrer should be kept at constant speed for each equilibrium point because a faster stirring decreases the reflux of the vapor phase (more liquid is entering the separation chamber).

The circulation method requires relatively large amounts of solvent compared to the static method, and the concentrations of both phases have to be determined. The advantage of the circulation method, however, is the quick appearance of phase equilibrium with simultaneously exact measurement of the boiling temperature.

4.9.3. Temperature Calibration

The equilibrium boiling temperature is measured with the help of a Pt-100 resistance thermometer (17) that reaches inside the separation chamber. Absolute values for the temperatures can be obtained after calibration of the Pt-100 within the temperature range of interest. The original values of resistance can be converted to temperature by means of a calibration curve. For that reason the boiling point of several pure liquid samples at ambient pressure are measured and related to the measured resistance as seen in Fig. 4.6. The actual boiling temperatures are obtained from pure components vapor pressure equations known from the literature (refer to Sec. 6.4.1). Typical for the characteristics of a Pt-100, its resistance

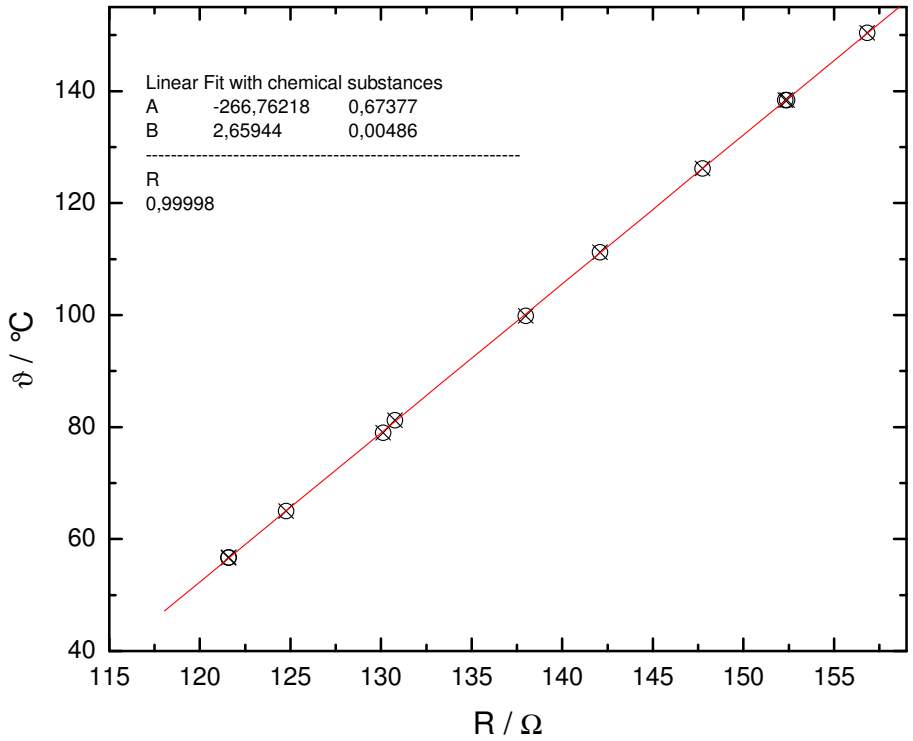

Figure 4.6.: Calibration of the Pt-100 thermometer of the VLE apparatus

changes nearly linear with temperature over a wide range of temperatures.
Temperature measurements in the liquid (16) is not advisable. The main problem is the correct determination of the equilibrium boiling temperature due to overheating around the immersion heater. This can be caused by the high temperature on the heater's surface, the surface tension and hydrostatic pressure in the liquid. Throughout all measurements the deviation between the two temperature signals indicate a liquid with a temperature being $0.3\,°C - 0.5\,°C$ higher than the actual value for the equilibrium condition.

4.10. Analytical Determination of Phase Composition

Equilibrium compositions of sampled liquid and condensed vapor phases were quantitatively analyzed with an `HP 6890` gas chromatograph (GC) equipped with an auto sampler `HP 6890 Injector` carrying 8 sample vials simultaneously. Gas chromatography as it is usually performed is correctly called gas-liquid chromatography. The gaseous analyte in the GC partitions between the mobile phase (carrier gas) and the liquid stationary phase that is coated on the inside of an open-tubular capillary column. Separation is mainly determined by boiling points and by the polarity of the substances. In order to be detected in the GC, the samples must be vaporized without decomposition.

4.10.1. Setup

The GC consists of 4 main components and is shown schematically in Fig. 4.7.

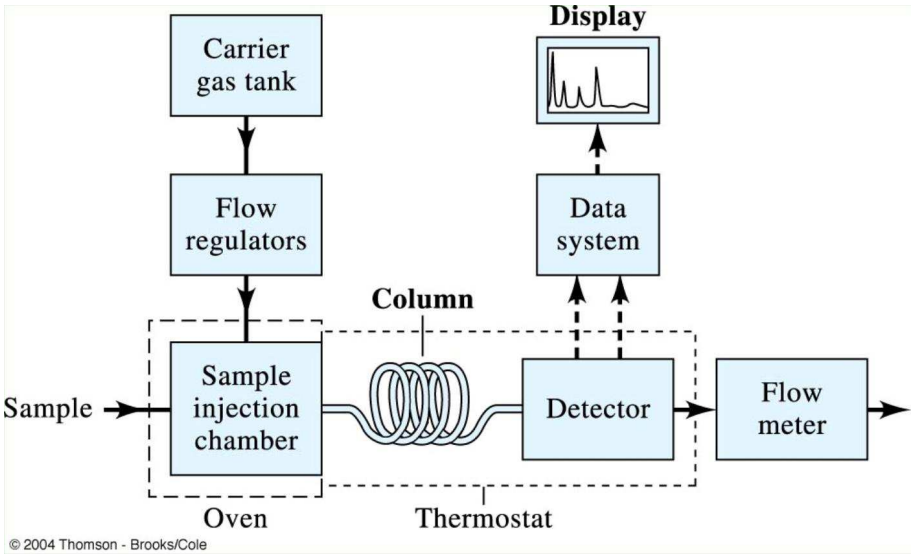

Figure 4.7.: General design of a GC as used in this study

1. The gas supplies have in-line traps to remove any water, oxygen, hydrocarbons or other "contaminants" from compressed gases. The carrier gas is He with a stated purity of 99.999 96 %. Its purpose is to sweep sample through the column, to protect the column from oxygen exposure at elevated temperature and to assist with functions of the detector. Gas flows are controlled with mass-flow controllers (electronic sensors).

2. An in-line injector with split injection. Samples are injected through a septum to keep oxygen out of the column and to provide a seal to keep the carrier gas pressure up at the head of the column. The injection volume is split, with only a portion of the sample actually making it to the column. The temperature is normally set to 250 °C evaporating the complete injected volume.

3. The capillary column is used for vapor liquid distribution chromatography and serves as the stationary phase. The GC column used is a (30 m long, 0.32 mm i.d., 0.25 μm film) capillary column packed with (5%-Phenyl)methyl-polysiloxane (HP- 5) for the PnP/(PM)/alcohol mixtures. Aqueous mixtures are analyzed with a thermal conductivity detector after successful separation in a (30 m long, 0.32 mm i.d., 0.25μm film) capillary column packed with poly(ethyleneglycol) (Supelcowax10).

4. The detector. Most commonly used is the **f**lame **i**onization **d**etector. The FID can be used for all carbon containing substances. The molecule is converted to radicals in the flame and

oxidized/ionized by oxygen atoms and OH-radicals. The second detector used is the **t**hermal **c**onductivity **d**etector, TCD. It is used for gases like carbon dioxide, oxygen, hydrogen and inert gases, also for water, because it is not detectable with the FID.

Data collection as well as peak integration is done using a computerized data system called `HP GC ChemStation, Rev. A. 06.01`.
For each binary system a suitable set of parameters has been chosen in order to guarantee a proper separation within a reasonable amount of time. Most importantly the split-ratio of the injection volume and the oven temperature are parameters which significantly alter the efficiency of separation. The following Table 4.5 summarizes the parameter settings of the GC.

Table 4.5.: Important parameters of the GC throughout the measurements

system	detector	column	split-ratio	column pressure / kPa	ϑ_{oven} / °C
PnP + MeOH	FID, 250 °C	HP-5	140 : 1	62.9	40
PnP + EtOH	FID, 250 °C	HP-5	120 : 1	74.9	60
PnP + 2-BuOH	FID, 250 °C	HP-5	80 : 1	65.6	70
PnP + 1-HeOH	FID, 250 °C	HP-5	80 : 1	62.9	70
PnP + H_2O	TCD, 210 °C	Supelcowax10	80 : 1	61.3	65
PnP + PM	FID, 250 °C	HP-5	80 : 1	65.6	70
PM + H_2O	TCD, 210 °C	Supelcowax10	40 : 1	61.3	65

4.10.2. Calibration

The magnitude of the detectors signal depends among other factors on the solvents ability to be ionized and its thermal conductivity. This means that the detector's sensitivity is different for every compound analyzed. Furthermore the relation between the amount of sample injected is not necessarily linear to the signal detected. It is not possible to get the composition of the injected sample by simply calculating the peak's areas on that account, but the apparatus has to be calibrated for every single binary mixture at first. It is known from experience that both the calibration and the subsequent measurements must be done on the same column and under the same experimental conditions. To obtain the calibration curve, various gravimetrically prepared samples over the whole composition range were injected. Due to the unknown dependency of the signal from the injected volume the injections for calibration have the same volume than for the measured samples. The obtained peak areas of component i are converted to area fractions ξ_i

$$\xi_i = \frac{\text{Area}_i}{\sum \text{Area}_i} \tag{4.58}$$

For each binary system a calibration is done using up to 20 different liquid mixtures of known compositions. Two samples were replicated for each mixture at fixed experimental conditions. The average area fraction from GC is converted into mole fraction with the help of a calibration equation, which correlates the mole fractions and area fractions using a fifth-order polynomial or a rational function. Vapor and liquid phase compositions were determined with this calibration curve. The average uncertainty in the measurement of the mole fraction is ±0.003, which has been obtained by comparison of the known composition with the composition calculated from the calibration curve.
A compilation of all calibration functions is given in the following Figs. 4.8- 4.14 together with the corresponding coefficients. Experimental values for ξ_i and x_i can be found in Appendix B.

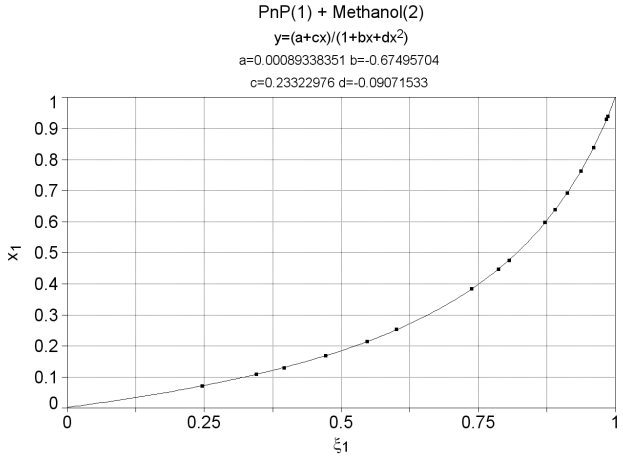

Figure 4.8.: Plot of x_1 vs. ξ_1 of PnP in the binary mixture with methanol

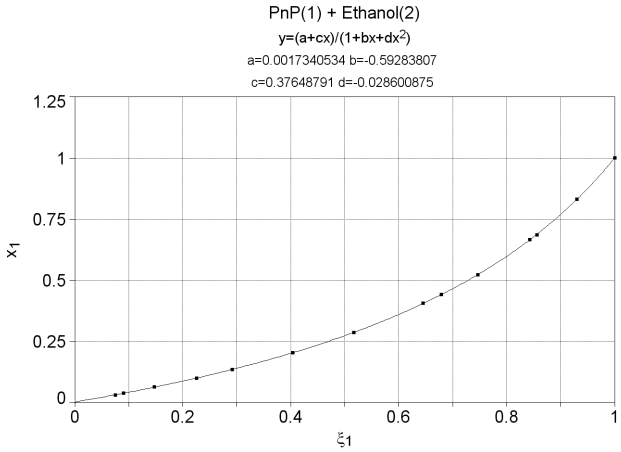

Figure 4.9.: Plot of x_1 vs. ξ_1 of PnP in the binary mixture with ethanol

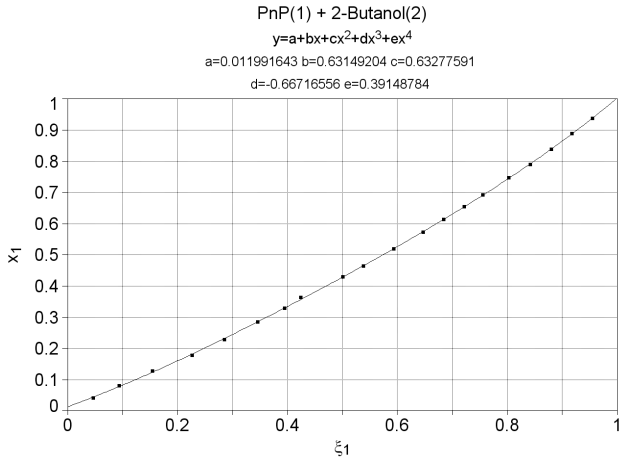

Figure 4.10.: Plot of x_1 vs. ξ_1 of PnP in the binary mixture with 2-butanol

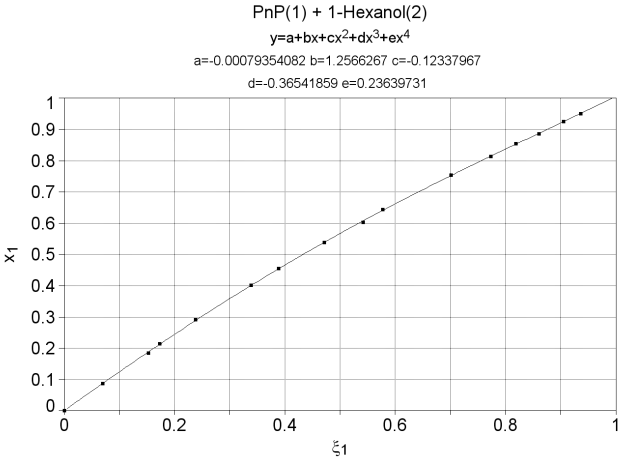

Figure 4.11.: Plot of x_1 vs. ξ_1 of PnP in the binary mixture with 1-hexanol

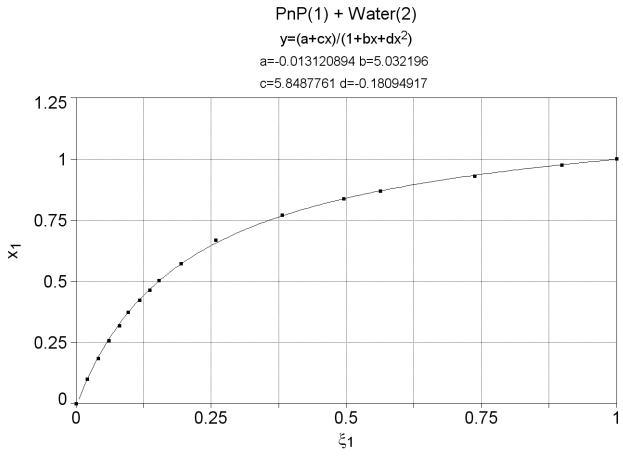

Figure 4.12.: Plot of x_1 vs. ξ_1 of PnP in the binary mixture with water

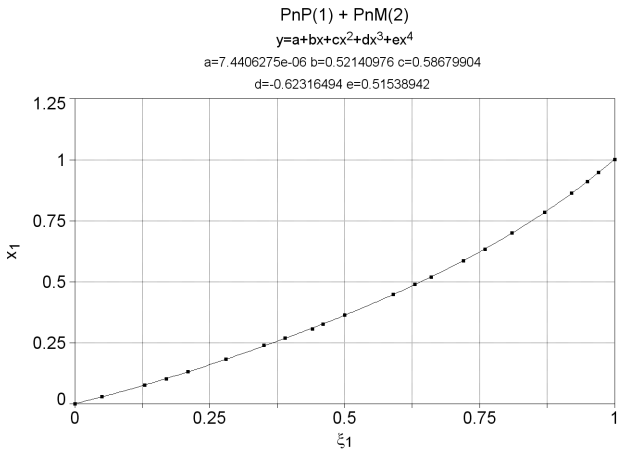

Figure 4.13.: Plot of x_1 vs. ξ_1 of PnP in the binary mixture with PM

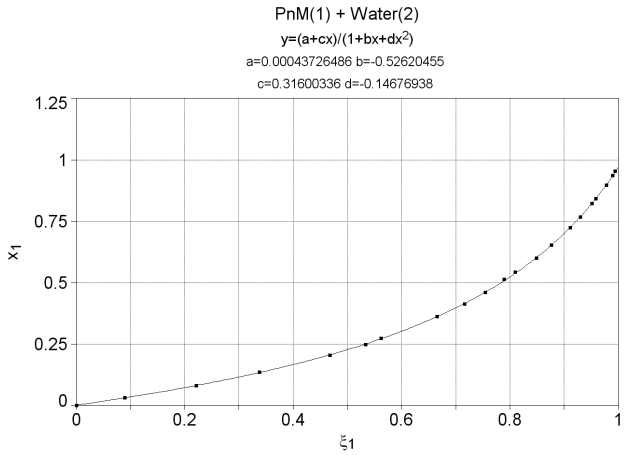

Figure 4.14.: Plot of x_1 vs. ξ_1 of PM in the binary mixture with water

The calibration curves show that it is evident that the different response of the GC signal on the chemical composition of the sample under investigation must be taken into consideration. The dependence of ξ_i on x_i in the systems containing PnP is clearly different.

Evaluation of the measured binary systems with respect to the excess Gibbs energy models are now possible with all the theoretical as well as experimental information given so far. The experimental data on the phase diagram are first converted to activity coefficients with which the binary interaction parameters of the models are evaluated to construct the boiling point diagrams. Before presenting the experimental and correlation results, however, a description of the predictive methods applied in this study must not be missing at this point. Their explanation is placed here because they can be used independently of any experimental data, but are based on general parameters, which allow for the calculation of the crucial thermodynamic value, the activity coefficients.

4.11. Predictive Models

Prediction of the isobaric VLE values is accomplished by using the modified UNIFAC (Dortmund) group-contribution model, which considers the variation in group interaction parameters with temperature [114] and by using the COSMO-RS method, nowadays a well-established predictive model for thermodynamic properties of fluids [115], based on a **con**ductor-like **s**creening **m**odel (COSMO) and described in more detail in 4.11.2.

4.11.1. UNIFAC (mod-UNIFAC (Do))

The group contribution method mod-UNIFAC (Do) is a excess Gibbs energy model for the calculation of activity coefficients in nonelectrolyte systems [116]. The activity coefficient is obtained as the sum of a combinatorial part (C) and a residual part (R):

$$\ln\gamma_i = \ln\gamma_i^{\mathrm{C}} + \ln\gamma_i^{\mathrm{R}} \tag{4.59}$$

The combinatorial part accounts for the contribution of the excess entropy, which results from the different shape and size of the molecules; the residual part represents the contribution of the excess enthalpy as a result of the energetic interactions. In that the model is based on UNIQUAC, different to that, however, contributions to the activity coefficient are of empirical nature.
The mod-UNIFAC (Do) calculation were not executed within this work but the results were gratefully supplied by Dr. Sven Horstmann[1]. Within the concept of UNIFAC (***uni****versal* ***f****unctional* ***ac****tivity coeffi-*

[1] Dr. Sven Hartmann, LTP GmbH, Oldenburg; www.ltp-oldenburg.de

cient) a molecule is divided into functional groups [117]. Molecule-molecule interactions are considered to be properly weighed sums of group-group interactions. For a multifunctional component in a multicomponent system, group-contribution methods assume that each functional group behaves independent of the molecule in which it appears. Necessary information on the group-group interactions is obtained from reduction of experimental data for binary systems. The modified UNIFAC concept used in this work makes advantage of a more sophisticated separation of molecules into groups and the temperature-dependence of the group-interaction parameters are explicitly taken into account [114, 118]. This allows for a better description of temperature-dependent systems involving molecules very different in size. The

```
(1)    712 1-PROPOXY-2-PROPANOL                                  C6H14O2
(2)    296 1-HEXANOL                                             C6H14O

+++++ ANTOINE CONSTANTS                REGION+++++
(1)    7.06799 1408.510  186.182  186- 186 C
(2)    7.86047 1761.260  196.660  -20- 330 C

+++++ DIPPR 101 CONSTANTS                                              REGION+++++
(1)    0.0000       0.0000       0.0000       0.0000          0.     0-    0 K
(2)    0.0000       0.0000       0.0000       0.0000          0.     0-    0 K

mod. UNIFAC (DO)

PRESSURE=  150.01 MM HG   (  0.200BAR  )

 #DDB    STRUCT. INFORMATION
  712   1003  1081  2001  2002  1025
  296   1001  5002  1014

REQUIRED UNIFAC AREAS AND SURFACES:
MAIN-          SUB-
GROUP        GROUP K          R(K)    Q(K)
   1 CH2        3 CH         0.6325  0.3554
   5 OH        81 OH (S)     1.0630  0.8663
   1 CH2        1 CH3        0.6325  1.0608
   1 CH2        2 CH2        0.6325  0.7081
  13 CH2O      25 CH2O       1.1434  1.2495
   5 OH        14 OH (P)     1.2302  0.8927

REQUIRED UNIFAC INTERACTION PARAMETERS:
 N  M   A(N,M)      A(M,N)      B(N,M)      B(M,N)      C(N,M)      C(M,N)
 1  5  2777.0      1606.0     -4.6740     -4.7460     0.15510E-02 0.91810E-03
 1 13   233.10     -9.6540    -0.31550    -0.32420E-01  0.0000      0.0000
 5 13   816.70      650.90     -5.0920     -0.71320    0.60650E-02 0.81500E-03
```

Figure 4.15.: Input data for mod-UNIFAC (Do) for the binary system PnP - 1-hexanol

model parameters are supplied in an input file, the text of which is shown in Fig. 4.15. $R(K)$ and $Q(K)$ are the values for the van-der-Waals volume and surface area of the subgroup designated with K, respectively. The group-interaction parameters $a_{nm}, a_{mn}, b_{nm}, b_{mn}, c_{nm}, c_{mn}$ describe the interaction between the groups n and m. The assignment of the main group number $n(m)$ to the functional groups can be found in Ref. [119].

4.11.2. COSMO-RS

4.11.2.1. Theory

The COSMO-RS method only requires the structures of the molecules involved in the mixtures. It is based on the theory of the ***P**olarisable **C**ontinuum **M**ethod , PCM* [120], an improved version of the classical quantum chemical ***C**ontinuum **S**olvation **M**odels, CSM* [121]. In the framework of the CSM the solvent surrounding the solvated molecule (solvate i) is represented by an infinitely extended electrical conductor characterized only by its permittivity ϵ. The influence of the solvent on the properties of the solvate is expressed only by the dipolar behavior of the continuum. Molecule i, embedded in the dielectric medium via a molecular surface or "cavity" that is constructed around molecule i, represents a system with ideal behavior (c.f. ideal gas state with no interactions to adjacent molecules). The cavities surface is divided into several surface segments. The transfer to the description of the real state of a solvated compound is accomplished by modelling the disturbance of the ideal state with a term combining contributions from van-der-Waals interactions, energy required to form the cavity of the solvate, and the electrostatic interactions between ions and dipoles.
The *conductor-like screening model*, COSMO, introduced by Klamt et. al. [122–124], considers the continuum as a perfect electric conductor ($\epsilon = 0$) instead of a dielectric medium of permittivity ϵ. This

boundary condition makes the calculation of interactions between solute and solvent much more feasible and gives a reason for its great efficiency. Herein the pure ensemble of compound i embedded in the conductor is the reference state, expressed by μ_i^0 in Eq. 4.66. A COSMO calculation gives the polarization charge density of every conductor's surface segment resulting from the screening of the solute electric field and is usually carried out at an adequate quantum level as provided by density functional theory (DFT). In addition, a COSMO calculation also gives the energy, the geometry and the screening charge density σ on the surface' segments of a solute after quantum chemical self-consistency and geometry optimization loops. Every single component of the mixture is characterized by the distribution of its screening charges instead of its geometrical arrangement of the atoms. The transfer of the ideal state of a molecule embedded in a virtual conductor to the real state of a solvent surrounding the solute is done by the second step in the COSMO-RS calculation [125], which is based on statistical thermodynamics of interacting molecular surface charges.
Therefore, a fluid is considered to be an ensemble of closely packed and pairwise-interacting pieces of surface as pictured in Fig. 4.16. The polarization charge densities σ and σ' are used for the quantification of the interaction energy of each pair of segments. The interaction energy for the ensemble is then

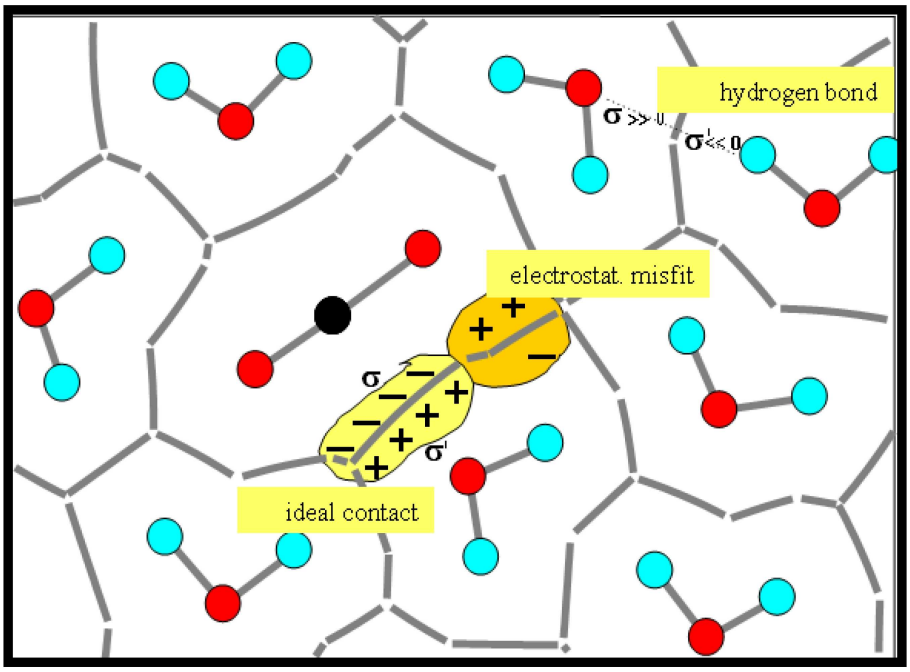

Figure 4.16.: Interaction of molecules described by an ensemble of pairwise interacting surface segments σ [126]

obtained by a statistically correct consideration of all possible pairs of pieces of surface. As can be seen in Fig. 4.16 the surface segments from the COSMO calculation with charge density σ and an effective area a_{eff} are consistently brought to contact. In case of pairwise segments of equal charge density, the charges compensate. The grey lines indicate the residual amount of conductor separating the cavities. In reality there is no conductor between the molecules. Interacting segments with different charge densities σ and σ' of opposite polarity or adjacent segments with equal polarity, therefore, give rise to an overall electrostatic misfit, whose contribution to the local electrostatic interaction energy is expressed by

$$E_{\text{misfit}}(\sigma, \sigma') = a_{\text{eff}} e_{\text{misfit}} = a_{\text{eff}} \frac{\alpha'}{2} (\sigma + \sigma')^2 \tag{4.60}$$

with α' adjusted to experimental data. Obviously, if σ equals $-\sigma'$ the misfit energy of a surface contact will vanish.
In mixture of strongly polar components the occurrence of hydrogen-bonding E_{hb} can also be taken into

account by the following contribution to E_{int}

$$E_{\text{hb}}(\sigma, \sigma') = a_{\text{eff}} e_{\text{hb}} = a_{\text{eff}} c_{\text{hb}} \min\{0, \min(0, \sigma_{\text{don}} + \sigma_{\text{hb}}) \ \max(0, \sigma_{\text{acc}} - \sigma_{\text{hb}})\} \tag{4.61}$$

Hydrogen bonds can be expected if two segments with sufficient polarity of opposite sign (σ_{don} and σ_{acc}) are in contact and if their charge density is greater than a certain threshold σ_{hb}; σ_{hb} and c_{hb} are also variables obtained from a parametrization on experimental data.
In addition to the electrostatic intermolecular interactions the contribution of the non-specific van-der-Waals interactions are effected by two parameters $\tau_{\text{vdW}}, \tau'_{\text{vdW}}$

$$E_{\text{vdW}} = a_{\text{eff}}(\tau_{\text{vdW}} + \tau'_{\text{vdW}}) \tag{4.62}$$

The link between the microscopic surface segment interaction energy E_{int} and the macroscopic thermodynamic potential of solute i in the mixture is provided by inspection of the molecular interactions of local pair-wise surface segments with σ as the only measure of interest. All possible combination of surface segments must be considered. The information on the distribution of the surface segments with respect to σ is provided by the distribution function $P_i(\sigma)$, also called σ-profile for each molecule i. The σ-profile results from a plot of the number of segments with a charge-density σ_i. The σ-profile and σ-potential ($\mu_{i,S}$) are characteristic for each molecule and are exemplified for PnP in Fig. 4.17. Both

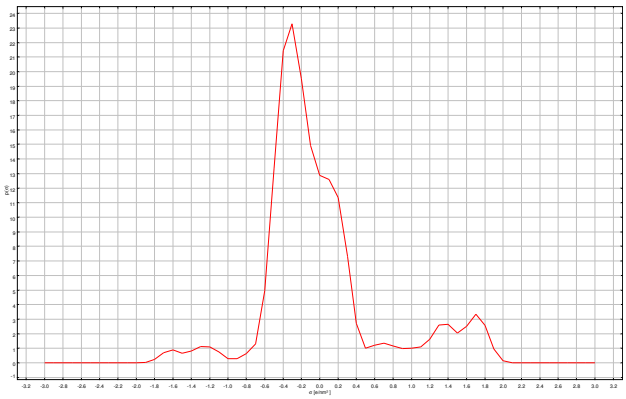

Figure 4.17.: $P(\sigma)$ of PnP

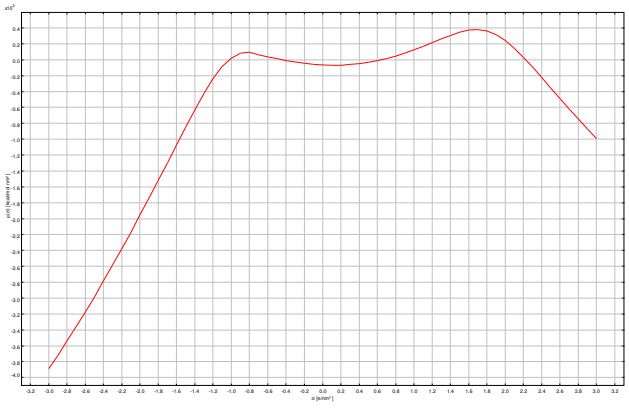

Figure 4.18.: $\mu_{\text{PnP,S}}(\sigma)$ of PnP

diagrams contain valuable information with respect to the intermolecular interactions. As a partially negative atom will cause an opposite positive charge density on the cavity's surface, the small peak at around $\sigma \simeq -1.4$ can be attributed to the hydrogen of the hydroxyl-group, whereas surface segments with $\sigma \simeq 1.5$ result from the negative charge of the oxygen atoms in the molecule. This distribution indicates the ability of PnP to act as hydrogen-bond acceptor and donor, respectively. There is a relatively narrow and high distribution of the charge densities around $-0.3\,\text{e/nm}^2$, which arises from the neutral carbon backbone of the molecule. The corresponding σ-potential in Fig. 4.18, which is a measure for the affinity of 1-Propoxy-2-propanol to a molecular surface with polarity σ, has a much higher value for polarities between $-1.0\,\text{e/nm}^2$ – $+1.5\,\text{e/nm}^2$ than in the outer region. This indicates a comparable unfavorable interaction with non-polar surfaces, but the possibility to form stronger interactions with molecular surfaces with higher polarity, namely hydrogen-bonding. Surfaces with $\sigma < -1.5$ (hydrogen bond-acceptor) or $\sigma > +2.0$ (hb-donor) of another compound can form hydrogen bonds to PnP.

In order to calculate the chemical potential of solute i in the solvent mixture S, the σ-profile of the whole system as the concentration-weighted average of the pure profiles $P_i(\sigma)$ is required.

$$P_{\text{S}}(\sigma) = \sum_i x_i P_i(\sigma) \tag{4.63}$$

The chemical potential of the contact surface segment $\mu_S(\sigma)$ on the cavity surface is as follows

$$\exp\left(-\frac{\mu_{\mathrm{S}}(\sigma)}{\mathrm{k}T}\right) = \int P_{\mathrm{S}}(\sigma')\exp\left[-\frac{E_{int}(\sigma,\sigma') - \mu_{\mathrm{S}}(\sigma')}{\mathrm{k}T}\right] d\sigma'. \tag{4.64}$$

$E_{int}(\sigma,\sigma')$ means the interaction energies of a segment pair $\sigma - \sigma'$. $\mu_{\mathrm{S}}(\sigma)$ are obtained by iterative calculation of Eq. (4.64). The integral range covers the number of molecular surface segments. $\mu_{\mathrm{S}}(\sigma)$ is a measure of the affinity of mixture S to a surface of polarity σ. Multiplication of $\mu_S(\sigma)$ with the frequency of occurrence of segments σ, $P_i(\sigma)$, gives the fraction of those segments on the chemical potential of the solute i. Integration over the cavities surface makes the chemical potential $\mu_{i,S}$ of species i available in the mixture

$$\mu_{\mathrm{i,S}} = \mu^{\mathrm{C}}_{\mathrm{i,S}} + \int P_i(\sigma)\mu_{\mathrm{S}}(\sigma)d\sigma \tag{4.65}$$

The first term of the right hand of Eq.(4.65) is a combinatorial contribution to the chemical potential [126]. Finally the obtained chemical potential is used to calculate the activity coefficient of component i, γ_i

$$\gamma_i = \exp\left[-\frac{\mu_{\mathrm{i,S}} - \mu^{0}_{\mathrm{i,S}}}{\mathrm{k}T}\right] \tag{4.66}$$

where the superscript '0' denotes the property of pure component i, which is obtained separately in a COSMO-RS simulation with $x_i = 1$.
Numerous examples of the application of COSMO-RS on the calculation of phase-equilibria [127–131], optimization of separation processes [132] and the effects on conformational distributions on σ-profiles in COSMO theories [133] can be found in the literature.

4.11.2.2. Calculation of Phase Equilibria

The input necessary for the calculation of VLE data is the temperature, phase composition and the molecular structure of each component, e.g. the connectivity of the atoms as well as their spatial orientation. For species which may occur as conformers, different COSMO-files for a single molecule are to be included.
The calculations were performed using a continuum model with density functional theory using BP functional with TZVP basis set. All DFT-COSMO calculations were carried out with the quantum chemical program `Turbomole` [134] (version 5.8). Geometry optimization of the molecules is done with `Turbomole` as well. The starting geometries of lots of different conformers are shown to reach the same energetic minima only in few cases for PnP. Conformers with energies more than 8 kJmol^{-1} greater than the most stable (lowest energy in COSMO calculation) are disregarded. The molecular structures of PnP are evaluated with the software `Molden` and serve as input parameter for the geometry optimization in `Turbomole`. The different starting geometries for PnP are chosen from the standpoint of a significantly different polarity. Rotational conformers of nonpolar groups result in no distinct change of the σ-surface. In the case of 1-propoxy-2-propanol, therefore, care is taken to generate stable conformers in which a possible, intramolecular hydrogen-bonding might occur, the position of the OH-group differs from other structures, and the final surface charge distribution has obviously different distribution of charged surface segments. Due to missing additional functional groups no more exceptional configurations are to be expected. The three most stable conformers of PnP which are generated and which are within the energy limit of 8 kJmol^{-1} are displayed in the following figure. The final results of these calculations, which have to be

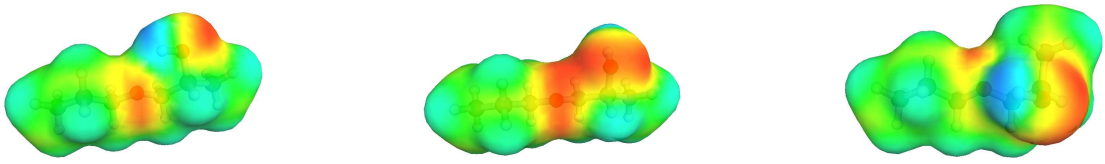

performed for every component only once, are the so-called *COSMO*-files (*.ccf* or *.cosmo*). They contain

all information on the potential energy, the optimized molecular geometry, and the corresponding charge distribution. It represents the structure of a single conformer. All files are favorable stored in a database for further use in the COSMO-RS calculation with systems containing these species. The final step to obtain the chemical potentials and activity coefficients is a COSMO-RS calculation with the help of COSMO*therm* software [135, 123]. Isobaric binary calculations for the mixture PnP and methanol, ethanol, 2-butanol, 1-hexanol and water at 20.0 kPa and 101.3 kPa, respectively, have been done at 30 different binary mixture compositions, using the standard grid of the COSMO*therm* software. For the aqueous system, an additional optional feature of the software is used to calculate the liquid-liquid-equilibrium compositions in the case of phase separation. In the COSMO-RS calculation, several conformers were taken into account for 1-propoxy-2-propanol, ethanol and 2-butanol. The overall proceeding in the application of the COSMO-RS model to the prediction of VLE phase diagrams as explained in the text above is shown schematically in Fig. 4.19.

4.11.2.3. Parametrization

The implementation of the COSMO-RS model into the software COSMO*therm* is accompanied by the specification of the global constants α', σ_{hb}, and c_{hb} as mentioned in 4.11.2.1. Furthermore the element-specific constants like the van-der-Waals parameter τ and an optimized atomic radius for the most important elements are included. All of those parameters result from their adaption to a multitude of experimental phase-equilibrium data sets. The combinatorial part of the potential contains another three parameters and thus the model depends on a relatively small amount of adjustable parameters (16), some of which are physically predetermined and not specific of functional parts or molecule types. They are required for the quantum-chemical calculation within the framework of *COSMO* and completely general to allow the prediction of nearly every imaginable mixture.

The graphical results of the COSMO-RS calculations are included in the binary diagrams in Fig. 4.21-4.27 together with the representation of the VLE curve obtained by the mod-UNIFAC model.

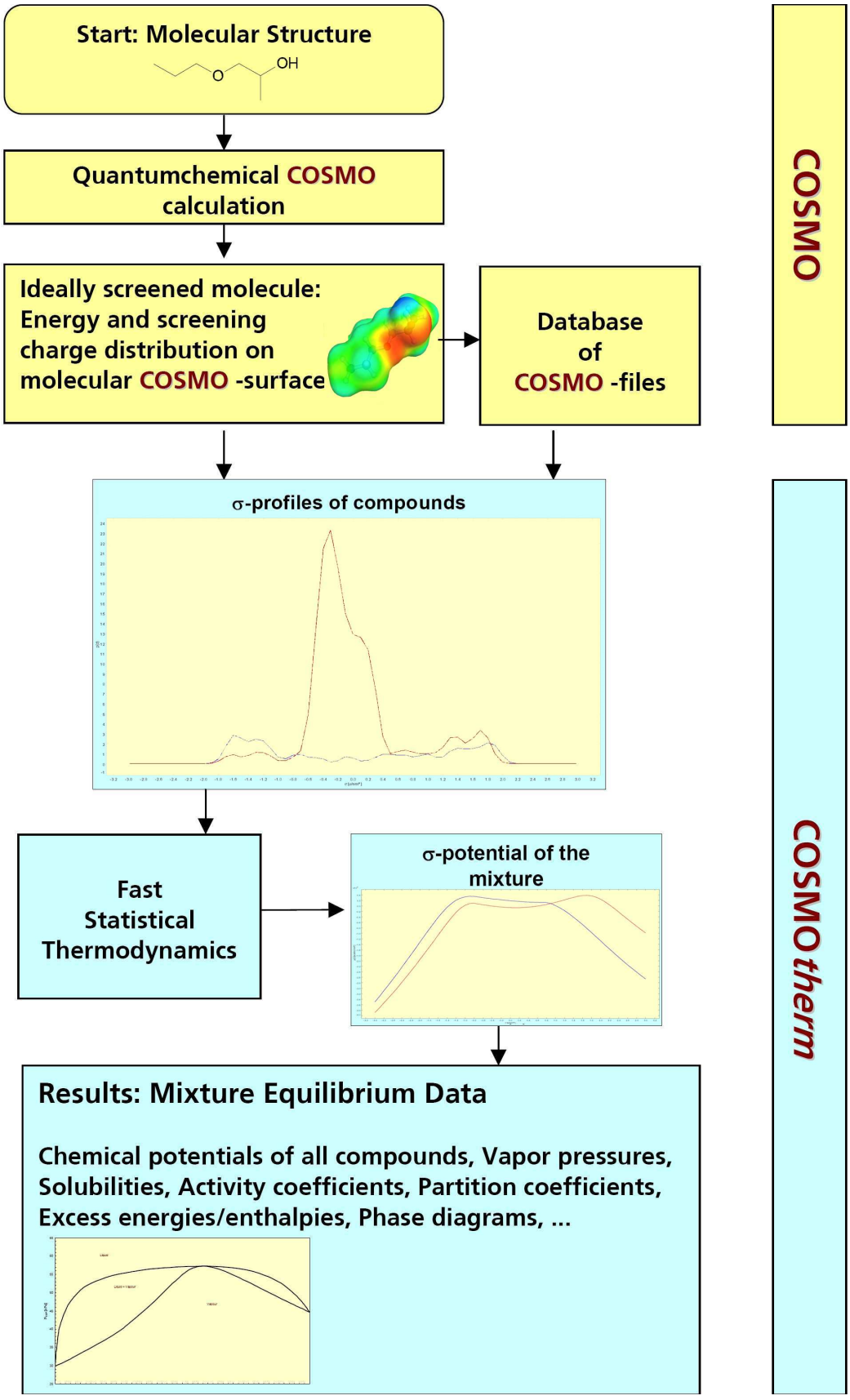

Figure 4.19.: Approach to the prediction of VLE diagrams with the COSMO-RS model [136]

4.12. Discussion of Experimental Results

In this section the presentation of all binary VLE data is dealt with according to the compilation of investigated systems in Table 4.3. The results of the phase equilibrium measurements are described below. The x, y, T data are presented in Appendix C. These tables give the calculated liquid, x, and vapor composition, y, the measured temperature, T, and the ratio of the activity coefficients, $\ln \gamma_1/\gamma_2$. The compositions are reported on a mole basis. Each binary system is described together with the results of data reduction by the excess Gibbs models. The activity coefficient parameters used in the correlation together with the values of the standard deviations in boiling point, $\sigma(T)$, and in vapor-phase mole fraction, $\sigma(y)$, are given in Table 4.7. Supplementary literature data on the solution behavior of the binary mixtures are listed whenever available in order to clarify the nature and magnitude of interactions and their impact on the phase behavior.
In this connection the molar excess volume, V_m^{ex}, of binary mixtures containing PnP and alcohols/water are of special interest and already available. Both of the components are well known to have the ability to form intra- and intermolecular hydrogen bonds having self-associated properties. Upon mixing together, these mixtures generate interesting properties reflecting their magnitude in the excess molar volume (mixing property). Experimental results on the volumetric properties of selected mixtures are shown in Fig. 4.20 for $T = 298.15\,\mathrm{K}$. The excess molar volume increase in the order water – methanol – ethanol –

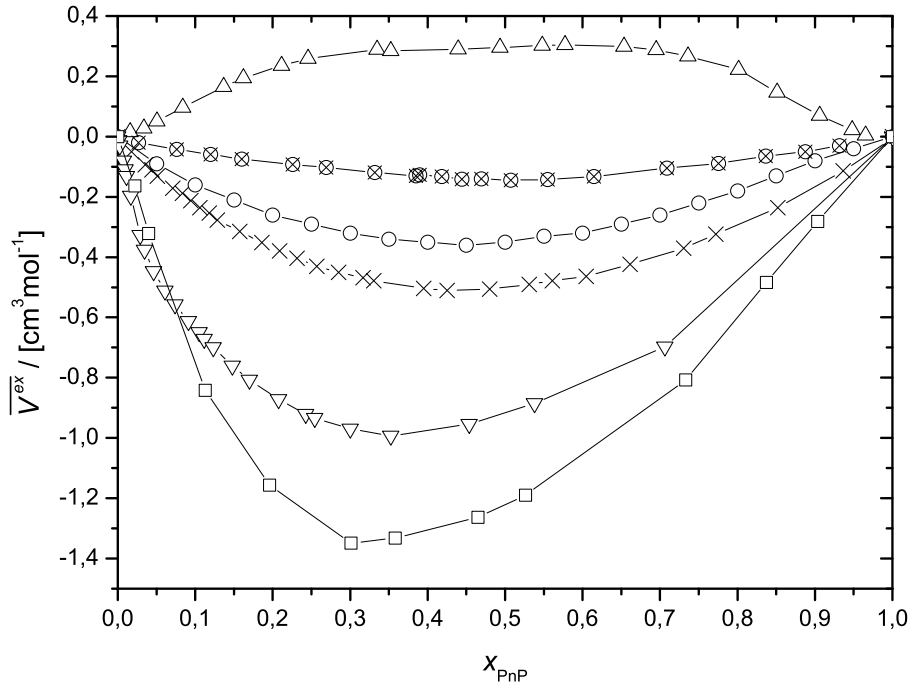

Figure 4.20.: Excess molar volume for 1-propoxy-2-propanol + methanol(×) [137]; PnP + ethanol(○) [138]; PnP + 1-butanol(⊗) [139]; PnP + 2-butanol(△) [139]; PnP + water(▽)[this work]; PM + water(□) [140]

1-butanol – 2-butanol. With the exception of 2-butanol, all values of V_m^{ex} are negative over the whole composition range. The composition dependence of the excess molar volume can be explained as a balance between positive contributions (hydrogen bond rupture between like molecules, dispersive interactions between unlike molecules) and negative contributions (intermolecular dipolar interactions and geometrical fitting between components). The interactions between PnP and alcohols most obvious lead to weak dispersion type and hydrogen bond effects (possibly due to the etheric and OH-groups), giving a negative contribution to V_m^{ex}. Rather large negative excess volumes indicate the existence of strong intermolecular interactions between PnP/PM and water. With increasing chain length of the alcohol, the interactions between unlike molecules become less important, V_m^{ex} is less negative (or positive as is the case for 2-butanol). Studies on different alkoxypropanols exhibit a decreasing V_m^{ex} with an increasing length

of the alkyl chain or the number of $-OC_3H_6-$ groups in the glycol molecules [138]. Opposite signs for the excess molar viscosities in these binary mixtures enhance the proposed order of intermolecular interactions [140, 138, 139].
Partial molar volumes of the alkoxypropanol at infinite dilution, v_1^0, in *n*-alcohols are listed in Table 4.6. All of these v_1^0 values for PnP are smaller than the corresponding v_1^* values of pure PnP. This observation is consistent with the idea that the molar volume is the result of the molecular volume plus the empty volume that arises from the intra- and intermolecular self-association of pure PnP [137].
It can also be noted that all of the v_2^0 values are smaller than the corresponding molar volumes of pure alcohols. One can say that the *n*-alcohol molecules are partially fitting into the empty spaces in PnP, resulting in negative excess volume.

Table 4.6.: Partial molar volumes of alkoxypropanols (1) and aliphatic alcohols/water (2) at infinite dilution at 298.15 K

System	$v_1^* 10^6$	$v_1^0 10^{6a}$	$v_2^* 10^6$	$v_2^0 10^{6a}$
	$m^3 mol^{-1}$	$m^3 mol^{-1}$	$m^3 mol^{-1}$	$m^3 mol^{-1}$
PM (1) + H_2O (2)	98.34	95.2	18.06	–
PnP (1) + H_2O (2)	134.15	123.7	18.06	–
PnP (1) + methanol (2)	134.15	131.3	40.74	38.68
PnP (1) + ethanol (2)	134.15	132.2	58.64	57.97
PnP (1) + 1-butanol (2)	134.15	133.4	91.31	91.74
PnP (1) + 2-butanol (2)	134.15	134.8	91.20	90.85

[a] obtained by extrapolation of experimental $\Phi_{v,i}$ towards $x_i = 0$

In terms of the phase diagrams it is noteworthy to say that the deviations from ideality are all rather small for the organic mixtures, whereby significant departures are detectable in the aqueous systems. The experimental data for the five systems at 20.0 kPa and seven systems at 101.3 kPa are shown in Fig. 4.21 - 4.27 together with the curves obtained with the excess Gibbs energy model equation, showing the smallest deviations in temperature and vapor-phase composition. The predictive power of applying the UNIFAC model as well as the COSMO-RS approach is demonstrated graphically in comparison with the experimental boiling points. No results of comparable measurements in the literature could be found. Only for PM + water exists a publication, dealing with the isothermal VLE behavior.

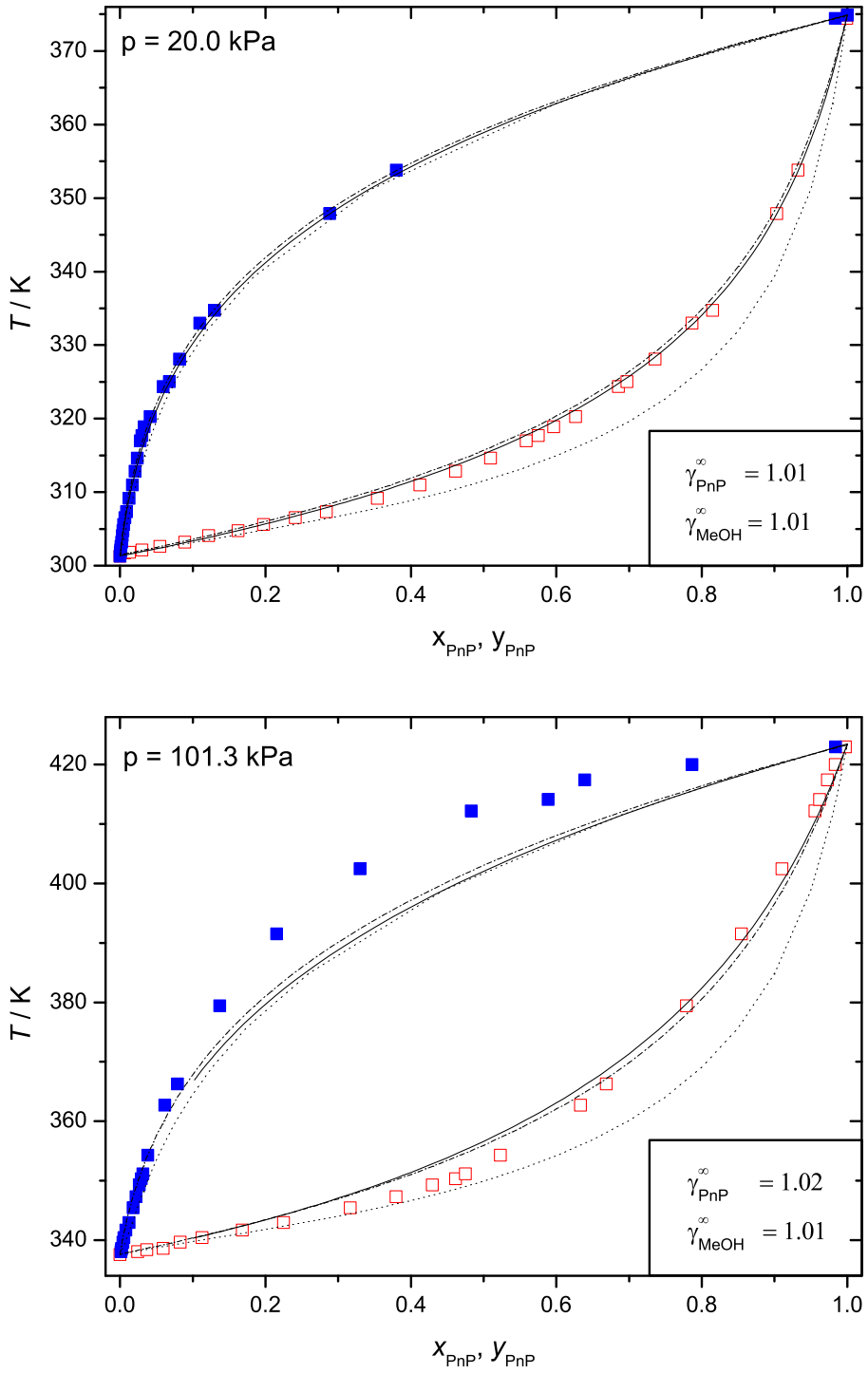

Figure 4.21.: Temperature-composition diagram for the PnP (1) + methanol (2) system at two different pressures: (□)x_1 measured; (■)y_1 measured; (—)NRTL; (–·–·)mod-UNIFAC and (· · ·)COMSO-RS

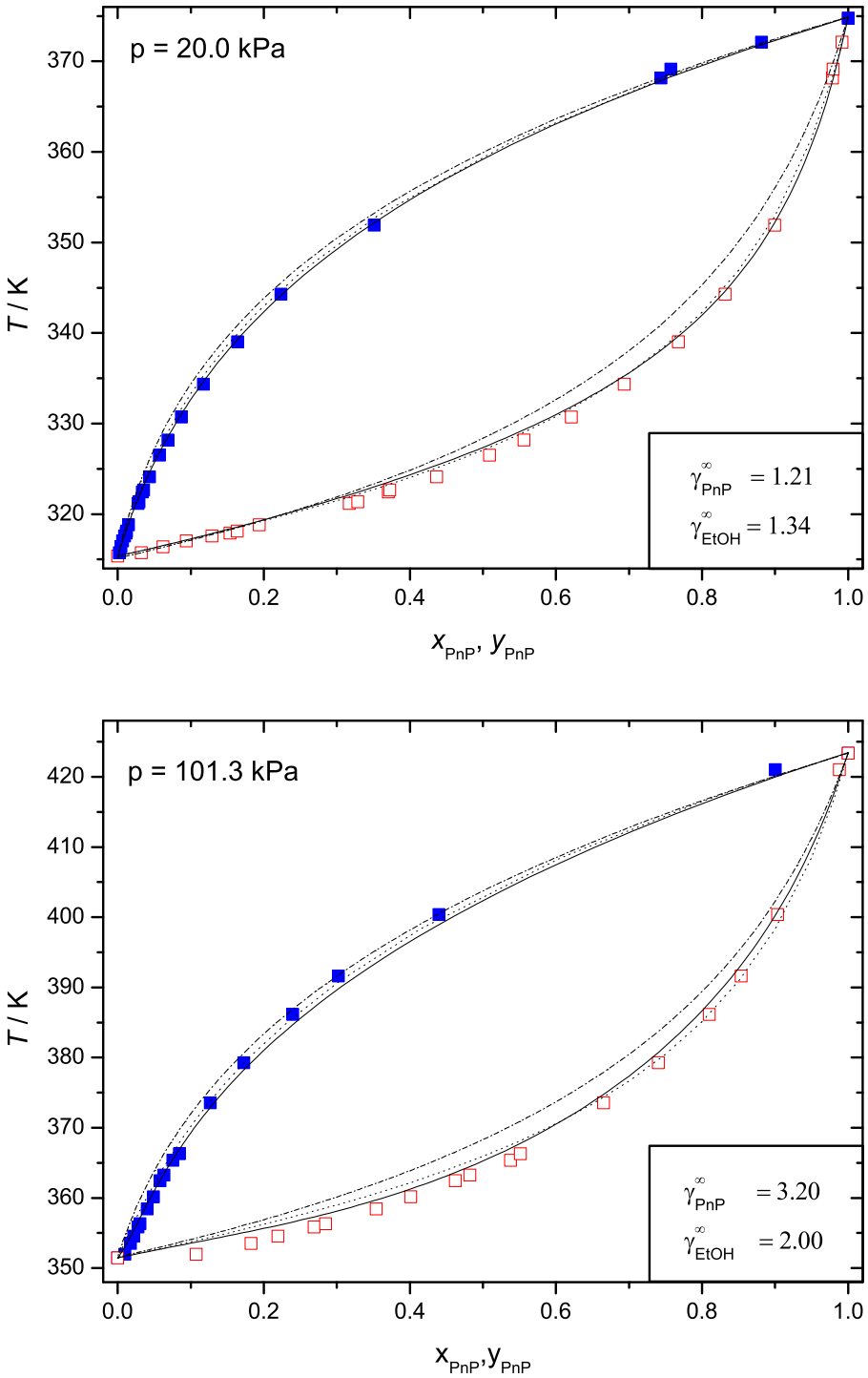

Figure 4.22.: Temperature-composition diagram for the PnP (1) + ethanol (2) system at two different pressures: (□)x_1 measured; (■)y_1 measured; (—)NRTL; (–·–·)mod-UNIFAC and (· · ·)COMSO-RS

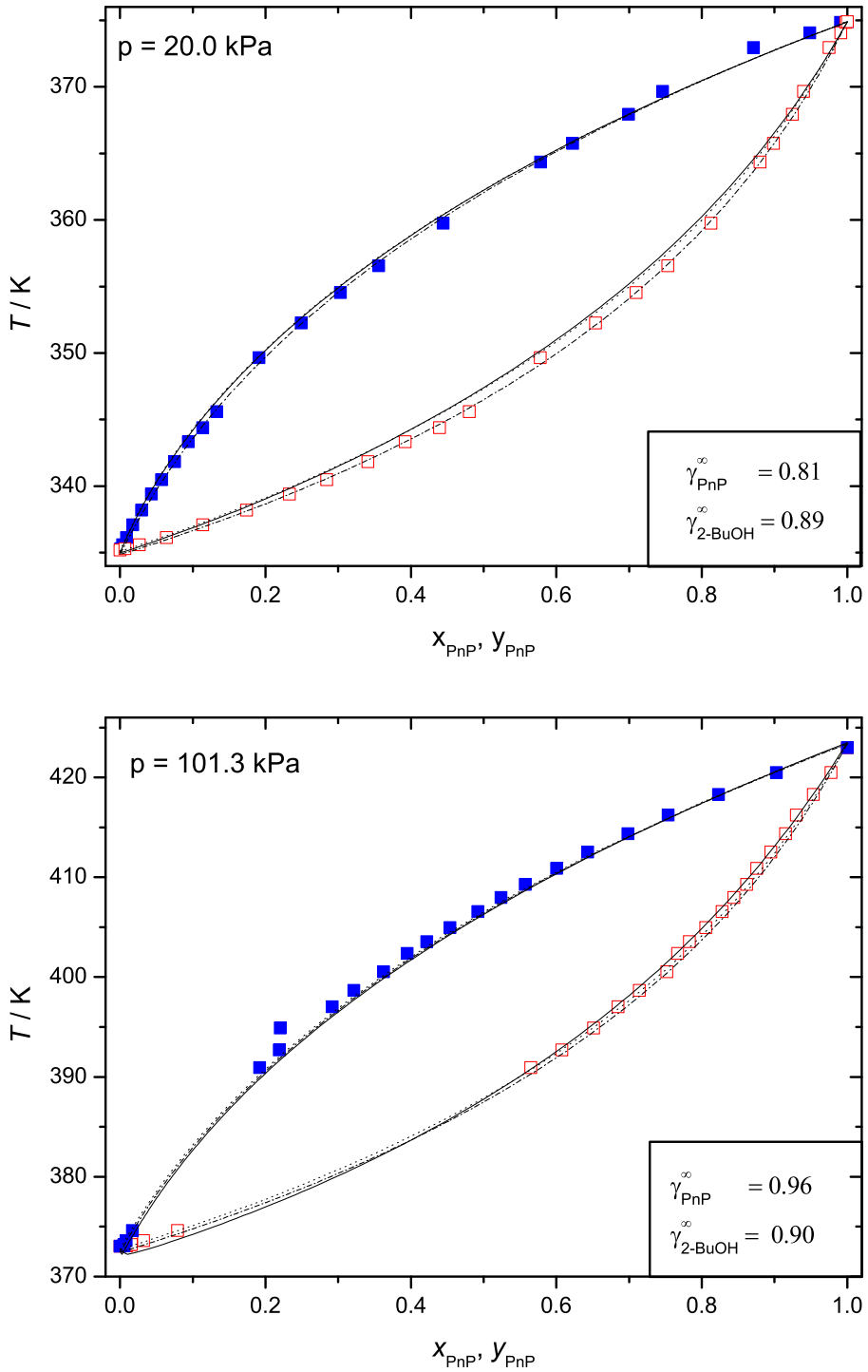

Figure 4.23.: Temperature-composition diagram for the PnP (1) + 2-butanol (2) system at two different pressures: (□)x_1 measured; (■)y_1 measured; (—)NRTL; (–·–·)mod-UNIFAC and (· · ·)COMSO-RS

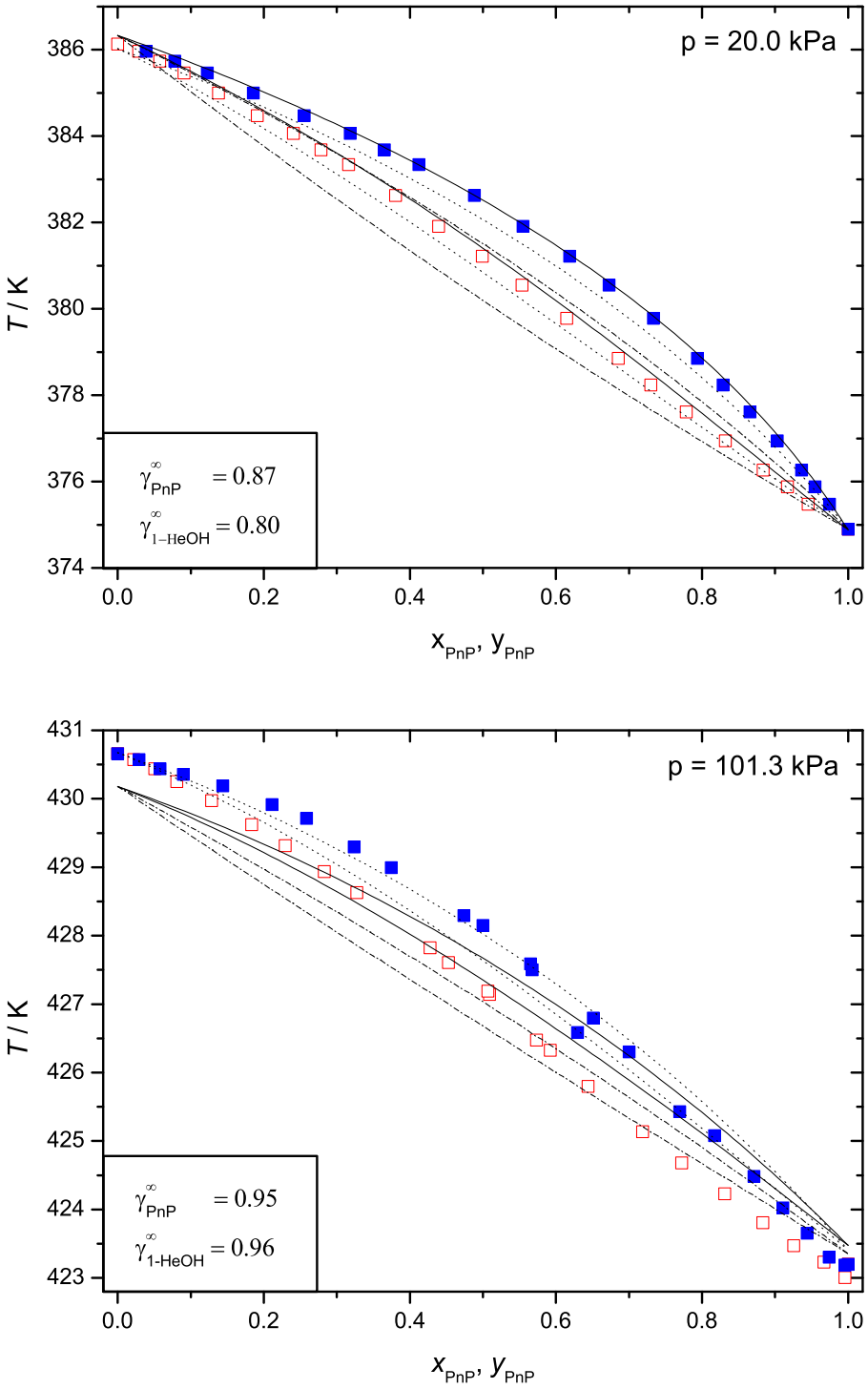

Figure 4.24.: Temperature-composition diagram for the PnP (1) + 1-hexanol (2) system at two different pressures: (□)x_1 measured; (■)y_1 measured; (—)NRTL; (–·–)mod-UNIFAC and (· · ·)COMSO-RS

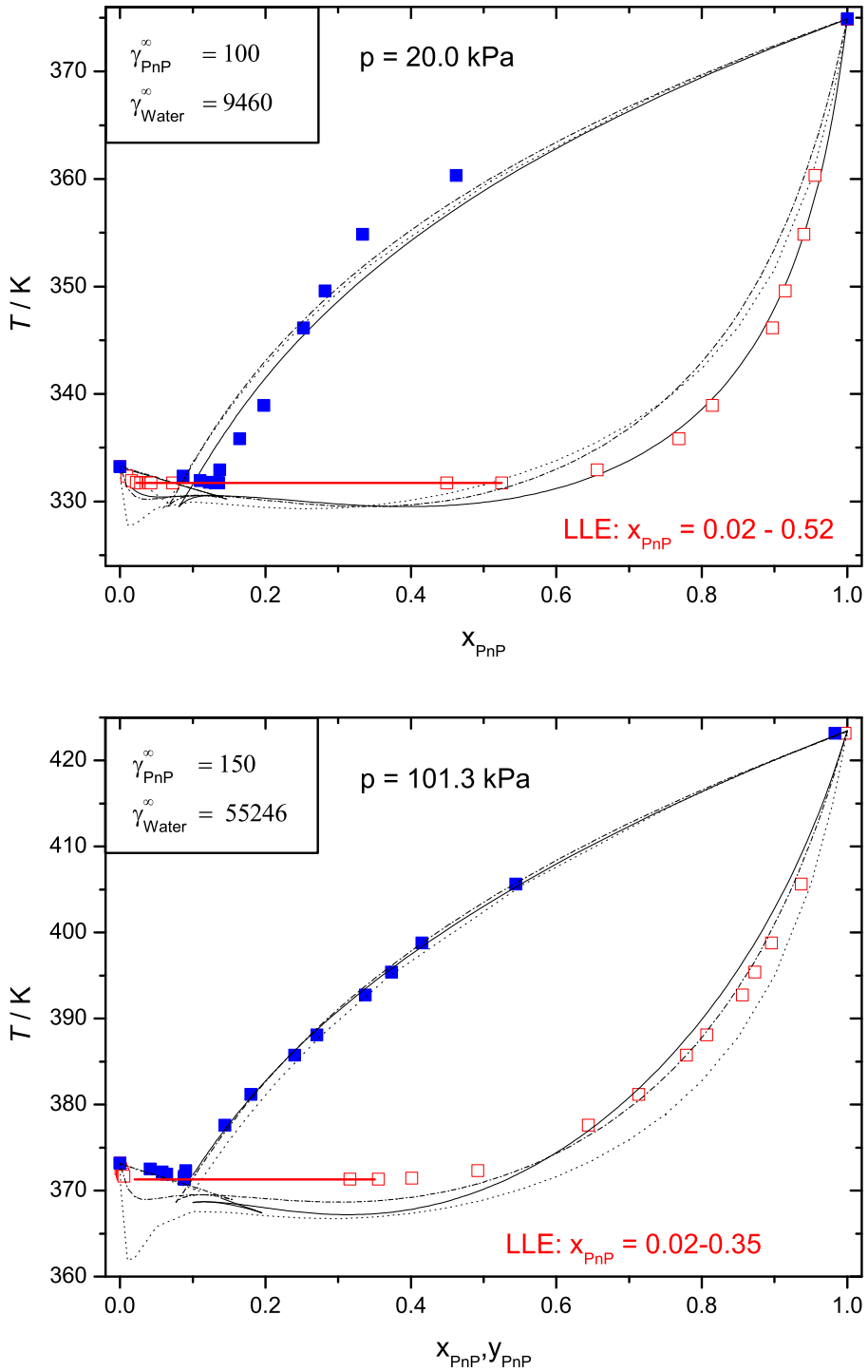

Figure 4.25.: Temperature-composition diagram for the PnP (1) + water (2) system at two different pressures: (□)x_1 measured; (■)y_1 measured; (—)NRTL; (–·–·)mod-UNIFAC and (· · ·)COMSO-RS

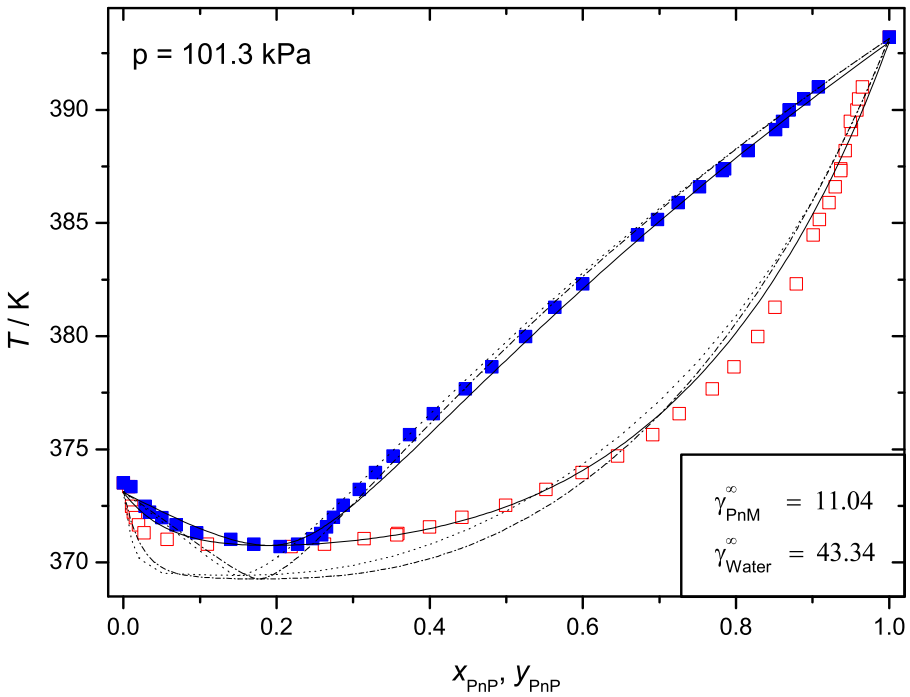

Figure 4.26.: Temperature-composition diagram for the PM (1) + water (2) system at 101.3 kPa: (□)x_1 measured; (■)y_1 measured; (—)NRTL; (–·–·)mod-UNIFAC and (· · ·)COMSO-RS

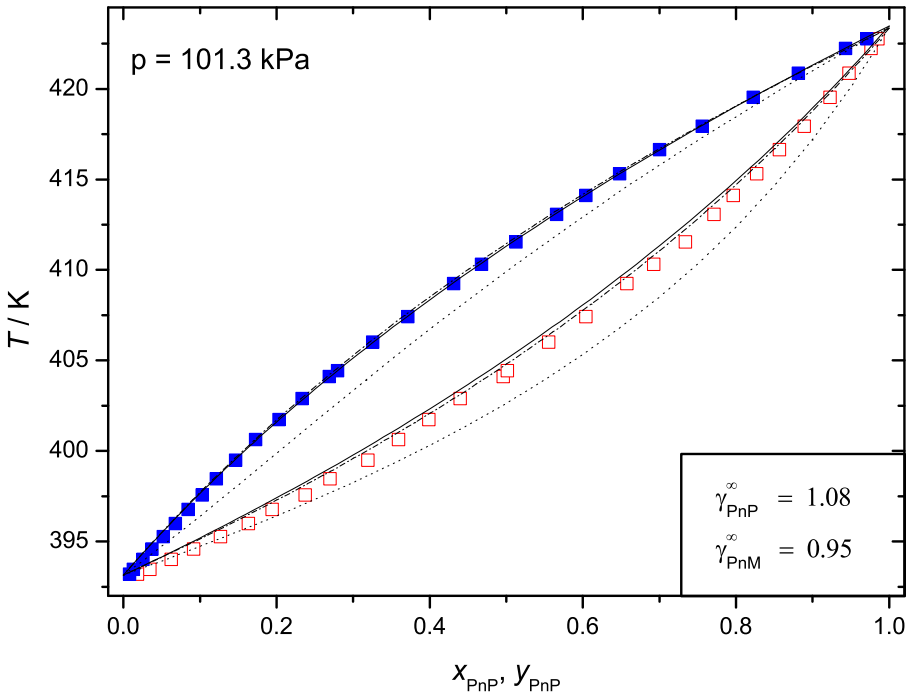

Figure 4.27.: Temperature-composition diagram for the PnP (1) + PM (2) system at 101.3 kPa: (□)x_1 measured; (■)y_1 measured; (—)NRTL; (–·–·)mod-UNIFAC and (· · ·)COMSO-RS

4.12.1. 1-propoxy-2-propanol + methanol

The systems temperature as a function of liquid and vapor composition at 20.0 kPa and 101.3 kPa are plotted in Fig. 4.21. No comparable investigations of this system in the literature could be found. In both cases the components have interaction energies strong enough to overcome a miscibility gap over the whole composition range and the boiling diagram resembles a comparably ideal system with a slightly positive deviation of Raoult's law, $\gamma_i > 1$. A change in pressure has no effect on the overall characteristics of the diagram. An inspection of the $y-x-$diagram reveals an regular shape with an enrichment of MeOH in the gas-phase due to the higher volatility and its lower boiling point compared to PnP. The ideal behavior can also be found in the values for the limiting activity coefficient of both components. Irrespective of the system's pressure, γ^{∞} is virtual unity.
Experimental findings of *Pal* and *Gaba* [137] on the volumetric properties of alkoxypropanol + n-alkanol systems allows for a better understanding of molecular interaction and the nature of interactions between PnP and methanol. They measured the excess molar volume of PnP of mixtures with methanol also, which is negative throughout the whole mole fraction range. Obviously there is a pronounced interaction between unlike molecules, comprehensible through hydrogen-bonding between the ethers oxygen and the OH-group of methanol, which can easily penetrate into the domain of the PnP molecule. This observation comes from the inspection of the partial molar volume at infinite dilution of methanol, being smaller than the pure molar volume. The γ values indicate the same strong interactions between unlike molecules and the well-known self-associated pure components. The dependence of the excess molar volumes on the chain length of the alcohols is highlighted in the context of the following binary systems.
The quality of correlating the experimental data to Wilson, NRTL, and UNIQUAC model can be observed from the plots as well as from the standard deviation, $\sigma(T)$, and $\sigma(y)$, listed in Table 4.7. The phase diagram at low pressure is best represented by the NRTL model equation showing good agreement with the experimental bubble-point and dew-point curve, respectively. No serious deviation in the dilute range of both components could be detected. The overall uncertainty in temperature of $0.67\,K$ and calculated vapor-phase composition of 0.006 is about what is expected in a number of other binary systems [88]. Wilson and UNIQUAC models with their two adjustable parameters give somewhat poorer quality in the representation of the boiling diagram. One reason might be the fact that the additional third parameter α (although restricted to a narrow range) introduces a greater flexibility for the algorithm to find the minimum of the objective function. Things become different at atmospheric pressure when both the bubble-point and dew-point curve expressed by the excess Gibbs models show remarkable deviation from the experiment. Especially the dew-point curve at concentrations $x_{\mathrm{PnP}} > 0.1$ is underestimated by all models considerably. The deviations are very poor when compared to the other systems. If this may be due to the bad consistency of the data is a question which requires a more extensive study.
Whereas mod-UNIFAC (Do) predicts the experimental equilibria data for PnP + methanol at 20.0 kPa very well, especially the bubble point curve predicted by COSMO-RS shows considerable departure from experimental and regressed data, though the dew-point curve predicted by COSMO-RS is in good agreement with experimental as well as calculated values by the NRTL model. Predictions by mod-UNIFAC (Do) are generally very similar to the correlation with NRTL at both pressures. For data at 101.3 kPa, however, the *conductor-like-screening-model* is not capable of representing the experimental diagram at all, underestimating the interaction energies between PnP and methanol, e.g. the boiling temperatures in case when $x_{\mathrm{PnP}} > 0.1$. Only the bubble-point curve at atmospheric pressure can be described by mod-UNIFAC (Do), whereas this model also fails for the description of $y-T$, except for the methanol-rich region.

4.12.2. 1-propoxy-2-propanol + ethanol

The results of the x, y, T measurements on PnP + ethanol at 20.0 kPa and 101.3 kPa are shown in Fig. 4.22. Again, the system shows complete miscibility at both pressures and a positive deviation from Raoult's law with activity coefficients calculated to be higher than in the system containing methanol. Changes in pressure does not alter the general behavior of this system, except that intermolecular interactions become lower at higher temperatures ($\gamma_i^{\infty}(20.0\,\mathrm{kPa}) < \gamma_i^{\infty}(101.3\,\mathrm{kPa})$). The limiting activity

coefficients of both species are also higher compared to PnP + methanol, which is an indication for weaker intermolecular energy contributions between unlike molecules. This is confirmed by the excess molar volume of the mixtures determined by *Ku* [138]. The excess volume being negative over the whole composition range, but to a less extent than in mixtures formed by PnP + methanol. Nevertheless, the interactions between PnP and ethanol molecules lead to weak dispersion type and/or orientated hydrogen bond effects, giving a negative contribution to V^{ex}. The interaction in PnP/EtOH becomes less, which can be attributed to the difference in the molecular size and the intramolecular self-association or hydrogen bonding present in the alcohols. This may be correlated to the packing effect as well as the interactive behavior between alcohol and ether. The partial molar volumes of ethanol at infinite dilution in PnP is also smaller than the corresponding molar volume, but the difference is smaller than in the methanolic mixture [137]. One can say that ethanol is partially fitting into the empty spaces in PnP, but to a lower extent than methanol does.
The two-parameter Wilson equation used to reduce the experimental data is plotted in the first graph. Comparable results are obtained with NRTL at 20.0 kPa, while the UNIQUAC equation leads to the poorest representation of the boiling diagram. Whereas the Wilson model show considerably smaller deviations in T, UNIQUAC results in the smallest $\sigma(y)$ (see Table 4.7). Therefore, the γ_i^∞ at 101.3 kPa are obtained with the parameters from UNIQUAC. No superiority of the three-parameter NRTL equation could be observed here.
Different to what is said for PnP/MeOH, the predicted results by COSMO-RS are in very close agreement with the experiment and also with the Wilson model in both cases. The bubble-point as well as dew-point curve are all well represented and the same uncertainties are assumed which are given for Wilson. Slightly overestimated dew-point curves and unacceptable overestimated bubble-point curves, however, are found for both pressures in case of UNIQUAC correlations.

4.12.3. 1-propoxy-2-propanol + 2-butanol

The observed binary VLE diagrams of PnP + 2-butanol exhibit a system of components with activity coefficients being lower than unity, e.g. the system shows negative deviation from Raoult's law. Interaction pattern keeps nearly the same with increased temperature (increasing the pressure).
Considering the volumetric properties of PnP + 2-butanol mixtures (at 298.15 K) shows that 1-propoxy-2-propanol + alcohol complex formation is sterically hindered in contrast to 1-butanol through the branched structure of the secondary alcohol. This fact is expressed in the slightly positive molar excess volumes of this particular mixture [139], which is caused by the breakup of the alcohol structure. Due to the low activity coefficients measured in this study, a considerable amount of dispersive interactions between PnP + 2-butanol is assumed, a result presumable of the increased hydrophilicity of the non-linear alcohol. The interactions are strong enough to overcome a miscibility gap, but the minor amount of H-bonding or the unfavorable geometrical fitting between the components lead to the small values of positive V^{ex}. A very similar behavior is found in the binary system of butanols with cyclohexanone [141].
Representation of the experimental phase diagram is best succeeded with the UNIQUAC model at low pressure, whilst the Wilson model very well reflects the ambient pressure measurements. Except for the description of UNIQUAC at 101.3 kPa, all models exhibit a comparable small deviation of T and y.
Excellent agreement is found for the predicted results of mod-UNIFAC at low pressure over the whole mole fraction range of both equilibrium curves of the diagram. The x, y, T values from COSMO-RS are identical with the UNIQUAC curves and slightly overestimating the bubble-point-curve. Both, prediction and correlation results, coincide at atmospheric pressure, assuming the same deviations as given in Table 4.7.

4.12.4. 1-propoxy-2-propanol + 1-hexanol

Mixtures of PnP with the alcohol of longest chain-length in this study, 1-hexanol, are described by a binary VLE diagram with activity coefficients lower unity and limiting activity coefficients of about 0.9. The negative deviation from Raoult's law is becoming smaller at higher boiling temperatures. Note that the difference in the pure component's boiling points is quite small. Although no reference data on

the volumetric properties could be found in the literature, one can directly follow a similar interaction behavior of 1-hexanol with PnP as compared to the system containing 2-butanol. A somewhat weaker complex formation can be expected due to the less-hydrophilic nature of the linear alcohol. But due to the variety of different and opposite effects influencing the intermolecular behavior, only experimental evidence can prove this argument.
There is an obvious excellent agreement between experiment and correlation for the system at 20.0 kPa with identical deviation for Wilson and NRTL, and acceptable accuracy for the UNIQUAC model. No significant deviation occurs in the whole range of the phase diagram. The results of the predictive models, however, give temperatures which are to low throughout the whole composition range (except for the very dilute ranges), with the deviations of mod-UNIFAC being worse than COSMO-RS. At 101.3 kPa a small discrepancy is noticeable in the range of $x_{\mathrm{PnP}} < 0.55$ with the experimental values being less than 0.6 °C higher than the corresponding temperatures calculated by the Wilson equation. This is also true for pure 1-hexanol. As the same exponential equation for the pure component's vapor pressure is used for all models at both pressures, incorrect parameters for the vapor pressure correlations can be excluded. One reason might be that those relatively small deviations simple come form experimental uncertainties. In the case of applying the UNIQUAC model, the minimization procedure does not converge, with unacceptable results for the phase diagram. The limiting activity coefficients, which directly follow from the binary interaction parameters, also have unreasonable values for this model. Again the COSMO-RS method seems to be superior to mod-UNIFAC (Do) with good agreement to the experiment.

In an investigation on the separation of PnP and some aliphatic alcohols by Frank et. al. [19] with their results of $\gamma^{\infty}_{\mathrm{PnP}}$ in the organic phase also indicates particularly attractive interactions between PnP and the organic solvent. In the case the alcohol shows a branched molecular structure, differences in $\gamma^{\infty}_{\mathrm{PnP}}$ become significant with values being much lower for the branched solvent. This may be due to the somewhat more hydrophilic nature of a branched alkyl group.

4.12.5. 1-propoxy-2-propanol + water

A miscibility gap occurs in the aqueous system in the composition range $0.02 - 0.52$ mole fraction of PnP at low pressure and at a temperature of 331.7 K. At 101.3 kPa the minimum heterogenous azeotrope temperature lies at 371.3 K. This is in accordance with the literature [1, 4, 142], which shows that there is a lower critical solution temperature around 305 K at ambient pressure. Above this temperature the system becomes partially miscible. This inverse solubility behaviour is characteristic for binary systems with temperature-sensitive hydrogen-bonds. At temperatures below the LCST (depending on composition and pressure), the glycol ether can form hydrogen-bonds with water and this attractive interactions leads to complete miscibility. Increasing temperatures followed by increasing molecular motion weaken the intermolecular forces, disrupting the hydrogen-bonding interactions between water and PnP and hydrophobic interactions become more significant.
This behaviour of increased hydrophobicity is quantitatively reflected by the high value for $\gamma^{\infty}_{\mathrm{PnP}} = 100$ in the aqueous systems, compared to $\gamma^{\infty}_{\mathrm{PnP}}$ in the other binary systems. Whether hydrophobic or hydrophilic interactions dominate in water + glycol ether liquid mixtures depends strongly upon temperature and structure of the ether [19]. A higher LCST value indicates a glycol ether with greater hydrophilic character. At the LCST both hydrophobic and hydrophilic interactions are balanced for the particular system. This trend of weaker interaction between unlike molecules can be very well followed by the increasing activity coefficient at higher temperatures (e.g. experimental results at 101.3 kPa) in Fig. 4.25. An occurrence of a LCST is shown to be indicative of an increase in γ_i^{∞} with increasing temperature [19]. The same authors presented a value for $\gamma^{\infty}_{\mathrm{PnP}}$ in water of 64, measured at a constant temperature of 353.15 K. Despite the different experimental conditions, an idea of the extent of hydrophobicity can be drawn for PnP. Please refer to Chap. 3 for an extensional experimental approach to the chemical behavior of aqueous mixtures containing PnP and the role of existing H-bond network formation.
The occurrence of strong hydrogen-bonding between the components is proven by the large negative molar excess volumes in Fig. 4.20. Although both species in their pure states are known to form self-aggregated complexes, strong interactions between PnP and water and the great difference in their molecular size

leads to negative V^{ex}.
The two-parameter form of Wilson's equation is not applicable to partially miscible binaries [143] and therefore not considered in the correlation procedure with the aqueous system. Also the results of UNIQUAC calculations do not show a reasonable correlation with the experiment and are omitted therefore. The NRTL bubble-point curves at both pressures can be regarded as satisfactorily described with regard to their deviation from experiment. In the water-rich region, the azeotropic behavior is not described as good as is the agreement at the dilute ranges of the other systems. The dew-point curve is only in agreement with experiment at low pressure.
The main difference if one compares the two predictive models is the fact, that only COSMO-RS is able to account for a miscibility gap ($0.001 - 0.4$ at 20.0 kPa; $0.001 - 0.5$ at 101.3 kPa; not shown in the figure). Inspection of the output data does not reveal the occurrence of the LLE when mod-UNIFAC (Do) is applied. Both models are showing similar prediction power with generally higher deviations from the experiment than the NRTL correlation.

4.12.6. 1-methoxy-2-propanol + water

The binary system PM + water exhibits an negative azeotrope at 101.3 kPa with a constant boiling temperature of 370.7 K and a phase-composition of $x_{PnP} = 0.22$. This homogenous azeotrope is obviously the result of stronger interactions between the unlike molecules compared to the mixture with PnP, as there is no occurrence of a liquid-liquid phase-split. The lower limiting activity coefficients support this chemical behavior with values much smaller than in the system PnP + water. Water sticks more likely to PM than it does to PnP. A look at the plot of the known molar excess volumes exhibits the same conclusions. The increased interaction reduces the volume of the binary mixture to a higher extent than in any other mixtures under investigation, $\overline{V^{ex}}(0.3) = -1.35\,cm^3mol^{-1}$. With respect to the alkoxyalcohol one can say, that an increase of the alkyl chain length gives rise to a less negative V^{ex}. This trend is opposite to what can be observed for binary mixtures of alkoxyalcohols with organic solvents [137–139].
Both the Wilson and the NRTL model provide accurate description of the bubble-point and dew-point curve with a slightly better representation by NRTL. Minor deviations occur in the range of $x_{PnP} = 0.6 - 0.9$ only. The azeotrope is very well expressed in both correlations with respect to temperature and phase-composition. With the structural parameters used for UNIQUAC, the results are regarded to be improper, with very large deviations from the experiment.
No satisfactory results can be obtained solely on the prediction by mod-UNIFAC (Do) or COSMO-RS. Both models considerably underestimate the boiling points of the mixture at mole fractions below 0.5. Nevertheless, in both cases a minimum azeotropic point is found at the correct phase-composition and the dew-point curve for $x > 0.3$ is in good agreement with the experiment.
The literature gives another investigation on this binary system with isothermal VLE data at 353.15 K and 363.15 K [144]. The authors report a azeotropic maximum in pressure at $x_{PM} = 0.15$. That is comparable to the measurements in this work, performed under different conditions and a different temperature range.

4.12.7. 1-propoxy-2-propanol + 1-methoxy-2-propanol

The binary mixture of both alkoxyalcohols exhibits a system of nearly ideal character with activity coefficients $\gamma_{PnP} \geq 1$ and $\gamma_{PM} \leq 1$. Due to the higher boiling point of PnP, the gas-phase is slightly enriched in PM. No supplementary experimental data on the excess volumes are available. It would be a matter of further work to determine the extent to which the self-associated pure components can also have favorable intermolecular interactions between unlike molecules in the binary solution. The structural similarity between these substances gives reason to assume no specific intermolecular interactions between unlike molecules or any preferential solvation effects, leading to the almost ideal behavior.
The phase behavior is described well by both Wilson and NRTL with virtual the same quality. The dew-point curve is somewhat better represented than $x-T-$binodal curve. Again, it is the UNIQUAC model which performs the correlation worse.
The final results of the group-contribution method is superior to predictions made by COSMO-RS. The later underestimates the intermolecular interactions and therefore the boiling points. This may also be

due to the approximate description of hydrogen-bondings in a structured liquid by COSMO-RS. The pure components boiling temperatures are exactly confirmed (which is an indication of proper vapor pressure parameters in all calculations).

4.13. Conclusion

Isobaric VLE data were determined experimentally for the binary mixtures composed of 1-propoxy-2-propanol + (methanol, ethanol, 2-butanol, 1-hexanol and water) at 20.0 kPa and 101.3 kPa. Measurements at atmospheric pressure also include the binaries composed of PM + (PnP, water). The thermodynamic consistency is tested for all the binary VLE data by Van Ness's direct test. Small positive deviations from Raoult's law of ideality were observed for systems with methanol, ethanol and water, whilst the remaining systems with 2-butanol and 1-hexanol show negative deviation. The remaining systems with PM have values of $\gamma_{\mathrm{PM}}^{\infty}$ being nearly unity for the organic and around 11 for the aqueous mixture. Supplementary information on the volumetric properties of these binaries may give some ideas on the structuring in solution also.
Partial miscibility in the liquid phase is found in PnP-water with large values of limiting activity coefficients. The strong deviations from ideality in both aqueous binaries can be rationalized in terms of the presence of temperature-dependent hydrogen-bonds. This specific characteristic is expressed by the large negative molar excess volumes and the occurrence of a lower critical solution temperature. A rather complex role of attractive and repulsive forces are assumed to act in those systems, with great sensitivity upon changes in temperatures and the structure of the species involved.
The effect of breaking and/or forming hydrogen bonds, and in general of association phenomena in solution, is emphasized by the activity coefficients of the components, γ_i, which are a measure of their tendency to escape from the solution. For all mixtures examined here the γ_i of both components increase with dilution reaching a maximum at infinite dilution. Due to the limited number of data points and the scattering of activity coefficients data no defined sequence with respect to the structure of the second component can be drawn. However, this behavior is likely to be evident for self-association, which is greatest in the pure liquid (low escaping tendency) and lowest in infinitely dilute solution (high escaping tendency).
The analysis of experimental data for the binary systems using the Wilson, NRTL and UNIQUAC equations shows marked differences. In most cases both Wilson and NRTL satisfactory correlate for non-aqueous mixtures, while the UNIQUAC model exhibit somewhat larger deviations from the experiments. One possible way to overcome the inadequate quality of correlation by UNIQUAC for systems containing PnP and PM would require the parameters r and q to be regressed from a large set of binary data. For the time being both values are either a sum of the corresponding values of molecular UNIFAC group-contributions (PnP) or taken from literature values estimated with the help of Aspen Plus [145].
The prediction with the help of mod-UNIFAC (Do) may lead to VLE curves representing the experimental values closely or with acceptable tolerance, respectively. The LLE for PnP + water could not be expressed by UNIFAC at all. COSMO-RS gives a rather accurate description of experimental findings for the non-aqueous systems. Despite the fact that the results for both aqueous systems are less satisfactory, this method is capable of predicting the occurrence of a miscibility gap and a homogenous azeotrope, which is confirmed by the experiment.

Table 4.7.: Correlation parameters and the absolute deviations in boiling points and vapor-phase mole fractions for the binary systems

	Ω_{12} [a]	Ω_{21} [a]	α	$\sigma(T)/K$ [b]	$\sigma(y)$ [c]
PnP(1) + methanol(2) at 20.0 kPa					
Wilson	−442.32	2046.22		1.58	0.016
NRTL	296.53	−294.53	0.9	0.67	0.006
UNIQUAC	−442.32	2046.22		1.62	0.017
PnP(1) + methanol(2) at 101.3 kPa					
Wilson	2197.54	493.52		1.95	0.068
NRTL	895.56	−1150.63	0.9	2.16	0.064
UNIQUAC	−406.09	1937.73		2.04	0.068
PnP(1) + ethanol(2) at 20.0 kPa					
Wilson	−3056.33	3980.92		0.78	0.003
NRTL	4947.43	−3592.50	0.1	0.81	0.003
UNIQUAC	4423.22	−1508.78		0.95	0.011
PnP(1) + ethanol(2) at 101.3 kPa					
Wilson	99511	−35.22		1.00	0.018
NRTL	−8530.78	13068	0.1	1.41	0.015
UNIQUAC	2371.21	−553.46		1.56	0.013
PnP(1) + 2-butanol(2) at 20.0 kPa					
Wilson	817.20	−751.33		0.67	0.006
NRTL	−1237.74	1151.41	0.9	0.66	0.005
UNIQUAC	−947.35	1063.07		0.45	0.005
PnP(1) + 2-butanol(2) at 101.3 kPa					
Wilson	−4025.90	5030.79		0.83	0.022
NRTL	1879.30	−1488.54	0.9	0.77	0.023
UNIQUAC	5043.13	−2501.34		1.80	0.027
PnP(1) + 1-hexanol(2) at 20.0 kPa					
Wilson	−2381.94	2605.58		0.19	0.007
NRTL	1198.76	−1306.59	0.9	0.20	0.008
UNIQUAC	−456.52	444.62		0.51	0.009
PnP(1) + 1-hexanol(2) at 101.3 kPa					
Wilson	803.68	−799.69		0.41	0.006
NRTL	−677.68	610.64	0.9	0.41	0.006
UNIQUAC	7383.00	−3216.14		2.07	0.029
PnP(1) + water(2) at 20.0 kPa					
NRTL	2152.00	9882.84	0.358	1.10	0.029
PnP(1) + water(2) at 101.3 kPa					
NRTL	−2299.19	17453	0.238	2.48	0.031
PnP(1) + PM(2) at 101.3 kPa					
Wilson	3424.20	−1819.15		0.64	0.014
NRTL	6075.20	−5085.09	0.1	0.69	0.017
UNIQUAC	5509.18	−2670.15		0.98	0.024
PM(1) + water(2) at 101.3 kPa					

Table 4.7.: (continued)

	Ω_{12} [a]	Ω_{21} [a]	α	$\sigma(T)/K$ [b]	$\sigma(y)$ [c]
Wilson	−780.08	5680.00		0.78	0.033
NRTL	−6268.10	12579	0.1	0.72	0.030

[a] Adjustable parameters [J mol^{-1}]:

Wilson	$\Omega_{ij} = \lambda_{ij} - \lambda_{ii}$
NRTL	$\Omega_{ij} = g_{ij} - g_{jj}$
UNIQUAC	$\Omega_{ij} = u_{ij} - u_{jj}$

[b,c] Standard deviation:

$$\sigma(T) = \sqrt{\frac{\sum_{i=1}^{N}\left(T^i_{calc} - T^i_{exp}\right)^2}{N}} \text{ [K]}$$

$$\sigma(y) = \sqrt{\frac{\sum_{i=1}^{N}\left(y^i_{calc} - y^i_{exp}\right)^2}{N}}$$

4.14. Isothermal Vapor-Liquid Equilibria for PnP + ethanol

The objective of this part of the work is to experimentally determine the vapor pressure data for the binary system 1-propoxy-2-propanol (1) + ethanol (2) at three different temperatures (313.15, 333.15, and 353.15 K). The isothermal VLE data reported here cover the whole range of mole fraction with 11 different compositions and the vapor pressure data of the pure solvents at each temperature. The vapor-pressure diagrams, as exemplified with the binary PnP + ethanol entails a possibility to deduce the temperature-dependency of the interaction parameters of the Gibbs excess models applied so far. These parameters, varying with temperature, can be successively used in the prediction of VLE data of the same binary system. The set of parameters for each of the three models and binary systems can be interchanged between both experimental techniques. Therefore, the negligence of temperature on the interaction parameters can be easily elucidated as significant or not.
All theoretical considerations concerning the calculation of vapor-liquid-equilibria data as described in the previous sections might also be applied for the binary system at fixed temperature. Because the system temperature is initially known, however, calculations of the key quantities p_i^{vap} can immediately be performed. The procedure applied is called

Bubble-P: calculate p and y_i for a given T and x_i

Before such an iteration scheme for this simple and direct bubblepoint calculation is presented, the liquid phase activity coefficients γ_i are calculated from the Wilson and NRTL equation, explained extensively in Sec. 4.5. Due to the fact of inadequate phase description in case of UNIQUAC, this model is not considered in the isothermal VLE data processing. Influences of temperature changes can now be accounted for by introducing a function which gives model interaction parameters with the following temperature-dependency:

$$\Delta\lambda_{ij} = \Delta\lambda_{ij}^{(0)} + \Delta\lambda_{ij}^{(1)}(T - 298.15) \tag{4.67a}$$

$$\Delta g_{ij} = \Delta g_{ij}^{(0)} + \Delta g_{ij}^{(1)}(T - 298.15) + \Delta g_{ij}^{(2)}(T - 298.15)^2 \tag{4.67b}$$

with 298.15 K as an arbitrarily chosen reference temperature.
To obtain the temperature-dependent parameters, a nonlinear optimization method is used to minimize the objective function

$$\zeta = \sum_{k=1}^{N}\left[\left(\frac{p^{\text{calc}} - p^{\text{exp}}}{p^{\text{exp}}}\right)^2\right]_k \tag{4.68}$$

ζ is the sum of the squared relative deviations of the experimental and calculated vapor pressure, respectively, at every sample composition k. The overall vapor pressure is calculated by means of Eq. (4.28). Therein fugacity coefficients are evaluated according to Eq. (4.25) and the pure species vapor pressure according to Eq. (6.28)-(6.30) in the usual way.

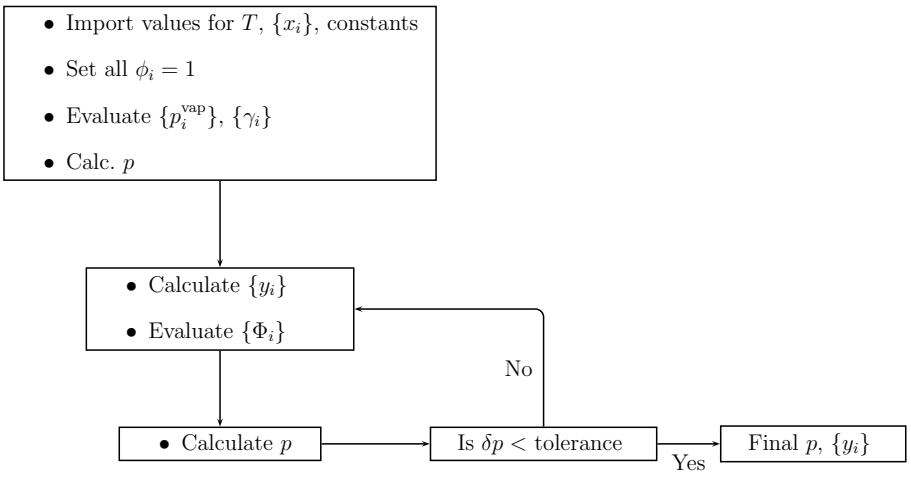

Figure 4.28.: Block Diagram for the calculation of vapor pressure p

With reference to a computer program comparable to that in Sec. 4.8, one reads and stores the given values of T and x_i, along with all constants required in evaluation of the p_i^{vap}, γ_i, and Φ_i. Since y_i is not given, values for the Φ_i can not be determined yet, and each is set equal to unity. Values for p_i^{vap} are found from vapor pressure equations and values of γ_i come from the activity coefficient correlations. Equations (4.28) and (4.26) are now solved for p and y_i. Values of Φ_i from Eq. (4.25) allow recalculation of p by Eq. (4.28). Iteration leads to final values for p and y_i. The iteration scheme for the calculation of the vapor pressure of a binary system at different temperatures is shown in Fig. 4.28. Consecutive data processing of isothermal VLE data is achieved in a very similar way as shown in Fig. 4.3.

4.14.1. Experimental Procedure

The experimental procedure is identical to that for determining the vapor pressure of pure components or electrolyte systems. A detailed explanation, therefore, will be given in Sec. 6.3. Only the procedure for the preparation of binary mixtures at different composition is explored here.
In order to obtain fully degassed mixtures, the composition of which can be approximately set up, two flasks with the pure solvents (PnP and ethanol) are be used in the same degassing line. Each solvent is delivered from its dissolved gases in the usual way by applying vacuum over a period of some hours under rigorous stirring.
Filling of the sample flasks is accomplished in a two-step procedure: starting with the solvent of highest boiling point (lowest volatility), it is distilled under vacuum into the measurement flask cooled by liquid nitrogen. Still kept frozen by means of liquid nitrogen, the second component is distilled from solvent reservoir 2 in the same way into the sampling flask. The order of solvents is chosen as to keep the amount of gaseous sample of solvent 1 as low as possible during the time of the second distillation process. After melting, $1 - 5\,\mathrm{mL}$ of solution, under continuous stirring, is removed under vacuum to obtain the final composition, which is believed to be adequately degassed. Experimental vapor pressures of pure PnP determined in this way perfectly coincide with the results obtained with the more elaborate degassing procedure described afterwards in this work.
Sample compositions are determined by GC after each temperature program with the help of the calibration polynomial given in Fig. 4.9. The same uncertainties regarding mole fraction applies. The change of phase composition can be well neglected during the measurements, due to the small amount of gas space and hence the minor loss of solvent by evaporation.

4.14.2. Results and Discussion

The results of the vapor pressure measurements on the binary system PnP + ethanol is described below. The measured x, p data are listed in Table Table C.3. These tables give the liquid x and gas-phase

composition y, the measured total vapor pressure p, the partial pressure of PnP p_{PnP}, and the activity coefficients γ_{PnP}. The compositions are reported on a mole basis. The binary system is described together with the results of data reduction by the excess Gibbs models. The activity coefficient parameters used in the correlation together with the values of the standard deviations in vapor pressure, $\sigma(T)$ are given in Table 4.8. Naturally the deviations in pressure increase with increasing temperature, due to the higher

Table 4.8.: The correlation results for binary system composed of PnP(1) + ethanol(2) and standard deviations $\sigma(p)$, $T_r = T - 298.15$

Wilson			
$\Delta\lambda_{12}^{(0)}$	174.77	$\Delta\lambda_{21}^{(0)}$	893.79
$\Delta\lambda_{12}^{(1)}$	−26.66	$\Delta\lambda_{21}^{(1)}$	18.59
NRTL ($\alpha = 0.1$)			
$\Delta g_{12}^{(0)}$	1329.4	$\Delta g_{21}^{(0)}$	−864.1
$\Delta g_{12}^{(1)}$	−97.95	$\Delta g_{21}^{(1)}$	101.70
$\Delta g_{12}^{(2)}$	0.690	$\Delta g_{21}^{(2)}$	−0.714

$\sigma(p)$[a]					
313.15 K		333.15 K		353.15 K	
Wilson	NRTL	Wilson	NRTL	Wilson	NRTL
89 (±1.01 %)	45 (±0.39 %)	160 (±0.63 %)	119 (±0.40 %)	263 (±0.41 %)	255 (±0.38 %)

[a] $\sigma(p) = \sqrt{\frac{\sum_{i=1}^{N}\left(p_i^{calc} - p_i^{exp}\right)^2}{N}}$ [Pa]

absolute values for p. Relative deviations, however, show an excellent quality of the correlation procedure and a favorable use of regressions based on the NRTL equation. Noteworthy to say that the deviations from ideality are all rather small for this binary system.
The experimental data (p, x_1, y_1) for the binary at 313.15 K, 333.15 K, and 353.15 K are shown in Fig. 4.29. The vapor phase compositions are calculated by the binary parameters. A comparison with the equivalent phase diagram at constant pressure, see Fig. 4.22, shows the well-known behavior of opposite deviations from ideality: a positive deviation on the $x-p-$plot corresponds to a negative deviation in a $x-T-$plot at constant system pressure. The same holds for the dew-point lines. Activity coefficients being greater than unity are the results of attractions between the unlike molecules being less than those between identical molecules in the pure components. Equivalent to this is the rising of vapor pressure, as the molecules do not "prefer" to stay in the liquid phase. This fact is visualized in Fig. 4.29 together with the curves obtained with the NRTL excess Gibbs energy model equation, showing the smallest deviations in vapor pressure.
As for the infinite dilution of isobaric VLE data, the activity coefficients γ_i^{∞} are calculated by means of the equations

$$\ln\gamma_1^{\infty} = \tau_{21} + \tau_{12}\exp\left(-\alpha\tau_{12}\right) \tag{4.69}$$

$$\ln\gamma_2^{\infty} = \tau_{12} + \tau_{21}\exp\left(-\alpha\tau_{21}\right) \tag{4.70}$$

Values for infinite dilution activity coefficients obtained in this way are listed in Table 4.9 for both components. Although, due to the different experimental parameters and conditions not directly comparable with the results in case of isobaric VLE measurements, the values within $313.15 < T/\mathrm{K} < 353.15$ are close to those obtained at 20.0 kPa. Obviously the temperature range covered there better resembles the

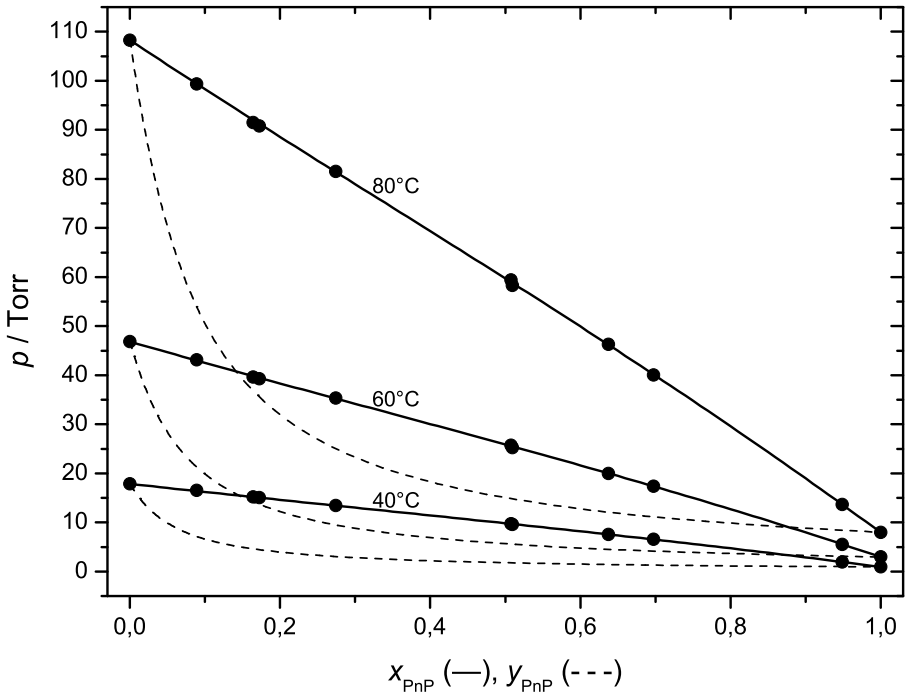

Figure 4.29.: VLE data for PnP + ethanol: (•) exp.; (- - -) NRTL; (· · ·) Raoult's law

Table 4.9.: Infinite dilution activity coefficients γ_i^∞ at different temperatures

T (K)	$\gamma_{\mathrm{PnP}}^\infty$	$\gamma_{\mathrm{EtOH}}^\infty$
313.15	1.218	1.014
333.15	1.230	1.238
353.15	1.228	1.235

intermolecular interactions like they are at 313.15 K. It must not be forgotten that values for γ_i^∞ are not gathered on an experimental basis, but calculated from interaction parameters with data points covering the whole composition range. Therefore the agreement between infinite values at constant pressure and temperature, respectively, are believed to be satisfactory.

A reevaluation of the binary boiling point diagrams of PnP + ethanol at 20.0 kPa and 101.3 kPa with the aid of the polynomial equations (4.67) is possible on the basis of the data processing in Sec. 4.8. In this case, excess Gibbs energy model parameters from isothermal vapor pressure measurements are used as input for the computation according to Fig. 4.1 and 4.3.

As a result, the vapor-liquid equilibrium diagram at 20.0 kPa is very well represented with the temperature-dependent interaction parameters. The standard deviations in temperature and vapor-phase composition amounts to 0.89 K and 0.013, respectively. Considering the independent approaches to obtain these interaction parameters, the agreement is very good. The situation becomes less accurate at the binary VLE at 101.3 kPa, where deviations $\sigma(T)$ and $\sigma(y)$ between experimental and calculated values account for 2.38 K and 0.020, respectively. Nevertheless, with the parameters from Table 4.8 at hand, one may very well represent the boiling point diagram and the $y-x-$plot at low pressure from independent results obtained by vapor-pressure measurements. This observation supports the speculation about the similarity of interactions taking place at temperatures in the range measured, and in the binary system at relatively low pressures.

The predictive power of applying the UNIFAC model as well as the COSMO-RS approach is demonstrated graphically in comparison with the experimental p for the lowest temperature in Fig. 4.30. At higher temperatures the characteristics of both models do not differ in quality at all. A graphical inspection reveals the results from COSMO-RS being in closer agreement to experimental $x-p-$data than

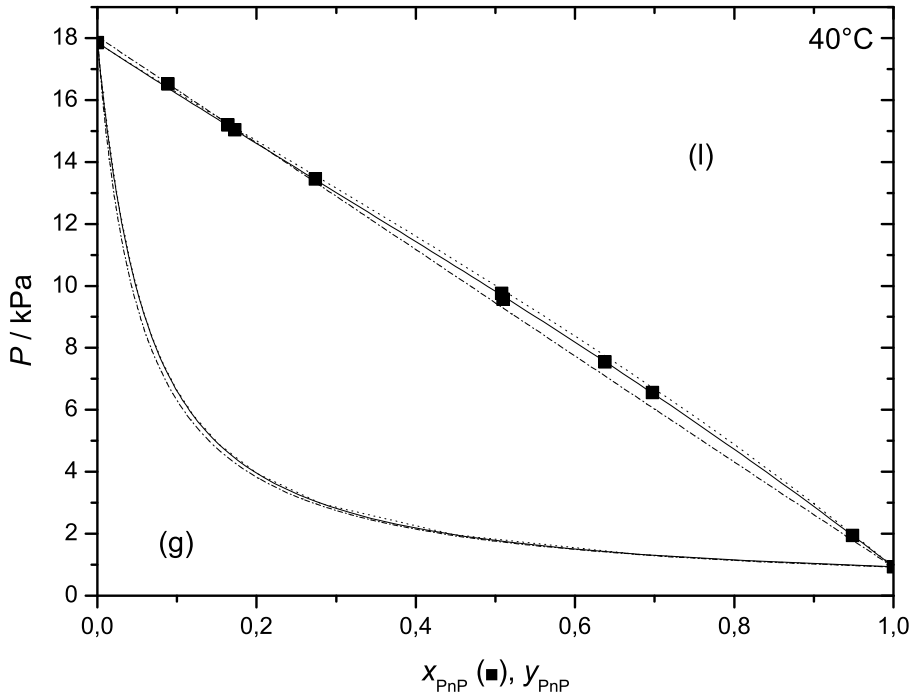

Figure 4.30.: VLE data for PnP + ethanol: (•) exp.; (—) NRTL; (–·–·) mod-UNIFAC and (· · ·) COMSO-RS

the curve obtained from UNIFAC. But with respect to the predictive nature of the models, both are accurately representing the phase diagram at all 3 temperatures. Both models are capable for the correct treatment of intermolecular interactions over the whole composition range. The overall agreement between the $y-p-$data calculated with excess Gibbs model parameters for the liquid state and predictive models is excellent. Despite the fact that no experimental values for the gas-phase composition of the binary system are determined, all information available about the dew-point line support its reliability and accuracy. It is believed that a simultaneous determination of (x, y, p) data triplets will lead to very similar results with respect to these vapor pressure diagrams.

5. Electrical Conductivity in 1-Propoxy-2-propanol

Apart from the non-electrolyte systems which have been described so far, extended studies on the conductance (this chapter) and the osmotic behavior of salt solutions in PnP will be the subject of the two following chapters over an extended temperature range.
Electrical conductivity is a very reliable experimental method, which provides a first basis for a detailed analysis of the intermolecular interactions between solvent- and ion-molecules. In the present work we report the results of our precise conductance measurements carried out on dilute solutions of *n*-tetrabutylammonium salts, Bu_4NX (X = Br^-, NO_3^-, SCN^- and OAc^-) covering the temperature range from 248.15 K to 313.15 K at electrolyte concentrations from $0.18 \times 10^{-3}\,\mathrm{mol\,L^{-1}}$ to $6.4 \times 10^{-3}\,\mathrm{mol\,L^{-1}}$. Many electrical conductance studies of these salts in aqueous and non-aqueous solvent systems have been reported and allow for a direct comparison of the results among different solvents. Nevertheless few reliable information is available on their solvation and association behavior in glycol ether solvents. Because there is also a lack of literature information on the properties of pure solvent PnP over the desired temperature range, the investigations are extended with precise measurements of the viscosity, density and permittivity of PnP. The experimental molar conductivities, Λ, are analyzed in terms of the chemical model and temperature-dependent limiting molar conductivities, Λ^∞, and association constants, K_A, are derived. Thermodynamic results on the ion-pair formation process are discussed in terms of coulombic and non-coulombic forces by an appropriate splitting of the Gibbs energy.
The range of concentration is extended up to more than $1\,\mathrm{mol\,L^{-1}}$ in a second series of measurements, the results of which are analyzed with the help of the *Casteel-Amis* equation.

5.1. Theoretical Aspects

5.1.1. Statistical Mechanical Principles

A basic approach to the theory of electrolyte conductivity of solutions is based on statistical mechanics and Liouville's theorem. The calculation of thermodynamic variables in electrolyte solutions, which illustrate a complex system, can be managed with reasonable effort only at *McMillan-Mayer* level. At this the interaction between two particles are accounted for regardless of the position and momenta of the others. In this context the potential of mean force $W_{ij}(\vec{r_1}, \vec{r_2})$ plays a major role. On the basis of distribution functions it is possible to formulate an association constant, as well as to describe any transport phenomena of electrolyte solutions. The association constant allows for the derivation of the thermodynamic values of the association process. The introduction of an additional contribution of short-range interactions (dipolar, induction, and dispersion forces) provides for the determination of the non-coulombic contribution to the ion-pair formation process.
The aim of statistical mechanics is to obtain a theoretically sound connection between the microscopic and macroscopic properties of a system, especially electrolyte solutions in this work. The experimentally accessible macroscopic properties illustrate an averaged information on the structural behavior of the solution's constituents; their motion and interaction [146].
In terms of statistical mechanics the electrolyte solution is regarded as a system made up of N solute particles (ions) at position $\vec{r}_1 \ldots \vec{r}_N$ and N_0 unstructured solvent particles $\vec{r}_{N+1} \ldots \vec{r}_{N+N_0}$ with momenta $\vec{p}_1 \ldots \vec{p}_N$ and $\vec{p}_{N+1} \ldots \vec{p}_{N+N_0}$, yielding the density function ρ [147]

$$\rho_{N+N_0}(\vec{r};\vec{p};t) = \rho_{N+N_0}(\vec{r}_1,\ldots,\vec{r}_N,\ldots,\vec{r}_{N+N_0};\vec{p}_1,\ldots,\vec{p}_N,\ldots,\vec{p}_{N+N_0}) \tag{5.1}$$

To overcome the enormous numbers of variables of the density function one make use of reduced distribution functions. The N-particle distribution function ρ_N

$$\rho_N(\vec{r}_1,\ldots,\vec{r}_N;\vec{p}_1,\ldots,\vec{p}_N;t) = \int \rho_{N+N_0}\mathrm{d}\vec{r}_{N+1}\ldots\mathrm{d}\vec{r}_{N+N_0}\mathrm{d}\vec{p}_{N+1}\ldots\mathrm{d}\vec{p}_{N+N_0} \tag{5.2}$$

which is obtained by averaging over all position and momentum variables of the solvent molecules N_0, indicate the probability of finding, at time t, the remaining particles N at positions $\vec{r}_1,\ldots,\vec{r}_N$ with momenta $\vec{p}_1,\ldots,\vec{p}_N$ regardless of the position and momenta of the solvent molecules.
Extending the integration range with regard to the remaining momentum variables $\vec{p}_1,\ldots,\vec{p}_N$ yields the molecular distribution functions f_N for N particles

$$f_N(\vec{r}_1,\ldots,\vec{r}_N;t) = \int \rho_N(\vec{r}_1,\ldots,\vec{r}_N;\vec{p}_1,\ldots,\vec{p}_N;t)\mathrm{d}\vec{p}_1\ldots\mathrm{d}\vec{p}_N \tag{5.3}$$

The total energy of an electrolyte system is made up of two contributions: a potential energy U_N as a function of the positions $\vec{r}_1\ldots\vec{r}_N$, and a kinetic energy as a function of momenta $\vec{p}_1\ldots\vec{p}_N$. The Hamiltonian is written as

$$H_N(\vec{r};\vec{p};t) = \sum_{i=1}^{N}\frac{\vec{p}_i{}^2}{2m_i} + U_N(\vec{r}_1\ldots\vec{r}_N;t) \tag{5.4}$$

U_N is approximated by a sum of direct pair-interaction potentials

$$U_N(\vec{r}_1\ldots\vec{r}_N;t) = \sum_{i=1}^{N}\sum_{j>i}^{N} U_{ij}(\vec{r}_i,\vec{r}_j;t) \tag{5.5}$$

Both momenta $\vec{p}_i$ and coordinates $\vec{r}_i$ are functions of time. Hamiltonian models based on Hamiltonians averaged with regard to the coordinates of the solvent molecules are referred to as Hamiltonian models at McMillan-Mayer (MM) level.
It can be shown that the density function $\rho_N(\vec{r}_1,\ldots,\vec{r}_N;\vec{p}_1,\ldots,\vec{p}_N;t)$ tends toward a time-independent equilibrium distribution $\rho_N^{eq}(\vec{r};\vec{p})$ in the limit of $t\to\infty$ [146, 148]

$$\rho_N^{eq}(\vec{r};\vec{p}) = \lim_{t\to\infty}\rho_N^{eq}(\vec{r};\vec{p};t) = \frac{\exp[-H/kT]}{\int\exp[-H/kT]\mathrm{d}\vec{r}_1\ldots\mathrm{d}\vec{r}_N\ \mathrm{d}\vec{p}_1\ldots\mathrm{d}\vec{p}_N} \tag{5.6}$$

With the help of the last equation it is in principle possible to calculate an averaged value of a macroscopic variable. But due to the large numbers of $6N$ variables, the complexity is further reduced by extending the integration range in Eq. (5.2) with respect to all positions and momenta except of particles 1 and 2. This will lead to the 2-particle density function $\rho_2(\vec{r}_1,\vec{r}_2,\vec{p}_1,\vec{p}_2,t)$. In most cases, however, only the relative position of the two particles to each other are of interest. Additional integration over momentum $\vec{p}_1$ and $\vec{p}_2$ gives the expression for the so-called pair distribution function $f_2(\vec{r}_1,\vec{r}_2,t)$

$$f_2(\vec{r}_1,\vec{r}_2,t) = \int \rho_2(\vec{r}_1,\vec{r}_2,\vec{p}_1,\vec{p}_2,t)\mathrm{d}\vec{p}_1\ \mathrm{d}\vec{p}_2 \tag{5.7}$$

Together with Eq. (5.6) the following form for the pair distribution arises

$$f_2(\vec{r}_1,\vec{r}_2) = f_{ij}(\vec{r}_1,\vec{r}_2) = \frac{\sigma^s}{Q_N}\int\exp\left(\frac{-U_N}{kT}\right)\mathrm{d}\vec{r}_3\ldots\mathrm{d}\vec{r}_N \tag{5.8}$$

The configurational integral Q_N is given by

$$Q_N = \int\exp\frac{-U_N}{kT}\mathrm{d}\vec{r}_1\ldots\mathrm{d}\vec{r}_N \tag{5.9}$$

$f_{ij}(\vec{r}_1, \vec{r}_2)$ stands for the propability of finding particle i at $\vec{r}_1$ and particle j at $\vec{r}_2$ simultaneously.
Based on the Liouville equation, statistical mechanics shows, e.g. via the BBGKY hierarchy of equations, that the knowledge of pair distribution functions, as the simplest form of a distribution function, is sufficient to construct any other density functions with an approximation process of superimposition [149]. This reasonable simplification of the theoretical description upon $f_{ij}(\vec{r}_1, \vec{r}_2)$ enables one to derive properties of electrolyte solutions.
The factor σ^s is $N_i N_j$ for different particles i and j and $\sigma^s = N_i(N_i - 1)$ for equal ones, N_i and N_j being the number of particles of i and j, respectively, in the solution. [150]
With increasing distance $\vec{r}_{21} = \vec{r}_2 - \vec{r}_1$ all interaction forces vanish so that the pair distribution function can be described as a product of particle densities $n_i = N_i/V$:

$$\lim_{\vec{r}_{12}\to\infty} f_{ij}(\vec{r}_1, \vec{r}_2) = n_i n_j \tag{5.10}$$

V is the volume occupied by the system. The departure from the limiting case in Eq. (5.10) is accounted for by the pair correlation function $g_{ij}(\vec{r}_1, \vec{r}_2)$

$$f_{ij}(\vec{r}_1, \vec{r}_2) = n_i n_j g_{ij}(\vec{r}_1, \vec{r}_2) = n_j n_i g_{ji}(\vec{r}_2, \vec{r}_1) = f_{ji}(\vec{r}_2, \vec{r}_1) \tag{5.11}$$

As the force $\vec{K}_i$ acting on a particle i at position $\vec{r}_i$ in a system of potential energy $U_N(\vec{r}_1 \ldots \vec{r}_N)$ is $K_i = -\partial U/\partial r_i$, a mean value of this quantity with fixed particles 1,2 and regardless of the position of the remaining ones can be expressed as

$$< \vec{K}_i(\vec{r}_1, \vec{r}_2) >= \frac{\int -\frac{\partial U_N}{\partial \vec{r}_i} \exp\left(\frac{-U_N}{kT}\right) \mathrm{d}\vec{r}_3 \ldots \mathrm{d}\vec{r}_N}{\int \exp\left(\frac{-U_N}{kT}\right) \mathrm{d}\vec{r}_3 \ldots \mathrm{d}\vec{r}_N} \tag{5.12}$$

which is the negative gradient of the potential of mean force $W_{ij}(\vec{r}_1, \vec{r}_2)$.
Together with Eq. (5.8), (5.11) this leads to the relationship Eq. (5.13), the definition of the potential of mean force with the help of the pair correlation function:

$$W_{ij}(\vec{r}_1, \vec{r}_2) = -kT \ln g_{ij}(\vec{r}_1, \vec{r}_2) \tag{5.13}$$

The logarithmic form ensures the limit of g_{ij} at increasing distance between ion 1 and 2 to be unity, because of the vanishing interactions

$$\lim_{\vec{r}_{12}\to\infty} g_{ij}(\vec{r}_1, \vec{r}_2) = \lim_{\vec{r}_{12}\to\infty} \exp\left[-\frac{W_{ij}(\vec{r}_1, \vec{r}_2)}{kT}\right] = 1 \tag{5.14}$$

The interaction potential W_{ij} comprises the contributions to the total potential energy of the system U due to polar, induction, dispersion and repulsive forces.
The derivation of the pair distribution functions, so far, is based on exact statistical mechanical considerations. Different models for electrolyte solutions starts to approximate W_{ij} with different interaction potential. As a result f_{ij} depends on the approximations put into the different model descriptions.
An attempt to set up a theory which takes into account all types of interaction energies U_{ij}, with the aim and purpose of determining potentials of mean force and subsequently pair distribution functions f_{ij} suffers from insuperable mathematical difficulties. The basic model of interaction potentials and its extension is the topic of the following section.

5.1.2. Electrostatic Potentials and Ion-Association

5.1.2.1. Debye-Hückel Model

The underlying chemical model of electrolyte solution at low concentrations on the MM level, developed by Debye and Hückel [151], represents the ions i as spherical particles of charge $e_0 z_i$ in a homogeneous and isotropic solvent of relative permittivity ϵ. The feature of their model is the concept of using the

fundamental potential equation of the electrostatic field in combination with a Boltzman distribution of the ions to express charge density together with appropriate boundary conditions for determining the potential W_{ij} of an equilibrium distribution. It takes into account only the long-range electrostatic interactions. At equilibrium the distribution of spherical charges can be assumed to be of spherical symmetry, i.e. $|\vec{r}_{12}| = |\vec{r}_{21}| = r$.
In the absence of external forces the electrostatic field around ion i at equilibrium generates the following potential of mean force

$$W_{ij}(r) = z_j e_0 \psi_i(r) \tag{5.15}$$

where $\psi_i(r)$ is the electrostatic potential of ion i in solution, z_i is the valence of ion i. The ions in the vicinity around i belong to the ion cloud. The required electrical potential $\psi_i(r)$ for calculation of the potential of mean force is provided by the Poisson equation, which presents a link between the electrostatic potential and the charge density $\rho_i^{el}(r)$ at distance r from ion i produced by the other ions in solution

$$\mathrm{div}\vec{E} = -\mathrm{div}\vec{grad}\ \psi_i(r) = -\Delta\psi_i(r) = \frac{1}{\epsilon\epsilon_0}\rho_i^{el}(r) \tag{5.16}$$

The charge density around ion i arises from a summation of the number of all ions j occurring at distance r around the central ion i, n_{ij}:

$$\rho_i^{el}(r) = \sum_j e_0 z_j n_{ij}(r) \tag{5.17}$$

Assuming a Boltzmann distribution of the ions j around i and a spherically symmetric Coulomb-potential leads to

$$\rho_i^{el}(r) = \sum_j e_0 z_j n_j \exp\left[\frac{-W_{ij}}{kT}\right] = \sum_j e_0 z_j n_j \exp\left[\frac{-e_0 z_j \psi_i(r)}{kT}\right] = \sum_j e_0 z_j n_j g_{ij}(r) \tag{5.18}$$

At infinite distance the electrostatic potential vanishes and the series expansion of the exponential term is truncated after the linear term in the framework of Debye-Hückel's theory

$$g_{ij}(r) = \exp\left[\frac{-e_0 z_j \psi_i(r)}{kT}\right] \simeq 1 - \frac{e_0 z_j \psi_i(r)}{kT} \tag{5.19}$$

and as a result, the charge density $\rho_i^{el}(r)$ follows:

$$\rho_i^{el}(r) = \sum_j e_0 z_j n_j - \sum_j \frac{e_0^2 z_j^2 n_j}{kT}\psi_i(r) \tag{5.20}$$

The first term on the right-hand side of Eq. (5.20) disappears because of the condition of electroneutrality

$$\sum_j e_0 z_j n_j = 0 \tag{5.21}$$

Combination of Eq. (5.16) with Eq. (5.20) gives the differential equation, which takes into account the ion-ion and ion-solvent interactions within the Debye-Hückel model theory

$$\mathrm{div}\vec{grad}\ \psi_i(r) = \Delta\psi_i(r) = \kappa^2\psi_i(r) \quad \text{with } \kappa^2 = \frac{e_0^2}{\epsilon\epsilon_0 kT}\sum_j n_j z_j^2 \tag{5.22}$$

The summation in κ has to be done with regard to all ions in solution. Solvation of equation (5.22) requires the proper setting of boundary conditions suitable for this problem:

$$\lim_{r\to\infty} \psi_i(r) = 0 \tag{5.23a}$$

$$z_i e_0 = \iint_a \vec{D} \mathrm{d}\vec{f} \tag{5.23b}$$

The boundary conditions state the vanishing potential $\psi_i(r)$ with increasing distance, (5.23a). Equation (5.23b) ensures that the region $a \leq r$ is free of other charges than the central ion itself by the assumption that the total flow of the displacement vector $\vec{D}$ through the surface r is equivalent to the central charge.
Finally the Coulomb potential $\psi_i(r)$ according to Debye and Hückel is obtained with Eqs. (5.22)-(5.23b) in the form

$$\psi_i(r) = \frac{z_i e_0}{4\pi\epsilon\epsilon_0} \frac{\exp[-\kappa(r-a)]}{r(1+\kappa a)} \tag{5.24}$$

It describes the electrostatic potential of ion i with a certain dimension, but as a point charge. κ is the reciprocal radius of the ion-cloud, a is some sort of a length, which may be regarded as the mean value of a distance, a counter-ion (anion or cation) can approach to the central ion [151]. Noteworthy to say, however, that considering a as the ionic radii (a_i, a_j) must be regarded as wrong, due to Eq. (5.11). An identity of a_i and a_j would have to be assumed in that case, which is contrary to the general meaning of an ionic radius. A possible explanation considers $a = a_i + a_j$ to be the distance of closest approach of two differently charged ions [148]. Also the strong interactions between an ion and an adjacent solvents molecule to form a kind of a complex species might be imposed in the interpretation of a. The values for the ionic radii can be identified with crystallographic radii [152, 153] as far as these exist (e.g. alkali metal cations, halides, etc.) or else are calculated from van der Waals volumes (e.g. tetraalkylammonium cations) [152, 153] or from bond length and bond angles [154].
As indicated in Eq. (5.19), the series expansion of $g_{ij}(r)$ is truncated after the linear term meaning a restriction to highly dilute solutions. As a further restriction, the limitation to only long range forces must be remembered. The Debye-Hückel model as given above can be regarded as an approximated theory for the description of electrolyte solutions at high dilution ($c \leq 10^{-5}\,\mathrm{mol\,L^{-1}}$) [155].

5.1.2.2. Chemical Model at Low Concentration

Solutions with solvents of low permittivity show already at their lowest realisable concentrations deviations from the Debye-Hückel limiting law and these have been the reason for introducing the **l**ow-**c**oncentration **C**hemical **M**odel (lcCM), combining the concept of the Debye-Hückel theory and the association hypothesis in a general way permitting the introduction of short range forces into the electrolyte theory [156]. The lcCM offers reliable property equations for wider concentration ranges over a wide range of solvents; restrictions to point charges in a homogenous dielectric medium of the Debye-Hückel mean force potential is abolished and knowledge of the structure of electrolyte solutions from chemical evidence, reflected by ion solvation and association, is included.
The Chemical Model of electrolyte solutions subdivides the space around an ion into three regions, distinct by different mean force potentials:

1. Region (I):
   $r < a$, a being the minimum distance of two ions, i and j, which is assumed to be the sum of the effective ion radii, $a = a_i + a_j$. Within this region no further ions are expected. This region is characterized by a hard-spere potential

   $$W_{ij}^{I}(r) = \infty \tag{5.25}$$

2. Region (II):
   $a \leq r \leq R$, within which a pair state of oppositely charged ions, the ion pair, suppresses long range

interactions with other ions in the solution. In dilute solutions the occupancy of this region by ions of equal sign can usually be neglected.
The mean force potential is split into two parts representing the coulombic, W_{ij}^{el}, and noncoulombic, W_{ij}^{*}, interactions

$$W_{ij}^{II}(r) = W_{ij}^{el}(r) + W_{ij}^{*} \tag{5.26}$$

The non-coulombic part is represented by a constant step potential, including all short-range ion-ion interactions, which are chosen to be independent of the central charge. R is chosen by chemical evidence as sum of the ionic radii plus the length of one or more orientated solvents molecules

$$R = a + ns \quad (n = 1, 2, \ldots) \tag{5.27}$$

3. Region (III):
   $r > R$, the region of long range ion-ion Coulomb interactions. The mean force potential introduced by Debye-Hückel is applicable.

The electric potential of the regions (II) and (III) can be calculated using the Poisson equation (5.16), assuming no free charges in (II)

$$\mathrm{div}\vec{grad}\ \psi_i(r) = \begin{cases} 0 & \text{if } a \le r \le R, \\ \kappa^2 \psi_i(r) & \text{if } r > R \end{cases} \tag{5.28}$$

Under the boundary conditions given in the literature [150, 157] the system of differential Eqs. (5.28) has the solution

$$\psi_i(r) = \begin{cases} \dfrac{e_0 z_i}{4\pi\epsilon\epsilon_0}\left(\dfrac{1}{r} - \dfrac{\kappa}{1+\kappa R}\right) & \text{if } a \le r \le R, \\ \dfrac{e_0 z_i}{4\pi\epsilon\epsilon_0}\dfrac{1}{r}\dfrac{\exp[-\kappa(r-R)]}{1+\kappa R} & \text{if } r > R \end{cases} \tag{5.29}$$

The quantity κ is the Debye parameter under the condition that the ionic concentrations are those of the free ions and has the following form:

$$\kappa^2 = 16\pi q N_A(\alpha c); \quad q = \frac{e_0^2 |z_i z_j|}{8\pi\epsilon\epsilon_0 kT} \tag{5.30}$$

where α is the degree of dissociation and q is the parameter originally given by Bjerrum as the maximum distance for the interaction of oppositely charged ions.
Then the complete mean force potential at finite concentration is given by the relationships

$$W_{ij}(r) = \begin{cases} \infty & \text{if } a < R, \\ \dfrac{2qkT}{r} - \dfrac{2q\kappa kT}{1+\kappa R} + W_{ij}^{*} & \text{if } a \le r \le R, \\ \dfrac{2qkT}{r}\dfrac{\exp[\kappa(R-r)]}{1+\kappa R} + 0 & \text{if } r > R \end{cases} \tag{5.31}$$

5.1.2.3. Thermodynamics of Association Process

The association of a binary 1:1-electrolyte $K^{z+} + A^{z-} \rightleftharpoons Y = K^{z+}A^{z-}$ is chemically described by application of the thermodynamic condition of equilibrium at constant p and T

$$\mu_Y' - \nu_+\mu_+' - \nu_-\mu_-' = 0 \tag{5.32}$$

The symbol $'$ refers to quantities based on the actual concentration of the corresponding species, which is related to the analytical concentration c_Y by the degree of dissociation α. The chemical potential of

the undissociated electrolyte and the single ions are given as follows

$$\mu'_Y = \mu'^{\infty}_Y + RT\ln c'_Y y'_Y; \quad c'_Y = (1-\alpha)c_Y \tag{5.33a}$$

$$\mu'_+ = \mu'^{\infty}_+ + RT\ln c'_+ y'_+; \quad c'_+ = \alpha\nu_+ c_Y \tag{5.33b}$$

$$\mu'_- = \mu'^{\infty}_- + RT\ln c'_- y'_-; \quad c'_- = \alpha\nu_- c_Y \tag{5.33c}$$

Combining Eq. (5.32) with the set of equations (5.33) yields the thermodynamic equilibrium constant of ion-pair formation K_A

$$\Delta G^0_A = \mu'^{\infty}_Y - \nu_+\mu'^{\infty}_+ - \nu_-\mu'^{\infty}_- = -RT\ln\frac{c'_Y y'_Y}{(c'_\pm y'_\pm)^\nu} = -RT\ln K_A \tag{5.34}$$

$$K_A = \frac{1-\alpha}{\alpha^2 c_Y}\cdot\frac{y'_Y}{y'^2_\pm} \tag{5.35}$$

$$c'_\pm = \sqrt{c'_+ c'_-}; \quad y'_\pm = \sqrt{y'_+ y'_-}; \quad y'_Y = 1; \quad \nu = \nu_+ + \nu_-$$

Eq. (5.35) is the link between a thermodynamic and a statistical-mechanical treatment. The ion-pair association concept for symmetrical electrolytes can now be introduced into the chemical model by assuming that the distance parameter R equals the upper limit of ion association. Within this distance pair configurations of oppositely charged ions are considered as ion pairs. Obviously a and R are suitable for definition of the region of ion-pair configurations.
The degree of association $(1-\alpha)$ from the Chemical Model is obtained by a summation with respect to all ion-pairs in $a \le r \le R$, adopted from an expression of Falkenhagen and Ebeling [158]

$$1-\alpha = 4\pi\alpha n_j \int_a^R r^2 g_{ij}(r)\mathrm{d}r \tag{5.36}$$

Implying the relations for the correlation function and the mean field potential for region (II), Eq. (5.31), gives the following equation

$$\frac{1-\alpha}{\alpha^2 c_Y} = 4\pi N_A \exp\left(-\frac{2\kappa q}{1+\kappa R}\right)\int_a^R r^2 \exp\left(\frac{2q}{r} - \frac{W^*_{ij}}{kT}\right)\mathrm{d}r \tag{5.37}$$

To derive an expression for the concentration-independent thermodynamic association constant K_A in terms of the mean field potential, e.g. to combine Eqs. (5.35) and (5.37), requires the knowledge of the mean activity coefficient $y'_\pm$ of free ions.
A starting point for its calculation is the separation of the contribution of the central i ion and that of the remaining ions to the potential $\psi^{II}_i(r)$, Eq. (5.29), yielding the potential of the ion cloud $\psi^{cloud}_i(r)$ within $a \le r \le R$. The activity coefficient of ion i can be calculated with the help of a charging process of the ion from zero to full charge under the action of the electrical potential of the ion cloud. The mean activity coefficient of the free ions within the chemical model, therefore, can be written as

$$\ln y'_\pm = -\frac{\kappa q}{1+\kappa R}; \quad y_\pm = \alpha y'_\pm \tag{5.38}$$

Finally, the expression for the association constant according to the Chemical Model turn out to be

$$K_A = 4\pi N_A \int_a^R r^2\left(\frac{2q}{r} - \frac{W^*_{ij}}{kT}\right)\mathrm{d}r \tag{5.39}$$

The upper limit of ion-pair association and the cutoff distance of short-range interactions, R, is considered identical in the framework of the chemical model.
Separation of ΔG^0_A, Eq. (5.34), into a part of the molar Gibbs free energy of ion-pair formation, which

is due to short-range interactions, $\Delta G_A^* = N_A W_{ij}^*$, and coulombic, long-range interactions, ΔG_A^{coul}, leads to a formal separation of these contributions in the association constant

$$\Delta G_A^0 = \Delta G_A^{coul} + \Delta G_A^*; \quad K_A = K_A^{coul} \cdot K_A^* = K_A^{coul} \cdot \exp\left(-\frac{\Delta G_A^*}{RT}\right) \tag{5.40}$$

$$K_A = 4\pi N_A \exp\left(-\frac{\Delta G_A^*}{RT}\right) \int_a^R r^2 \exp\left(\frac{2q}{r}\right) \mathrm{d}r \tag{5.41}$$

5.1.2.4. Transport Properties

Transport equations for conductance are obtained on the basis of Onsager's continuity equation [159], which is obtained from the BBGKY hierarchy of equations.
The origin of the ion's movement in the external fields is

- electric forces
  - external electric field
  - electric fields emerging from the unsymmetrical charge distribution around i upon the interactions with another j ion
- concentration gradients
- hydrodynamic flow of the solvent at position r_1 itself: $\vec{v}(r_1)$

The applied external field causes the radial distribution functions to be disturbed with respect to their definitions so far. The disturbed distribution in the region $r \geq R$ is described by the unsymmetrical function $f_{ij}(r_1, r_2) = f_{ij}(r) + F_{ij}(r_1, r_2)$. The same holds for a consideration of the influence of the external field on the potential $\psi_i(r_1, r_2)$. If the interaction between i and j is assumed to be caused by coulombic forces only, an expression for the potential $\psi_i(r_1, r_2)$ can be deduced in accordance with the Poisson equation.
On the basis of these presuppositions, the continuity equation yields a differential equation, the solution of which depends on

- the choice of the pair distribution function f_{ij}
- the approximations made in the calculation of ψ_i
- the boundary conditions selected for solution of the differential equation

In the context of this work, the following form of a complete conductivity equation is used

$$\Lambda = \alpha \left[\Lambda^\infty - S\sqrt{\alpha c} + E(\alpha c)\ln(\alpha c) + J_1(\alpha c) + J_2\sqrt{(\alpha c)^3}\right] \tag{5.42}$$

It was firstly introduced in the theory of Fuoss and Onsager [159] and expresses the molar conductivity in a solution of a single binary electrolyte as a function of concentration, c, distance parameter a, solvent permittivity, ϵ, viscosity, η and temperature, T

$$\Lambda = \Lambda^\infty - \Lambda^{rel} - \Lambda^{el} \tag{5.43}$$

showing the three contributions to conductivity:

- unperturbed ion movement in the external electric field (Λ^∞)
- relaxation effect, Λ^{rel}, caused by the unsymmetrical charge distribution around moving ion i
- electrophoretic term, Λ^{el}, expressing the hindrance of the undisturbed movement of the ions, produced by hydrodynamic interactions of ions and solvent molecules.

Eq. (5.42) is a series expansion of the original expressions with respect to concentration. The coefficients $S, E, J_1(R), J_2(R)$ are the coefficients of the CM concept applied; S and E are independent of ionic distances, whereas $J_1(R)$ and $J_2(R)$ depend on the upper limit of association R defining the free ions contributing to the charge transport. Every coefficient contains contributions of the relaxation as well as electrophoretic term. The analytical forms of these coefficients are given elsewhere [160].
Application of Eq. (5.42) to experimental data yields the quantities Λ^{∞}, R and W_{ij}^{*} and thus provides the fundamental parameters of the theory [22].

5.1.3. Conductance of Concentrated Solutions

Most often electrical conductance equations, applied for the dilute range, do not allow for the proper description of experimental data at moderate to high concentration within the assumptions and approximations on which they are based. Equations based on empirical extensions of the equations for dilute solutions use the fact that the viscosity of the system is the most important effect on the transport properties and introduce appropriate viscosity corrections. Today, also empirical equations of concentrated electrolyte solutions are available, as well as equations which are rigorous statistical mechanical approaches.
Nevertheless, an excellent description of conductance data of high quality is still best achieved by empirical transport equations. Representation of physical properties of electrolyte solutions by the use of fitting equations is commonly executed with polynomials or mathematical functions known for the appropriate representation of the shape of the experimentally determined curves.
One of the most useful expressions of this type is given by Casteel and Amis for the specific conductivity of concentrated solutions as function of concentration [161]

$$\kappa = \kappa_{max} \left(\frac{\mathrm{m}}{\mu}\right)^{a} \exp\left[b(\mathrm{m}-\mu)^2 - \frac{a}{\mu}(\mathrm{m}-\mu)\right] \tag{5.44}$$

It fits very well specific conductances in a wide concentration range around the point of maximum specific conductance κ_{max} attained at concentration μ. Equation (5.44) fulfills the condition $\kappa = \kappa_{max}$ if $\mathrm{m} = \mu$. a and b are regressed parameters without physical meaning. Misrepresentations can occur at very low and high concentrations. The physically necessary condition $\kappa \to 0$ if $m \to 0$ is only fulfilled if $a \geq 0$, otherwise $\kappa \to \infty$. Regressions performed with experimental data only at $c < \mu$ (low solubility) or $c > \mu$ might result in numerical problems with no convergence.
The maximum of specific conductivity, κ_{max}, is a feature of every electrolyte solution permitting sufficiently high solubility of the solute. It follows from the competition between the increase $\mathrm{d}c$ of the electrolyte concentration and the decrease $\mathrm{d}\Lambda$ of the ion mobility when c increases. The variation $\mathrm{d}\kappa$ of the specific conductivity is given by the relationship

$$\mathrm{d}\kappa = \Lambda \mathrm{d}c + c\mathrm{d}\Lambda \tag{5.45}$$

The reason for a decreasing ion mobility lies in the increasing interactions between ion-ion and ion-solvent molecules [162] and ion association process [163].

5.2. Temperature Control

In order to obtain the sufficiently accurate conductance data which could be used in conductance equations, it is necessary to have an equipment which allows reasonably quick and accurate measurements at different temperature values.
The thermostat assembly, as displayed in Fig. 5.1, is built up from 4 units: a Lauda P Cryomat (model RUK 40S) with an operation temperature between (−40 °C - 100 °C) serving as the cold bath; a power supply (B60-10R, Oltronix) for the immersion heater; the measurement thermostat; a temperature control unit [164, 165].
The measurement thermostat with a volume of about 60 L filled with silicon oil (Baysilon M5, Bayer) is

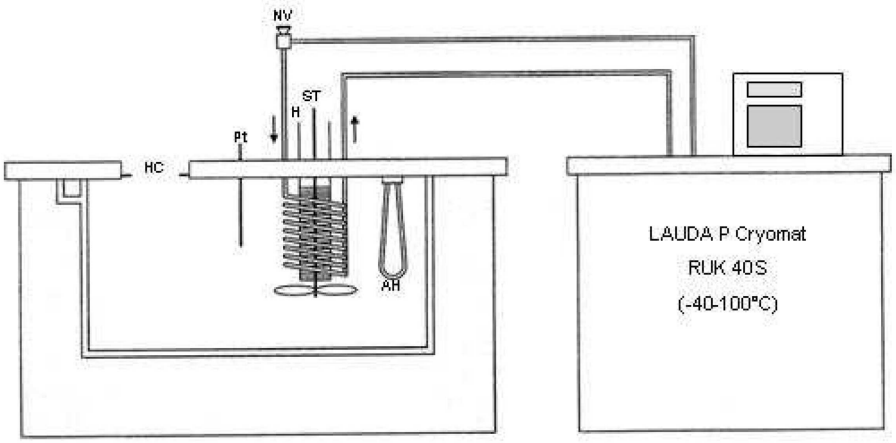

Figure 5.1.: Cold bath (right side) in connection with the main thermostat for conductivity and permittivity measurements in the range between −25 °C and 40 °C

coupled to the cold bath by means of a heat exchanger. The operation range of the thermostat is between −30 °C and +40 °C and is limited at high temperatures by the vapor pressure and at low temperatures by the viscosity of the bath liquid. The flow-velocity of the cold source's fluid (Ethanol) is controlled with the help of a needle valve (NV), allowing for a suitable heat-exchange and the reduction of the flow at higher temperatures. The heat exchanger is located within a cylindric chamber which contains a powerful stirrer (ST) and the heater (H). An excellent, homogenous temperature-distribution in the oil is achieved. In order to bridge large temperature-ranges, e.g. during the heating-up, two additional heating devices (AH) with a power of 1000 W each are installed and can be controlled manually. Optimal temperature regulation is maintained when the necessary heating continuously supplied during the operation is about 50 W and 200 W. In this context a temperature of the cold bath being about 12 °C lower than the expected temperature in the main thermostat has to be chosen over the whole range of operation. The thermostat is hermetically sealed to prevent atmospheric moisture entering the bath. A circular opening (HC, ø = 18.5 cm) in the cover plate permits the immersion of measuring cells for electrical conductivity (Fig. **??** and relative permittivity (Fig. 5.7), which for their part are supplied with assembly plates guaranteeing hermetical sealing of the opening (HC).
The temperature of the measurement thermostat is controlled by a PID controller joined to an a.c. wheatstone-bridge which contains a platinum resistance thermometer (Pt) (appr. 500 Ω at 0 °C). The platinum resistance is connected as one arm of the bridge with a three-core cable in order to compensate for the resistance of the supply line. Errors introduced by the warming of the Pt resistance are negligible due to the supply voltage being restricted to a value of 300 mV at 130 Hz. Adjustment of the set-point temperature is accomplished by a decade resistance box. The error voltage of the bridge is used both for temperature measurement and, via the PID controller, for controlling the heating power of the source of heat (H). Wachter et. al. stated an overall accuracy in temperature of better than 0.01 K with a precision of 0.001 K by means of the described temperature control [164]. The long-term stability of temperature is proven to be better than 0.001 K.
Because the complete equipment have not been used for a long time, the accuracy of temperature was verified prior to all measurements by a Pt-100 temperature sensor (model F250, Automatic Systems Laboratories), which was previously calibrated according to the triple-point of water.
A plot of $R = f(T)$ is shown in Fig. 5.2. Least-square procedure for the regression of the platinum resistance $\ln R$ as a function of the measured absolute temperature T is performed with the polynomial equation (5.46), the coefficients of which are displayed in Table 5.1. The temperature calibration procedure is based on *The International Temperature Scale of 1990 (ITS-90)* [166] and done in the temperature-range of (248.15 - 313.15) K. The temperature dependence is very well described by that 4th order polynomial, as the high accuracy and precision of data is obtained. Although a linear regression model represents well $R(T)$ data points (see 4.6).
A complete and detailed description of the electronic setup of the temperature control unit and the PID

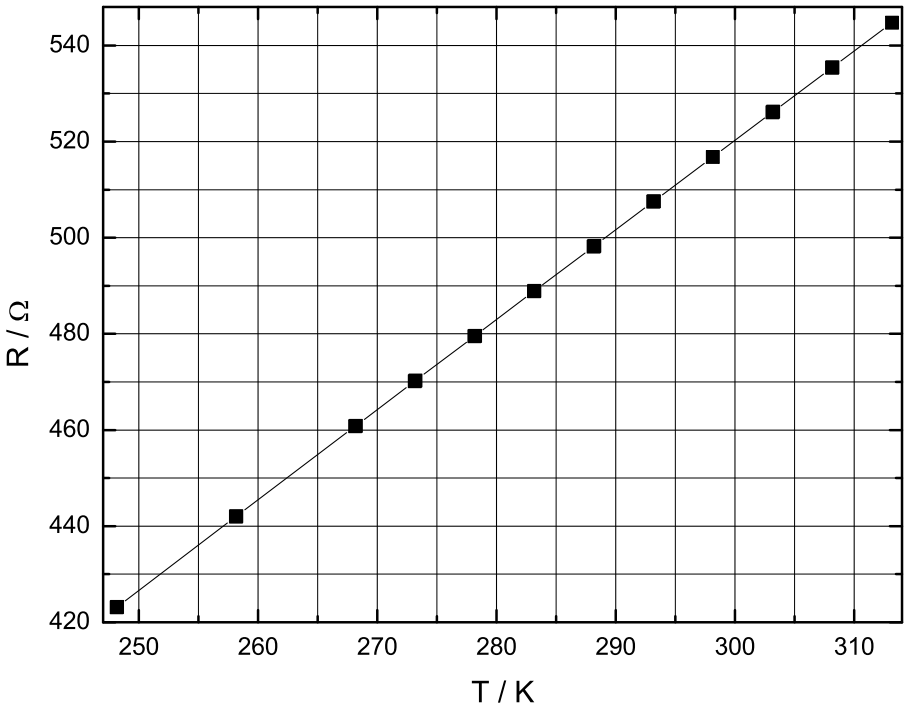

Figure 5.2.: Calibration curve of the Pt-resistance thermometer in the main thermostat

$$R = a_0 + a_1\frac{T}{K} + a_2\left(\frac{T}{K}\right)^2 + a_3\left(\frac{T}{K}\right)^3 + a_4\left(\frac{T}{K}\right)^4 \qquad (5.46)$$

Table 5.1.: Parameters of Eq. (5.46), $\sigma = 2.6 \times 10^{-4}$

Coeff.	a_i	$\sigma(a_i)$
a_0	-90.8	4.4
a_1	2.37	0.06
a_2	-1.8×10^{-3}	0.3×10^{-3}
a_3	3.0×10^{-6}	0.8×10^{-6}
a_4	-2.7×10^{-9}	0.7×10^{-9}

controller can be found in the literature [164].

Evaluation of the experimental conductivity data with the help of Eq. (5.42) requires the knowledge of the relative solvent permittivity, ϵ, solvent viscosity, η, and also the density, d, when concentrations like molonity (mol / kg of solution) or molality (mol / kg of solvent) are used. Their precise determination is described in the following sections.

5.3. Density Measurements

The density of PnP along with the density coefficients (D) of Bu_4NBr, Bu_4NNO_3, Bu_4NOAc and Bu_4NSCN in 1-propoxy-2-propanol, and the binary system's densities of PnP/water (see Sec. 3.3) are determined with a vibrating tube densimeter. The device consists of a remote measuring cell (model DMA 602, Anton Paar), an electronic processing unit (DMA 60, Anton Paar) and a PC interfaced to the densimeter by the help of a data logger (designed at the electronic workshop). An on-line monitoring of the oscillating periods throughout the measurements with subsequent storing on a harddisc is possible.

5.3.1. Principle of Density Measurements

The density determination is based on measuring the period of oscillation of a vibrating U-shaped sample tube, which is filled with sample liquid. The following relationship exists between the period, T, and the density d:

$$d = A\left(T^2 - B\right) \tag{5.47}$$

A and B are instrument constants that are determined through calibration measurements with substances of known density.
For the purpose of density determination the sample is introduced into a device that is capable of oscillating. In this way, the natural frequency in influenced by the mass and, therefore, also by the density of the sample. The oscillating device (Fig. 5.4) is a hollow glass oscillator, which is electronically excited to oscillate in an undamped fashion. The direction of oscillation is perpendicular to a plane through the inlet and outlet opening of the sample tube.
For the purpose of mathematical derivation, it is also possible to consider an equivalent system consisting of a hollow body with the mass, M, which is suspended on a spring with a spring constant (c). Its volume, V, is assumed to be filled by a sample of the density d.
The natural frequency, f, of such a system is then given by

$$f = \frac{1}{T} = \frac{1}{2\pi}\sqrt{\frac{c}{M + d \cdot V}} \tag{5.48}$$

with the period of oscillation T.
After expression (5.48) is squared and simplified by

$$A^{-1} = \frac{4\pi^2 V}{c} \quad \text{and} \quad B = \frac{4\pi^2 M}{c} \tag{5.49}$$

one obtains Eq. (5.47).
Constants A and B contain the spring constants of the oscillator as well as the empty oscillator's mass and that volume of the sample which participates in the oscillation.
These constants are, therefore, instrument constants for each individual oscillator and can be determined by two calibration measurements with samples of known density. From the calibration measurements (see Sec. 5.3.4) the corresponding periods of oscillation, T_1 and T_2

$$d_1 = A\left(T_1^2 - B\right) \qquad d_2 = A\left(T_2^2 - B\right) \tag{5.50}$$

and hence the apparatus constants are obtained unambiguously

$$A = \frac{d_2 - d_1}{T_1^2 - T_2^2} \quad B = T_1^2 - \frac{d_1}{A} = \frac{d_1 T_2^2 - d_2 T_1^2}{d_1 - d_2} \tag{5.51}$$

5.3.2. Measuring Unit

The measuring device consists of two separated units: the remote measuring cell and an electronic processing unit [167]. A PC is used for online monitoring and storage of the data by means of a data

logger [168]. The oscillator or sample tube, made out of borosilicate glass (Duran 50) is fused into a dual wall glass cylinder. An additional shorter capillary tube (ø = 2 mm) inside the inner space of the dual wall cylinder, filled with a heat-conductive paste, is for the accurate determination of the measuring cell's temperature by means of a NTC (see Fig. 5.4).
The temperature sensor NTC5K is calibrated with the help of the thermostat assembly described in Sec. 5.2 at 8 temperatures between −25 °C and 40 °C. For the temperature range extending that required for the conductivity data, calibration of a NTC10K covers the range from −27 °C to 115 °C.
The thermistors non-linear $R-T$ characteristics are modeled to a high degree of accuracy using the 4-parameter polynomial equation (5.52).

$$\ln\left(\frac{R}{\Omega}\right) = a_0 + a_1\left(\frac{\vartheta}{°C}\right) + a_2\left(\frac{\vartheta}{°C}\right)^2 + a_3\left(\frac{\vartheta}{°C}\right)^3 \tag{5.52}$$

The resistance of the NTCs is measured with a specially designed measuring bridge built in our institute. Values of R at different temperatures are plotted in Fig. 5.3 with coefficients obtained from (5.52) in a least-square procedure displayed in Table 5.2. The rest of the instrument consists of the electronic

Table 5.2.: Values of the parameters of polynomial Eq. (5.52) with a standard deviation of $\sigma_{5K} = 2 \times 10^{-4}$ and $\sigma_{10K} = 3 \times 10^{-3}$

Coefficients NTC5K	a_0	a_1	a_2	a_3
a_i	9.5403	-4.499×10^{-2}	1.568×10^{-4}	-4.8×10^{-7}
$\sigma(a_i)$	1×10^{-4}	1×10^{-5}	3×10^{-7}	1×10^{-8}
Coefficients NTC10K	a_0	a_1	a_2	a_3
a_i	10.3998	-5.145×10^{-2}	1.57×10^{-4}	-3.11×10^{-7}
$\sigma(a_i)$	10^{-4}	4×10^{-5}	1×10^{-6}	9×10^{-9}

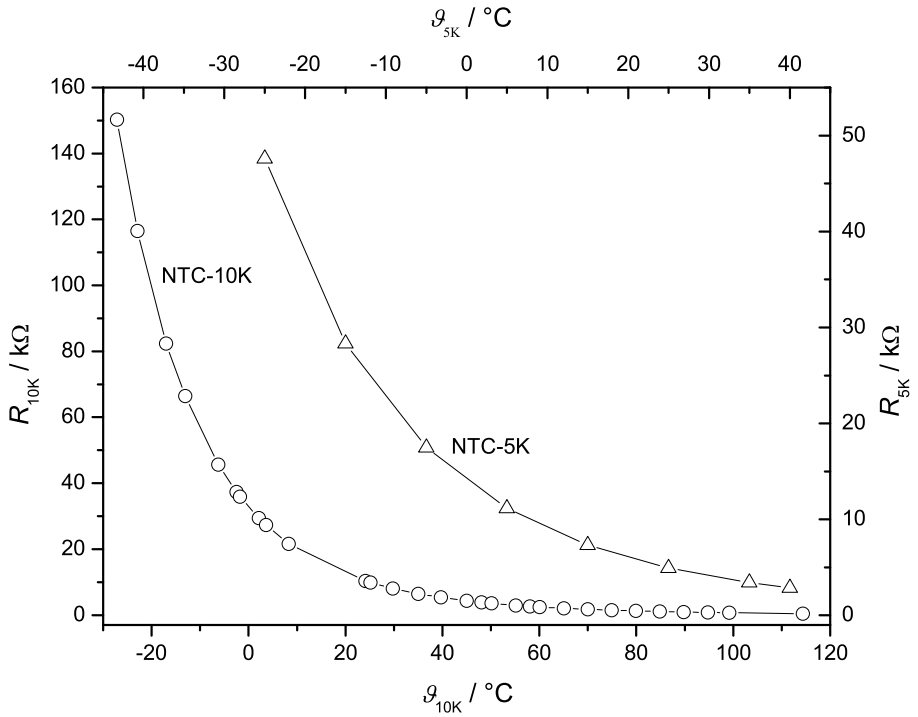

Figure 5.3.: Measured resistance values of two NTC's as a function of temperature

excitation system for the oscillator and portion of the electronics that assures an interference-free transmission of the period signal to the processing unit. The processing unit allows for different modes of

data processing. Throughout all measurements in this work the period of oscillation is a mean value as averaged over 10.000 periods. For this purpose the DMA60 counts the clock pulses of an integrated, high-precise oscillator, occurring with a frequency of $f = 10^5$ Hz. A sample with a density of approximately 1 g cm^{-3} ($T = 3.4 \times 10^{-3}$ s), for instance, generates a signal after 34 s. During that time 3.4×10^6 clock pulses occurred, corresponding to a resolution of 3×10^{-7} in the measured density. This theoretical resolution, however, is limited by the display and practical factors (temperature fluctuations, calibration, preparation).
The DMA60 signal output is processed by a PC linked to the data logger. A specially designed software (MYV24[1]) allows for the on-line monitoring and storage of the periods of time for further treatment (controlling for time stability, averaging over long time periods).
For accurate measurements two thermostats are used in cascade with proportional control of the thermostat close to the densimeter. The cold bath is a cryostat (model RC6, Lauda), filled with ethanol and set to a constant temperature lower than the desired temperature in the main thermostat (Thermomix 1480, Braun), in order to maintain a most stable temperature within the sample tube. The fluid for temperature equilibration used is a synthetical oil (Baysilon M50, Bayer) for all measurements above 20 °C with a deviation of less than ±0.01 °C ($T < 50$ °C) and less than ±0.025 °C ($T > 50$ °C). Measurements at temperatures below 20 °C are performed with a single cryostat (model FP40, Julabo) connected to the oscillator with fluctuations in T being smaller than ±0.01 °C and a bath fluid of low viscosity (Baysilon, M5, Bayer). In order to keep the energy loss between thermostat and measuring cell as small as possible, short tubes made of *Viton* are used with additional insulation of the sample tube by means of foam rubber.

5.3.3. Execution of Measurements

All measurements presented in this work are those when sample preparation, sample filling and measurements are performed under a steady atmosphere of nitrogen. Therefore the measuring cell is equipped with a pressure-tight adapter (DA) which is capable of fixing two PTFE-screws at the inlet and outlet of the oscillator (V). The screws connect the sample tube with sample solution (HS), the waste container (VB1, VB2) and the inlet for N_2 by means of PTFE-tubes (TL) and gastight PTFE body valves (H1, H2, H3). Fig. 5.4 highlights the main parts of the oscillator and the equipment for sample filling. Each

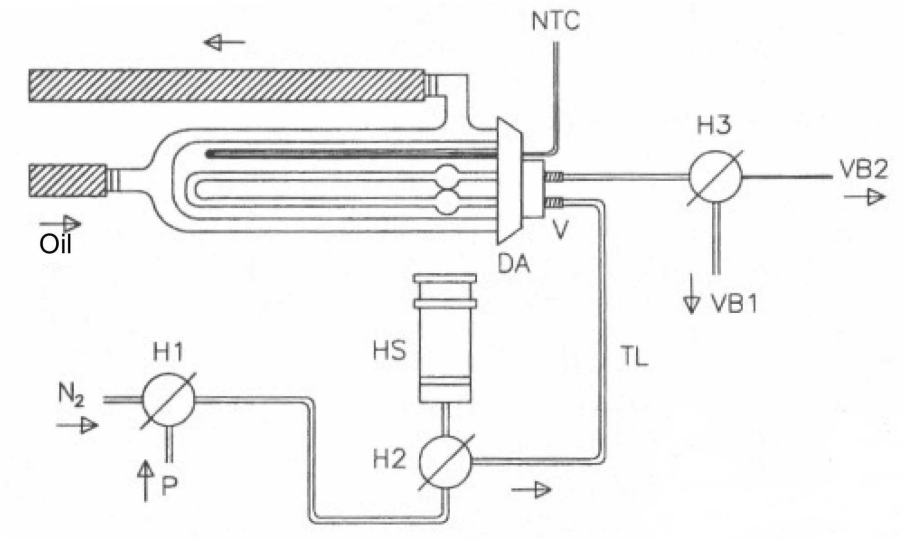

Figure 5.4.: Setup for density measurements under protective gas: (H1,H2,H3) gastight PTFE body valves, (N_2,P) connections to nitrogen or an integrated pump, (TL) PTFE tubes, (HS) gastight syringe with sample, (VB1,VB2) waste containers

sample is introduced into the measuring device with a gastight syringe (10 mL, Hamilton) whilst a steady

[1] MYV24, RS232-Terminal program, Elektronik/Chemie, University of Regensburg, 2007, vers. 2.2

flow of N_2 is applied through valve H1. Great care has to be taken to avoid any gas bubbles within the U-shaped sample tube. It is recommendable to introduce the sample slowly through the lower entrance port to enable the liquid to properly wet the walls of the sample tube. It is completely filled when the liquid meniscus has passed the upper enlarged portion of the sample tube.
Prior to use the equipment is completely rinsed with ethanol, water, and acetone. Solvent residues are removed upon flushing with nitrogen for at least 20 min, avoiding any condensation of atmospheric moisture at low temperatures.
The volume of the sample tube is 0.7 mL, but due to the extra equipment for filling, at least 2 mL of each sample is required. Some parts of the PTFE tubes must be left filled with nitrogen to allow for thermal expansion of the liquid sample at temperatures away from ambient. Measurements on the same sample can easily be repeated when the liquid is replaced by a sample volume of the attached syringe without additional cleaning.
The pure solvent samples are degassed for 30 min under rigorous stirring and transferred to the syringe (HS) under a low pressure of N_2. Electrolyte solutions used for determination of the density coefficient (D) are introduced without degassing to avoid concentration changes. Experimental investigations dealing with the influence of the gas content on the liquid density can be found elsewhere [169, 170]. The process of degassing must be considered as important at very low or high temperatures due to the rapid occurrence of gas bubbles, which leads to unstable signal readings of the period of oscillation.

5.3.4. Calibration

Constants A and B are related to the experimental period of oscillation by Eqs. (5.51). Two suitable standard samples with known density of high accuracy enable the constant's determination. In this work the calibration is done with samples of pure, dry nitrogen and water. Their reference values for the density are taken either as results of the van-der-Waals equation for N_2 with coefficients [24]

$$a = 1.390\,\mathrm{dm^6\,atm\,mol^{-2}}$$
$$b = 0.039\,13\,\mathrm{dm^3\,mol^{-1}}$$

or as polynomial functions in temperature for water. For temperatures below 40 °C values for coefficients are taken from [61], whilst at higher temperatures Kell [171] thoroughly investigated the temperature dependence of the water density. Conversion of temperatures to the basis of the international temperature scale of 1990 is taken into account in the density calculations [166].
Due to the possible effect of hysteresis described by Roch [172], the coefficients are determined at each temperature along with the measurements on the density of PnP. In the temperature range between 10 °C and 90 °C the coefficients obtained can be described well by a quadratic function in T and enables the extrapolation to temperatures outside that interval. Extended studies on the period of oscillation of N_2 outside the accessible temperature range of A and B show a very smooth transition of T_{N_2}.
The water samples used in the calibration is freshly taken form the Millipore purification system and distilled twice. It is degassed under rigorous stirring under vacuum and transferred to the sample syringe under an atmosphere of nitrogen. Repeated measurements on pure water give periods of oscillation having deviation from each other of less than $\pm 1 \times 10^{-5}$ at ambient temperatures and less than $\pm 1 \times 10^{-4}$ at high and very low temperatures.
Nitrogen is purified according to the procedure in Sec. 2.3 before use. The following approach is recommended for gaseous samples: with valves H1, H2, and H3 open nitrogen is flushed through the PTFE and sample tube for at least 15 min. The system is equilibrated at the desired temperatures whilst H2, H3 are closed until constant reading on the instrument. The system pressure is released by deflating slowly to atmospheric pressure by means of H3. The actual atmospheric pressure is obtained by a commercial barometer.
From various calibration measurements the error in A and B can be estimated to ±0.005 % at ambient temperature and ±0.02 % at high and very low temperatures, respectively. The accuracy of reading is 1×10^{-6}. The error in the density of water is specified as $2 \times 10^{-5}\,\mathrm{g\,cm^{-3}}$ [61], those of nitrogen as $3.4 \times 10^{-7}\,\mathrm{g\,cm^{-3}}$ [24]. Fluctuations in temperature have an impact on the precision of the readings of

1×10^{-5} or up to 1×10^{-4} at extreme temperatures. Error propagation calculation for the density of an unknown sample, using the equations given, account for an uncertainty of $5 \times 10^{-5}\,\mathrm{g\,cm^{-3}}$ (ambient) and up to $3 \times 10^{-4}\,\mathrm{g\,cm^{-3}}$ towards the ends of the temperature range.

5.3.5. Results

For determination of liquid density each sample is successively injected for three times and the period of oscillation recorded after thermal equilibration. The temperature dependence can be well represented by a 4-parameter polynomial function with coefficients and corresponding standard deviations compiled in Table 5.3. A graphical representation is shown in Fig. 5.5 together with the experimental densities of PnP in the range of temperatures between 251 K - 408 K, see Table D.1. The standard deviation of the regression accounts for $\sigma_d = 4.6 \times 10^{-4}\,\mathrm{g\,cm^{-3}}$. For reasons of comparability, calculated densities are listed at even temperatures with the coefficients from Eq. (5.53) in Table 5.4. The advantage of the

$$\frac{d}{\mathrm{g\ cm^{-3}}} = a_0 + a_1(T - 298.15) + a_2(T - 298.15)^2 + a_3(T - 298.15)^3 \tag{5.53}$$

Table 5.3.: Values of the coefficients of the polynomial equation for density

Coeff.	a_i	$\sigma(a_i)$
a_0	0.88097	8×10^{-5}
a_1	-0.929×10^{-3}	3×10^{-6}
a_2	-3×10^{-7}	1×10^{-7}
a_3	-3×10^{-9}	1×10^{-9}

Table 5.4.: Experimental densities (d_{PnP}) of PnP at different temperatures T

T / K	d_{PnP} / g cm^3
248.15	0.92696
258.15	0.91778
268.15	0.90861
278.15	0.89943
288.15	0.89023
298.15	0.88097
308.15	0.87165
313.15	0.86695

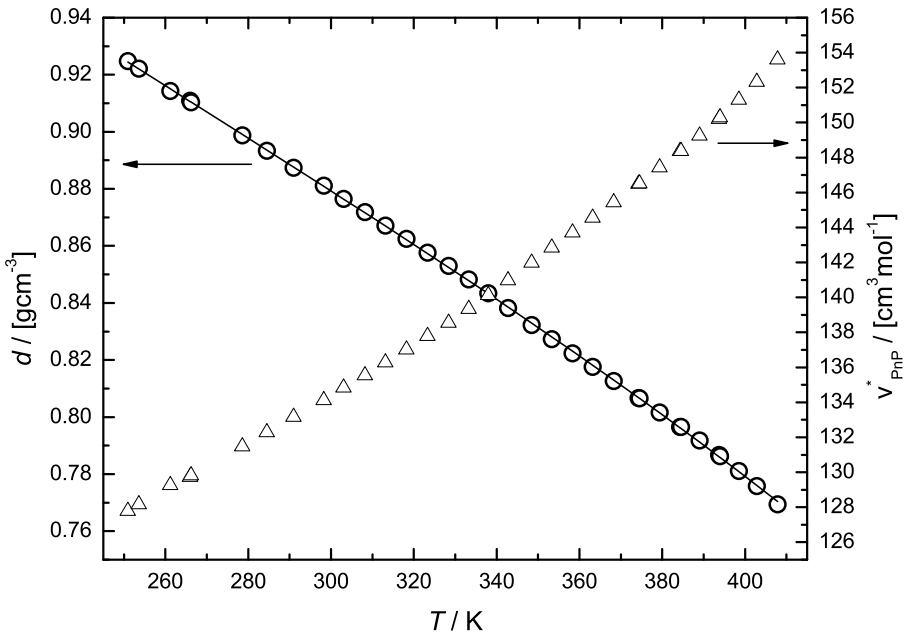

Figure 5.5.: Temperature dependency of density d of 1-propoxy-2-propanol and its molar volume ν^*_{PnP}; ($\circ$, $\triangle$) experiment, (—) from Eq. (5.53)

Table 5.5.: Comparison between literature and experimental density data of PnP at different temperatures, $\Delta d = d - d^{\mathrm{Lit}}$

T [K]	d_{PnP} [g cm^3]		$\frac{\Delta d}{d} \cdot 100$ [%]
	this work	Lit.	
298.15	0.88097	0.88128 [137]	−0.035 %
298.15	0.88097	0.8813 [138]	−0.037 %
308.15	0.87165	0.8718 [138]	−0.017 %
318.15	0.86223	0.8622 [138]	0.003 %
283.15	0.89484	0.8951 [14]	−0.029 %
293.15	0.88561	0.8860 [14]	−0.044 %
303.15	0.87632	0.8764 [14]	−0.009 %
313.15	0.86695	0.8669 [14]	0.006 %
323.15	0.85749	0.8572 [14]	0.034 %
333.15	0.84790	0.8471 [14]	0.080 %
343.15	0.83817	0.8375 [14]	0.080 %
353.15	0.82828	0.8273 [14]	0.118 %

chosen equation for representation of density data lies in its compatibility with a large database on pure solvent properties [173].
The molar volume (ν^*_{PnP}) of PnP is also displayed in the figure. It is obtained from the relation $\nu^*_{\mathrm{PnP}} = \mathrm{M}_{\mathrm{PnP}}/d^*_{\mathrm{PnP}}$ and required for the correlation of binary VLE data in section 4.5.1.

5.3.6. Comparative Study of Literature

Comparative results from the literature are known only for few temperatures at atmospheric pressure. An assessment of the agreement between the measured and published data is possible with an evaluation of densities at defined temperatures with Eq. (5.53). Table 5.5 compiles the measured densities of PnP found in literature and this work. As one might expect deviations are becoming greater at higher temperatures, probably due to the increased uncertainty in temperature. Due to the smooth curve of the measured points and the good agreement to published data, the density of 1-propoxy-2-propanol is expected to be determined with good accuracy over the temperature range of (248 − 408) K.

5.3.7. Density Coefficients of four Tetrabutylammonium Salts

The molar concentrations, c, the electrical conductivity is referring to, are obtained from the experimentally given temperature-independent molonities, $\tilde{m}$, with the help of the relationships

$$d = d_S + D\tilde{m} \tag{5.54}$$

$$c = \tilde{m}(d_S + \tilde{m}D), \tag{5.55}$$

where d, d_S are the solution's and pure solvent's densities, respectively. D is the density coefficient for a particular electrolyte solution. Its experimental determination is based on density measurements on solutions of varying concentration. For this reason the most concentrated solution in a conductance measurement (normally after the eighth concentration) of an electrolyte is withdrawn from the conductance cell under a protective atmosphere of nitrogen and injected into the densimeter. Together with the pure solvent's density and that from an electrolyte stock solution, a linear regression over three density data $d = f(\tilde{m})$ is performed for each salt system. A linear dependency of the relation between solution density and molonity can be assumed with sufficient validity for concentrations below $\tilde{m} < 10^{-2}\,\mathrm{mol\,kg^{-1}}$, but may be even used for concentrations up to $0.2\,\mathrm{mol\,kg^{-1}}$, accepting errors in D of $\pm 20\,\%$ [174, 175]. All values for the density coefficients are those as obtained from data regression at 25 °C. Their temperature-dependence is neglected, an assumption justified by Roch [172], who determined constant values for D over a temperature-range of 50 K. Eq. (5.54) can be regarded as a truncated series development with D being a correction factor, the error of which does not have significant influence on the accuracy of the concentration values [164].
The results are shown in Fig. 5.6 with values for the density coefficient of each salt system listed in Table 5.6.

Table 5.6.: Density coefficients D as slope of the function $d = f(\tilde{m})$

System	Bu_4NBr	Bu_4NNO_3	Bu_4NOAc	Bu_4NSCN
$D\,[\mathrm{kg^2\,m^{-3}\,mol^{-1}}]$	54	33	21	21

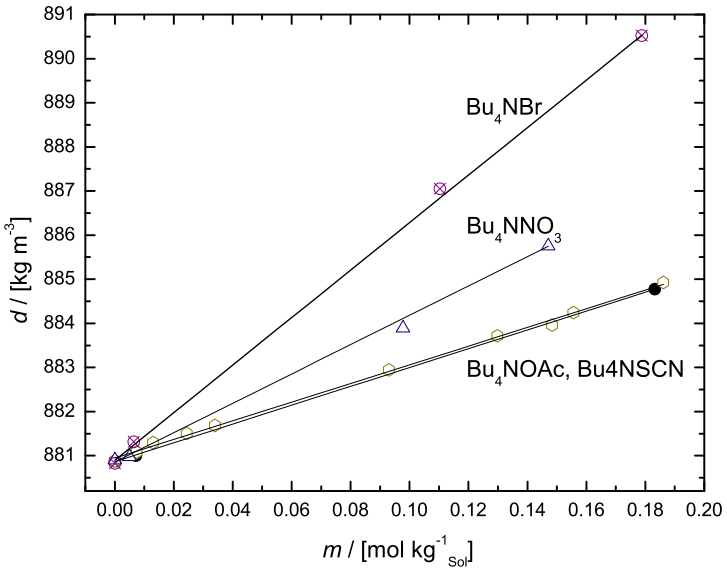

Figure 5.6.: Solution densities of tetrabutylammonium salts in PnP

5.4. Relative Permittivity

As a supplement to measurements of density (section 5.3) and of viscosity (section Sec. 5.5) the evaluation of experimental conductivity data requires also temperature-dependent data on the static dielectric constant, ϵ, of 1-propoxy-2-propanol in the temperature-range between (248,15 and 313.15) K.

5.4.1. Experimental Set-up

Temperature-dependent permittivity measurements on PnP are executed with a low-frequency (1 - 15) kHz capacitance bridge (General Radio, model 1616) in conjunction with a conductance-balancing network and a three-terminal dielectric cell designed for high-precision measurements as shown in Fig. 5.7. The electrical capacitor was developed in our institute several years ago [176]. It consists of two coaxial cylindrical electrodes, which are composed of chromium nickel steel. The resistance to chemically aggressive substances of the electrodes surface is enhanced by a coating with a thin layer of gold. Homogeneity of the electric field between both electrodes is accomplished by an additional shielding with the help of a grounded guardring. It is isolated from the inner electrode by a very thin mica washer (100 μm thickness). The outer electrode is connected to the *high*-potential, the inner electrode to the *low*-potential port of the capacitance bridge by means of double-shielded coax cables. The volume of the cell amounts to approximately 50 mL.
The assembly lid allows for easy immersion in the main thermostat (see section 5.2). The same specifications with respect to temperature stability and accuracy can be stated as described there.
Capacity measurements are performed at different frequencies ($C = f(\nu)$) and extrapolated to $1/\nu \rightarrow 0$, obtaining the static dielectric constant (relative permittivity) ϵ after calibration. This has its reason in the equivalent circuit diagram of the filled capacitor and the condition of equal impedance of measuring cell and capacitance bridge [177]. The capacitance bridge can be operated for capacitances between 0.1 aF and 10 μF and is based on the principle of a transformer bridge [178]. Therefore at each frequency both the capacity as well as the conductivity of the sample must be balanced. Gaseous samples are recommended to be analyzed with a maximum voltage of 5 V in the range of $(0.5 - 1)$ kHz, whilst liquids allow only up to 1.5 V in the frequency range of $(2 - 10)$ kHz [177]. The comparable large conductance, even of highly purified solvents compared to gases, results in a higher current at a given voltage, which might damage the cell. The proper settings of operation allow for the measurement of capacities with a precision of better than 0.01 % [179], regardless of the type of sample.

5.4.2. Measuring Method

5.4.2.1. General Procedure

The configurational set-up for preparation of the cell prior to measurement and the filling procedure is very similar to that discussed in the case of density measurement (section 5.3.3). Preparation includes the proper, bubble-free filling of the capacitor, its cleaning and drying after each series of measurements. Because of its use as calibration standard, purified Argon serves as protective atmosphere in permittivity recording as well. Due to the unfeasible monitoring of the cell's content, special care has to be taken in the degassing and subsequent filling of the capacitor in order to avoid any gas bubbles. A specially designed glass vessel, keeping the PnP under a steady atmosphere of inert gas, allows for the connection to the vacuum pump for degassing and is used to carry the solvent over to the measuring cell (see Fig. 2.1). According to the procedure described above, the liquid sample is filled in with the aid of the filling tube from the bottom of the capacitor. Argon is supplied to press the degassed solvent slowly into the cell, completely displacing the atmosphere therein. The volume change of the liquid during the temperature program has to be accounted for, in order to establish a constant pressure and to avoid any damage to the cell. Therefore the outlet pipe is connected to a vessel containing enough solvent after the filling to balance the volume expansions or contraction.
Temperature equilibration may take a long time due to the missing device for stirring. Especially at low temperatures and moreover with gaseous samples, a stable instrument reading was obtained not before

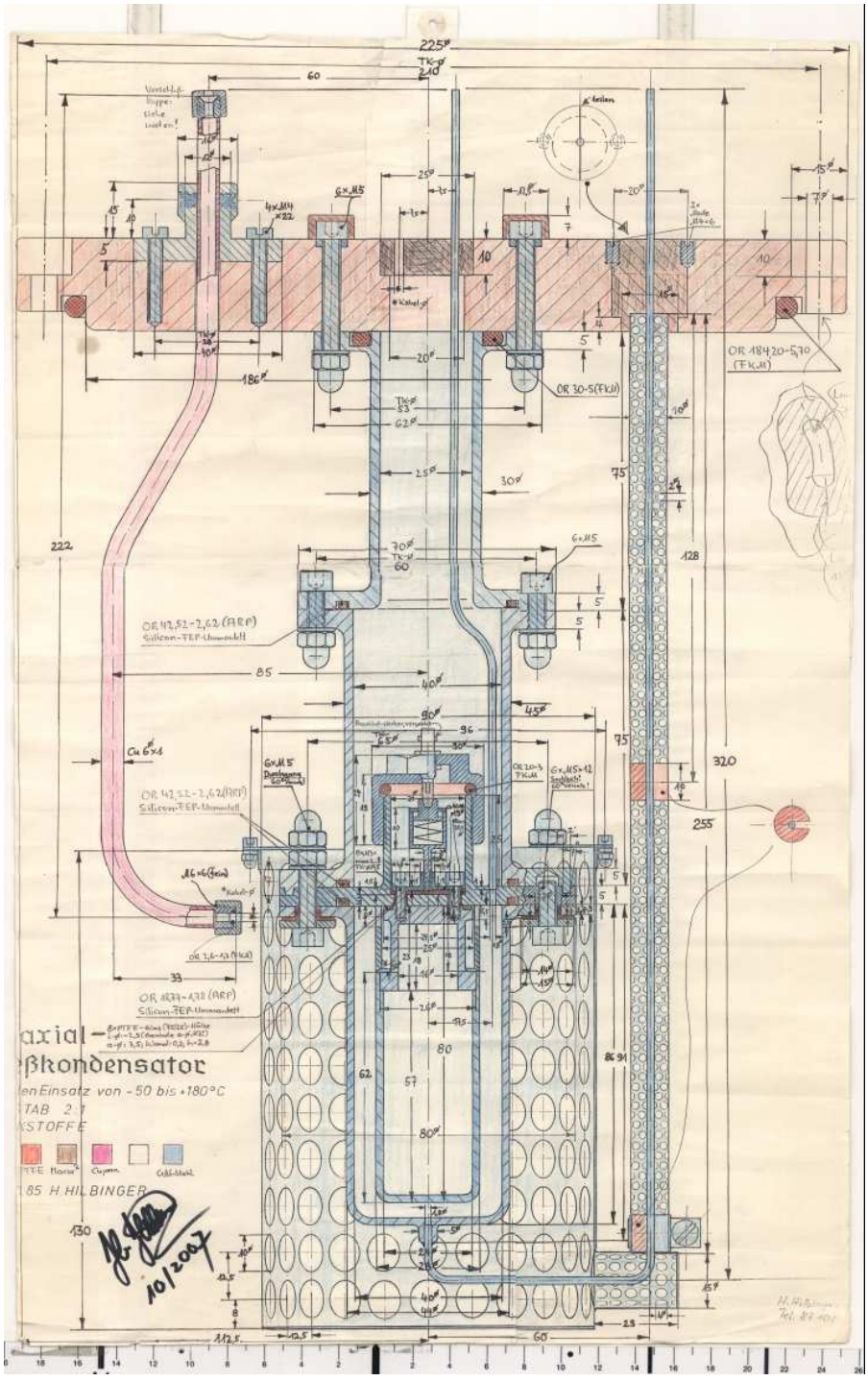

Figure 5.7.: Detailed engineering drawing of capacitance measuring unit [kindly supported by H. Hilbinger]

2 h.
The experimental setup has to be modified when argon is used in the calibration procedure. The sample flask is replaced by an inlet for the purified argon, which is piped through the cell for 24 h prior to calibration measurements. The capacitor is equilibrated at each temperature under excess pressure of argon, which is released to atmospheric pressure before measurement starts. The atmospheric pressure is read from an in-house barometer.

5.4.2.2. Calibration and Evaluation

The determination of the relative permittivity, ϵ_S, of a sample requires the knowledge of the cell's capacitance under vacuum, C_0, as a function of temperature. Within the International System of Units (SI) the dielectric constant of vacuum is equal to unity.

$$\epsilon_S = \frac{C_S(T,p)}{C_0(T)} = \frac{C_S(T,p)\epsilon_{Ar}(T,p)}{C_{Ar}(T,p)} \tag{5.56}$$

This general equation is valid for any sample. A direct measurement of C_0 is not possible due to unexpected influences on the capacitor itself. Therefore a calibration consists of a precise experimental determination of the capacitance of the cell filled with dry, pure argon, for which temperature- and pressure-dependent data are available in the literature [180]. The static dielectric constant of argon (ϵ_{Ar}) is known with high accuracy according to the *National Bureau of Standards (USA)* with $\epsilon_{Ar}(20\,°C, 1\,atm) = 1.0005172 \pm 4 \times 10^{-7}$ and follows the temperature- and pressure dependence given as

$$\frac{(\epsilon_{Ar} - 1)\left(\frac{\vartheta}{°C}, \frac{p}{atm}\right)}{(\epsilon_{Ar} - 1)\,(20\,°C, 1\,atm)} = \frac{\frac{p}{atm}}{1 + 0.003411\left(\frac{\vartheta}{°C} - 20\right)} \tag{5.57}$$

This equation is shown to be valid even at temperatures up to 150 °C [181–183]. The authors' temperature-dependent series of measurements stated an deviation of only 1 ppm. Due to the low pressure-dependence of the relative permittivity of argon, the accuracy in atmospheric pressure as provided by the barometer is sufficient.
The calibration is performed in the temperature interval between −25 °C and 40 °C before and after the measurement procedure with PnP and reference solvents and yields the desired value for ϵ_S. Within this two calibration series, no hysteresis in the values of C_0 could be observed.
The experimental results for the vacuum capacity C_0 are illustrated in the Fig. 5.8. The corresponding values can be gathered from Table 5.7. Each value is the averaged capacity of experimental determinations replicated triply. Within the given temperature-range a quadratic polynomial is chosen to represent C_0

Table 5.7.: Calibration results for capacitor filled with argon in the temperature range between −25 °C and +40 °C: experimental capacity C_{Ar}^{exp}, ${\epsilon_{Ar}}^{calc}$ according to Eq. (5.57), resulting vacuum capacity according to Eq. (5.56)

ϑ	C_{Ar}^{exp}	${\epsilon_{Ar}}^{calc}$	C_0
°C	pF		pF
+40	11.163430	1.0004962	11.157893
+35	11.162790	1.0005043	11.157164
+25	11.161185	1.0005212	11.155371
+15	11.159655	1.0005393	11.153640
+5	11.157880	1.0005586	11.151650
−5	11.156480	1.0005795	11.150019
−15	11.154510	1.0006019	11.147800
−25	11.152840	1.0006262	11.145861

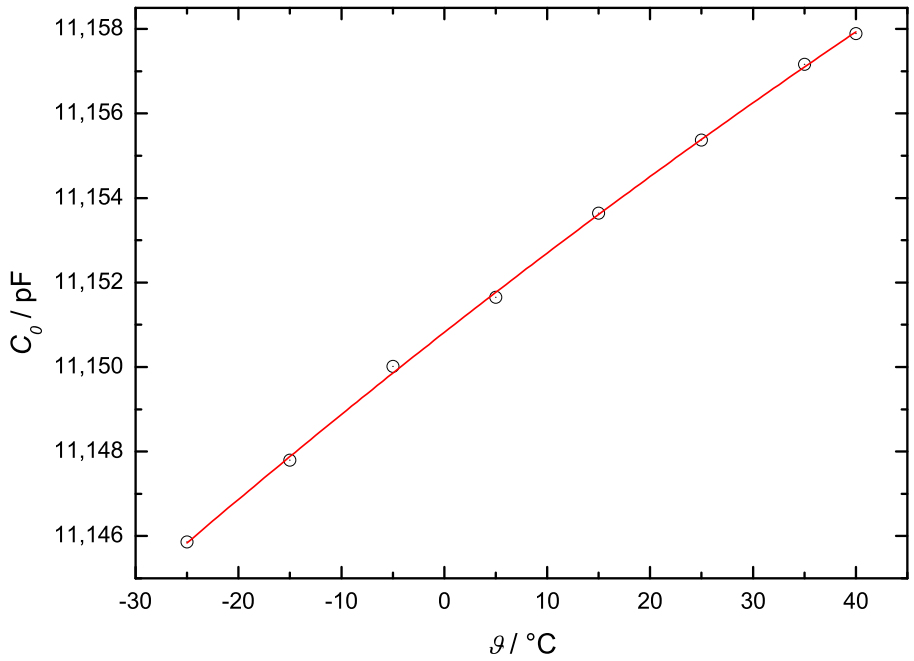

Figure 5.8.: Vacuum capacity $C_0(T)$ of the capacitor for measuring permittivity as function of temperature; ($\odot$) experiment, (—) from Eq. (5.58)

as function of temperature ϑ with the obtained coefficient from least-square procedure listed in Table 5.8.

$$\frac{C_0}{\mathrm{pF}} = a_1 + a_2\left(\frac{\vartheta}{^\circ\mathrm{C}}\right) + a_3\left(\frac{\vartheta}{^\circ\mathrm{C}}\right)^2 \tag{5.58}$$

The long-term stability of the measuring cell and the quality of the capacitance bridge can be estimated

Table 5.8.: Coefficients of least-square regression for vacuum capacity of the cell $C_0(T)$, see Eq. (5.58). The functional dependence is shown in Fig. 5.8

Coefficients	a_1	a_2	a_3
a_i	11.15082	1.91×10^{-4}	-3.3×10^{-7}
$\sigma(a_i)$	6×10^{-5}	2×10^{-6}	9×10^{-8}

from the close agreement between the actual calibration values and those from Wolf [22]. The deviations are generally smaller than $\pm 0.2\,\%$ at all temperatures.

5.4.2.3. Possible Sources of Errors

As already mentioned in section 5.4.2.1 a crucial point for reliable and reproducible measurements is to ensure a bubble-free filling of the capacitor. Otherwise very erroneous and unreasonable results would be obtained. Additional influence of dissolved gases have been reported to occur [184]. Roch has analyzed the change of ϵ upon the amount of nitrogen dissolved in acetonitrile [172]. The changes between completely degassed and acetonitrile saturated with nitrogen amount to $0.2\,\%$.
Deviations of repeated measurements under identical conditions are smaller than $0.0007\,\%$, regardless if a gaseous or liquid sample is investigated. Comparisons with well-known permittivity data on ethanol and ethylacetate [157] show an accuracy being better than $0.3\,\%$.

5.4.2.4. Results

According to Eq. (5.56) and the function for the temperature-dependent vacuum capacity (5.58), obtained from the calibration results in Table 5.7, experimentally determined capacities of liquids and gases yield the static dielectric constant ϵ.
Results for the relative permittivity of PnP are obtained from temperature-dependent measurements of the pure solvents capacity in the range of 248.15 K and 313.15 K in three independent runs. The mean values of ϵ_{PnP} at each temperature are presented in Fig. 5.9 as function of temperature and listed in Table 5.10. A suitable analytical expression for the representation of ϵ with temperature is given

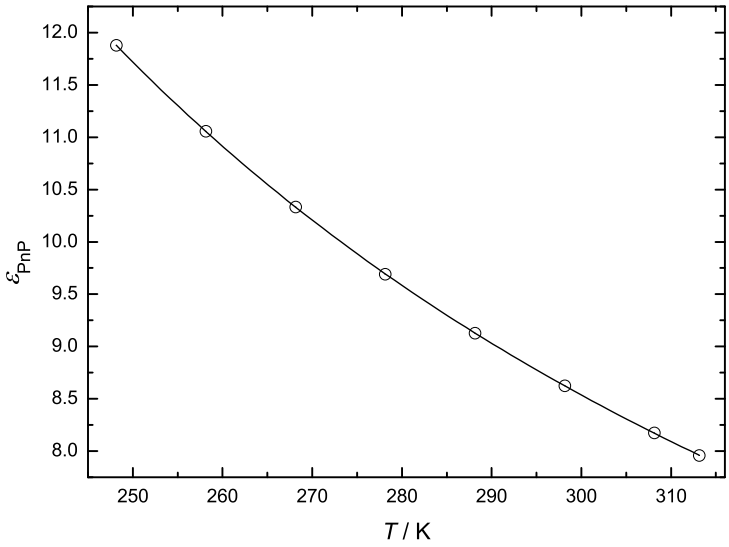

Figure 5.9.: Relative permittivity ϵ_{PnP} as function of temperature; ($\odot$) experiment, (—) from Eq. (5.59)

elsewhere [173]. The coefficient of this least-square procedure and their standard deviations are listed in Table 5.9. The standard deviation of the polynomial to the experimental data accounts for $\sigma(\epsilon_{\mathrm{PnP}}) = 2.6 \times 10^{-3}$.

$$\epsilon = \frac{a_0}{T^2} + \frac{a_1}{T} + a_2 + a_3 T \qquad (5.59)$$

Table 5.9.: Coefficients for polynomial equation (5.59)

Coeff.	a_i	$\sigma(a_i)$
a_0	$1.215\,81 \times 10^6$	2×10^5
a_1	$-5.391\,96 \times 10^3$	2.5×10^3
a_2	18.0014	9
a_3	$-0.016\,671\,6$	0.01

Table 5.10.: ${\epsilon_{\mathrm{PnP}}}^{\mathrm{exp}}$ as a function of temperature

T / K	ϵ_{PnP}
248.15	11.879
258.15	11.056
268.15	10.333
278.15	9.6913
288.15	9.1279
298.15	8.6235
308.15	8.1734
313.15	7.9580

5.5. Viscosity Measurements

The viscosity of a solution is an important factor influencing the ion's mobility. Thus it will have a great impact on the conductivity behavior of electrolyte solutions. The precise determination of both, the kinematic as well as dynamic viscosity of PnP at different temperatures is supplementary to the measurements on the solvent's density (Sec. 5.3) and relative permittivity (Sec. 5.4).

5.5.1. Principle of Measurement

Viscosity data obtained in this work are based on the measurements with a capillary Ubbelohde viscometer [185, 186] (Schott). It is the most exact method for determining the viscosity of liquids with newtonian flow behavior. As shown in Fig. 5.10 the viscometer basically consists of three tubes:

1. capillary tube (1) consists of a pre-run sphere (9), the measuring sphere (8), the capillary (7), which ends in the upper part of the reference level vessel (5)
2. venting tube (2), attached shortly underneath the dome-shaped top part (6)
3. filling tube (3), which ends in the reservoir (4) with filling marks indicating the filling capacity of approximately 18 mL (limited to a very narrow range of volume for a proper operation of the viscometer)

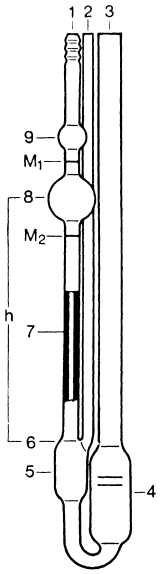

1	Capillary tube
2	Venting tube
3	Filling tube
4	Reservoir
5	Reference level vessel
6	Dome-shaped top part
7	Capillary
8	Measuring sphere
9	Pre-run sphere
M1	Upper timing mark
M2	Lower timing mark

Figure 5.10.: Ubbelohde Viscometer

Above and below the measuring sphere (8) are printed on timing marks M_1 and M_2. These marks not only define the flow-through volume of the sample, but also the mean hydrostatic head.
Applying vacuum to capillary tube with simultaneously closing the venting tube will cause the successive filling of the reference level vessel, the capillary tube, the measuring tube, and the pre-run sphere. Now suction is discontinued and the venting tube opened again. This causes the liquid column to separate at the lower end of the capillary and to form the suspended level at the dome-shaped top part. Under this geometrical conditions no corrections regarding the surface tension have to be applied [187]. What is measured is the time interval (flow time t) it takes the leading edge of the meniscus of the sample to descend from the upper edge of the upper timing mark M_1 to the upper edge of the lower timing mark M_2 (corresponding to the measuring levels N_1 and N_2 in case of opto-electronic detection).
The viscometer is called *suspended level* because the liquid initially drawn into the small upper bulb is not connected to the reservoir as it flows down the capillary during measurement. The capillary is suspended above the reservoir. In conjunction with the pressure-equalization tube (2), this ensures that

the only pressure difference between the top of the bulb and the bottom of the capillary is that due to he hydrostatic pressure, i.e. the weight of the liquid.
Inside the capillary viscometer, the velocity drop required for viscosity measurements is built up in the form of a laminar tube flow within the measurement capillary. The *Hagen-Poiseuille Law* is the physical basis of viscometers working according to the capillary principle [188, 189]

$$\frac{V}{t} = \frac{\pi R^4 \Delta p}{8 L \eta} \tag{5.60}$$

Here, V is the quantity of fluid flowing through the capillary for a given time t, R is the capillary radius, Δp is the pressure difference between the two ends of the capillary, η is the fluid viscosity, and L is the capillary length.
The driving force is the hydrostatic pressure of the liquid column in the form of the mean pressure height h_m. Considering that the volume flow $\dot{V}$ is recorded via the measurement of the flow time t, the following equation results for kinematic viscosity ν

$$\nu = \frac{\eta}{d} = \frac{\pi R^4 g h_m}{8 L V} \cdot t \qquad \text{with} \quad \Delta p = \rho g h_m \tag{5.61}$$

For a given viscometer the constants in Eq. (5.61) can be summarized into one characteristic constant K

$$\nu = K \cdot t \tag{5.62}$$

When applying the flow model in the form of the Hagen-Poiseuille Law, additional pressure losses occurring at the capillary ends are not taken into account. Owing to the finite capillary length, however, the pressure losses occurring at the in- and outflow affect measurement accuracy. As a consequence the measured flow time t_g is greater than the time t resulting from Hagen-Poiseuille Law. The difference between theoretical and measured flow time is accounted for by the Hagenbach-Couette (HC) correction $t_H = t_g - t$ [190, 191]. This results in the following corrected working equation for glass capillary viscometers:

$$\nu = K \cdot (t_g - t_H) \tag{5.63}$$

It can be shown that the HC-correction for a funnel-shaped capillary end is incorporated in the final working equation for the viscosity calculation in the following form [192]

$$\nu = K \cdot t - \frac{B}{t^2} \tag{5.64}$$

with B/t^2 being the kinetic energy correction. K and B are device-specific constants to be obtained from calibration measurements.

5.5.2. Instrumentation

Great care has to be taken for a vibration-free operation. Therefore viscosity measurements are performed in a remote Dewar vessel, the oil of a cryostat (model FP 40) is pumped through. The Dewar is embedded in an outer glass body, allowing for the visual inspection of the bath fluid and the capillary viscometer. The flexible tubes connecting cryostat and Dewar consists of Viton and are isolated additionally. Due to energy losses the temperature within the Dewar might differ from the set-point of the cryostat. For this reason the temperature control is effected by the same Pt-100 resistance thermometer as described in Sec. 5.2 and provides for the temperature correction in the viscosity measurements. The results will be quoted as those obtained at the temperature actually measured within the Dewar after sufficient equilibration time.
Kindler [193] described the mounting of the viscometer in the Dewar in very detailed form. The engineering detail drawings and procedures there also account for the assembly of capillary tube in order to adjust it in a perfectly vertical manner.
Experiments are run with an automated viscosity-measuring instruments by *SCHOTT-Geräte*. Subjec-

tive measuring errors are eliminated, and the efflux times measured appear as a 6-digit displayed result. A measuring stand is required for optoelectronic sensing of the meniscus with the help of a LED, glass fiber cables and a receiver. When the sample liquid meniscus passes through the measuring levels, a measuring signal is produced in each case, providing for an exact determination of the flow-time.

5.5.3. Measuring Unit

The viscosity measuring unit AVS 361 automatically carries out measurements of the flow-through times in the capillary viscometer. It accepts the input parameters controlling the speed of pump, the number of measurements and the the extra period of time to allow for an extended filling above the upper measuring level. Before the actual measurement, the sample liquid is drawn up in the capillary viscometer passing the two measurement levels N_1 and N_2. The vacuum pump, the venting process and the flow-time detection is controlled automatically by the AVS. The program execution sequence ensures that the hanging sphere level has formed in the Ubbelohde viscometer before the measurement is started. In this respect, all pneumatic operation tubes are connected to one main glass container (1), ensuring an atmosphere of inert atmosphere throughout all measurements in the whole apparatus (see Fig. 5.11). The timing range extends up to 9999.99 s with 0.01 s resolution. The results of up to 10 measurements

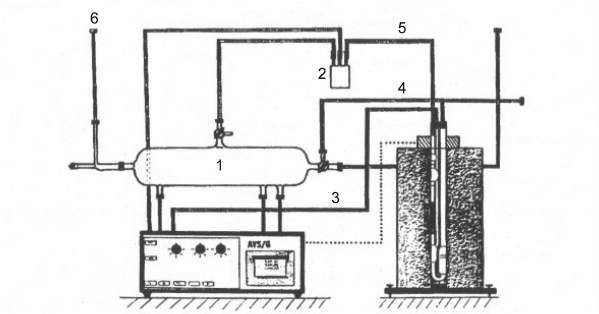

1 inert gas reservoir
2 containment
3 connection to venting tube
4 connection to filling tube
5 connection to capillary tube

Figure 5.11.: Automatically controlled viscosity equipment

in one sequence can be stored in the memory of the unit for further evaluation.

5.5.4. Measurement Procedure

In order to obtain a reproducibility of flow-times of 0.01 %, the required minimal period of time is about 100 s, if the stated resolution of 0.01 s is valid. Before any measurement is being started the viscometer is thoroughly washed with water and acetone, which are sucked off with metal syringes to avoid contamination with dust particles. The dry glass body is filled with sample liquid with the help of a gas-tight syringe, equipped with a syringe filter (0.2 μm) so as to have the particle-free liquid between the two filling marks. Prior to the measurement sequence, the liquid is repeatedly pumped up and it flows through the viscometer as it would during a measurement to achieve quick temperature equilibration (for at least 5 times). A maximum of 10 successively measurements at each temperature on the same sample filling have been performed and are done triply under the same conditions with a fresh aliquot of solvent. The effect of solvent degassing was investigated by Roch [172]. Degassed water shows an decreasing flow-time, approaching a stable value after 10 min. The final flow-time is identical to a sample of freshly prepared water without degassing. Due to the measurement procedure with an intensive contact of the solvent with the inert gas atmosphere, degassing is unreasonable.

5.5.5. Calibration

For the determination of flow-through time periods of both water and PnP a type I capillary viscometer is employed. To get the values of K and B, water is used to calibrate the instrument at two temperatures: (293.15 and 298.15) K. At both temperatures the requirements for the flow-time are fulfilled with $t_{20\,^\circ\mathrm{C}} =$

92.53 s and $t_{25\,^\circ\mathrm{C}} = 103.76\,s$. The kinematic viscosities for the reference fluid water are taken from the literature [194, 61] with values of

$$\nu_{20\,^\circ\mathrm{C}} = (1.0038 \pm 0.0025)\,\mathrm{cSt} \qquad \nu_{25\,^\circ\mathrm{C}} = (0.8929 \pm 0.0022)\,\mathrm{cSt} \tag{5.65}$$

Repeated calibration runs confirm a reproducibility of $t_{20\,^\circ\mathrm{C}}$ and $t_{25\,^\circ\mathrm{C}}$ being better than 0.1 %. With respect to Eq. (5.64) the following two relations for the instrument constants are

$$K = \frac{\nu_{25} \cdot t_{25}^2 - \nu_{20} \cdot t_{20}^2}{t_{25}^3 - t_{20}^3} \tag{5.66}$$

$$B = K \cdot t_{20}^3 - \nu_{20} t_{20}^2 \tag{5.67}$$

Obtained values for the constants and the radius of the capillary are listed in Table 5.11, together with the uncertainties. These arise from a error estimation as described in the next section. Calibration

Table 5.11.: Constants for capillary viscometer according to Eqs. (5.66)(5.67)

K	B	d
$10^{-3}\,\frac{\mathrm{cSt}}{s}$	$\mathrm{cSt\,s^2}$	mm
9.7 ± 0.2	66 ± 255	0.63

is performed before and after the measurement series with PnP, showing no significant changes of the constants. The temperature-dependence of K and B is within the uncertainty of themselves and can be neglected therefore [195].

5.5.5.1. Possible Sources of Errors

First off all small capillary diameters are prone to any particles or small solid contaminations, which would disturb the newtonian flow and result in unreasonable and un-reproducible flow-times. Care has to be taken when cleaning and filling the cell in order to avoid those issues.
The error of the calibration constants K and B mainly result from the uncertainty of the viscosity reference data for water, deviation from perpendicular mounting, the temperature fluctuations and temperature offsets inside the Dewar. Influences due to oscillation in temperature can be well eliminated by the long measurement cycle with 10 repeated measurements at each temperature. Effects of dissolved gasses have already been mentioned (Sec. 5.5.4).
An error propagation considering all sources of uncertainties with respect to Eq. (5.64) yields

$$\mathrm{d}\,\nu = \left(K + \frac{2B}{t^3}\right)\,\mathrm{d}\,t + t\,\mathrm{d}K - \frac{1}{t^2}\,\mathrm{d}B \tag{5.68}$$

From experiment follows: $\mathrm{d}\,t = 0.08$ (averaged deviations amongst all measurement sequences), $\mathrm{d}K = 2 \times 10^{-4}$, $\mathrm{d}B = 255$. As a result the measured viscosity data is stated to have an uncertainty of a few percent, mainly due to the errors in the reference data of water and they are quoted together with the results in the next section.

5.5.5.2. Results

According to Eq. (5.64) and with the constants K and B from calibration measurements, one can obtain values for the kinematic viscosities of 1-propoxy-2-propanol ($[\nu] = \mathrm{cm^2}/s = 1\,\mathrm{St}$). For that purpose, three consecutive runs with 10 recorded flow-times each are measured in the temperature-range between (253 and 313) K.

Data are translated to dynamic viscosities with the help of the temperature-dependent density (Sec. 5.3.5)

$$\frac{\eta}{\mathrm{Pa\,s}} = \frac{d}{\mathrm{g\,cm^{-3}}} \cdot \frac{\nu}{\mathrm{St}} \cdot 10^{-1} \tag{5.69}$$

Attention should be paid to the different units commonly in use for the dynamic viscosity η:

$$1\,\mathrm{P} = \frac{\mathrm{g}}{\mathrm{cm\,s}} = 0.1\,\frac{\mathrm{kg}}{\mathrm{m\,s}} = 0.1\,\mathrm{Pa\,s} \tag{5.70}$$

The temperature dependence of dynamic viscosities is well represented with a polynomial of third order, the coefficients and corresponding standard deviations of which are compiled in Table 5.12. A graphical

$$\ln\left(\frac{\eta}{\mathrm{Pa\,s}}\right) = \frac{a_0}{T^2} + \frac{a_1}{T} + a_2 + a_3 T \tag{5.71}$$

Table 5.12.: Values of the coefficients for the polynomial equation

Coeff.	a_i	$\sigma(a_i)$
a_0	2.8×10^6	5×10^5
a_1	-2.3×10^4	5×10^3
a_2	64	19
a_3	−0.08	0.02

Table 5.13.: Calculated viscosities (η_{PnP}) of PnP at the designated temperatures T

T	η_{PnP}
K	10^{-3} Pa s
248.15	22.06
258.15	11.99
268.15	7.21
278.15	4.69
288.15	3.26
298.15	2.38
303.15	2.06
308.15	1.81
313.15	1.59

representation is shown in Fig. 5.12 together with the experimental viscosities of PnP in the range of temperatures between 253 K - 313 K, see Table D.2. The standard deviation of the regression accounts for

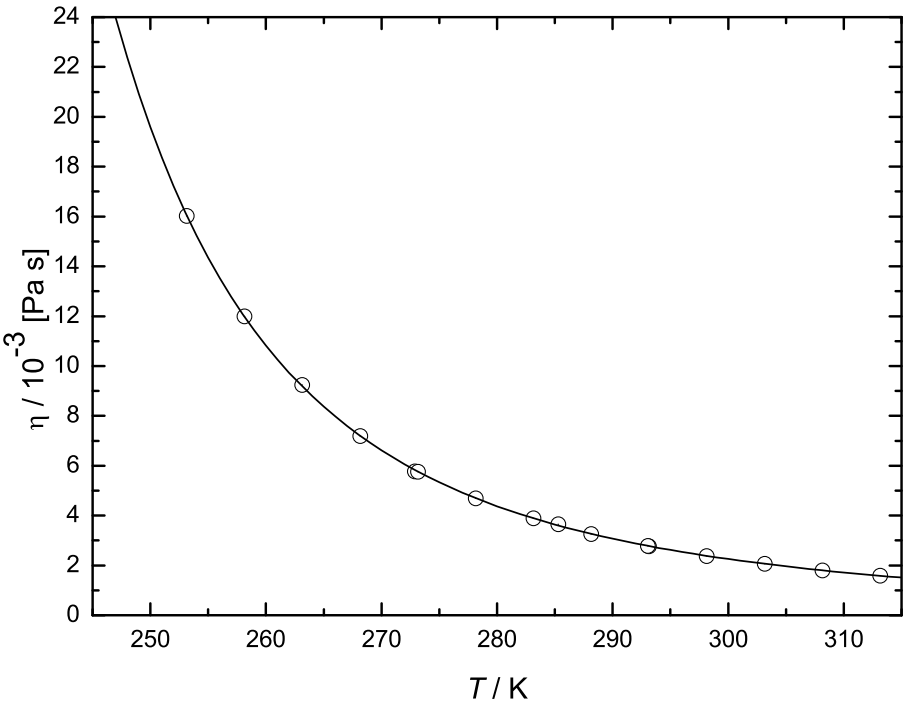

Figure 5.12.: Dynamic viscosity η_{PnP} as function of temperature; (⊙) experiment, (—) from Eq. (5.71)

$\sigma_\eta = 5.6 \times 10^{-3}$ Pa s. For reasons of comparability, calculated viscosities are listed at even temperatures with the coefficients from Eq. (5.71) in Table 5.13.

5.5.6. Comparative Study of Literature

Comparative results from the literature are known only for few temperatures at atmospheric pressure. An assessment of the agreement between the measured and published data is possible with an evaluation of dynamic viscosities at defined temperatures with Eq. (5.71). Table 5.14 compiles the measured viscosities of PnP found in literature and this work. When compared with the published data available so far, the

Table 5.14.: Comparison between experimental and literature viscosity data of PnP at different temperatures, $\Delta d = d - d^{\mathrm{Lit}}$

T [K]	η_{PnP} [10^{-3} Pa s]		$\frac{\Delta\eta}{\eta} \cdot 100$ [%]
	this work	Lit.	
298.15	2.38	2.389 [138]	−0.26 %
308.15	1.82	1.822 [138]	−1.1 %
318.15	1.42	1.416 [138]	−1.1 %
298.15	2.38	2.396 [137]	−0.5 %

experimental data from this work are lower with deviations of 1 % and less. Due to the few literature data and the inherent error ranges in viscosity measurement, statements on possible systematic errors would be risky. Besides that a significant influence of the involved equations on the results are also discussed by Weber et. al. [196] and may explain the systematic deviations. Literature data are quoted as result of calculations with the kinetic energy correction in the form B/t in Eq. (5.64). Approved uncertainties of few percent in viscosity measurements, however, permit the conclusion of good agreement of this work data with published viscosities of PnP at different temperatures.

5.6. Conductance of Dilute Electrolyte Solutions

Within the next few sections a compilation of the basic experimental principles of electrical conductivity, a description of the measuring cells which are in use and a description of the main measuring principle is given. The measuring procedures with sample preparation as well as the analysis of the frequency-dependent solution's resistance follows. Fundamental for the evaluation of any experimental conductivity data is the precise knowledge of the cell's constant.
The requirements for precise measurement of electric conductivity may be summed up as

- accurate temperature control
- avoidance of polarization at the electrodes
- accuracy in the electrical measurements themselves

The use of alternating current, as the standard method for general applications in electric conductivity, enormously complicates the electrical technique required for high-accuracy measurements, owing to the need for compensation of capacitive, and inductive effects in the circuit. In this respect one should note the definition of the complex impedance

$$Z = R + \mathrm{i}X = |Z|\, e^{i\phi}, \tag{5.72}$$

as the a. c. analogue of resistance R, which is a quantity dependent on the frequency of the alternating current. Two impedances are equal, if they are of equal amplitude R and exactly in phase ϕ.

5.6.1. Three-electrode Measuring Cell

Electrical conductivity of dilute solutions are measured with a specially designed cell, explained in very detail by Wolf [22]. It is a three-electrode cell, with an arrangement of three compartments of different cell constants, C connected to the same mixing chamber as depicted in Fig. 5.13. The outer electrodes E_1 and E_3 are connected and thus restrict the electric field to the interior of the measuring system [165]. The Fig. 5.14 shows the three different geometrical arrangements of the electrodes, with three different cell constants C_i. The object of the measurements is to determine the pure ohmic resistance R_S of the solution between the electrodes, e.g. to eliminate electrical impedances at the phase interface between solution and electrode and to obtain ideally polarized electrodes. Polarization errors are usually minimized by the use of audio frequency alternating current for the measurements and by employing platinum electrodes covered with a colloidal deposit of "platinum black", a system initiated by Kohlrausch [197]. As a result those electrodes have an extremely large surface area to facilitate the adsorption of the tiny quantities of electrode reaction products produced so that no measurable emf is produced. This chemical deposition will also lead to a fortunately reduced frequency-dependence of the electrolyte's resistance (see Sec. 5.6.2), but will not alter significantly the cell constant [198]. In practice, however, there are several other sources of impedance which cause appreciable frequency dependence. Some of these can already be avoided by proper design (e.g. spacing the cell leads well away from parts of the cell containing solution as in the designs shown in Fig. 5.14). The use of water as a thermostat liquid is avoided, owing to undesirable capacity effects across the cell walls in a. c. measurements, but a synthetic oil with a low dielectric constant $\epsilon = 2 - 3$ is used instead (see Sec. 5.2). Additional measures to reduce further parasitic couplings to a tolerable degree are taken by careful shielding and arrangement of parts [165].
A ratio of cell constants being 1 : 13 : 243 allows for a wide variability of temperatures and concentrations to be measured with high precision in this arrangement. Measurements in the region of optimal resistance values can be performed under all experimental conditions in this work. Periodic control of the cell constants by measuring their ratio of resistance is possible, therefore.
The minimal filling volume of the cell is about 300 mL to ensure optimal mixing in all three compartments through the upper joints of each single electrodes arrangement. An additional volume in the experimental program of 40 mL is admissible with the whole solution still being tempered inside the thermostat.
An electric stirrer mounted on the bottom of the whole unit propels the magnetic stir bar inside the cell for proper mixing of the solution. This will also ensure a good thermal equilibration and a fast homogenous adjustment of concentration.
A specially designed adapter at the top of the cell (Fig. 5.13 [199]) enables the introduction of pure solvent or small amounts of electrolyte stock solution, and sampling of electrolyte solution under a steady atmosphere of nitrogen. The adding of solvent into the cell is accomplished by a PTFE tube directly attached to the solvent vessel (c.f. Fig. 2.1). The Young-stopcock is removed during the filling. Aliquots of the stock solutions are added with the help of a 10 mL gastight Hamilton syringe being equipped with a long steel needle.
To avoid condensation of the solvent at those upper parts of the cell not being tempered by the bath fluid, an infrared lamp is used to heat this part of the cell for system temperatures above ambient.

5.6.2. Alternating Current Conductance Bridge

The design and construction of high-precision conductance bridges was studied intensively by Jones [200, 201] and Shedlovsky [202] and the principles they laid down are the basis of this work's cell designs, with novel improvements enabling a resolution of 10^{-6} with the apparatus used in this work [165, 164].
In order to obtain the impedance of an electrolyte solution, the measuring cell is one part of a symmetrical Wheatstone bridge with a Wagner ground [203]. The object of Wagner's ground is to ensure that at balance the potentials at C and D are not merely equal but are actually earth-potential so that pick-up of hum and stray noise by the detector is minimized. Its implementation in the present apparatus is explained elsewhere [165]. In a symmetrical Wheatstone bridge as illustrated in Fig. 5.15, both impedances Z_1 and Z_2 are equal, simplifying the condition for balance and increasing the sensitivity [178]. Two matched metal film resistors (Vishay) of 1 kΩ constitutes to one ratio arm. The bridge is supplied via a

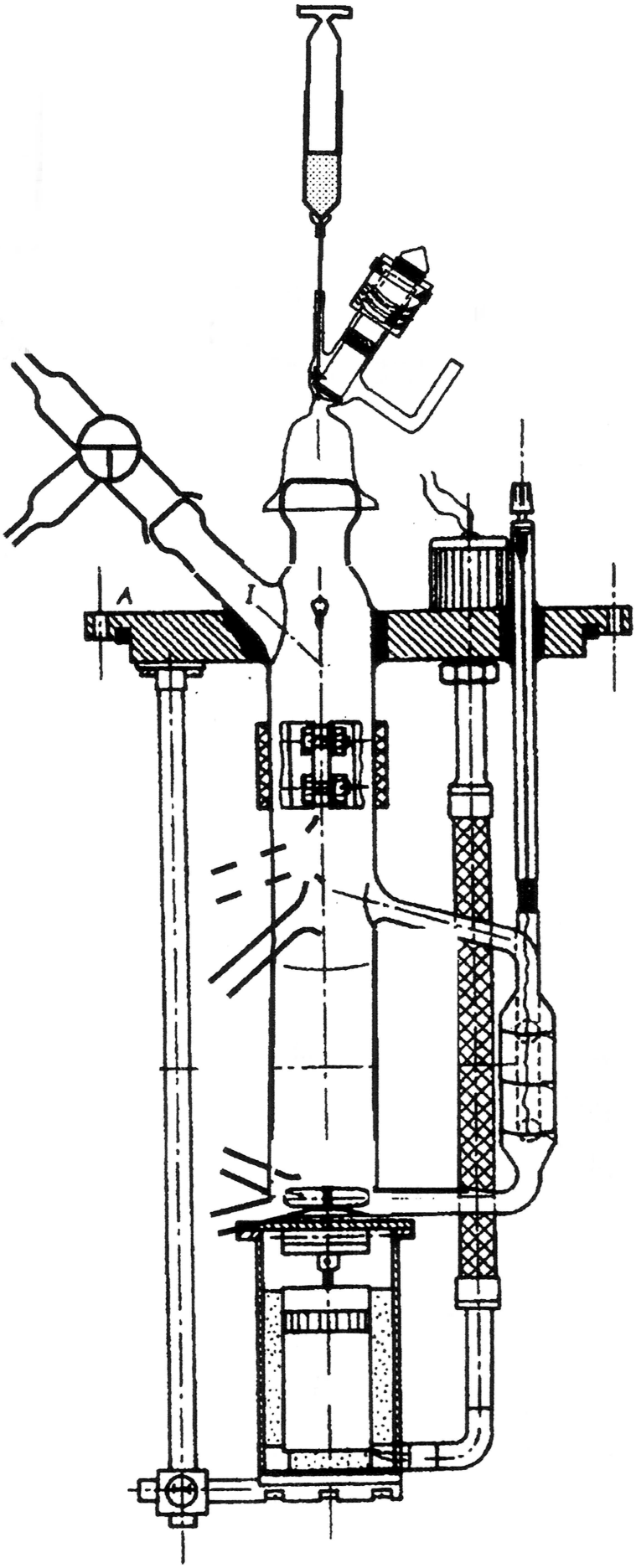

Figure 5.13.: Three-electrode measuring cell and mixing chamber with assembly lid (A) for immersion in the temperature bath (cf. Fig. 5.1); only one electrode assembly shown

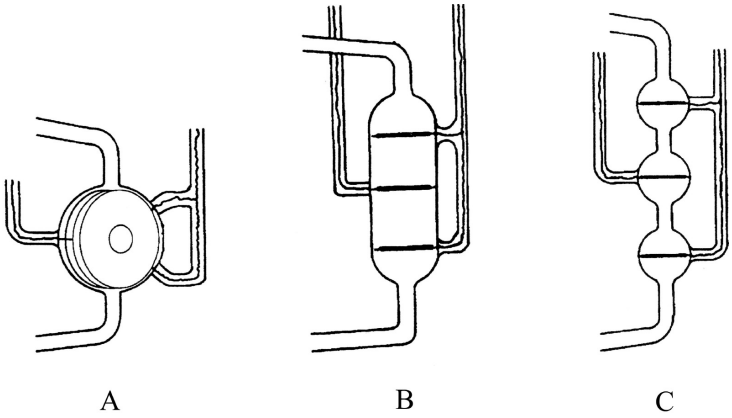

Figure 5.14.: Three-electrode cell assembly for low A, medium B, high C concentrations with cell constants of $C_1 = 0.8760\ \mathrm{m}^{-1}$, $C_2 = 11.614\ \mathrm{m}^{-1}$, $C_3 = 2.128 \times 10^2\ \mathrm{m}^{-1}$

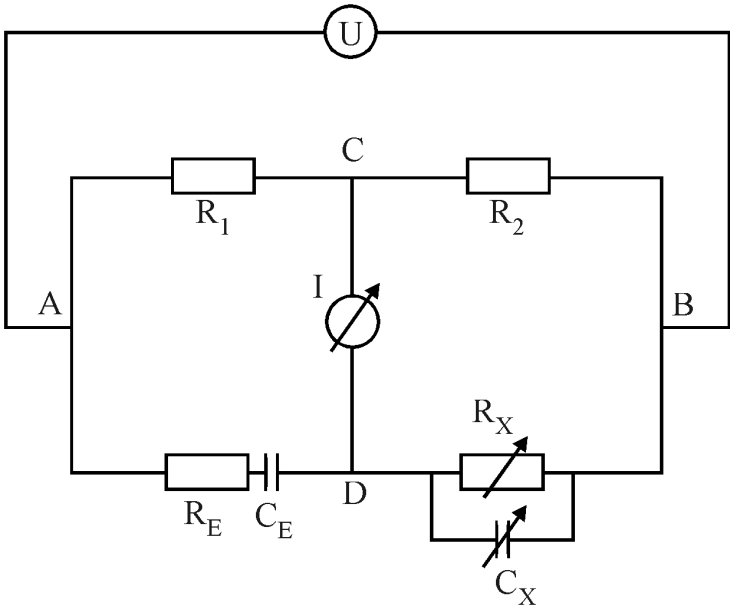

Figure 5.15.: Schematic diagram of the serial-to-parallel transformation for precise determination of the electrolyte's resistance R_E

transformer by an audiofrequency generator developed for this purpose, which can supply a distortion-free sine voltage of 100 mV, low enough to avoid chemical decomposition. The detector consists of a highly sensitive and selective null indicator I [165]. The condition for balance, i.e. no signal in the detector, is that the alternating potentials at C and D are of equal amplitude and exactly in phase, which leads to the relation

$$\frac{Z_1}{Z_E} = \frac{Z_2}{Z_X} \tag{5.73}$$

Taking into account the identity of Z_1 and Z_2 and the condition that equality of two impedances demands equality of both real and imaginary parts, it follows

$$R_E = R_X; \qquad X_E = X_X \tag{5.74}$$

A special resistance decade (1433-G, General Radio, USA), which consists of resistors of a calibration accuracy of better than 0.01 % and a very low time constant, is used.
The exact value for the solution's resistance R_E is obtained from a balanced Wheatstone bridge with known resistance R_X (amplitude) and capacity X_X (phase) of a variable impedance Z_X. In Fig. 5.15 the impedance of the measuring cell is represented by a serial connection of an ohmic resistance (depending on

the electrolyte's conductivity) and a capacitance (in case of "ideal" polarization effects on the electrode's surface). Balancing would, therefore, require the use of a variable resistance and a variable capacitance. As the double-layer capacity of an electrolyte solution is quite high, a transformation of the equivalent circuit into a parallel connection of a resistance R_X and a capacity X_X avoids the need for elaborate capacitors with high capacity. In that case the balance of the bridge is achieved even with condensers with a capacity of $\approx 100\,pF$. By means of this serial-to-parallel transformation the measured resistance becomes frequency-dependent.
According to Fig. 5.15 and Eq. (5.74) the equivalent circuit diagram is expressed in terms of the definitions of impedances for the components:

- Conductance Cell: Serial connection of R_E and C_E

$$Z_E = R_E + \frac{1}{\mathrm{i}\omega C_E} = R_E - \mathrm{i}\frac{1}{\omega C_E} \tag{5.75}$$

- Compensating impedance: Parallel connection of R_X and C_X

$$\frac{1}{Z_X} = \frac{1}{R_X} + \mathrm{i}\omega C_X = \frac{1 + \mathrm{i}\omega C_X R_X}{R_X} \Rightarrow Z_X = \frac{R_X}{1 + \mathrm{i}\omega C_X R_X} \tag{5.76}$$

Expansion of the denominator in the last equation to make it real and comparison between the real and imaginary parts of impedances Z_E and Z_X yields the following expressions for the frequency-dependent resistance of the electrolyte solution R_E:

$$R_E = R_X - \frac{1}{\omega^2 C_E^2 R_E}; \qquad \omega = 2\pi\nu \tag{5.77}$$

R_X will approach the real value for the electrolyte resistance R_E in case when either the measuring frequency ν and/or the electrodes capacity C_E are high. Possible solutions to increase the capacity by increasing the electrodes surface to a certain extent have already been mentioned, but are restricted to a thin layer deposition to avoid erroneous ion adsorption at high dilution. The usage of higher frequencies is limited because of the increased non-ideal behavior of the electronic components. Rule of thumb: as higher the resistance, as smaller the range of frequencies. Numerous investigations on the electrical conductivity performed at our institute suggest an optimal frequency range between 100 Hz and 10 kHz. In all cases of the experimental measurements $(\omega R_E C_X)^{-2} < 10^{-5}$ is achieved.

5.6.3. Measuring Principle

5.6.3.1. Experimental Procedure

The long disuse of the conductance cell describe above necessitates its thorough cleaning prior to all measurements. The procedure involves the treatment with a solution of Extran, a basic laboratory cleaning agent, before treatment with 60 °C warm *iso*-propanol/*n*-propanol mixtures over several days. Stable values of pure solvent's resistances are obtained after 2 weeks of repeated flushing with Millipore water. The preparation of the cell is completed by routinely rinsing with water, ethanol, and acetone (p.A.) ans subsequent drying under a steady flow of dry nitrogen. The nitrogen is flushed through the cell for at least 24 h by means of a long capillary reaching to the bottom of the cell.
The experimental methods for determining the concentration and temperature dependence of conductance is a stepwise concentration by successive additions of weighed samples of the electrolyte compound, starting from the pure solvent [164, 204]. This method of isologous sections, proves to be the most promising way for dilute solutions and is superior to the common procedures of stepwise dilution of a concentrated solution or the preparation of each solution by mixing the solvent and electrolyte compound by weight. The technique used is as follows: the purified solvent is introduced into the mixing chamber of the conductance cell through the inlet (I) under protective gas. In order to avoid the occurrence of gas bubbles especially at low temperatures, a short period of degassing precedes the filling and care is taken

to pour it in along the wall of the cell to decrease the uptake of nitrogen. The resistance of the solvent at different frequencies is measured at the various temperatures of the program. Afterwards the electrolyte is added for 8 times and the temperature program is repeated for each concentration. Temperatures in this study cover the range of 248.15 K and 313.15 K at 8 different values. Concentration covers the range between (10^{-4} and 10^{-2}) mol kg^{-1}. The method of isologous sections has two main advantages: the quantity of solvent required is small, but a large number of concentration steps are possible; the accuracy of measurement, which is determined by the accuracy with which the concentration of the most dilute solution is known, is higher than in a dilution method [205].
The stepwise concentration is accomplished by successively addition of weighed amounts of an electrolyte stock solution to the preceding filling of the cell by means of a gas-tight syringe [206]. Stock solutions are prepared in a glove box under an atmosphere of dry nitrogen. The salt is weighed in a specially designed flask for preparing the stock solution. A weighed amount of pure solvent is added outside the glove box to obtain the concentrated solution, which can be withdrawn easily under nitrogen with the syringe.
The electrolyte as well as the stock solution are weighed on a balance (AE240, Mettler Toledo) with four digits. Determination of the solvent mass initially introduced into the measuring cell is done by differential measurement of weight of the solvent container (Fig. 2.1) before and after addition. The same applied for the added amount of stock solution in each step of the concentration procedure. The precision of the pure solvent mass is indicated with 2 digits.
Displayed mass values m^{dis} together with the density of the balance inherent standard weights d_{stw} and that of air d_{air}, the buoyancy correction for each sample is taken into account in the exact measure of its mass m_i^{corr}:

$$m_i^{corr} = m_i^{dis} \left(\frac{1 - \frac{d_{air}}{d_{stw}}}{1 - \frac{d_{air}}{d_i}} \right) \tag{5.78}$$

The molar concentrations, c, are obtained from the experimentally given temperature-independent molonities, $\tilde{m}$, with the help of the relationships

$$c = \tilde{m}(d_S + \tilde{m}D) \tag{5.79}$$

$$\tilde{m}_n = \tilde{m}^* \cdot \frac{\sum_{i=1}^{n} g_i}{G + \sum_{i=1}^{n} g_i}, \tag{5.80}$$

where G is the weighed amount of solvent, $\tilde{m}^*$ the molonity of stock solution and g_i the mass of stock solution added to the conductance cell at each step.

5.6.3.2. Frequency Extrapolation

The transformation of the serial connection to a parallel connection of resistance and capacitance requires the mathematical consideration of the frequency dependence of the measured electrolyte resistance $R_E(\nu)$. From a physical point of view, e.g. Eq. (5.77), a indirect proportional dependence of $R_E(\nu)$ with the frequency raised to the second power is imposed. The adopted measure to reduce or eliminate parasitic impedances of the measuring apparatus allows for a commonly used linear regression function in the reciprocal frequency

$$R_E(\nu) = R_\infty + A\nu^{-1} \tag{5.81}$$

the origin of which does not lie in the described transformation, but is due to the characteristics of the "platinum black" electrodes [153]. R_∞ corresponds to the desired resistance of the electrolyte, as obtained by an extrapolation of the measured, frequency dependent $R_E(\nu)$ to infinite frequency, i.e. $\lim_{\nu^{-1}\to 0} R_\nu = R_\infty$. In any case of deviation from that linear behavior, Gores [206] suggested a substantial weighting of higher frequencies at low solution's resistance and vice versa. For that reason pure solvent conductivities are obtained as an extrapolation of low frequency data ($\nu < 500\,Hz$), whilst for the

electrolyte solutions a modified relation proposed by Hoover [207] is applied in this work

$$R_{\mathrm{E}}(\nu) = R_{\infty} + A\nu^{-B} \tag{5.82}$$

The exponent B is purely an empirical parameter to be fitted to the experimental data and is limited to the range between 0.5 and 1. Data points considered for regression should cover a frequency range of at least one order of magnitude, i.e. 1 kHz - 10 kHz. The extrapolation corrects results by 0.01 % to 0.5 %, compared to the resistance value found at the highest frequency measured. The desired accuracy in the conductivity would allow even a 20 % error in the extrapolation [204].
Several other equations are proposed in the literature, which mainly account for the influence of different exponents B on the frequency dependence [208, 209].
One additional correction accounts for the resistance of the supply lines of the cell, which was determined once with the cell short-out with mercury [172] and constitutes about 25 Ω. This resistance value is substracted from each single measured electrolyte's resistance R_{∞} to yield R_S, the solution's resistance.

5.6.3.3. Molar Conductivities Λ

Resistance values for each concentration and temperature are transformed into values for the specific conductivity κ with the help of the cell constant C in a first step

$$\kappa_i = \left(\frac{1}{R_{S,i}} - \frac{1}{R^*}\right) \cdot C \tag{5.83}$$

with R^* being the resistance of pure solvent as determined in the separate temperature cycle and used for solvent correction. Eq. (5.83) explicitly implies the additivity of the specific conductances of both solution and pure solvent. Both R^* and R_S are extrapolated values corrected for the resistance of the supply line. Barthel [156] pointed to that assumption of being not unproblematic.
The molar conductivity Λ is defined as

$$\frac{\Lambda_i}{\mathrm{S\,cm^2\,mol^{-1}}} = \frac{\kappa_i\,[\mathrm{S\,m^{-1}}]}{c_i\,[\mathrm{mol\,dm^{-3}}]} \cdot 10 \tag{5.84}$$

with the molar concentration c_i. Calculations of electric conductance require the knowledge of the cell's constant C, which is obtained in a separate cylce.

5.6.3.4. Cell Calibration

The cell constant may be regarded as a geometric characteristic of the cell. A direct determination, however, according to $C = l/A$ (l: distance between the electrodes; A: electrodes' surfaces) is only achieved approximately and not applicable for precision measurements. Calibrations are therefore performed by application of proper equations, reproducing in an exact manner the concentration dependence of the molar conductivity. For that reason, all results in this work are based on calibrations with aqueous solutions of potassium chloride at different concentrations [210].
The conductance cell used throughout this work for dilute solutions consists of an arrangement of three different electrode assemblies, i.e. three different cell constants (see Fig. 5.14). For the reason of calibration, aqueous solutions of potassium chloride are surveyed at 298.15 K. Experimental data with high precision of the molar conductance of aqueous KCl solutions at (273.15, 283.15, 291.15, 298.15) K within concentrations of $10^{-4} < c < 5 \times 10^{-2}\,\mathrm{mol\,L^{-1}}$ are taken from the literature [210]. For each temperature a conductance equation is available in the form

$$\Lambda_{cal} = \Lambda_{\infty} - S\sqrt{c} + Ec\log c + J_1 c - J_2\sqrt{c^3} \tag{5.85}$$

and the corresponding coefficients listed in Table 5.15 at 298.15 K. Combination of Eq. (5.83) and (5.84)

Table 5.15.: Coefficients of Eq. (5.85) for aqueous potassium chloride solutions

T [K]	Λ_∞	S	E	J_1	J_2
25	149.873	95.01	38.48	183.1	176.4

displays the mathematical connection between C and Λ_{cal}:

$$C = \Lambda_{cal} c_i \left(\frac{1}{R_{cal}} - \frac{1}{R^*} \right)^{-1} \tag{5.86}$$

The conductance cell is calibrated in three independent measurement cycles at 10 different concentrations each. All three runs are performed with a newly prepared KCl stock solution. For this purpose, the measurement at a single concentration include the experimental procedure at 298.15 K, as described above. All results necessarily have to be corrected for the pure water conductivity. In that connection the following tabulated values are due to the calibration process and list the cell constants for each electrode assembly as mean value of 3·10 single measurements. The specific conductivity of the electrolyte solutions

Table 5.16.: Cell constants C at 298.15 K

Cell i	C_i / m^{-1}	ΔC_i / m^{-1}
1	0.876	0.003
2	11.61	0.01
3	212.80	0.02

being investigated in this work does not make it necessary to evaluate $R_\mathrm{E}(\nu)$ by cell 3.
In consideration of the wide experimental temperature range, one has to take into account the variation of the cell constants with T. In principle the temperature-dependence can be expressed by the formula [153]

$$C(T) = C_{298} \left[1 + \frac{1}{C_{298}} \left(\frac{\mathrm{d}C}{\mathrm{d}T} \right)_{298} (T - 298.15) \right] \tag{5.87}$$

On the basis of the geometric definition of the cell constants, $C = l/A$, the relation

$$\frac{\mathrm{d}C}{\mathrm{d}T} = \frac{\mathrm{d}C}{\mathrm{d}l}\frac{\mathrm{d}l}{\mathrm{d}T} + \frac{\mathrm{d}C}{\mathrm{d}A}\frac{\mathrm{d}A}{\mathrm{d}T} = \frac{1}{A}\frac{\mathrm{d}l}{\mathrm{d}T} - \frac{l}{A^2}\frac{\mathrm{d}A}{\mathrm{d}T} \rightarrow \frac{1}{C}\frac{\mathrm{d}C}{\mathrm{d}T} = \frac{1}{l}\frac{\mathrm{d}l}{\mathrm{d}T} - \frac{1}{A}\frac{\mathrm{d}A}{\mathrm{d}T} \tag{5.88}$$

is obtained. For the measuring cell of the type shown in Fig. 5.14 (A,B), A is determined approximately form the circular electrode's surface ($A = r^2\pi$). Therefore, $1/A \cdot \mathrm{d}A/\mathrm{d}T = 2/r \cdot \mathrm{d}r/\mathrm{d}T = 2\alpha_\mathrm{Pt}$, where $\alpha_\mathrm{Pt} = 9 \times 10^{-6}\,\mathrm{K}^{-1}$ is the linear expansion coefficient of platinum [24]. Expansion upon temperature change of the glass is accounted for by $\alpha_\mathrm{Py} = 1/l \cdot \mathrm{d}l/\mathrm{d}T = 3.5 \times 10^{-6}\,\mathrm{K}^{-1}$. Finally an approximated value can be deduced, which allows to describe the temperature-dependence of the cell constant C:

$$\frac{1}{C}\frac{\mathrm{d}C}{\mathrm{d}T} = -15 \times 10^{-6}\,\mathrm{K}^{-1} \tag{5.89}$$

Starting from the cell constant determined at 298.15 K, changes of C within the temperature program are evaluated and collected in Table 5.17. Despite the fact that also cell constants were determined at two further temperatures (273.15 K and 283.15 K), no significant change within the range of $\Delta T = 25\,K$ could be found unambiguously. The very little effect upon temperature change is rather within the limits of errors (see Table 5.16). Numerous works performed in our institute with similar cells suggested a close similarity between calculated and experimentally determined temperature coefficients [176, 210] and permit its usage within the accuracy achieved in this work.

Table 5.17.: Cell constants C at different temperatures calculated according to Eq. (5.87)

T	C_1	C_2	C_3
K	m^{-1}	m^{-1}	m^{-1}
248.15	0.8767	11.619	212.960
258.15	0.8765	11.617	212.928
268.15	0.8764	11.615	212.896
278.15	0.8763	11.613	212.864
288.15	0.8761	11.612	212.832
298.15	0.8760	11.610	212.800
308.15	0.8759	11.609	212.784
313.15	0.8759	11.608	212.768

5.6.4. Results

The present work reports the results of precise electrical conductance measurements of dilute electrolytic solutions of Bu_4NBr, Bu_4NNO_3, Bu_4NOAc and Bu_4NSCN in 1-propoxy-2-propanol. Temperatures are varied between (248.15 and 313.15) K and data are obtained at $8 - 9$ different concentrations for each salt. To our knowledge no comparable data on conductivity for electrolyte systems in PnP exist in the literature at all.

In the following graphical representations, the molar conductivity Λ as a function of the square-root of concentration $\sqrt{c}$ is shown, the raw data of which are listed in Sec. E.1. Values for the different results of the evaluation for each electrolyte are compiled in Tables 5.18-5.21 according to the theoretical model analysis explained in Sec. 5.6.5. The figures and tables contain all data of one electrolyte at 8 different temperatures. Density coefficients required for the concentration conversion are experimentally determined for all systems (see Sec. 5.3.7) and used for the concentration conversion there.

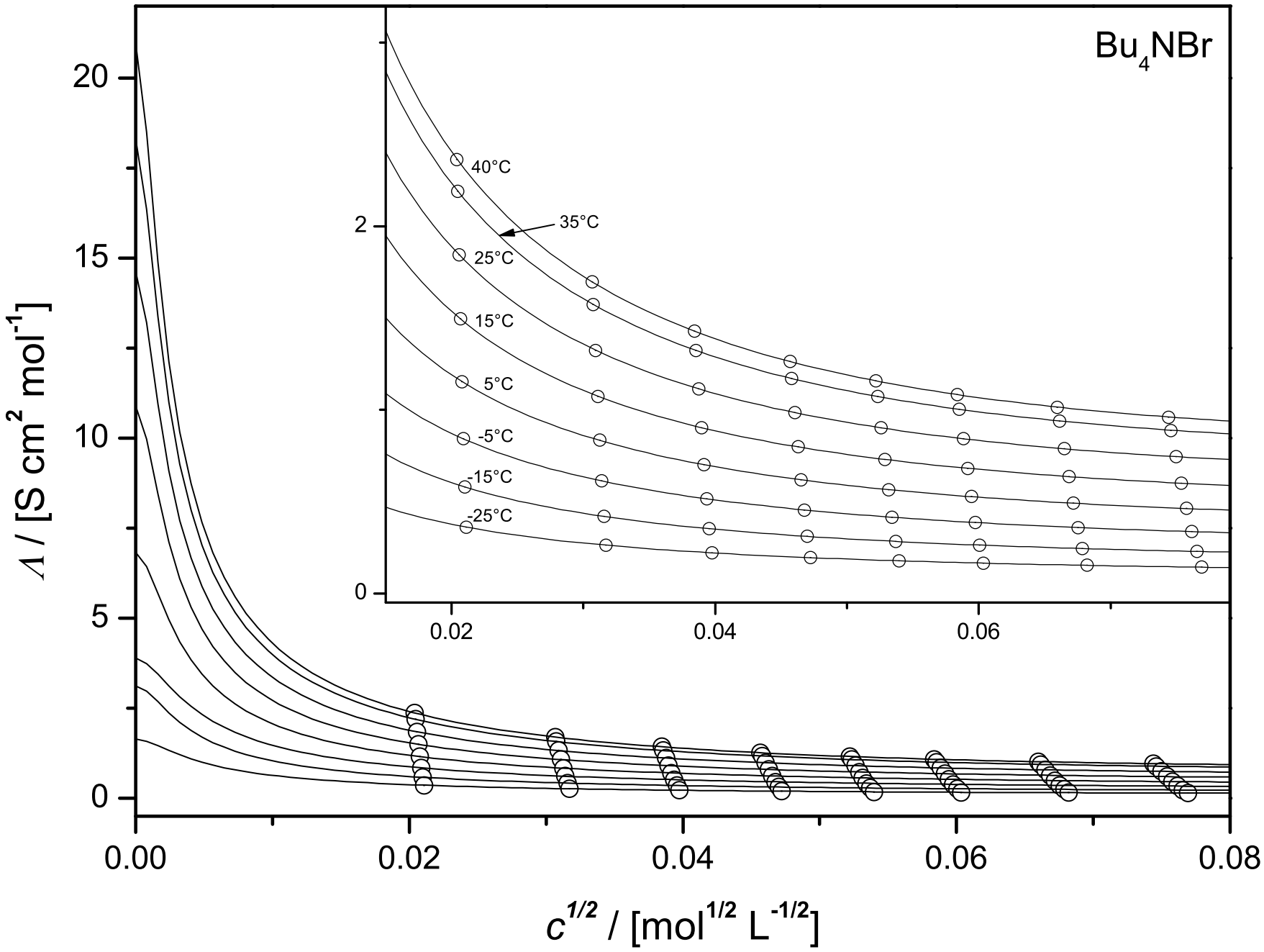

Figure 5.16.: Molar Conductivity $\Lambda(\sqrt{c}, T)$ of Bu_4NBr in 1-propoxy-2-propanol

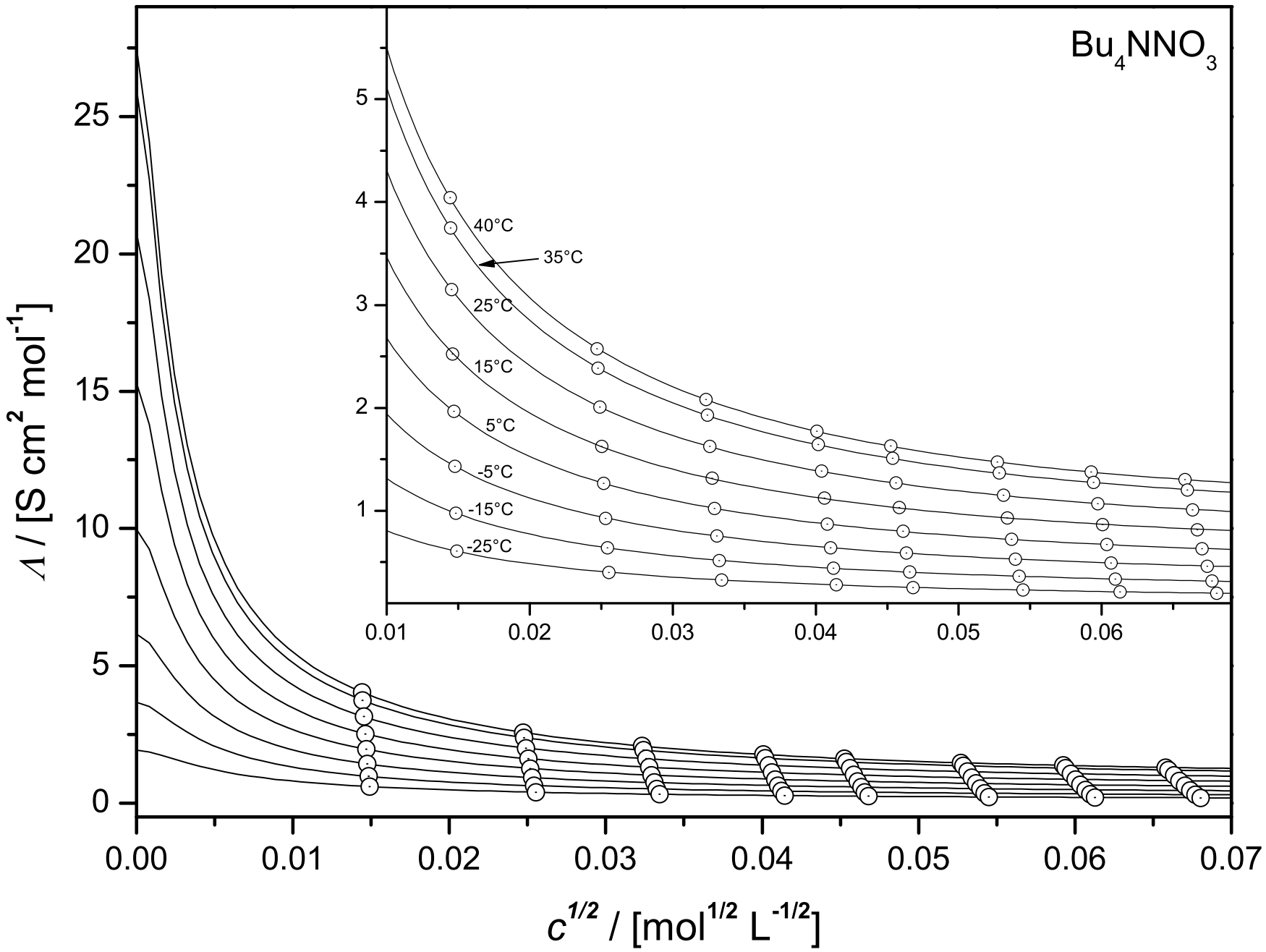

Figure 5.17.: Molar Conductivity $\Lambda(\sqrt{c}, T)$ of Bu_4NNO_3 in 1-propoxy-2-propanol

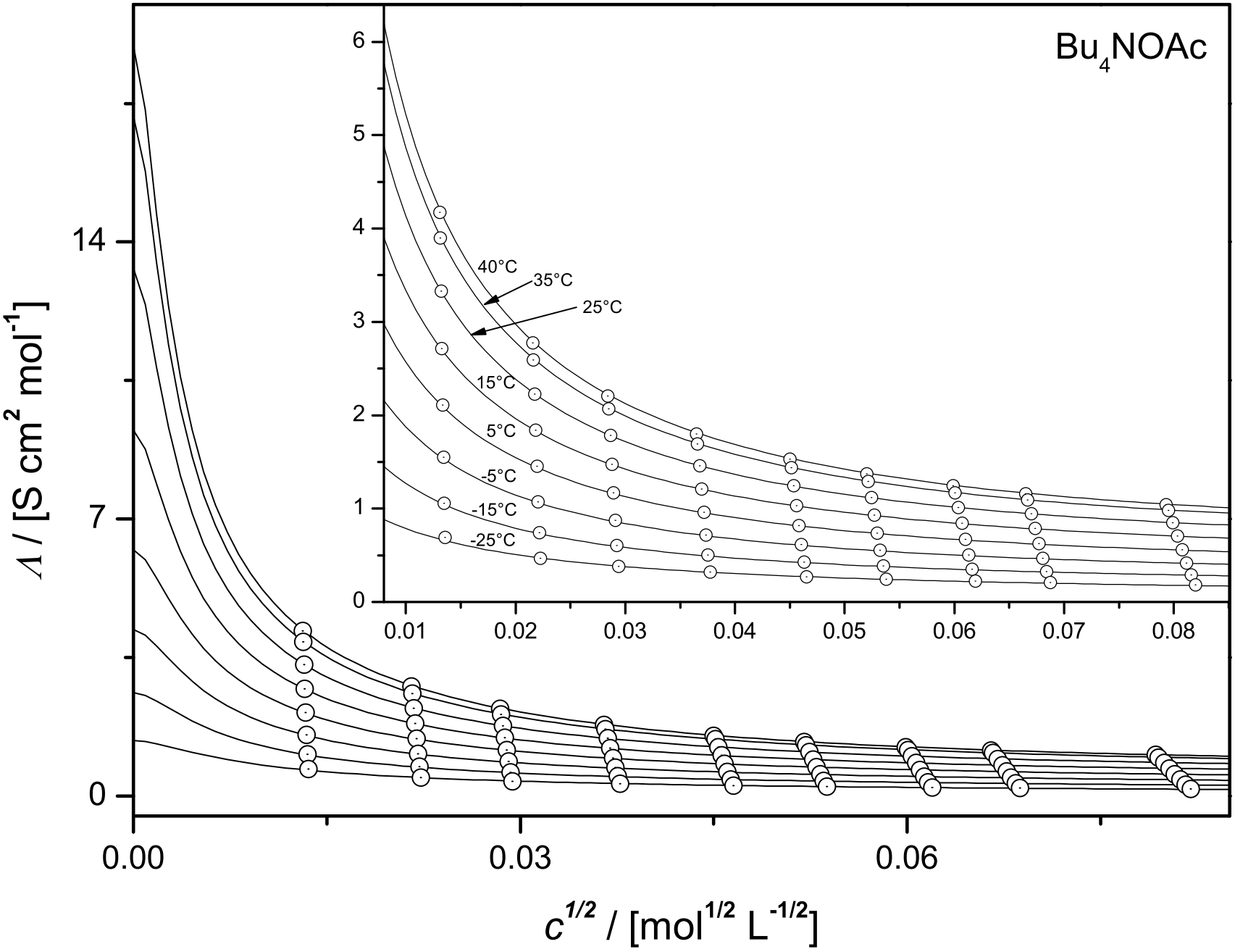

Figure 5.18.: Molar Conductivity $\Lambda(\sqrt{c}, T)$ of Bu_4NOAc in 1-propoxy-2-propanol

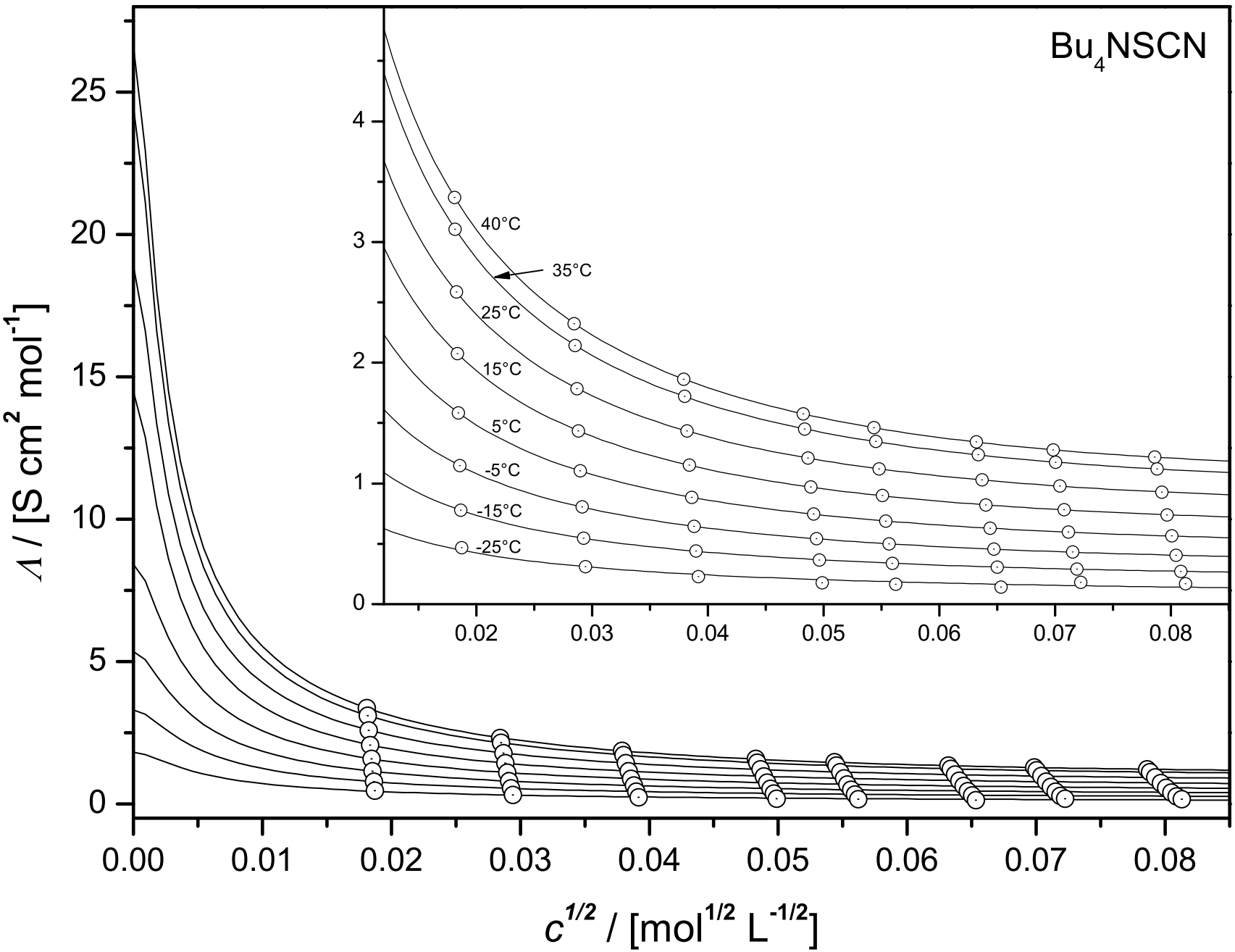

Figure 5.19.: Molar Conductivity $\Lambda(\sqrt{c}, T)$ of Bu_4NSCN in 1-propoxy-2-propanol

Table 5.18.: Results of FJ3-analysis of dilute conductivity measurements of Bu_4NBr in PnP

$R = 14.20\,\text{Å}$	T [K]							
	248.15	258.15	268.15	278.15	288.15	298.15	308.15	313.15
Λ^∞ $\left[\text{S cm}^2\,\text{mol}^{-1}\right]$	1.64 ±0.06	3.13 ±0.20	3.89 ±0.14	6.83 ±0.19	10.89 ±0.66	14.63 ±0.53	18.31 ±0.23	20.98 ±0.47
K_A $\left[10^4\,\text{L mol}^{-1}\right]$	4.74 ±0.41	4.20 ±1.10	5.01 ±0.38	8.92 ±0.45	14.27 ±1.49	17.33 ±1.33	19.59 ±0.63	22.40 ±0.96
J_1 $\left[\text{S cm}^2\,\text{L mol}^{-2}\right]$	134	274	367	699	1291	1789	2197	2511
σ	0.000	0.001	0.001	0.001	0.001	0.001	0.002	0.002
$100\,\kappa q$	26-56	25-55	29-64	27-59	24-53	25-54	26-57	26-58
ΔG_A^* $\left[\text{J mol}^{-1}\right]$	−6313	−6956	−5995	−7095	−8035	−8361	−7848	−8036
$\Lambda^\infty \cdot \eta$	3.6	3.7	2.9	3.2	3.6	3.5	3.3	3.3

Table 5.19.: Results of FJ3-analysis of dilute conductivity measurements of Bu_4NNO_3 in PnP

$R = 14.44\,\text{Å}$	T [K]							
	248.15	258.15	268.15	278.15	288.15	298.15	308.15	313.15
Λ^∞ $\left[\text{S cm}^2\,\text{mol}^{-1}\right]$	1.93 ±0.04	3.67 ±0.08	6.17 ±0.16	9.98 ±0.17	15.30 ±0.20	20.77 ±0.84	26.00 ±0.88	27.49 ±0.79
K_A $\left[10^4\,\text{L mol}^{-1}\right]$	3.88 ±0.16	5.91 ±0.24	8.21 ±0.61	12.10 ±0.65	18.07 ±0.08	22.09 ±1.91	24.91 ±1.79	25.18 ±1.50
J_1 $\left[\text{S cm}^2\,\text{L mol}^{-2}\right]$	165	342	628	1078	1449	2674	3537	3925
σ	0.001	0.001	0.002	0.001	0.005	0.003	0.002	0.004
$100\,\kappa q$	22-55	21-53	21-52	20-50	21-53	19-47	19-47	19-49
ΔG_A^* $\left[\text{J mol}^{-1}\right]$	−6163	−6867	−7420	−8151	−8094	−9374	−9595	−9440
$\Lambda^\infty \cdot \eta$	4.3	4.4	4.4	4.7	5.0	4.9	4.7	4.4

Table 5.20.: Results of FJ3-analysis of dilute conductivity measurements of Bu_4NOAc in PnP

$R = 13.81$ Å	T [K]							
	248.15[a]	258.15	268.15	278.15	288.15	298.15	308.15	313.15
Λ^∞ $\left[\mathrm{S\,cm^2\,mol^{-1}}\right]$	1.70	2.62 ±0.01	4.19 ±0.04	6.27 ±0.08	9.26 ±0.05	13.33 ±0.23	17.00 ±0.32	18.76 ±0.20
K_A $\left[10^4\,\mathrm{L\,mol^{-1}}\right]$	2.41 ±0.28	2.37 ±0.03	3.07 ±0.08	3.96 ±0.13	5.69 ±0.07	8.45 ±0.34	10.41 ±0.45	11.20 ±0.27
J_1 $\left[\mathrm{S\,cm^2\,L\,mol^{-2}}\right]$	110	234	410	654	1053	1642	2245	2547
σ	0.007	0.001	0.001	0.002	0.001	0.003	0.003	0.002
$100\,\kappa q$	25-81	24-74	24-74	24-75	23-72	23-68	22-67	22-68
ΔG_A^* $\left[\mathrm{J\,mol^{-1}}\right]$	−6829	−5443	−5817	−6211	−6908	−7741	−8161	−8287
$\Lambda^\infty \cdot \eta$	3.7	3.1	3.0	2.9	3.0	3.2	3.1	3.0

Table 5.21.: Results of FJ3-analysis of dilute conductivity measurements of Bu_4NSCN in PnP

$R = 15.61$ Å	T [K]							
	248.15[a]	258.15	268.15	278.15	288.15	298.15	308.15	313.15
Λ^∞ $\left[\mathrm{S\,cm^2\,mol^{-1}}\right]$	1.81	3.30 ±0.08	5.36 ±0.25	8.42 ±0.13	14.48 ±0.60	18.90 ±0.72	24.49 ±0.76	26.62 ±0.94
K_A $\left[10^4\,\mathrm{L\,mol^{-1}}\right]$	4.50 ±0.53	5.13 ±0.30	6.49 ±0.70	8.87 ±0.31	16.31 ±0.14	18.24 ±1.48	21.75 ±1.41	21.97 ±1.68
J_1 $\left[\mathrm{S\,cm^2\,L\,mol^{-2}}\right]$	152	309	536	936	1713	2488	3384	4008
σ	0.026	0.001	0.002	0.001	0.001	0.002	0.002	0.002
$100\,\kappa q$	25-59	25-61	25-62	25-60	23-55	23-55	23-55	22-55
ΔG_A^* $\left[\mathrm{J\,mol^{-1}}\right]$	−7478	−7684	−8128	−8776	−10 191	−10 469	−11 144	−11 184
$\Lambda^\infty \cdot \eta$	4.0	4.0	3.9	4.0	4.7	4.5	4.4	4.2

[a]calculations are based on a FJ2 procedure with extrapolated values of fixed Λ^∞, assuming constancy of W

5.6.5. Data Analysis

The evaluation of measured conductivity data is based on the complete conductivity equation according to Fuoss and Justice (5.90) for associating electrolytes [211], an equation for the activity coefficient (5.91) and for the association constant in the framework of the lcCM [157] model, (5.92).

$$\frac{\Lambda}{\alpha} = \Lambda^{\infty} - S(\alpha c)^{1/2} + E(\alpha c)\ln(\alpha c) + J_1(R)\alpha c - J_2(R)(\alpha c)^{3/2} \tag{5.90}$$

$$y'_{\pm} = \exp\left(-\frac{\kappa q}{1+\kappa R}\right) \tag{5.91}$$

$$K_A = \frac{1-\alpha}{\alpha^2 c_Y} \cdot \frac{y'_Y}{y'^2_{\pm}} = 4\pi N_A \exp\left(-\frac{\Delta G^*_A}{RT}\right) \int_a^R r^2 \exp\left(\frac{2q}{r}\right) \mathrm{d}r \tag{5.92}$$

$y'_{\pm}$ is the mean activity coefficient of the free ions, referred to molarity as the measure of concentration. A detailed form of the parameters in Eq. (5.90) can be found elsewhere [212]. The limiting slope S and parameter E are dependent only on pure solvent properties and the ion charge. J_1 and J_2 show additional dependence on the distance parameter R representing the distance to which oppositely charged ions can approach as freely moving particles in the solution.
Data analysis is carried out with the help of the set of equations by a least-squares method [213]. The method used, applicable to accurate conductivity data, is a three-parameter fit (FJ3 evaluation) yielding Λ^{∞}, J_2 and K_A with calculated values of S and E, and a preset distance parameter R. This distance parameter is chosen by chemical evidence, mostly as $R = a+s$, where s is the length of an oriented solvent molecule and a is the sum of the ionic radii of cation and anion. Difficulties in the proper assignment of ionic radii of tetraalkylammonium cations are dealt with in the literature. Different ways for their experimental and theoretical determination are given elsewhere [214, 153, 215, 155]. In this study the distance parameter R is fixed at $R/\mathrm{nm} = a+0.73$. The length of an orientated PnP molecule is estimated by comparison with different molecules of the same class. Data for distance parameters and ionic radii of the ions under investigations are taken from Ref. [173] and given in Table 5.22. Best values of Λ^{∞}, K_A

Table 5.22.: Ionic radii and diameter of solvent PnP

	Bu_4N^+	Br^-	NO_3^-	OAc^-	SCN^-	PnP
a_i or s [Å]	4.94	1.96	2.2	2.7	3.37	7.3

and J_2 are obtained by minimizing the standard deviation σ_Λ, which is defined as the difference between the calculated Λ_{fit} and experimental Λ_{exp} conductivity values:

$$\sigma_\Lambda = \sqrt{\sum_{j=1}^{n} \left[\Lambda_{j,\mathrm{fit}} - \Lambda_{j,\mathrm{exp}}\right]^2 / (N_p - 3)} \tag{5.93}$$

with N_p being the number of measuring points. No significant changes in σ_Λ could be observed when the values of the parameters a and R were varied from 6.5 to 7.6 Å and 4.0 to 7.3 Å, respectively in a series of least-square calculations. Thus values for a and R as given above are used.
The derived values of limiting molar conductance $\Lambda^{\infty}(\pm 1\%)$ and $K_A(\pm 8\%)$ of the investigated salts in PnP show a higher uncertainty than that commonly expected in electrical conductivity studies. Due to the large association constants in PnP the molar conductance increase rapidly at low concentrations (c.f. Fig. 5.16-5.19). This leads to uncertainties in Λ^{∞} which are admittedly larger than the corresponding values from conductivity data in usual protic or aprotic solvents [216–218]. The same holds for the accuracy of the association constant: K_A as a regression parameter defines the curvature of the molar conductivity in the range of lower concentrations together with the fixed limiting slope and the limiting molar conductance. As a result also this value is given with greater uncertainty due to the numerical

problem of regression, especially if no accurate values for Λ are known at such low concentrations of $\sqrt{c} < 0.01$, which would account for the steep increase of Λ in that region. Nevertheless, the consistent trend of K_A and Λ^∞ as function of temperature is an evidence for their reliability within the chemical model and its association hypothesis. A negative temperature coefficient for the association, as a result of misleading curve fitting of such low conductivity data [22], could not be found. The given standard deviations show excellent agreement of experimental and calculated molar conductivity.
The strong interdependence, however, between K_A and J_2 in the evaluation process (FJ3) is responsible for the strong lowering of J_2, even to negative values, as all systems exhibit strong association. This fact is expressed in negative, and therefore meaningless, values of $R(J_2)$. The later is calculated from J_2 which is obtained by the data analysis. The internal consequence when applying Eq. (5.90)-(5.92) is the so-called compatibility control [157]

$$R = R(J_1) = R(J_2) \tag{5.94}$$

not applicable for the systems investigated in this work and therefore not mentioned in the results. One way to overcome this problem is a two-parameter fitting with Λ^∞ and K_A as regression parameter. Doing so, J_2 is calculated from the solvent's properties and R. This, however, leads to erratic values for the association constant and much higher standard deviations.
Consequently, the numerical difficulties in the representation of low conductivity data with the resulting values of both the association and the limiting conductivity being regular, allows for the assumption of J_2 being purely a regression parameter, which accounts for the proper description of the experimental data. As this parameter emphasizes the upper, reliably measured concentrations ($J_2 \sim c^{3/2}$), this is even more evident.
Data of the systems Bu_4NOAc and Bu_4NSCN at the lowest temperature show either unreasonable values for K_A and Λ^∞ or lead to a non-converging least-square fit with 3 parameters being adjustable. Therefore the Walden product of each salt system provides us with the possibility to calculate the limiting molar conductivity at $-25\,°C$ in a (FJ2) procedure, leaving only K_A and J_2 as adjustable parameters. Despite the higher errors in the regression (see Table 5.20-5.21), reasonable values for the association constants within the expected range are obtained. Reasons for the lower quality of data may lie in the possible occurrence of gas bubbles, which are present most likely at low temperatures. Although all electrolyte solutions are obtained with the pure solvent being degassed prior to the filling of the cell, the presence of inert nitrogen leads to a continuous saturation of the solution with gas over the time of measuring. Data analysis with resistance values obtained solely from the cell 2 does not improve the situation. The idea behind that is to avoid adhesive bubbles on horizontal electrode plates as is the case with cell 1.
All results of conductivity measurements at low concentrations are collected in Tables 5.18-5.21 as obtained from the FJ3-evaluation, unless otherwise stated. They specify the association constant K_A and limiting molar conductivity Λ^∞ with the corresponding errors. Besides that parameter J_1, standard deviation σ_Λ, the non-coulombic contribution to the association process ΔG_A^*, and the Walden product $\Lambda^\infty\eta$ are tabulated. Parameter κq is a measure of the relation between Bjerrum's distance q and the radius of the ionic cloud κ within the model of Debye and Hückel. A value $(\kappa q)_{max} < 1$ is recommended for evaluating data according to the Chemical Model [219, 164]. This condition is clearly fulfilled in all cases.

5.6.6. Discussion

5.6.6.1. Limiting Molar Conductivity

Tables 5.18-5.21 shows the limiting electrolyte conductances obtained from the data in Table E.1 with the help of the described evaluation process. As expected within the framework of electrolyte theory, the Λ^∞ values of four salts in PnP are not very sensitive to the choice of the distance parameter R (agreement within less than 1 % for the range of R given in Sec. 5.6.5). Furthermore, Λ^∞ values increase monotonically with the increase in temperature due to the increase of the mobility of the free ions, as can be seen in Fig. 5.20. The values of Λ^∞ vary almost inversely with the viscosity of the solvent medium and the Walden product $\Lambda^\infty\eta$ is nearly constant and independent of the temperature within the limits of error. The results indicate that the mobility of the "free" ions is completely controlled by the bulk

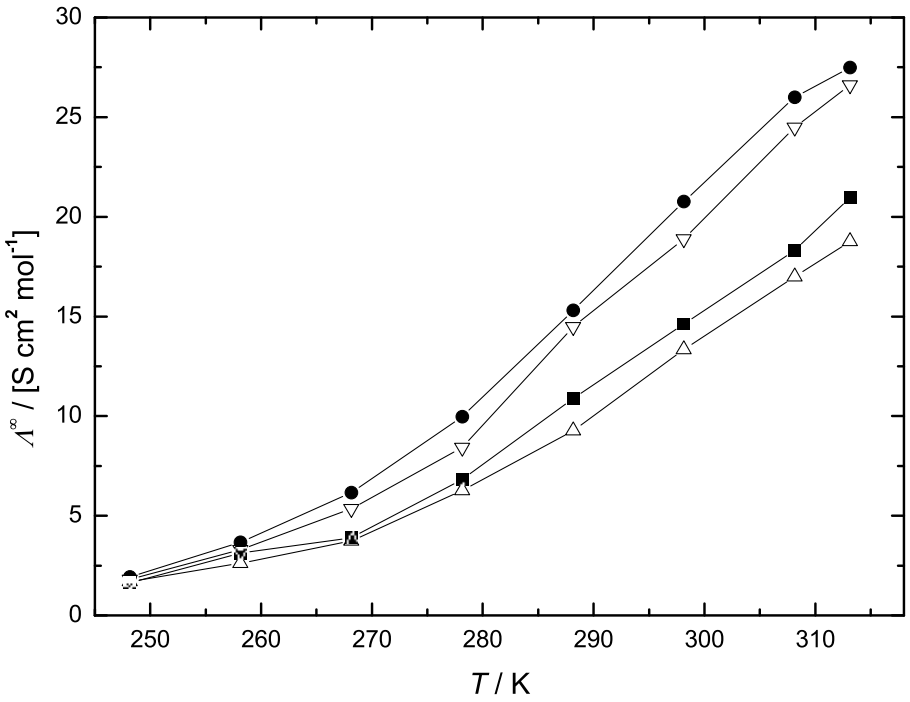

Figure 5.20.: Plot of the limiting molar conductivities Λ^{∞} vs. temperature for Bu_4NNO_3 (●), Bu_4NSCN (▽), Bu_4NBr (■) and Bu_4NOAc (△) in the temperature range from 248.15 to 313.15 K

viscosity.
The limiting conductivity can be interpreted as a quantity free of ion-ion interactions, which describes the mechanism of ionic migration in the solvent. Thus it permits statements on ion-solvent interactions. The temperature dependence of Λ^{∞} can be approximated in the framework of the kinetic theory of conductance [220, 221] by the equation

$$\ln\Lambda^{\infty} + \frac{2}{3}\ln d = -\frac{\Delta H^{\ddagger}}{RT} + B \tag{5.95}$$

which connects the enthalpy of activation of the charge transport $\Delta H^{\ddagger}$ to the limiting conductance Λ^{∞} and the solvent density d. B is the integration constant. Values for $\Delta H^{\ddagger}$ from the slope of the function at the left-hand side of Eq. (5.95) versus the inverse temperature are tabulated in Table 5.23. Within

Table 5.23.: Enthalpy of activation of the charge transport, $\Delta H^{\ddagger}$, in the temperature range from 248.15 to 313.15 K.

Salt	$\Delta H^{\ddagger}$
	$kJmol^{-1}$
Bu_4NBr	24.3
Bu_4NNO_3	25.9
Bu_4NOAc	25.3
Bu_4NSCN	27.1

a reasonable limit of error, $\Delta H^{\ddagger}$ for four salts are roughly equal, indicating that the energy needed for the rearrangement of ions and solvent molecules during the charge transport process mainly depends on the properties of the solvent. Needless to say that a discussion of the limiting conductance based on the limiting ionic conductances λ^{∞} would be more fruitful with regard to the ion-specific solvation, mobility and size. For example, assuming equal mobilities of Ph_4As^+ and of Ph_4B^- at infinite dilution, $\lambda^{\infty}(Ph_4As^+) = \lambda^{\infty}(Ph_4B^-)$ [222], the limiting molar conductivities of ions $\lambda^{\infty}_{\pm}$ in PnP are becoming

calculable.
Another possible concept to overcome the lack of information on limiting ionic conductances is successfully proposed by Krumgalz [223]. His approach aims to the fact that the product $\lambda_{\pm}^{\infty}\eta$ is constant for non-solvated molecules, e.g. Bu_4N^+. It is caused firstly by the impossibility of the formation of donor-acceptor bonds by tetrabutylammonium ions with solvent molecules, and secondly by the extremely weak electrostatic interaction between the solvent molecules and these large ions due to the low surface charge of the latter. The non-solvated character of this cation in organic solvents is confirmed by a number of experimental data [224–226]. The authors showed that the Bu_4N^+ cation does not affect the valence bonds of the solvents at all. The phenomenon of the non-solvation is evident from the independency of $\lambda_{\pm}^{\infty}\eta$ irrespective of the chemical nature of the organic solvent. This constancy is used to separate the equivalent conductances of the solutes at infinite dilution into ionic components $\Lambda^{\infty} = \lambda_{+}^{\infty} + \lambda_{-}^{\infty}$. Krumgalz obtained an anchor value for $\lambda_{Bu_4^+}^{\infty}/\mathrm{S\,cm^2\,mol^{-1}} = 0.213 \pm 0.002$ at 25 °C for many kinds of different solvents. The limiting ionic conductivities of the anions are calculated at 25 °C by means of the Kohlrausch additivity rule.
Temperature variation of the limiting ionic conductivity was firstly introduced by Walden et. al. [227]. They suggested that the products $\lambda^{\infty}\eta$ of all ions are independent of temperature. The suggestion is in fact correct only for large tetraalkylammonium ions [228] as dealt with in this work and gives

$$\lambda^{\infty}(T) = \lambda^{\infty}(25\,^{\circ}C)\frac{\eta(25\,^{\circ}C)}{\eta(T)} \tag{5.96}$$

Considering the motion of a solvated ion in an electrostatic field as a whole, it is possible to calculate the radius r of the moving particle by the Stokes equation [153]:

$$r_i = \frac{N_A e_0^2 |z_i|}{6\pi\eta\lambda_i^{\infty}} \tag{5.97}$$

Despite the fact reliable experimental transference numbers are not available yet, the method suggested is extremely useful for the approximation of individual ionic conductances. Walden's rule for non-solvated ions is applied for calculation of the temperature-dependency of $\lambda_{Bu_4^+}^{\infty}$, initially starting from the anchor value at 25 °C. Secondly Kohlrausch's rule of additivity is used to obtain the anion's limiting ionic conductivity at every temperature with the experimentally determined values for Λ^{∞}. Results for λ^{∞} and the hydrodynamic radii r are listed in Table 5.24 at different temperatures. Due to the estimation

Table 5.24.: Limiting ionic conductivities λ_i and Stoke's radii r_i in PnP

T	$\lambda^{\infty}_{Bu_4N^+}$	$\lambda^{\infty}_{Br^-}$	$\lambda^{\infty}_{NO_3^-}$	$\lambda^{\infty}_{OAc^-}$	$\lambda^{\infty}_{SCN^-}$	$r_{Bu_4^+}$	r_{Br^-}	$r_{NO_3^-}$	r_{OAc^-}	r_{SCN^-}
K	$\mathrm{S\,cm^2\,mol^{-1}}$					Å				
248.15	0.97	0.68	0.96	0.74	0.84	3.9	5.5	3.9	5.0	4.4
258.15	1.78	1.35	1.90	0.84	1.52	3.9	5.1	3.6	8.2	4.5
268.15	2.96	0.93	3.21	1.23	2.40	3.9	12.0	3.5	9.2	4.7
278.15	4.54	2.29	5.44	1.74	3.89	3.9	7.6	3.2	10.0	4.5
288.15	6.53	4.36	8.77	2.73	7.94	3.9	5.8	2.9	9.2	3.2
298.15	8.95	5.68	11.82	4.38	9.94	3.9	6.1	2.9	7.9	3.5
308.15	11.78	6.53	14.22	5.22	12.71	3.9	7.0	3.2	8.7	3.6
313.15	13.36	7.62	14.13	5.40	13.26	3.9	6.7	3.6	9.5	3.9

procedure, the temperature coefficients obtained for the anions are identical to that of Λ^{∞}. The constancy of $r_{Bu_4^+}$ results from the assumption of Bu_4^+ being non-solvated in PnP. The values of λ^{∞} for Bu_4N^+ and SCN^- show a very small difference, pointing to the fact of similar ionic radii. According to the averaged decrease of the limiting ionic conductance in the order $NO_3^- > SCN^- > Br^- > OAc^-$ at all temperatures follows a corresponding increase in mobility at the opposite direction. Now, a comparison

of this trend in mobility with the crystallographic sizes of these ions, which are in the order $Br^- < NO_3^- < OAc^- < SCN^-$ shows a different solvation of the anions. For example, the mobility of the bromide ion is smaller than that of the nitrate ion, thus indicating that the relative actual size of the bromide ion is greater than that of the nitrate ion in this medium. That is, the bromide ions must be solvated to a higher extent in 1-propoxy-2-propanol, thus making them bigger hydrodynamic entities as compared to the nitrate ions. Similar conclusions can be drawn for acetate, the solvation shell is greater than that of the thiocyanate ion. Nitrate and thiocyanate tend to be less solvated with the nitrate ion having nearly the same dimension in solution as compared to the crystalline state.
Further evidence of the specific solvation of the ions in PnP comes from a comparison between the Stoke's radii and crystallographic radii of these ions: $SCN^- < NO_3^- < r_S/r_c < OAc^- < Br^-$.
More comprehensive information would require the acquisition of conductance data of additional salts in order to put the results in a broader context. Statements on the acceptor and donor abilities of the solvent PnP, explaining the order of ion solvation, would also be of particular interest. This work is meant to present a first basic study on the conductivity behavior of classical electrolytes in 1-propoxy-2-propanol.

5.6.6.2. Association Constants

Due to the relatively low permittivity of PnP, classified according to *Barthel* [156] as a neutral, amphiprotic solvent, the values for the association constants in Tables 5.18-5.21 are very high when compared to different alcohols, ketones and esters. [173] Hence all salts are considered to be highly associated in PnP and regarded as weak electrolytes. As seen in the Tables 5.18-5.21, the difference in the association constants of the bromide, nitrate and thiocyanate salts, however, is far less distinct than observed in solvating type solvents like acidic 1,1,1,3,3,3-Hexafluoro-2-propanol [229] and aprotic acetone [230]; for example in acetone, the association constant of NBu_4^+ salts is 435 for the chloride, 264 for the bromide and 143 for the iodide. Only Bu_4NOAc shows considerable smaller association in the present study. Mayer also showed increased variations in the association constants as a function of the cation radius observed in protic solvents, whilst the reverse trend is found for aprotic solvents. [231]
The solutions show a strong variance of association constant with temperature, an effect much more pronounced in solvents with small ϵ. The change of K_A with temperature for all salts is described by a positive temperature coefficient $dK_A/dT > 0$. There is no indication for a minimum, which is characteristic for tetraalkylammonium salts in other solvents [232, 233]. Inspection of the variation of K_A with the permittivity of the solvent at different temperatures shows a regular behavior, e.g. $\log K_A$ increases monotonically with $(\epsilon T)^{-1}$ due to the decreasing permittivity of PnP with increasing temperature. This fact is illustrated in Fig. 5.21 The small effect of the anion on the association pattern in tetrabutylammonium salts is best seen at temperatures above 0 °C. For a given cation we found the order: $OAc^- < Br^- \leq SCN^- < NO_3^-$ which is not in accordance to the sequence of the anion's crystallographic radii $Br^- < NO_3^- < OAc^- < SCN^-$. Increasing associations as the crystallographic size of the anions decrease was found elsewhere for electrolyte solutions of tetraalkylammonium salts in nonhydrogen-bonding solvents like acetone, nitrobenzene and acetonitrile. [232, 234] The reverse behavior is reported for the same salts in water and some short-chain alcohols. [233, 235, 236] Despite the higher errors of K_A in PnP solutions, neither trend of size-effect is evident from the presented results. Hence, an attempt is made to deduce some quantitative information on the hydrodynamic (solvated) radii of the ions at infinite dilution, estimated from Walden's product ($W = \eta\Lambda^\infty$), see Tables 5.18-5.21. Given that for tetraalkylammonium salts the cations are coordinately saturated, the occurrence of specific solute–solvent interactions is assumed to be restricted to interactions between the anion and the solvent molecules. [231] As a result any change in Λ^∞ amongst the four investigated salts can be assigned to differences in r^-. In doing so an order of increasing W and Λ^∞ is related to a decreasing order of the solvated anion's radii.
An inspection of W reveals the following sequence of r^-: $NO_3^- < SCN^- < Br^- < OAc^-$. Together with the opposite trend in K_A it permits us to show an increasing association with decreasing radii of the solvated anions.
A comparison of the K_A values from the present work with literature values obtained in the same solvent is not possible due to lack of any experimental data. A comparison to dichloromethane, a solvent of almost equal dielectric constant ($\epsilon^{25\,°C} = 8.93$) [81] can be made for Bu_4NBr, Bu_4NNO_3 and Bu_4NSCN

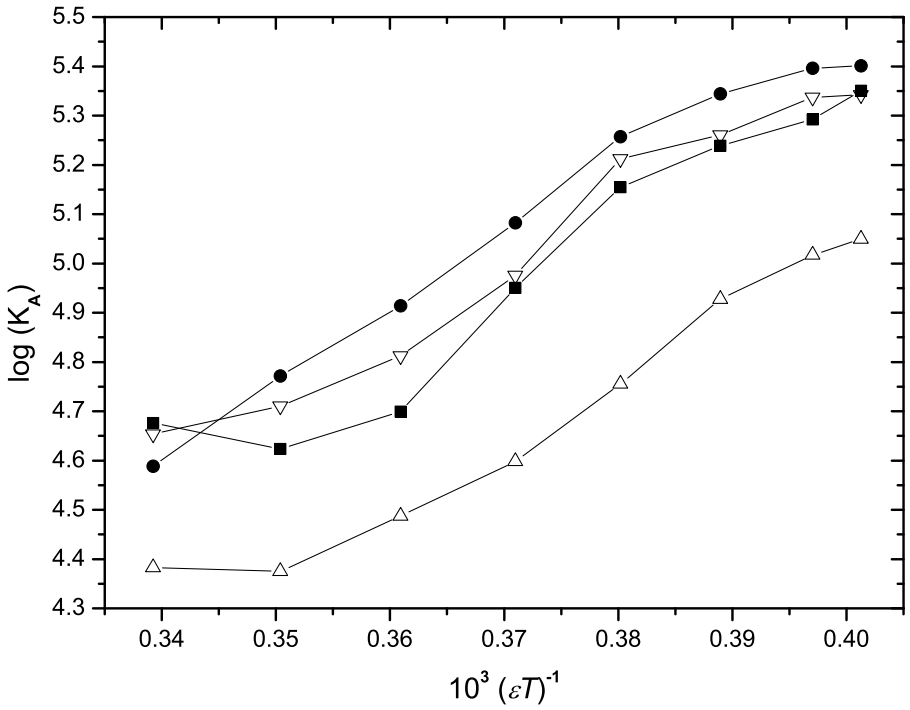

Figure 5.21.: Plot of $\log K_A$ vs. $(\epsilon T)^{-1}$ for Bu_4NNO_3 (●), Bu_4NSCN (▽), Bu_4NBr (■) and Bu_4NOAc (△) in the temperature range from 248.15 to 313.15 K

at 298.15 K [237], which show association constants almost one order of magnitude lower than those in PnP. Since experimental data are not given in the literature, reevaluation of K_A using Eqs. (5.90)-(5.92) could not be executed and it could not be excluded that these differences arise partially from different calculation procedure. Nevertheless the increased association of NBu_4^+ salts in PnP may be due to different short range forces, such as H-bonding, which produce different competing effects of ion solvation and association, apart from purely electrostatic behavior.

5.6.6.3. FJ2–re-Evaluation

All solutions show very high association constants, increasing strongly with temperature due to the low solvent permittivity. As a consequence of this conductivity behavior, the estimation of reliable values of Λ^∞ is open for errors in the data analysis due to the extrapolation (see Sec. 5.6.5). The experimentally accessible concentration range is limited at values where the measured equivalent conductance at 313.15 K attains only approximately 15 % (whereas at 248.15 K data attain approximately 30 % at least) of Λ^∞. Precise conductance measurements at concentrations of less than 10^{-6} mol kg^{-1} as required for an appropriate extrapolation at higher temperatures cannot be carried out.
In order to check the quality and reliability of the mentioned data on association constants and limiting molar conductivity, an approximation suitable for the evaluation of the temperature dependence of Λ^∞ is carried out with the help of the Walden rule [238]. This estimation at higher temperatures is based on the feature that conductance at infinite dilution and fluidity of the solution show the same temperature coefficient. Supposing Λ^∞ (248.15 K) to be the correct value, Walden's rule states

$$\Lambda^\infty(T) = \Lambda^\infty(248.15\,\mathrm{K})\frac{\eta(248.15\,\mathrm{K})}{\eta(T)}$$

A three-parameter fit at 248.15 K is followed at the higher temperatures by two-parameter fits with Λ^∞ values fixed to results obtained with the help of Walden's rule and the temperature dependent viscosities η of PnP (see Sec. 5.5.5.2). Comparison of values for Λ^∞ and K_A obtained from both evaluation methods in Table 5.25 show that changes in Λ^∞ and K_A occurs only to a minor extent at all temperatures. Both properties being in the same range of order, compared to results obtained from the FJ3-procedure. The

Table 5.25.: Limiting molar conductivities and association constants of Bu_4NBr in PnP

T (K)	248.15	258.15	268.15	278.15	288.15	298.15	308.15	313.15
FJ3-Evaluation (conductance equation Eq.(5.90))								
Λ^∞	1.64	3.13	3.89	6.83	10.89	14.63	18.31	20.98
($S\,cm^2\,mol^{-1}$)	± 0.06	± 0.20	± 0.14	± 0.19	± 0.66	± 0.53	± 0.23	± 0.47
K_A 10^{-4}	4.74	4.20	5.01	8.92	14.27	17.33	19.59	22.40
($dm^3\,mol^{-1}$)	± 0.41	± 1.10	± 0.38	± 0.45	± 1.49	± 1.33	± 0.63	± 0.96
σ-fit	0	0.001	0.001	0.001	0.001	0.001	0.002	0.002
FJ2-Evaluation (Walden rule)								
Λ^∞	(1.64)	3.02	5.02	7.71	11.10	15.20	19.99	22.75
($S\,cm^2\,mol^{-1}$)	-	-	-	-	-	-	-	-
K_A 10^{-4}	(4.74)	6.55	8.92	11.65	14.87	18.80	23.61	26.58
($dm^3\,mol^{-1}$)	(± 0.41)	± 0.02	± 0.50	± 0.24	± 0.20	± 0.18	± 0.51	± 0.55
σ-fit	0	0.001	0.002	0.001	0.001	0.001	0.002	0.002

strategy described here also does not change the situation of finding negative values for the adjustable parameter $R(J_2)$. Due to the fact, that all evaluation results in a FJ2-procedure would rely on the accuracy of Λ^∞ at the lowest possible temperature, the assumption of using Walden's rule might also be seen critically. Therefore and because of the non-significant changes in Λ^∞, data analysis is based on a 3-parameter regression yielding the parameters as described.
Similar results for the three remaining salts confirm that originally obtained values for the limiting molar conductivity and association constant, based on FJ3-calculations, are supposed to be reliable, despite the extrapolation toward zero concentration in case of the steep increase of molar conductivity at very low concentrations. This discrepancy between the measured equivalent conductivity at lowest concentration and the value at infinite dilution is less than described [238, 239] and allows for a determination of Λ^∞ in the usual way.
No change in the order of the values for K_A for the different electrolyte systems are observed in case Λ^∞ is regarded as fixed at every temperature.

5.6.6.4. Thermodynamics of the Ion-Pair Process

The temperature-dependent equilibrium constants K_A for the ion association reaction allows the investigation of the thermodynamics of this process. Consequently, the standard Gibbs energy ΔG_A^0 is calculated at all temperatures according to

$$\Delta G_A^0(T) = -RT\ln K_A(T) \tag{5.98}$$

The temperature dependence of $\Delta G_A^0(T)$ is expressed with the help of a linear function

$$\Delta G_A^0(T) = A_0 + A_1(298.15 - T) \tag{5.99}$$

Discussion of ion-pair equilibria is based on the temperature dependence of $\Delta G_A^0(T)$ leading to the enthalpy ΔH_A^0 and entropy ΔS_A^0, as

$$\Delta S_A^0(T) = -\left(\frac{\partial \Delta G_A^0(T)}{\partial T}\right)_p = A_1 \tag{5.100}$$

$$\Delta H_A^0(T) = \Delta G_A^0(T) + T\Delta S_A^0(T) = A_0 + 298.15A_1 \tag{5.101}$$

and summarized in Fig. 5.22. From the ΔG_A^0 values at all temperatures of the program the coefficients A_0 and A_1 were obtained by the usual least squares methods and are given in Table 5.26. The absolute values of the thermodynamic properties depend on the choice of the conductance equation and the con-

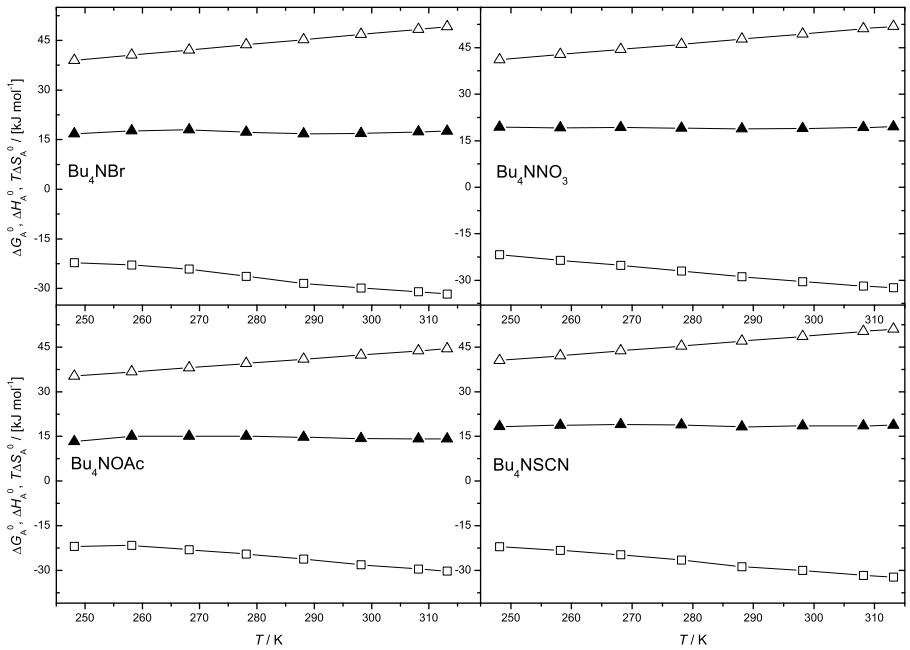

Figure 5.22.: Temperature dependence of thermodynamic functions of association. (□) ΔG_A^0, (△) $T\Delta S_A^0$, (▲) ΔH_A^0

Table 5.26.: Coefficients of equation $\Delta G_A^0(T) = A_0 + A_1(298.15 - T)$ and $\Delta H_A^0(298.15K)$ for the systems under investigation.

	$A_0 = \Delta G_A^0(298.15K)$	$A_1 = \Delta S_A^0(298.15K)$	$\Delta H_A^0(298.15K)$
	kJmol^{-1}	kJ mol^{-1} K^{-1}	kJ mol^{-1} K^{-1}
Bu_4NBr	-29.5	+0.147	+14.3
Bu_4NNO_3	-30.1	+0.161	+17.9
Bu_4NOAc	-27.9	+0.161	+14.1
Bu_4NSCN	-29.8	+0.161	+19.6

centration scale, but allow for a comparable study with their differences being significant. The values of ΔG_A^0 and ΔS_A^0 at 298.15 K are $\Delta G_A^0 = A_0$ and $\Delta S_A^0 = A_1$.
The positive ΔH_A^0 values indicate that the process of the ion-pair formation is endothermic in nature and energy consuming. The enthalpic contributions appear not to vary much with temperature. Because of the choice of a linear temperature-dependence of ΔG_A^0 the temperature-dependence of the entropy of ion-pairing is neglected yielding constant ΔS_A^0 values. Based on that fact, presumably the number of the degrees of freedom does not change considerably due to the weak solvation of the ions. Nevertheless, the $T\Delta S_A^0$ term is sufficiently positive to compensate the positive contribution of the ΔH_A^0 term. Consequently, the standard Gibbs free energy is negative and the ion-association process can be recognized as an exergonic process. The increase of the temperature leads to more negative ΔG_A^0 values indicating that the ion-association equilibrium is shifted toward ion-pairs at elevated temperatures. The behavior of tetraalkylammonium salts in PnP show the pattern of methanol [240], ethanol [241], propanol [242], acetonitrile [217], and acetone [218].
According to Eq. (5.92) the Gibbs' energy of association can be split in two parts, one containing contributions of coulombic ion-ion-interactions

$$\exp\left[\frac{-\Delta G_{\mathrm{A}}^{\mathrm{coul}}}{RT}\right] = K_{\mathrm{A}}^{\mathrm{coul}} = 4\pi N_{\mathrm{A}} \int_a^R r^2 \exp\left[\frac{2q}{r}\right] \mathrm{d}r \tag{5.102}$$

and a non-coulombic part, $\Delta G^*_A = N_A W^*_{+-}$. Analysis of the temperature dependence of the non-coulombic contribution gives values of $\Delta G^*_A < 0$, whilst $\Delta S^*_A, \Delta H^*_A > 0$ and small for all salts. There is no pronounced change of enthalpy and entropy with temperature. Low entropies indicate that the process of ion-pair formation is accompanied by only weak rearrangement of the solvent molecules in the surroundings of the respective ions. There is no solvation shell comparable to that of alkali salt ions in organic solvents, indicating a different interaction between the solvent around ions, ion-pairs and these species [243]. Interaction forces are mainly dispersion forces. The Walden product ($W = \eta\Lambda^\infty$) does not show a dependence on temperature confirming that the ions are only weakly solvated. The constancy of the ΔS^0_A values in the whole temperature range supports the last conclusion.
Small enthalpy values ΔH^*_A are the result of only minor changes in ion-solvent interaction of tetrabutylammonium salts, which is the main contribution to the non-coulombic potential ΔG^*_A. Although there are no comparable investigations along with PnP, the thermodynamic behavior of the four tetraalkylammonium salts obviously indicate a missing solvation shell comparable to that of alkali salt ions. As ΔG^*_A constitutes only a minor part of ΔG_A, we suggest a preference of electrostatic interactions contributing to the association process. The same conclusion can be drawn for the negligible contribution of ΔH^*_A to the enthalpy of association ΔH^0_A.
There has been so far no report on the conductivity study of tetrabutylammonium salts in 1-propoxy-2-propanol. In a first experimental attempt comprising Bu_4NBr, Bu_4NNO_3, Bu_4NSCN and Bu_4NOAc, results provide information on the effect of the physical properties of the solvent medium on the association and the transport properties of the electrolyte. The investigation has been performed through the determination of the limiting molar conductivity (Λ^∞), the association constant (K_A), and the thermodynamic quantities of the ion association process as well as the Eyring's activation enthalpy of the ionic movement ($\Delta H^\ddagger$). Conductivity studies were accompanied with precise measurements of pure solvent's properties like relative permittivity (ϵ), density (d), and dynamic viscosity (η), covering the range of temperatures between 248.15 and 313.15 K. On the basis of the results discussed, corresponding conclusions have been drawn.
It is out of question that comprehensive studies on electrical conductivity in PnP would be necessary to build up more reliably statements on the competing effects of solvation and association (temperature-dependencies), effects of short-range forces (non-coulombic contributions), and specific ion solvations (deviations from elementary electrostatic models).

5.7. Conductance of Concentrated Electrolyte Solutions

The accurate determination as well as optimization of the specific conductivity κ of electrolytic solutions is a major topic in various fields of applied research. Measurements carried out over wide ranges of concentration, temperature and also solvent composition yield concrete pieces of knowledge on academically and technologically interesting electrolyte solutions. A maximum in the specific conductivity, κ_{max} clearly visualizes the interplay between the conductance determining effects in moderately and highly concentrated electrolyte solutions. Despite the fact, that no similar results on electrical conductivity in 1-propoxy-2-propanol are known in from the literature, at all, the importance of themselves is obvious: the performance of the Karl-Fischer reagent [9] depends to a great extent on the mobility of the reacting species in the electrochemical process. Besides other properties like the choice of chemical species and their electrochemical stability, specific conductivity ought to be optimized with respect to concentration and solution composition.
Similar to the conductance studies of dilute solutions, the measuring setup consists of the complete balancing bridge with the sinus generator, Wheatstone bridge and the decade resistance box. The conductivity measurements at moderate to high concentrations ($0.05 < c/\mathrm{mol\,L^{-1}} < 1.4$) are performed with a set of capillary cells of different cell constants as these are required for concentrated solutions. Measures were taken during the construction of the cells to reduce their volume to a maximum of a few milliliters. Advantageous of this small volume is a reduced usage of chemicals and the possibility of arranging several cells inside the thermostat simultaneously. Different concentrations can therefore be measured at each temperature at the same time. The temperature programs and the statements about its accuracy and

precision are identical to those mentioned in case of dilute conductivity measurements. An assembly lid equipped with six conductivity cells and a switching equipment connecting these cells to the conductivity bridge permits the measurement of the conductivity.
A crucial requirement for precise and reliable data is the choice of cells with a proper cell constant, in order to measure the solutions resistance within an optimal range of $(1 - 100)\,\mathrm{k\Omega}$. Very low conductivity as verified with the evaluation of the dilute conductivity data demands for cell constants in the range of $(1\text{-}1000)\,\mathrm{m^{-1}}$ [244]. A set of cells described in that work excellently fulfills the requirements for precise measurements of moderately to concentrated solutions over the desired temperature range.

5.7.1. Conductivity Cells

Fig. 5.7.1 displays a graphical drawing of one cell. The cells consists of one single solution chamber and are designed as a polarization-free three-electrode cell (E) equipped with glass tubes, into which the solutions are filled in. Their small inner diameter together with small dimensions of the electrodes

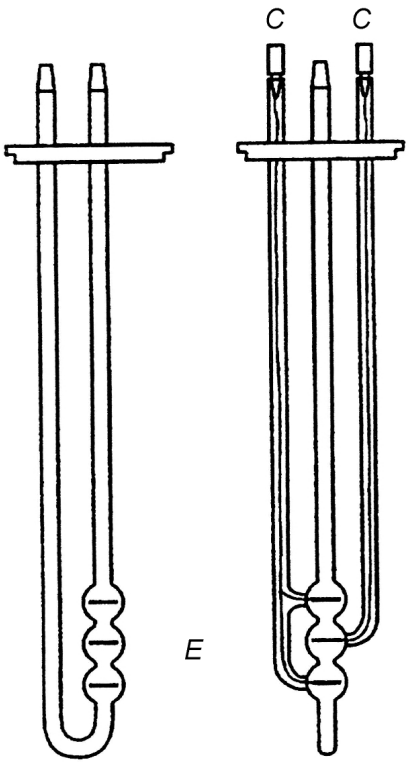

Figure 5.23.: Capillary cells with three electrode assembly (E) indicating the inlet for bubble-free filling under protective gas; electrical connections (C)

assembly enables a total volume less than 12 mL. Depending on the cell's constant, slight differences in the geometry of the electrodes assembly exist notwithstanding of the given drawing. Electrodes are provided as circular pieces of platinum, mounted inside the chamber by thin wires of platinum [175].
A precise determination of the solution's electrical conductivity requires the knowledge of the supply line's resistance. As these correction values can be determined only once, the tabulated resistance of approximately $0.40\,\Omega$ given in [244] is used in this work.
Prior to use a similar purification procedure as explained in Sec. 5.6.3.1 is applied for the capillary cells. Great care has to be taken in the filling of the cells in order to avoid any irretrievable deformation of the platinum electrodes by the filling device. Liquids and gaseous nitrogen, therefore, are supplied through the cell's glass tubes not containing the electrodes assembly.
Since precisely determined cell constants are available for the set of capillary cells, only their ratio of constants C_i/C_j is experimentally verified and compared to those originally published [244]. Aqueous solutions of potassium chloride at appropriate concentrations were used to compare the cell's solution resistances with each other. Based on that control measurements at different concentrations an excellent

Table 5.27.: Cell constants C of capillary cells for concentrated electrolyte solutions at 298.15 K

	C_i / m^{-1}	ΔC_i / m^{-1}	$\frac{\Delta C_i}{C_i} \cdot 100$
Cell 1	2.0842	0.00005	2×10^{-3}
Cell 2	24.611	0.004	2×10^{-2}
Cell 3	53.638	0.003	6×10^{-3}
Cell 4	223.98	0.02	9×10^{-3}
Cell 5	469.80	0.04	8×10^{-3}
Cell 6	1160.7	0.2	2×10^{-2}

agreement on the ratio between the cell constants could be obtained, differing not more than 0.1 % from the values obtained in Ref. [244] at 298.15 K. No change of C_i/C_j is detectable at a different temperature of 288.15 K. For that reasons the usage of cell constants given in Table 5.27 and determined by Meier seems to be reasonable. Please note that uncertainties are given as results of the primary calibration; the obtained ratios C_i/C_j in this work do not allow for assigning single cell's errors in the constant C. The cell constants at temperatures different to 298.15 K are calculated with the help of the temperature coefficient β of the cell constants. Similar to the explanations given in the sections for the dilute solutions, it may be determined either experimentally or approximated with regard to the expansion of the glass and platinum material. Due to the comparable geometric assembly of the electrodes within the cells the same value for the temperature coefficient $\beta = -15 \times 10^{-6}\,\mathrm{K}^{-1}$ is used for measurements at elevated concentrations and enables the calculation of $C_i(T)$ according to Eq. (5.87).

5.7.2. Experimental Procedure

In principle there are two different ways of preparing the electrolyte solutions

(1) each solutions is prepared by weighing solvent and electrolyte separately

(2) a stock solutions of high concentration is diluted to obtain every other solution

Both methods are used in this work. For concentrations below 0.2 mol kg^{-1} procedure (2) is normally used. All steps during sample preparation (weighing, dissolution) are performed under a steady atmosphere of purified, dry nitrogen in a glove box. All glass parts were stored in a hot-air cabinet till shortly before use, whilst the fittings were kept under vacuum in an desiccator. Solutions are prepared in narrow-necked volumetric flasks (10-50) mL and rigorously stirred for 30 min, to achieve best homogeneity, especially of solutions with high concentration. Net weights are determined on a balance with a resolution of 10^{-3} g with the masses of electrolyte and solvent chosen in such a way to maintain an accuracy of better than 0.1 % in mass. According to method (1) the molarity of each solution m is obtained with m_E as electrolyte mass, m^* as solvent mass, and M_E as molar mass of electrolyte by the following equation

$$\mathrm{m} = \frac{m_E}{M_E m^*} \tag{5.103}$$

Method (2) is a dilution method with the molarity m of electrolyte solution after solvent addition to the stock solution m^*

$$\mathrm{m} = \frac{\mathrm{m}^*}{1 + \frac{G}{g}\,(1 + M_E \mathrm{m}^*)} \tag{5.104}$$

Here g and G are the mass of the added stock solution and the mass of added solvent, respectively. m^* is the molality of stock solution.
All solutions under investigation are filled carefully and slowly into the conductivity cells with the help of gas-tight syringes ensuring a bubble free filling, during which time slight pressure of nitrogen is applied on the other glass tube of each cell. Appropriate filling with liquid levels in both arms being equal is

completed with the removing of the nitrogen supply and the proper closing of the cells by female joint caps (NS 14). The set consisting of 6 cells is immersed in the thermostat and connected as one arm of the Wheatstone bridge.
The temperature program is started at the highest temperature 313.15 K and reduced in steps of (5 or 10) K to the minimum temperature of 248.15 K. Temperature regulation, resistance measurement and resistance extrapolation to infinite frequency is performed identically to the dilute measurements. At times when irregularities of solution's resistance at frequencies below 480 Hz do not allow for proper extrapolation, they were disregarded. The deviation between R^{∞} and $R(10\,\mathrm{kHz})$ is always markedly smaller than 0.08 %.
Calculation of the specific conductivity of each solution comes about with the consideration of the pure solvents conductance κ^*, which is taken into account from the corresponding results with the measuring cell in Fig. 5.13. Each solutions's resistance R_S is converted to specific conductivity κ for every temperature according to the following equation

$$\kappa = \frac{C}{R_S} - \kappa^* \qquad R_S = R_\infty - R^{sl} \tag{5.105}$$

with R^{sl} being the resistance of the supply lines (see Sec. 5.7.1). In order to keep the influence of the inherent pure solvent's conductivity insignificantly low, the term $\frac{C}{R} - \kappa^*$ must be kept sufficiently high. This means, that not every concentration is able to be measured with any cell, but an optimal range of concentration (and hence specific conductivity) for every cell exists. Finally the molar electric conductivity Λ is obtained with Eq. 5.84.

5.7.3. Data Analysis

The representation of conductance data of electrolyte solutions by the use of fitting equations is commonly executed with polynomials of concentration, temperature, pressure, or mathematical functions known for the appropriate representation of the shape of the experimentally determined curves.
One of the most useful expressions of this type is given by Amis and Casteel for the specific conductivity of concentrated solutions [161]:

$$\kappa = \kappa_{max} \left(\frac{\mathrm{m}}{\mu}\right)^a \exp\left[b(\mathrm{m}-\mu)^2 - \frac{a}{\mu}(\mathrm{m}-\mu)\right] \tag{5.106}$$

It makes use of four parameters $(\kappa_{max}, \mu, a, b)$ and fits well specific conductances κ of all presented solutions as a function of molal concentration m in the range of concentration around the point of maximum specific conductance κ_{max} attained at concentration μ; a and b have no physical meaning.
The four quantities are adjusted by a least-squares method, all measuring values contributing with equal weight. Standard deviations of the single values are observed with an order of magnitude of $7 \times 10^{-6} < \sigma < 4 \times 10^{-4}$, depending mainly on the temperature. Convergence is usually found after 2-4 iteration steps providing reasonable initial guesses for κ_{max} and μ, easily found by visual inspection of the conductance plots.
In order to reduce the number of adjustable parameters for the description of the conductivity behavior as function of molality and temperature, a multiple regression procedure according to Casteel-Amis is performed with all experimental data points. For that reason, each parameter in Eq. (5.106) ($\kappa_{\max}$, μ, a, and b) is supposed to show the following temperature-dependency:

$$\begin{aligned} \kappa_{\max} &= \sum_{i=0}^{3} a_i^{\kappa} \cdot \frac{T-T_0}{\mathrm{K}} & \mu &= \sum_{i=0}^{2} a_i^{\mu} \cdot \frac{T-T_0}{\mathrm{K}} \\ a &= \sum_{i=0}^{2} a_i^{a} \cdot \frac{T-T_0}{\mathrm{K}} & b &= \sum_{i=0}^{2} a_i^{b} \cdot \frac{T-T_0}{\mathrm{K}} \end{aligned} \tag{5.107}$$

The problem of bad convergence with the simultaneous adjustment of these 14 parameters is addressed by introduction of a analytical form of $\mu(T)$ for each electrolyte system. This means that prior to the multiple regression, the $\kappa(\mathrm{m})$ curves at every temperature are used to obtain an expression for $\mu(T)$ in the form presented above. In doing so, the overall number of adjustable parameters for calculating the specific conductance at any temperature and any concentration is reduced to 10.
Regression comprises the solution of a non-linear equation insofar as the coefficients ($\kappa_{\max}$, a, and b) appear in a non-linear fashion. For every salt system, data points $\kappa(\mathrm{m}, T)$ are subjected to a procedure using the Levenburg-Marquardt algorithm for fitting its non-linear equations. It minimizes the sum of squares of the residuals between calculated and experimental values of specific conductivity. Calculations are performed with `TableCurve 3D`, which provides the user with a graphical representation of the three-dimensional κ-surface as well.
Initial values for each parameter of the multiple regression and the expressions for $\mu(T)$ are retrieved from previous investigations of $\kappa(\mathrm{m})$, results of which are shown in Tables 5.28-5.31. This approach warrants a very fast convergence with a small number of iterations and avoids finding a local minimum with an unrealistic surface plot. No peculiarity could be observed within the range of concentration and temperatures under investigation.
Henceforth calculations of κ in the range of (248.15 to 313.15) K for every concentration and temperature are easily possible. Otherwise attempts would require temperature-interpolation of ordinary Casteel-Amis fits, much more time-consuming and not necessarily more precise.

5.7.4. Results and Discussion

All data on the electrical conductivity of Bu_4NBr, Bu_4NNO_3, Bu_4NOAc and Bu_4NSCN in 1-propoxy-2-propanol can be found in Sec. E.2. Results reproducing the specific conductivities at all temperatures of the temperature program between (248.15 and 313.15) K with the help of Eq. 5.106 are summarized in Tables 5.28-5.31. Therein are listed all four parameters with corresponding σ_i. Additionally the temperature- and concentration-dependent characteristic of the specific conductivity in terms of the experimental data points and the regression curves are presented in Fig. 5.25-5.28 for all systems. The independently determined values μ and $\kappa_{\max}$ are contained in the figures as dashed lines showing that investigation of the complete $(\kappa - \mathrm{m} - T)$ – field yields compatible information. A missing point at -25 °C for Bu_4NBr is caused by a missing resistance measurement at this temperature and not by experimental problems.
To our best knowledge this is the first systematic investigation on the electrical conductivity behavior in PnP covering a concentration range from high dilution to concentrations near the limit of solubility.
Tables 5.28-5.31 show values of a being all positive, thus fulfilling the requirement of $\lim_{\mathrm{m}\to 0} \kappa = 0$. The situation of $a < 0$ never occurs in the measurements and is probably caused by the fact that precise data are available for $\mathrm{m} < \mu$. With regard to parameter b, both results with $b \lesseqgtr 0$ are observable. At high concentrations, $\mathrm{m} > \mu$, finite values of κ are obtained only if $b < 0$, otherwise κ attains a minimum at $\mathrm{m} = a/(2b\mu)$ and then increases steadily, in contrast to a real behavior of κ [245]. The situation $b > 0$ is found when the concentration range is limited to values of $\mathrm{m} \approx \mu$. Examples can be found in all system for all or selected temperatures, due to the highest concentration measured being below or around the maximum of conductance $\kappa_{\max}$. Extrapolation of the curve up to higher concentration for those cases will always result in unreasonable increases of κ at very high concentrations (not shown in the figures). Despite this unrealistic description, the capability of Eq. 5.106 over the given range of molalities allows for its use in representation empirically the conductance behavior. This is evident from an investigation of the different curves obtained from this equation, if only a limited number of experimental data is provided. In Fig. 5.24 absolute deviations in specific conductivities are given for the case of data regression with varying sets of data points, the lowest concentrations of which are indicated in the plot. The deviations are quite similar with the exception of the results obtained by using only 4 points of high concentration, a possible reason for the largest errors in representing data points below $0.75\,\mathrm{mol\,kg^{-1}}$. In all three other cases similar behavior is found with a slightly increasing deviation for data sets with decreasing number of data points and starting concentrations more apart from the range of low concentration. The effect is evident from the graph at $\mathrm{m} < 0.5\,\mathrm{mol\,kg^{-1}}$, but is still in the range

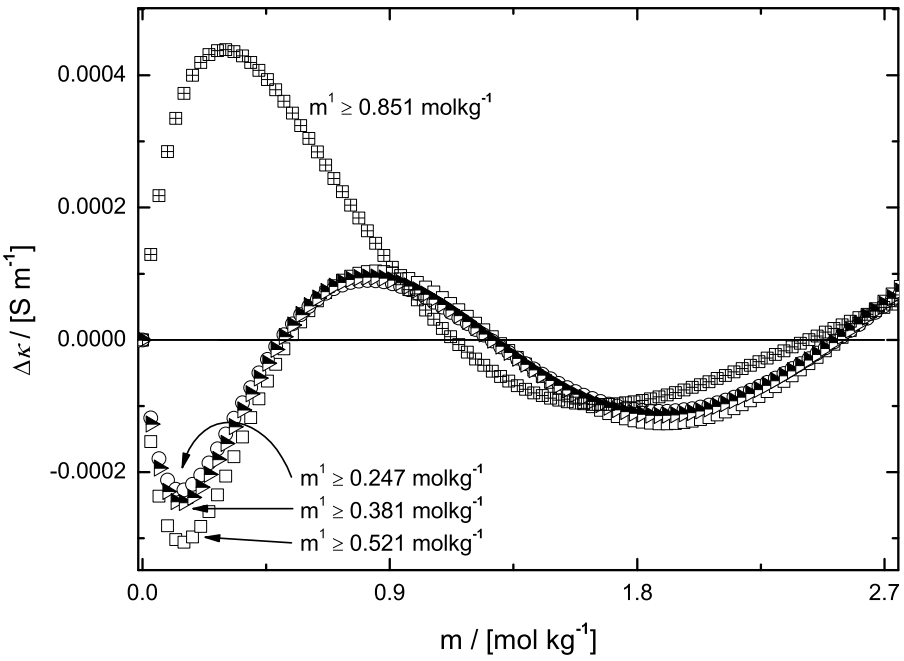

Figure 5.24.: Absolute deviations between κ as obtained from Eq. (5.106) and with different initial concentrations m^1, exemplary presented with Bu_4NBr at 298.15 K

of not more than 8 % at very low molality.

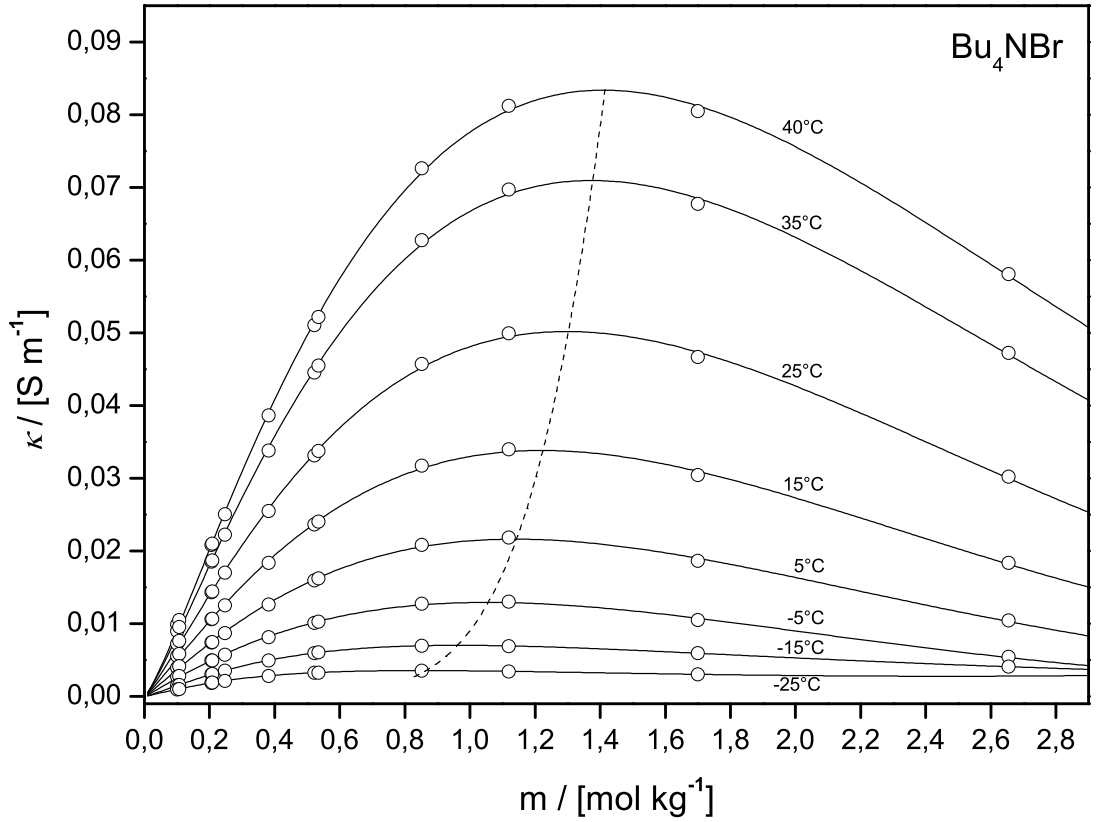

Figure 5.25.: Specific conductivity κ $\left[\mathrm{S\,cm^{-1}}\right]$ of Bu_4NBr in 1-propoxy-2-propanol at temperatures from -25 °C to 40 °C. Solid curves as obtained from plots according to Eq. (5.106). The dotted curve represents the independently determined $\kappa_{max} = \kappa_{max}(\mu)$

Table 5.28.: Conductance parameters, Equation (5.106) and their standard deviations

θ	κ_{max}	$\sigma(\kappa_{max})$	μ	$\sigma(\mu)$	a	$\sigma(a)$	b	$\sigma(b)$
°C	$10^{-3}\frac{S}{m}$	$10^{-6}\frac{S}{m}$	$\frac{mol}{kg}$	$10^{-3}\frac{mol}{kg}$		10^{-3}	$\left(\frac{mol}{kg}\right)^{-2}$	$10^{-2}\left(\frac{mol}{kg}\right)^{-2}$
−25	3.554	4	0.8450	3.3	1.144	8	0.277	0.8
−15	7.029	3	0.9660	1.1	1.190	3	0.118	1.5
−5	12.917	28	1.0601	4.3	1.052	12	−0.104	7.2
5	21.703	75	1.1426	6.9	1.092	19	−0.098	1.1
15	33.837	53	1.2234	3.2	1.124	8.7	−0.087	0.4
25	50.214	85	1.3021	3.6	1.160	9.7	−0.075	4.7
35	70.938	117	1.3767	3.6	1.217	9.6	−0.049	0.4
40	83.454	135	1.4145	3.5	1.240	9.4	−0.040	0.4

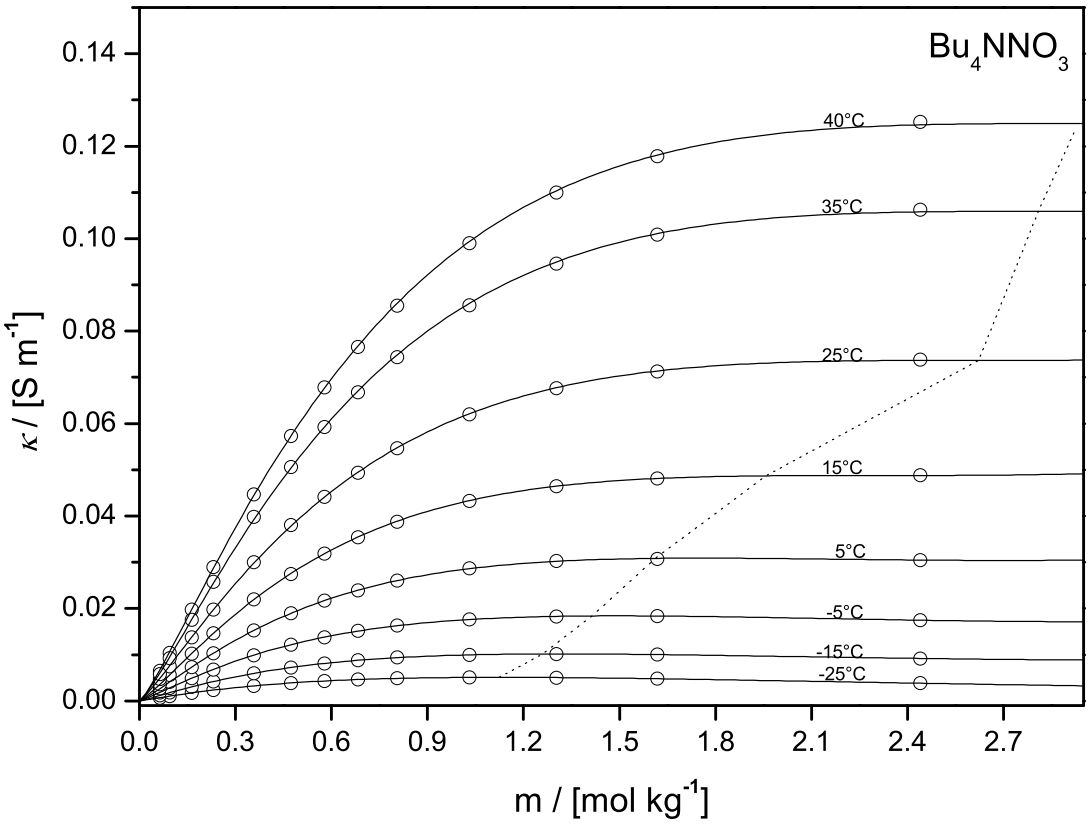

Figure 5.26.: Specific conductivity κ $\left[\mathrm{S\,cm^{-1}}\right]$ of Bu_4NNO_3 in 1-propoxy-2-propanol at temperatures from -25 °C to 40 °C. Solid curves as obtained from plots according to Eq. (5.106). The dotted curve represents the independently determined $\kappa_{max} = \kappa_{max}(\mu)$

Table 5.29.: Conductance parameters, Equation (5.106) and their standard deviations

θ	κ_{max}	$\sigma(\kappa_{max})$	μ	$\sigma(\mu)$	a	$\sigma(a)$	b	$\sigma(b)$
°C	$10^{-3}\frac{S}{m}$	$10^{-6}\frac{S}{m}$	$\frac{mol}{kg}$	$10^{-3}\frac{mol}{kg}$		10^{-3}	$\left(\frac{mol}{kg}\right)^{-2}$	$10^{-2}\left(\frac{mol}{kg}\right)^{-2}$
−25	5.110	2	1.1277	2.3	1.069	4	0.076	0.3
−15	10.171	6	1.3173	5.8	1.137	8	0.132	0.4
−5	18.407	24	1.4965	5.9	1.168	7	0.127	0.4
5	30.884	21	1.753	3.1	1.202	4	0.127	0.2
15	48.760	116	2.290	10.4	1.218	14	0.116	0.7
25	73.630	205	2.623	16.7	1.191	18	0.087	0.8
35	106.100	341	2.849	30.7	1.215	22	0.075	1.1
40	124.000	309	2.941	26.4	1.216	18	0.070	0.8

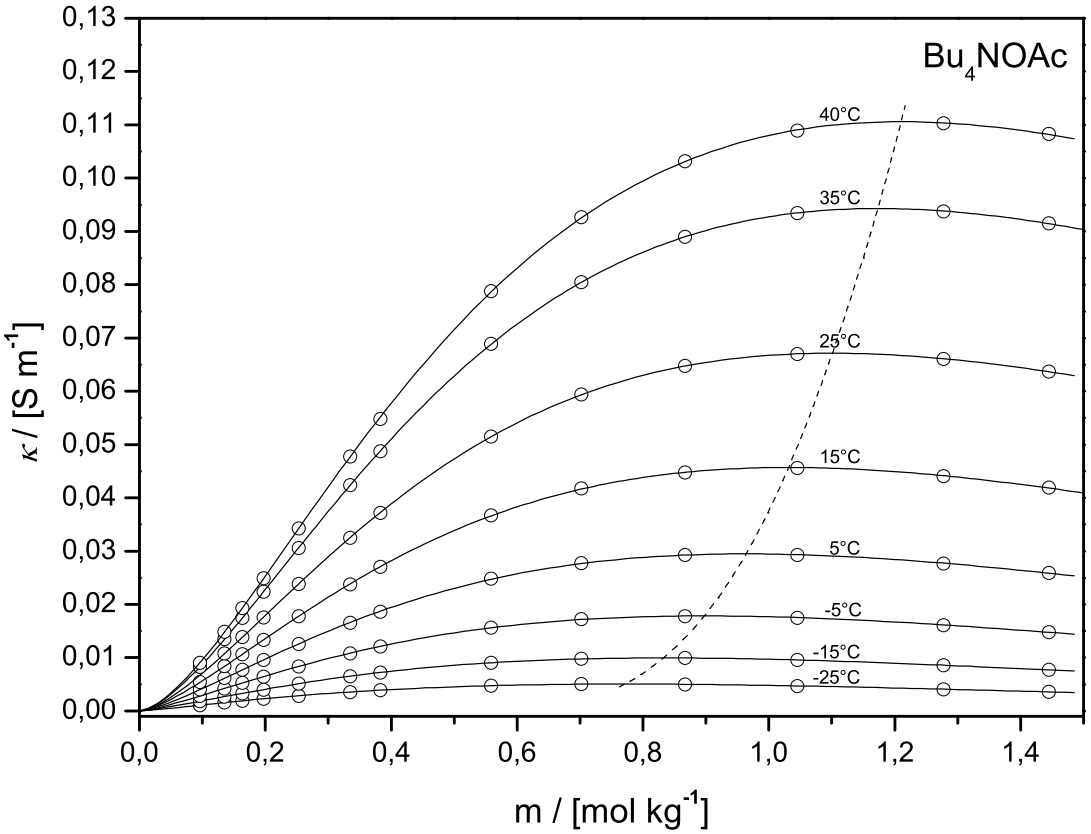

Figure 5.27.: Specific conductivity κ $\left[\mathrm{S\,cm^{-1}}\right]$ of Bu_4NOAc in 1-propoxy-2-propanol at temperatures from -25 °C to 40 °C. Solid curves as obtained from plots according to Eq. (5.106). The dotted curve represents the independently determined $\kappa_{max} = \kappa_{max}(\mu)$

Table 5.30.: Conductance parameters, Equation (5.106) and their standard deviations

θ	κ_{max}	$\sigma(\kappa_{max})$	μ	$\sigma(\mu)$	a	$\sigma(a)$	b	$\sigma(b)$
°C	$10^{-3}\frac{S}{m}$	$10^{-6}\frac{S}{m}$	$\frac{mol}{kg}$	$10^{-3}\frac{mol}{kg}$		10^{-3}	$\left(\frac{mol}{kg}\right)^{-2}$	$10^{-2}\left(\frac{mol}{kg}\right)^{-2}$
−25	5.049	8	0.7707	2.3	1.242	14	−0.082	1.9
−15	9.954	13	0.8327	2.0	1.313	13	−0.039	1.6
−5	17.841	25	0.8971	2.1	1.368	14	−0.020	1.7
5	29.485	45	0.9641	2.4	1.429	16	0.014	1.9
15	45.702	46	1.0313	1.8	1.484	11	0.036	1.2
25	67.148	37	1.1009	1.3	1.567	7	0.087	0.8
35	94.299	36	1.1730	1.4	1.602	5	0.091	0.5
40	110.587	89	1.2101	3.7	1.626	11	0.095	1.2

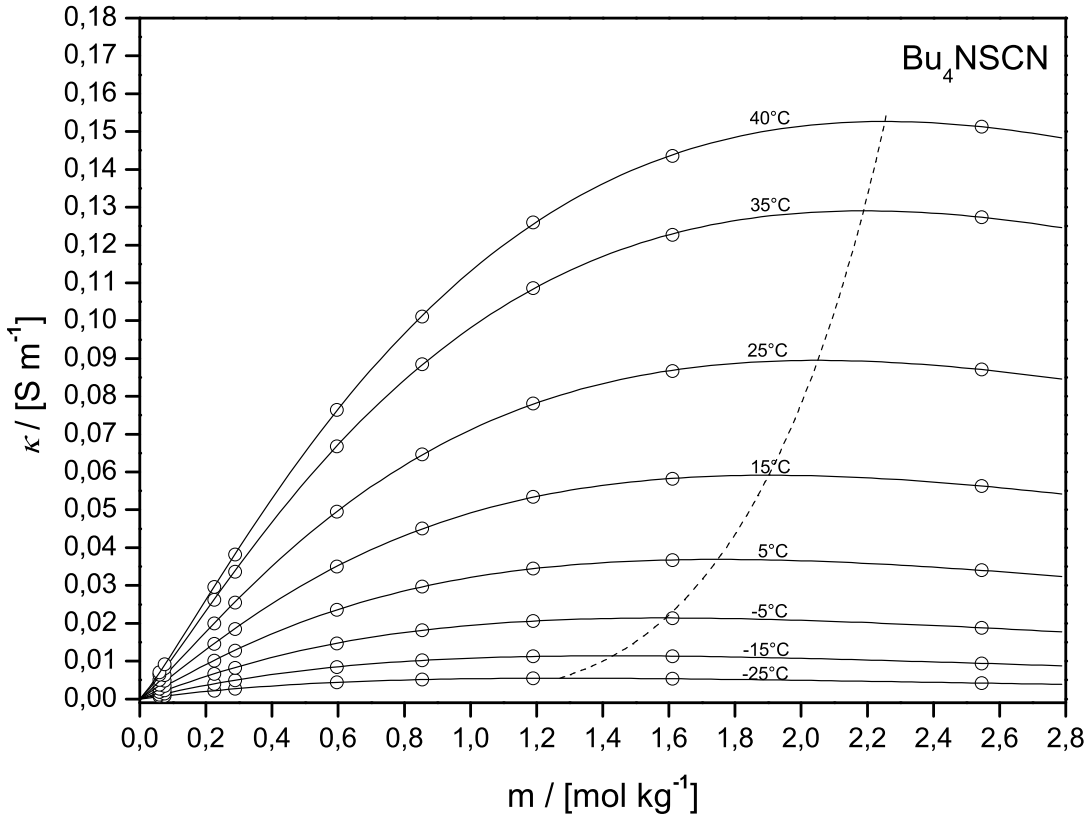

Figure 5.28.: Specific conductivity κ of Bu_4NSCN in 1-propoxy-2-propanol at temperatures from -25 °C to 40 °C. Solid curves as obtained from plots according to Eq. (5.106). The dotted curve represents the independently determined $\kappa_{max} = \kappa_{max}(\mu)$

Table 5.31.: Conductance parameters, Equation (5.106) and their standard deviations

θ	κ_{max}	$\sigma(\kappa_{max})$	μ	$\sigma(\mu)$	a	$\sigma(a)$	b	$\sigma(b)$
°C	$10^{-3}\frac{S}{m}$	$10^{-6}\frac{S}{m}$	$\frac{mol}{kg}$	$10^{-3}\frac{mol}{kg}$		10^{-3}	$\left(\frac{mol}{kg}\right)^{-2}$	$10^{-2}\left(\frac{mol}{kg}\right)^{-2}$
−25	5.478	15	1.2730	8.9	1.046	15	0.033	0.8
−15	11.407	34	1.4295	9.6	1.068	17	0.020	0.8
−5	21.403	63	1.5882	8.9	1.095	17	0.016	0.8
5	36.888	98	1.7483	8.0	1.116	16	0.012	0.7
15	59.141	146	1.9039	9.2	1.132	15	0.008	0.7
25	89.513	207	2.0483	12.8	1.154	16	0.007	0.7
35	129.045	255	2.1894	17.0	1.168	15	0.005	0.6
40	152.656	310	2.2527	20.3	1.161	16	−0.002	0.7

A compilation of data in Tables 5.32-5.35 shows the results of the multiple regression according to the set of Eqs. (5.107). Also included are the standard deviations $\sigma_{\kappa(\mathrm{m},T)}$ as obtained from the regression. Based on the fact that the complete set of data points irrespective of concentration and temperature is represent by one single equation, the quality of the representation is admittedly good. Although the absolute accuracy for a single $\kappa(\mathrm{m})$ curve is higher, it does not hide the advantage of the general applicability of the multiple optimization results, with respect to its simplicity in calculating specific conductance at any $(\mathrm{m}-T-\mathrm{value}$.
A typical plot of the conductivity surface as function of its molality and temperature within the range of $0 \leq \frac{T-248.15}{\mathrm{K}} \leq 70$ and $0 \leq \frac{\mathrm{m}}{\mathrm{mol\,kg^{-1}}} \leq 1.5$ is displayed in Fig. 5.29 for Bu_4NOAc. Concrete evidence for the quality is well seen from the 3-dimensional plot of residuals between calculated and experimental values of specific conductivity, shown in Fig. 5.30. It exhibits the same range of deviation (%) than those plots representing single $\kappa(\mathrm{m})$ curves and justifies the proper use of a multiple Casteel-Amis regression curve. The data are not limited to significant decimals so as to enable the reproduction of the data with their original precision. Irrespective of the salt, a maximum in the specific conductivity occurs, which

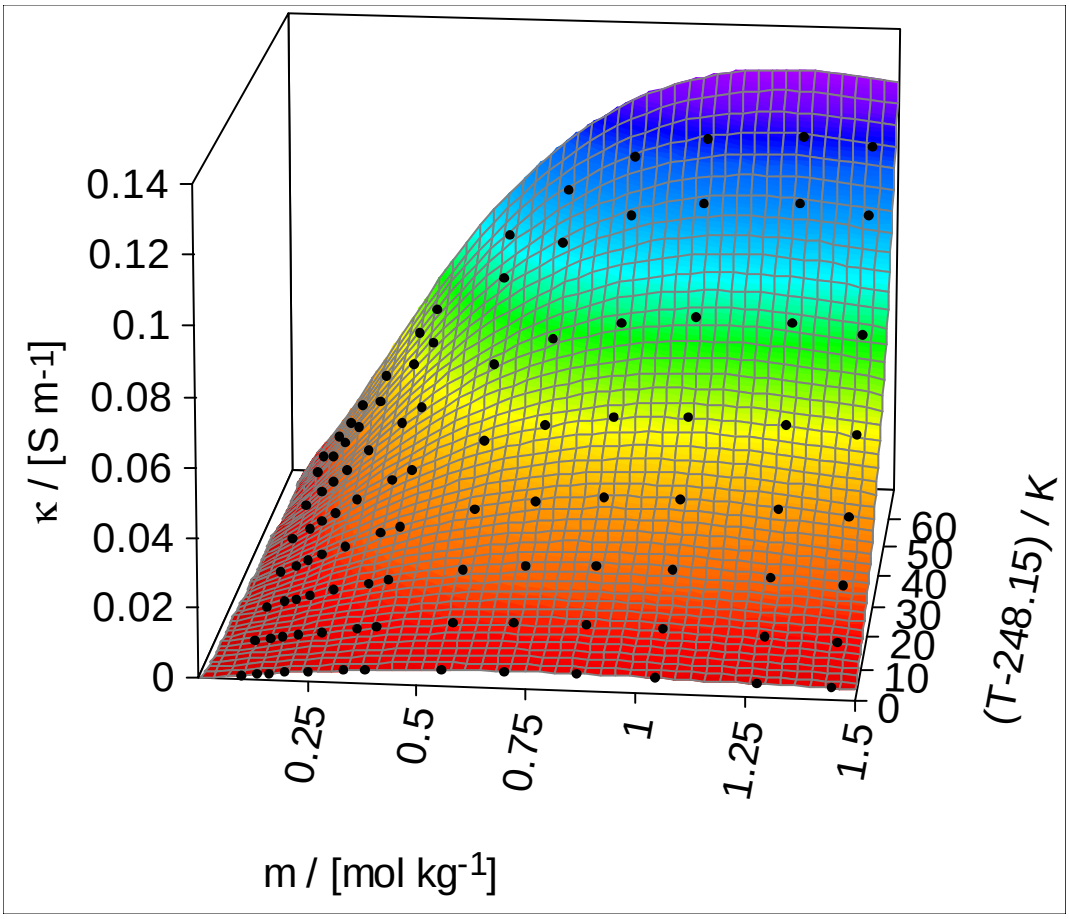

Figure 5.29.: 3-dimensional illustration of $\kappa(\mathrm{m}, T)$ of Bu_4NOAc in PnP

is explainable in the context of two competing effects. Based on the functional relation $\kappa = \Lambda c$ for 1:1 electrolytes, Eq. 5.45 describes the opposite effects $\Lambda \mathrm{d}c$ and $c\mathrm{d}\Lambda$. The term $\Lambda \mathrm{d}c$ is equivalent with the increase of conductivity due to the increasing amount of the number of ionic species $\mathrm{d}c$. The second term $c\mathrm{d}\Lambda$ describes the decrease of specific conductivity κ as a result of the decreasing ion mobility $\mathrm{d}\Lambda$ at increasing concentration. At the point of maximum conductivity, $\mathrm{d}\kappa = 0$, both terms are equal, $\Lambda \mathrm{d}c = |c\mathrm{d}\Lambda|$.
The conductivity maximum shows the interplay of the conductivity-determining parameters such as solvent permittivity, fluidity, solvating ability, and ionic size. This curve of $\kappa = \kappa(\mathrm{m}, T)$ is made clear by

Table 5.32.: Coefficiens of multiple regression for Bu_4NBr in PnP according to Eqs. (5.107)

248.15 K - 313.15 K	$\sigma_{\text{fit}} = 3.74 \times 10^{-4}$		
κ_{max} [S m^{-1}]		a	
a_0^κ	$3.847\,19 \times 10^{-3}$	a_0^a	1.20966
a_1^κ	$1.983\,57 \times 10^{-4}$	a_1^a	-7.7173×10^{-3}
a_2^κ	$1.076\,55 \times 10^{-5}$	a_2^a	$1.279\,65 \times 10^{-4}$
a_3^κ	$7.685\,05 \times 10^{-8}$		
μ [mol kg^{-1}]		b	
a_0^μ	0.852 96	a_0^b	0.142 16
a_1^μ	1.071×10^{-2}	a_1^b	-1.0917×10^{-2}
a_2^μ	$-3.287\,09 \times 10^{-5}$	a_2^b	$1.268\,21 \times 10^{-4}$

Table 5.33.: Coefficiens of multiple regression for Bu_4NNO_3 in PnP according to Eqs. (5.107)

248.15 K - 313.15 K	$\sigma_{\text{fit}} = 3.49 \times 10^{-4}$		
κ_{max} [S m^{-1}]		a	
a_0^κ	$4.485\,64 \times 10^{-3}$	a_0^a	1.15733
a_1^κ	$3.676\,31 \times 10^{-4}$	a_1^a	$3.513\,75 \times 10^{-3}$
a_2^κ	$2.502\,65 \times 10^{-5}$	a_2^a	-4.8064×10^{-5}
a_3^κ	-2.1502×10^{-8}		
μ [mol kg^{-1}]		b	
a_0^μ	1.011 98	a_0^b	0.155 08
a_1^μ	3.019×10^{-2}	a_1^b	9.697×10^{-4}
		a_2^b	-7.0167×10^{-6}

Table 5.34.: Coefficiens of multiple regression for Bu_4NSCN in PnP according to Eqs. (5.107)

248.15 K - 313.15 K	$\sigma_{\text{fit}} = 1.68 \times 10^{-4}$		
κ_{max} [S m^{-1}]		a	
a_0^κ	$5.522\,41 \times 10^{-3}$	a_0^a	1.00375
a_1^κ	$4.222\,34 \times 10^{-4}$	a_1^a	$5.064\,26 \times 10^{-3}$
a_2^κ	$1.433\,02 \times 10^{-5}$	a_2^a	-4.0038×10^{-5}
a_3^κ	$2.155\,95 \times 10^{-7}$		
μ [mol kg^{-1}]		b	
a_0^μ	1.268 67	a_0^b	5.0273×10^{-3}
a_1^μ	1.668×10^{-2}	a_1^b	5.6196×10^{-4}
a_2^μ	$-2.274\,72 \times 10^{-5}$	a_2^b	-9.9859×10^{-6}

Table 5.35.: Coefficiens of multiple regression for Bu_4NOAc in PnP according to Eqs. (5.107)

248.15 K - 313.15 K	$\sigma_{\text{fit}} = 7.69 \times 10^{-5}$		
κ_{max} [S m^{-1}]		a	
a_0^κ	$5.070\,33 \times 10^{-3}$	a_0^a	1.21997
a_1^κ	$3.583\,13 \times 10^{-4}$	a_1^a	$8.088\,84 \times 10^{-3}$
a_2^κ	$1.158\,69 \times 10^{-5}$	a_2^a	-2.7917×10^{-5}
a_3^κ	$1.209\,75 \times 10^{-7}$		
μ [mol kg^{-1}]		b	
a_0^μ	0.770 61	a_0^b	$-0.117\,52$
a_1^μ	6.14×10^{-3}	a_1^b	5.8412×10^{-3}
a_2^μ	$9.461\,05 \times 10^{-6}$	a_2^b	-3.9167×10^{-5}

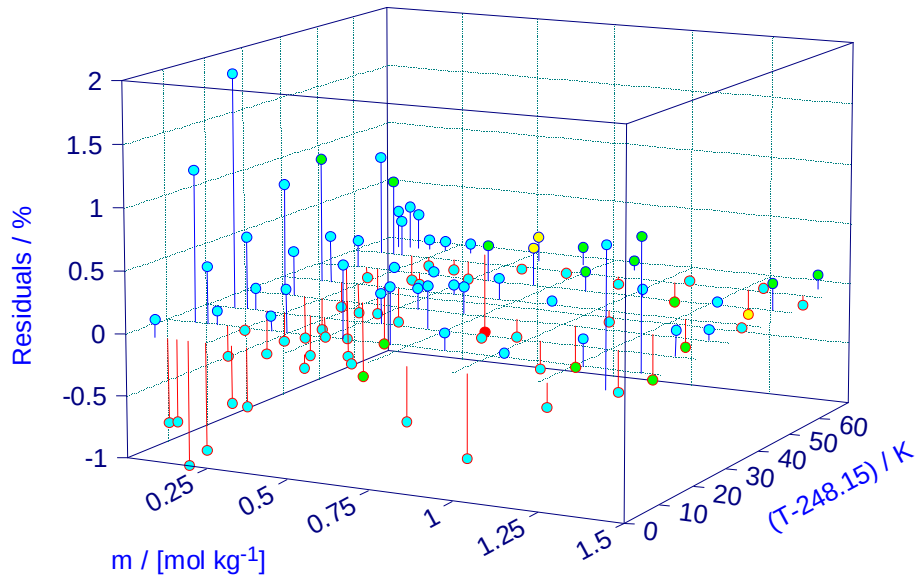

Figure 5.30.: Residual plot $(\kappa^{\mathrm{calc}} - \kappa^{\mathrm{exp}})/\kappa^{\mathrm{exp}} \cdot 100\,\%$

considering κ as a function of the molar conductivity Λ:

$$\kappa = c\Lambda = c\alpha \left[\Lambda^{\infty} - \Lambda^{\mathrm{rel}}(\alpha c;\, \Lambda^{\infty};\, R;\, \epsilon;\, T) - \Lambda^{\mathrm{el}}(\alpha c;\, R;\, \epsilon;\, \eta;\, T)\right] \tag{5.108}$$

In Eq. 5.108, Λ^{∞} depends on the radii of the solvated or unsolvated ions and on the viscosity of the solvent η, according to Stokes law. The viscosity, however, has a direct impact on the electrophoretic contribution Λ^{el}. Solvation effects will have an influence on the association behavior and association constant of the electrolyte and therefore alter the degree of dissociation α. For a given concentration (including κ_{max}) the following dependency of κ arises:

$$\kappa = \kappa\left(\frac{1}{\eta}, \frac{1}{r_+}, \frac{1}{r_-}, \frac{1}{K_A}, \ldots\right) \tag{5.109}$$

Unfortunately, it is almost impossible to change only one of the solvent parameters for systematic studies. For instance, the change of conductivity in a solvent mixture with the mole fraction of one component may be the result of changing viscosity, permittivity, and the change in the Stokes radius of the ions as a consequence of preferential solvation. All of them affect the ion-solvent (solvation) and ion-ion (association) interactions. Because of the interdependency between the parameters, a separate discussion of the single contributions is normally not possible and all possible factors, determining the conductivity, must be considered. Exceptions to this are comparable results of unsolvated tetraalkylammonium salts with similar association constants, showing the unperturbed effect of the anion's radii according to Stoke's law with linear dependency of κ_{max} with $1/r_+$ [245]. The increase of κ_{max} as unperturbed effect of decreasing association constant with constant ionic radii, solvation, and solvent parameters is known in DME with chemically modified, but similar anions [246].

5.7.4.1. Low permittivity Solvent PnP

Observing the correlation between specific conductivity and concentration for electrolyte systems with solvents of different dielectric constants and comparing them to the system of this work, a typical characteristic, very well known from the literature, can be detected.
In solvents with moderate to high dielectric constants there is a strong increase of conductivity with increasing concentration even at low concentrations. The maximum conductance is reached without a point of inflection in the $\kappa - \mathrm{m} -$curve. Numerous examples for such systems are known in the literature and collected in Ref. [173]. This behavior is typical for either 1:1 - or 1:2 - electrolytes. All those systems

are characterized by a high degree of dissociation with low values for K_A. According to Eq. (5.45) the term Λdc initially prevails and causes the increase of κ with increasing amount of electrolyte and its conducting constituents. Only now the amount of electrolyte is increased further, the contrarious effect $cd\Lambda$ of decreasing mobility due to the higher viscosity of the solution gives rise to the maximum and a following reduction of κ. This decrease is also caused by a higher degree of association with increasing number of ions. At concentrations below the maximum, the ion-pair process and the increasing viscosity do not play a major role. The later effects come into play at $m > m(\kappa_{max})$.
Contrary to that a different course of the electrical conductance in solvents or solvent mixtures with low permittivity can be observed. Beginning at the lower concentrations, see Fig. 5.25-5.28, the conductivity increases to a lower extent and reaches its maximum at increasing m passing an point of inflection. As the association constants are pretty high (see Sec. 5.6.6.2), the number of free ions does not appreciable increase with increasing concentration, as most ions are bound in the form of non-conducting ion-pairs (c. f. Sec. 5.1.2.3). According to Eq. (5.45) also the change of κ is rather small. Upon further concentration increase the specific conductivity shows a rise, which is explainable by assuming another equilibrium between uncharged ion-pairs and charged ion-triples:

$$\left[K^+A^-\right]^0 + \left[K^+A^-\right]^0 = A^- + \left[K^+A^-K^+\right]^+$$
$$\left[K^+A^-\right]^0 + \left[K^+A^-\right]^0 = K^+ + \left[A^-K^+A^-\right]^-$$

After those species are arising, the characteristic course and the occurrence of the maximum in conductivity is explainable in terms of the Eq. (5.45), again.
Similar results are also known in the literature, e. g. investigations on lithium salts in dimethoxyethane [238] and in propylene carbonate [246]. The temperature coefficients of molar conductivity show regular behavior for all salts under investigation, e. g. increasing conductivities with increasing temperature [247].
Considering systems with solvents of low permittivity the values for κ_{max} and μ are influenced by the different equilibria reactions, which are responsible for the increase of number of conductivity-determining, charged species. The position of κ_{max}, therefore, defines the amount of free ions in solutions. Thereby not only single ions, but also charge aggregates with different Stokes radii and different mobilities account for the specific conductivity [248]. Further applications of conductivity equations for dilute solutions, including the chemical equilibria of triple-ion formation as described above, would be required for a quantitative approval (see Sec. 5.8) [238].
An attempt to correlate the specific conductivity κ/m to the reciprocal ionic radii $1/r^-$ (or Stoke's radii $1/R^-$) of the anions at constant r^+, being an appropriate expression for investigating ion-solvent interactions in the framework of conductance-determining effects, fails. No reasonable dependency could be observed with the data obtained and therefore no correlation between the electrolyte mobility $\sim \lim_{m\to 0} \frac{\kappa}{m} \sim \Lambda^\infty$ and the dimension of the ions can be stated. Obviously, more conductance-determining effects beside geometrical considerations are playing an important role. A non-linear dependency in $1/r$ indicates a possible change in the anion's solvation with increasing electrolyte concentration [249], compared to the results of dilute measurements. This would then give a different mobility pattern and would not allow for an unambiguous trend in κ_{max}, according to Eq. (5.109).
As a result of the mutual dependencies of parameters, also the plot of $\kappa_{max} = f(\mu)$ does not correlate in a distinct manner, as would be expected from a solely dependency on η^{-1}, with both κ_{max} and μ expected to depend on η^{-1} in the same way. Consequently the solutions do not show Stoke's behavior.

5.7.4.2. Temperature Dependence of μ

For many practical reasons a proper estimation of the position of highest specific conductivity κ_{max} is advisable and preferable. Electrical conductance ought to be known approximately, in a first instance, covering the temperature range one is interested in. This might be of great interest in order to select measuring cells having proper cell constants for proper measuring, to design commercially usable electrolyte systems operating at the highest conductivity and to propose experimental parameters (m, T) aiming at a desired conductivity behavior.

Estimations of $\mu(T)$ are best described by the following simple relation

$$\mu = f(\eta_0^{-1}), \tag{5.110}$$

being η_0 the viscosity of pure solvent 1-propoxy-2-propanol. A corresponding plot in Fig. 5.31-5.32 makes this clear. Apparent from this plot is the strong influence of solvent's viscosity on the position μ of maximum conductivity for all salt systems. Decreasing viscosity, by increase of temperature, increases ion mobility. This effect is opposed by the less significant decrease in permittivity which diminishes the number of charged particles. The concentration μ at maximum specific conductance decreases with decreasing temperature for each system, i.e. with increasing viscosity. This proves that solvent viscosity is an important property controlling the energy barrier of the transport process [250]. The decrease of

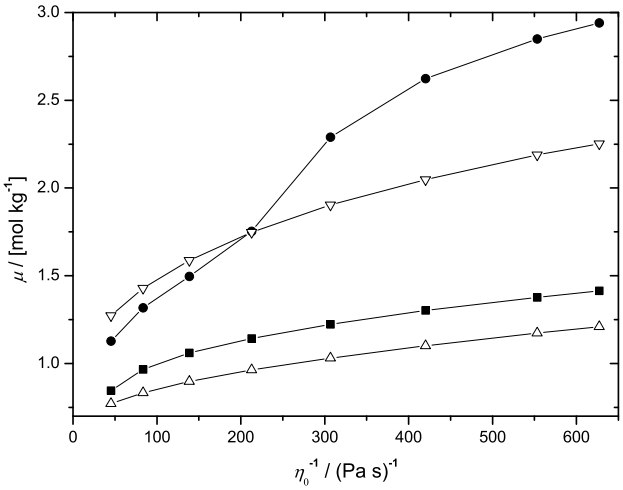

Figure 5.31.: Positions μ of the conductance maxima for Bu_4NNO_3 (●), Bu_4NSCN (▽), Bu_4NBr (■) and Bu_4NOAc (△)

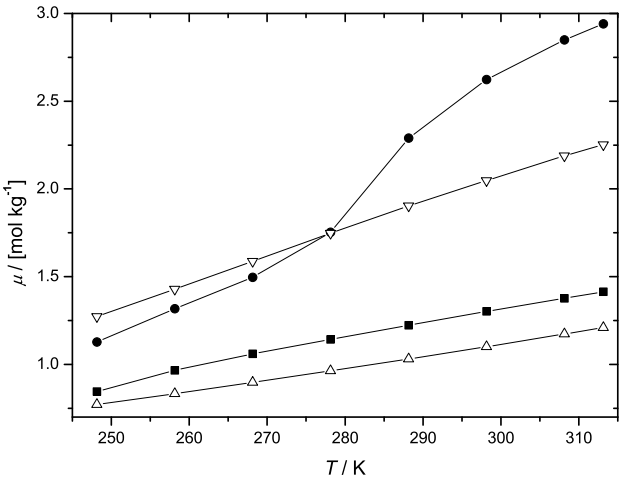

Figure 5.32.: Positions μ of the conductance maxima at various temperatures

viscosity reduces the activation energy of transport, and hence causes the shift of μ values to higher concentrations. The maximum κ_{max} also increases with decreasing viscosity, e.g. increasing temperature as visualized in the plots of $\kappa = \kappa(m)$.

The most obvious relation between electrical conductivity results at low concentrations and measurements at moderate to high concentrations is the trend of μ as function of ionic radii at constant temperature. That is evident from Fig. 5.32. Increasing Stokes radii in the order $NO_3^- < SCN^- < Br^- < OAc^-$ (see Sec. 5.6.6.2 which, in turns, is the reason for reversed order of K_A) lead to the opposite trend in the position of the conductance maximum. When compared at constant temperature, values of μ differ distinctly, $\mu(Bu_4NNO_3) > \mu(Bu_4NSCN) > \mu(Bu_4NBr) > \mu(Bu_4NOAc)$, in accordance with the order given before. As a result, the increased mobility of ions with small radii is apparent in the increase of μ. The uneven course in the system Bu_4NNO_3 may be rationalized by a similar trend of $\kappa_{max} = f(\mu)$, the reason of which most probably lies in experimental deficiencies.

The clear relationship between the position of maximum conductivity and viscosity for these systems are particularly conspicuous, as the salts have all very high association constants. Assuming the general functional form, an first approximation on the position of κ_{max} can be made previously to conductivity measurements or as basis for any electrochemical application.

5.8. Equivalent Conductance from Infinite Dilution to Saturation

Additionally to the experiments described up to now, completing conductivity measurements in the concentration range between infinite dilution (Sec. 5.6.4) and high concentration (Sec. 5.7.4) are performed in order to obtain a complete set of data covering the whole range of temperature and concentration.

Required density data of electrolyte solutions must not be missing for the conversion of molonity to molarity. Intermediate data points are completed by experimental conductance results with the help of the capillary cells explained in Sec. 5.7.1.
The dependence on concentration and temperature of molar conductance from infinite dilution to concentration close to saturation is illustrated in Fig. 5.8 for Bu_4NNO_3 in PnP. For the sake of clarity only three sets of data points at 313.15, 298.15, and 268.15 K are shown. The plots of Λ versus $c^{1/2}$ show a minimum

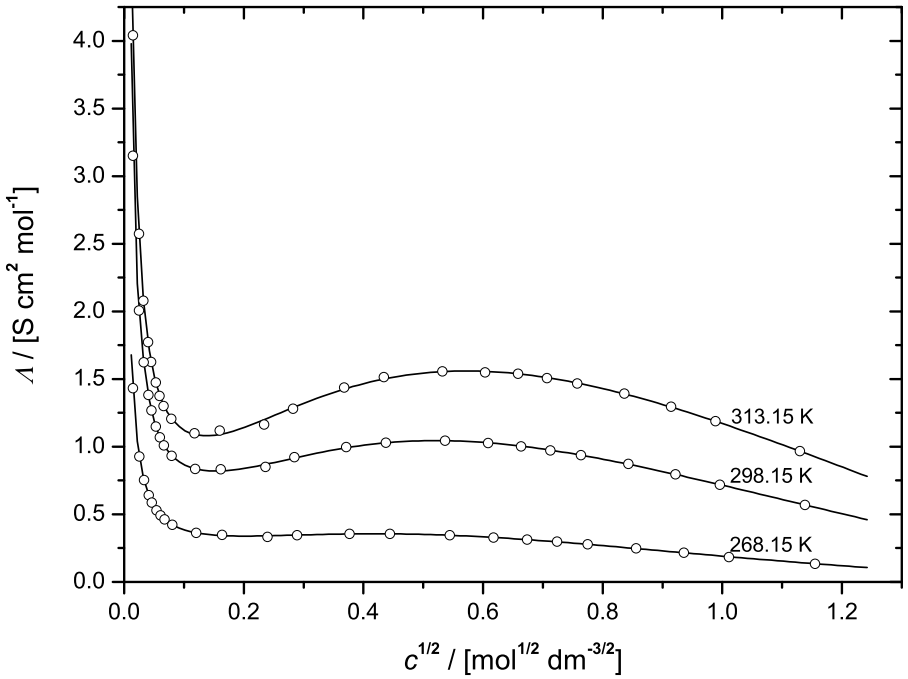

Figure 5.33.: Molar conductance of Bu_4NNO_3 solutions in PnP at different temperatures

at moderate concentrations and a maximum at high concentrations. Both the minima and maxima show a strong displacement with temperature. The minima of conductance, $\Lambda_{\min}^{\exp}$, and their position, $c_{\min}^{\exp}$, compiled in Table 5.36 are the consequences of competing species for the contribution to conductivity, free ions and triple-ions, and non-conducting species, ion-pairs and higher aggregates. Obviously the equilibria between these species in the solution depend on the solvent permittivity, which increases with decreasing temperature. The higher permittivity at low temperatures results in higher concentrations of free ions and a shift of the minimum $c_{\min}^{\exp}$ to higher values. Missing data points for Bu_4NBr close to the minimum do not enable a precise determination of this characteristic point. No distinct minima occur at the two lowest temperatures in the system Bu_4NSCN. The position dependence and reasons for the occurrence of the maximum in conductance have already been described in Sec. 5.7.4. The minimum is commonly found for systems in which bilateral triple-ion formation occurs

$$\left[C^+\,A^-\right] + C^+ \overset{K_T^+}{\rightleftharpoons} \left[C^+\,A^-\,C^+\right]^+ ; \tag{5.111a}$$

$$\left[C^+\,A^-\right] + A^- \overset{K_T^-}{\rightleftharpoons} \left[A^-\,C^+\,A^-\right]^- , \tag{5.111b}$$

where generally the triple ion formation constant K_T^+ is assumed to be equal to K_T^-. This concept of triple ion formation was first introduced by Fuoss and Kraus [251] as early as 1933 to explain the occurrence of a minimum in the concentration dependence of electrical conductivity of electrolytes in solvents of low dielectric constant (additional notes on mathematical consequences are given by Baughan [252]). Instead of using their inverse values for the formation constants, the following equation takes into account the

Table 5.36.: The minimum of molar conductance, $\Lambda_{\min}^{\exp}$ ($\mathrm{S\,cm^2\,mol^{-1}}$), and its position, $c_{\min}^{\exp}$ ($\mathrm{mol\,dm^{-3}}$), at various temperatures as calculated with the help of the interpolation polynomial $\ln\Lambda = a_0 + a_1 \ln c + a_2\,(\ln c)^2 + a_3\,(\ln c)^3$.
Calculation is based on measurements No. 1-9 (Bu_4NBr), 1-11 (Bu_4NNO_3), 1-13 (Bu_4NOAc), 1-9 (Bu_4NSCN)

T / K	248.15	258.15	268.15	278.15	288.15	298.15	308.15	313.15
				Bu_4NBr				
$10^2\,c_{\min}^{\exp}$	5.593	11.189	4.326	3.667	3.045	2.608	2.205	2.016
$\Lambda_{\min}^{\exp}$	0.1073	0.1714	0.2839	0.4071	0.5470	0.6997	0.8580	0.9378
				Bu_4NNO_3				
$10^2\,c_{\min}^{\exp}$	7.932	5.971	4.641	3.713	3.120	2.464	2.349	2.006
$\Lambda_{\min}^{\exp}$	0.1288	0.2193	0.3368	0.4803	0.6414	0.8208	0.9992	1.0947
				Bu_4NOAc				
$10^2\,c_{\min}^{\exp}$	6.525	4.955	3.923	3.313	2.857	2.740	2.362	2.271
$\Lambda_{\min}^{\exp}$	0.1329	0.2193	0.3276	0.4505	0.5796	0.7043	0.8297	0.8872
				Bu_4NSCN				
$10^2\,c_{\min}^{\exp}$	–	–	5.068	4.384	1.702	1.395	1.165	1.093
$\Lambda_{\min}^{\exp}$	–	–	0.3545	0.5258	0.6917	0.8856	1.0864	1.1871

equilibria between ions–ion pairs, K_A, and ion-pairs–triple-ions ($K_T = K_T^+ = K_T^-$):

$$g(c)\Lambda\sqrt{c} = \frac{\Lambda\gamma_\pm'\sqrt{c}}{1 - S\sqrt{\Lambda^\infty}^3\sqrt{\Lambda c\,(1 - \Lambda\,/\,\Lambda^\infty)}} = \frac{\Lambda^\infty}{\sqrt{K_A}} + \lambda_T^\infty \frac{K_T}{\sqrt{K_A}}\,(1 - \Lambda\,/\,\Lambda^\infty)\,c \tag{5.112}$$

It is the appropriate equation for reproducing the conductivity curve up to concentrations near the conductivity minimum. The range of points included in the data analysis is indicated in Table 5.36 for each salt system. In Eq. (5.112) $\gamma_\pm'$ is the mean activity coefficient of the free ions as given by Eq. (5.91); S is the limiting slope given in [160]; λ_T^∞ the limiting value of the triple ions $C^+A^-C^+$ and $A^-C^+A^-$, which must be estimated. Fuoss and Kraus propose to set $\lambda_T^\infty = 1/3\Lambda^\infty$ [251]; later this value was corrected to $2/3\Lambda^\infty$ [253, 254] and used within this work. The quantity Λ^∞ is known from Tables 5.18-5.21.
Plots of $g(c)\Lambda\sqrt{c}$ against $(1 - \Lambda\,/\,\Lambda^\infty)\,c$ were fitted in a linear fashion to obtain $\sqrt{K_A}$ from the intercept and consequently K_T from the slope. The results are reported in Table 5.37. Values quoted are the results of evaluation taking explicitly into account the additional equilibria for triple-ion formation (K_A, K_T), as well as the results of the low-concentration Chemical Model (K_A). Although the association constants of the independent evaluation methods differ to a certain extent from each other at every temperature, they can be regarded as similar within the overall accuracy and are in the same range of magnitude. It is worth to note that both ion-pair and triple-ion formation decrease with decreasing temperature in accordance with increasing solvent permittivities and, therefore, shows temperature coefficients with meaningful sign. Variation of λ_T^∞ within the limits set by the different authors is shown to have no significant influence on the absolute value of K_T.
Using the results from Table 5.37, the triple-ion formation is admittedly small but detectable. Differences to values as obtained by a 2-parameter evaluation with Λ^∞ being introduced in Eq. (5.90) with a fit carried out to yield K_A^{FJ2}, may be partially attributed to the different model, neglecting the possibility of triple-ion formation. In consideration of the uncertainty in the evaluated parameters (mainly due to problems of proper extrapolation to infinite dilution), however, this discrepancies can be put into perspective by the fact that the same trend of K_A with the anions can be found and a reasonable, positive

Table 5.37.: Ion-pair and triple-ion formation constants of solutions in PnP for the temperature range $248.15 < T/\mathrm{K} < 313.15$

Temp. / Method	$\frac{T}{\mathrm{K}}$	248.15	258.15	268.15	278.15	288.15	298.15	308.15	313.15
					Bu_4NBr				
FK extended	$\frac{10^{-4}\,K_A}{\mathrm{mol^{-1}\,dm^3}}$	6.07	8.75	6.84	11.28	17.27	20.93	23.92	27.18
	$\frac{K_T}{\mathrm{mol^{-1}\,dm^3}}$	60	67	77	83	90	98	107	110
					Bu_4NNO_3				
FK extended	$\frac{10^{-4}\,K_A}{\mathrm{mol^{-1}\,dm^3}}$	5.09	7.37	9.92	14.10	20.16	24.78	26.77	27.58
	$\frac{K_T}{\mathrm{mol^{-1}\,dm^3}}$	56	62	68	74	80	86	91	96
					Bu_4NOAc				
FK extended	$\frac{10^{-4}\,K_A}{\mathrm{mol^{-1}\,dm^3}}$	3.57	3.57	4.50	5.70	7.83	11.12	13.61	14.71
	$\frac{K_T}{\mathrm{mol^{-1}\,dm^3}}$	51	55	58	61	63	65	67	68
					Bu_4NSCN				
FK extended	$\frac{10^{-4}\,K_A}{\mathrm{mol^{-1}\,dm^3}}$	–	6.91	8.55	11.28	19.38	21.63	25.60	25.98
	$\frac{K_T}{\mathrm{mol^{-1}\,dm^3}}$	–	85	90	95	99	103	107	108

temperature coefficient $\mathrm{d}K_A\,/\,\mathrm{d}T$ is observable.
Noteworthy to say that the concept of conducting triple-ion formation, very recently included in a comprehensive review on ion pairing [255], became so popular, that conductance minima alone were often given as proof for the presence of triple-ions [256]. Alternatively, Sukhotin and Timofeeva [257] challenged this theory arguing that transference data are not consistent with this model. They explain the existence of a minimum in the molar conductance as a function of concentration as attributable to the redissociation of ion pairs, formed initially at lower concentrations. An increase in the permittivity, which results from the polarization of the solution under the influence of dipolar ion pairs, entails a decrease of the ion-pair formation constant leading to an increase in the fraction of free or solvated ions [258]. A different approach determining the association constant for ion pairing in terms of multibody interaction, expresses the various kinds of interactions in terms of activity coefficients [259]. Applying the mean spherical approximation (MSA) for the activity coefficients, the description of conductance minima can be accounted for without the additional assumption of triple-ion formation [260]. Microwave dielectric relaxation measurements have confirmed the increase of the dielectric permittivity of electrolyte solutions with electrolyte concentration for many systems [261]. It is evident from that point of view, that only more comprehensive investigations on the electrolyte's influence on the dielectric behavior of PnP may serve as proof for the possible existence of triple-ions in those systems.

6. Vapor Pressure of Pure PnP and its Solutions of Electrolytes

In addition to the precise determination of electrical conductance properties of Bu_4NX ($X = Br^-$, NO_3^-, SCN^- and OAc^-) salts in PnP in the range of temperatures between $248.15 - 313.15\,K$, experimental results on the vapor pressure measurements on the same electrolyte systems are communicated in this chapter. They cover a different temperature region between $323.15 - 413\,K$ and are restricted to the medium to high concentration range. Values of Δp are used to obtain the osmotic coefficient ϕ, which is compared to results of different model equations. These equations are known to represent the concentration dependency of osmotic coefficients with high precision and allow for the calculation of the mean activity coefficient of the electrolyte. From the inspection of $\phi = f(\mathrm{m})$ and the influence of different interactions on the value of ϕ, one can obtain (qualitative) information on the ion-ion (association) and ion-solvent (solvation) interactions.
Combining the results of both methods, conductance studies on dilute solutions and vapor pressure studies at moderate concentrations, should extended the range of temperature, within which a comparison of the interactions between ions and solvent molecules is made possible.
Direct vapor pressure measurements are a very reliable method for the experimental determination of osmotic coefficients over a wide electrolyte concentration range. These osmotic coefficients come along without any need for external standards and are independent of any adjustment parameters. Further examples of different approaches to osmotic coefficients are

- isopiestic vapor pressure method: the solution in question is equilibrated with a reference solution containing a nonvolatile solute with precisely known solvent activity. The two solutions are placed in an enclosure at constant T until their vapor pressures are equal, i. e. the activity of solvent is equal. They are then analyzed for their concentration by weighing

- vapor pressure osmometry: the difference in vapor pressure of pure solvent and its solution is compensated by condensation of the solvent saturating the gas phase until both vapor pressures are balanced. This condensation leads to the measurable temperature difference between the droplets applied on two thermistors.

- head-space gas chromatography: following the standard relation, the vapor pressure of solvent over the studied solutions, p, is evaluated with the direct proportionality between vapor pressure and the response factor of detector (peak area). Measurements at different temperatures are easily possible

These methods, however, require precisely known reference data for the activity of the solvent in a selected reference system, which are often not available in good quality. Such standards are provided by the measurements of vapor pressure lowering on the solvent system under investigation. The number of organic solvent systems for which osmotic coefficients from vapor pressure are known is actually still limited [157].
Based on the fact that PnP has a relatively low vapor pressure, it is believed to become no reliable reference standard for osmotic coefficients in electrolyte systems. Nevertheless, direct vapor pressure measurements allow for the comparable determination of solute and solvent activities over a wide range of temperatures.
As there are values for PnP as pure solvent missing over the given temperature range in the literature, one part of this work is devoted to the precise measuring of p^* between 298.15 and 413.15 K. The present measurement extends the relatively small temperature range of previous investigations with the same apparatus [15]. Their results show higher values for the vapor pressure without exception, indicating an insufficient degassing procedure or residual impurities within the solvent.

6.1. Activity Coefficients and Osmotic Coefficients

The chemical potential of the solvent in electrolyte solutions are always used with reference to the pure solvent

$$\mu_S(p,T) = \mu_S^*(p,T) + \mathrm{R}T\ln a_S = \mu_S^*(p,T) + \mathrm{R}T\ln x_S f_S \tag{6.1}$$

$$\mu_S^*(p,T) = \lim_{x_S\to 1}\mu_S(p,T); \qquad \lim_{x_S\to 1} f_S = 1 \tag{6.2}$$

and that of the electrolyte is given either in the molarity or in the molality scale m (shown here exclusively). The reference is given by the infinite dilute solution of electrolyte.

$$\mu_Y(p,T) = \mu_Y^\infty(p,T) + \mathrm{R}T\ln a_Y = \mu_Y^\infty(p,T) + \mathrm{R}T\ln(\mathrm{m}_Y\gamma_Y) \tag{6.3}$$

a_S, a_Y, f_S und γ_Y represent the activity and activity coefficients, respectively, of solvent S and electrolyte Y. x_S is the mole fraction of the solvent. Molality is a reasonable choice for concentration scale of the solute, due to its easy experimental accessibility.
In order to interconvert between the activity coefficients of both concentration scales, the following relations

$$c = \mathrm{m}\,d_S\,F(\mathrm{m}) = \mathrm{m}\,d_S\,\frac{1+(A/d_S)\cdot\mathrm{m}}{1+(M/1000)\cdot\mathrm{m}}; \qquad d = d_S + A\cdot\mathrm{m} \tag{6.4}$$

might be applied to obtain a relationship between the activity coefficients y in the molarity and the molality γ scale [262]:

$$\ln\gamma = \ln y + \ln(F(\mathrm{m})). \tag{6.5}$$

$F(\mathrm{m})$ describes the linear density coefficient, very similar to Eq. (5.79).
According to Eq. (5.32) the chemical potential of the electrolyte Y can be split into its contribution from cations and anions:

$$\mu_Y = \nu_+\mu_+ + \nu_-\mu_- \tag{6.6}$$

with the stoichiometric factors ν_+, ν_-. Combining the reference potentials according to $\mu_Y^\infty = \nu_+\mu_+^\infty + \nu_-\mu_-^\infty$ yields an expression for the chemical potential of the electrolyte compound

$$\mu_Y = \mu_Y^\infty + \nu\mathrm{R}T\ln(\mathrm{m}_\pm\gamma_\pm) \tag{6.7}$$

$$\mathrm{m}_\pm^\nu = \mathrm{m}_+^{\nu_+}\mathrm{m}_-^{\nu_-} \tag{6.8}$$

$$\gamma_\pm^\nu = \gamma_+^{\nu_+}\gamma_-^{\nu_-} \tag{6.9}$$

$$\nu = \nu_+ + \nu_- \tag{6.10}$$

with $\nu = 2$ and $\mathrm{m}_\pm = \mathrm{m}_Y$ for a symmetrical 1:1 electrolyte, used exclusively in this work.
Making use of the Gibbs-Duhem Eq. (4.52) at constant pressure and temperature

$$\mathrm{d}\mu_S + \frac{n_Y}{n_S}\mathrm{d}\mu_Y = \mathrm{d}\mu_S + \mathrm{m}M_S\mathrm{d}\mu_Y = 0 \tag{6.11}$$

and considering the definition of the chemical potentials (6.1)(6.3), simple conversions yield

$$\mathrm{d}\ln a_S + \nu\mathrm{m}\,M_S\,\mathrm{d}\ln(\mathrm{m}\gamma_\pm) = 0 \tag{6.12}$$

Together with the definition of the osmotic coefficient ϕ:

$$\phi = -\frac{1000\ln a_S}{\nu\,\mathrm{m}\,M_S} \Rightarrow \mathrm{d}\ln a_S = -\nu\,M_s\,\mathrm{d}(\mathrm{m}\phi) \tag{6.13}$$

Eq. (6.12) yields the basic equation for the calculation of the solute activity coefficient from the osmotic coefficient and vice versa.

$$-\mathrm{d}(\mathrm{m}\phi) + \mathrm{m}\,\mathrm{d}\ln(\mathrm{m}\gamma_\pm) = 0 \tag{6.14}$$

Finally the integration of Eq. (6.14) with regard to the variable m between the limits m_1 and $m = 0$ in the calculation of $\ln\gamma_\pm$ give

$$\ln\gamma_\pm = \phi(m_1) - 1 - \int_0^{m_1} \frac{1-\phi}{m}\,dm \tag{6.15}$$

on the other hand, it follows from Eq. (6.14) that

$$\phi = 1 + \frac{1}{m_1}\int_0^{m_1} m\,d(\ln\gamma_\pm) \tag{6.16}$$

Weak Electrolytes Ionophore electrolytes of high ionic charge or in solvents of low permittivity are very likely to form ion associates, in accordance with the evaluation of electrical conductivity data in Sec. 5.1.2.3. The association constants may be taken into account by splitting the activity coefficient $\gamma_\pm$ according to Eq. (5.91).
The corresponding degree of dissociation α follows from the association constant in the molarity scale, $K_A^{(m)}$:

$$K_A^{(m)} = \frac{1-\alpha}{\alpha^2 m}\frac{\gamma_0}{\gamma'_\pm} \tag{6.17}$$

with γ_0, $\gamma'_\pm$ being the activity coefficient of the ion associate and the mean activity coefficient of the free ions, respectively. γ_0 may be regarded as unity for dilute solutions [262].
Taking into consideration Eq. (5.91), similar conclusions starting from Eq. (6.12) can be derived for the relationship between mean activity coefficient of the free ions, $\gamma'_\pm$ and osmotic coefficient ϕ. Therefore, a partially dissociated electrolyte give rise to a mean activity coefficient expressed as $\gamma_\pm = \alpha\gamma'_\pm$:

$$\ln\left(\alpha\gamma'_\pm\right) = \phi(m_1) - 1 - \int_0^{m_1}\frac{1-\phi}{m}\,dm \qquad \phi = 1 + \frac{1}{m_1}\int_0^{m_1} m\,d(\ln\alpha\gamma'_\pm) \tag{6.18}$$

The reader is referred to Ref. [262] for a detailed description of the thermodynamic treatment of association in terms of the chemical potential and the osmotic coefficient.
The set of Eqs. (6.17)(6.18) may be used either for the data analysis to yield the quantities K_A from the measured osmotic coefficients. On the other hand the equations can be used for the simulation of osmotic coefficients with the help of association constants K_A from other methods, e. g. electrical conductivity (see Chap. 5).

6.2. Experimental Osmotic Coefficients

Vapor pressure measurements of an electrolyte solution made up from a solvent and a non-volatile electrolyte at different concentrations enables the calculation of the solvent's activity a_S and therefore of the osmotic coefficient ϕ.
As a prerequisite, an vapor-liquid equilibrium at temperature T with equal potentials of the pure solvent's vapor, $\mu_S^{*(g)}$, and that of the liquid phase, $\mu_S^{(l)}$, must be established.

$$\mu_S^{*(g)} = \mu_S^{*(l)} + RT\ln a_S \tag{6.19}$$

Rearrangement gives

$$d\ln a_S = \frac{1}{RT}\left[\left(\frac{\partial\mu_S^{*(g)}}{\partial p}\right)_T - \left(\frac{\partial\mu_S^{*(l)}}{\partial p}\right)_T\right] dp \tag{6.20}$$

With the defining equation for the molar volume

$$v^{*(g)} = \left(\frac{\partial\mu_S^{*(g)}}{\partial p}\right)_T \qquad v^{*(l)} = \left(\frac{\partial\mu_S^{*(l)}}{\partial p}\right)_T \tag{6.21}$$

Eq. (6.20) is rewritten as

$$\mathrm{d}\ln a_S = \left(\frac{v^{*(g)} - v^{*(l)}}{\mathrm{R}T}\right) \mathrm{d}p \tag{6.22}$$

This differential is subsequently integrated within the limits of the pure solvent vapor pressure p^* and the vapor pressure above the solution p to obtain

$$\ln a_S = \int_{p^*}^{p} \left(\frac{v^{*(g)} - v^{*(l)}}{\mathrm{R}T}\right) \mathrm{d}p \tag{6.23}$$

Taking into account the second virial coefficient B_S of the solvent vapor, $v_\mathrm{S}^{*(g)} = \dfrac{\mathrm{R}T}{p} + B_\mathrm{S}$, from the virial equation of state, neglecting the pressure dependence of the liquid molar volume, integration of Eq. (6.22) yields the activity of the solvent

$$\ln a_S = \ln\frac{p}{p^*} + \left(\frac{v^{*(l)} - B_S}{\mathrm{R}T}\right)(p^* - p) \tag{6.24}$$

Upon combination of Eq. (6.24) with the definition of osmotic coefficient, Eq. (6.13), the final expression for the experimentally accessible osmotic coefficient is readily obtained.

$$\phi = -\frac{1000}{\nu\,\mathrm{m}\,M_S}\left(\ln\frac{p}{p^*} + \left(\frac{v^{*(l)} - B_S}{\mathrm{R}T}\right)(p^* - p)\right) \tag{6.25}$$

It is calculable from the vapor pressure of the pure solvent and the vapor pressure decrease, $\Delta p = p^* - p$, caused by the solute at molality m [263]. In these equations a_S is the activity of the solvent, ν is the stoichiometric ionization number of the salt, M_S is the molecular weight of the solvent, T is the absolute temperature, p is the vapor pressure of the solution, p^* is that of the pure solvent and $v^{*(l)}$ is the molar volume of the pure liquid solvent. The necessary data for calculation of the second virial coefficient for PnP in the studied temperature range are taken from [264] and the second virial coefficients are calculated with a method described by Xiang [83]. The second virial coefficient of the solvent, B_S, molar volume of solvent, $v^{*(l)}$ and pure solvent vapor pressure, p^*, from $T = (323.15$ to $413.15)$ K with 10 K intervals are presented in Table 6.1.

6.3. Experimental Section

The differential-pressure measurement apparatus used in this work for operations at temperatures between 323.15 and 413.15 K, as described in detail in the following section, is based in principle on the highly precise measuring system built in our institute several years ago [265]. The constructive set-up, sample preparation, measuring procedure as well as data processing is used in a similar form in this original work to extend the vapor pressure of pure PnP down to the region around room temperature and will be briefly described in Sec. 6.3.2.

6.3.1. Measuring Device for Elevated Temperatures

The structure and main parts of the apparatus capable to measure the vapor pressure and vapor pressure depression up to high temperatures (depending on the thermostat oil) is shown in Fig. 6.1 and is graphically depicted in the photograph 6.2. The apparatus consists of a liquid thermostat (`Lauda UB 30J`) filled with a silicone oil (`M10, Bayer`) of low viscosity. The liquid bath is surmounted by an air thermostat specially designed to fit closely on top of the thermostat and to accommodate the pipeline system, heater (4), fan (6) and temperature sensors (5). It is composed of stainless steel double-walls filled with insulation material. The front-side of the air thermostat can either be closed by a removable insulation wall or by a transparent window made of plexiglass. The later is practically used to visualize

Table 6.1.: Second virial coefficient, B_S, molar volume, $v^{*(l)}$ and vapor pressure, p^*, of pure PnP at different temperatures.

T	$B_S\,(\mathrm{x}\,10^3)^{\mathrm{a}}$	$v^{*(l)}\,(\mathrm{x}\,10^4)^{\mathrm{b}}$	$p_{\mathrm{PnP}}^{\mathrm{vap\ c}}$
K	$\mathrm{m^3\,mol^{-1}}$	$\mathrm{m^3\,mol^{-1}}$	Pa
323.15	−4.180	1.378	1707
333.15	−3.745	1.394	2967
343.15	−3.377	1.410	4951
353.15	−3.063	1.427	7963
363.15	−2.791	1.444	12385
373.15	−2.556	1.463	18697
383.15	−2.350	1.482	27424
393.15	−2.168	1.502	39182
403.15	−2.007	1.523	54753
413.15	−1.864	1.546	74983

[a] Xiang [83]
[b] Eq. (5.53)
[c] Sec. F.1

the homogenous distribution of some smoke, illustrative for an equal temperature profile within the thermostat box. In the connection line between solvent and solution flask the differential pressure sensor Δp (`MKS Baratron`, Type 616A01TRE) is mounted, connected to a remote preamplifier by triaxial cables outside the thermostat. It has a pressure range of ±1 Torr and a stated accuracy of ±0.25 % of reading. To prevent condensation of the solvent's vapor in the gas phase, the temperature of the air thermostat is always kept approximately 10 K higher than the liquid thermostat. For that purpose an electronic control unit (9, `Juchheim GmbH, type LTR 4200`) is connected to 2 temperature sensors (5), located inside the thermostat box. Upon exceeding a preselected maximum temperature the safety shutdown of the heating (4) will occur.
For the absolute pressure measurement up to 133 kPa (1000 Torr), an internally thermostatted absolute pressure sensor p_{abs} (`MKS Baratron`, type 690A13TRB) positioned outside the air thermostat is used. It has an accuracy of ±0.12 % of reading; each pressure sensor is operated in conjunction with an MKS Type 670 Electronic Unit. A personal computer, equipped with a program to read out both sensor signals, transfers the data points and saves it to disc. Typically a time-dependent measurement will have the form display in Fig. 6.4.
The absolute pressure sensor's reading was checked by measuring the temperature dependent vapour pressure of water [266, 267] and ethanol [268] with deviations from literature values being smaller than 0.25 %. Aqueous solutions of sodium chloride are employed in the calibration of the differential sensor within the range of 1 Torr [269]. No corrections are applied for the absolute value of the differential pressure sensor's signal when being used only as null device (see page 144).
The liquid thermostat is calibrated with the help of a precision platinum resistance thermometer (see Sec. 5.2) with an uncertainty of less than 10^{-2} K. Each temperature is programmed with the help of unit control (8). Temperature fluctuations are less than 0.004 K. A silicon oil is used in the liquid bath, the atmosphere of which is steadily flushed with inert nitrogen to avoid degradation at high temperatures. The temperature gradient inside the air thermostat, depending on the distance to the heater, is proven to be less than 3 K. Homogenous temperature inside is promoted by the fan (6) on top of the insulation box. To maintain a great tolerance for high temperatures the pipeline system within the air thermostat consists of stainless steel pipes of 6 mm internal diameter, flask sockets and valves (`Swagelok`). It connects the differential pressure sensor to the sample (V1), the solvent (V2) and the external buffer vessel (7) via valve (V4). Establishing equalized pressure on both sides of the differential sensor is achieved by valve (V3), necessary to adjust the zero point. Valve (V5) connects the apparatus to the vacuum system

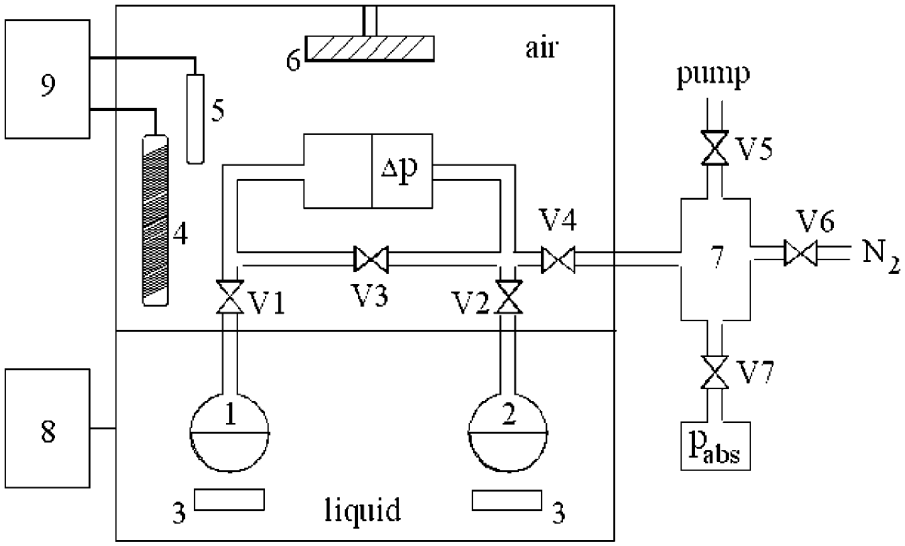

Figure 6.1.: Scheme of the vapor pressure apparatus. 1 and 2, glass flasks with solution and pure solvent; 3, magnetic stirrer; 4, heater regulating air temperature; 5, temperature sensor; 6, circulating ventilator; 7, buffer vessel (only high-temperature apparatus); 8 and 9, control units for heating device; V1 to V7, valves.

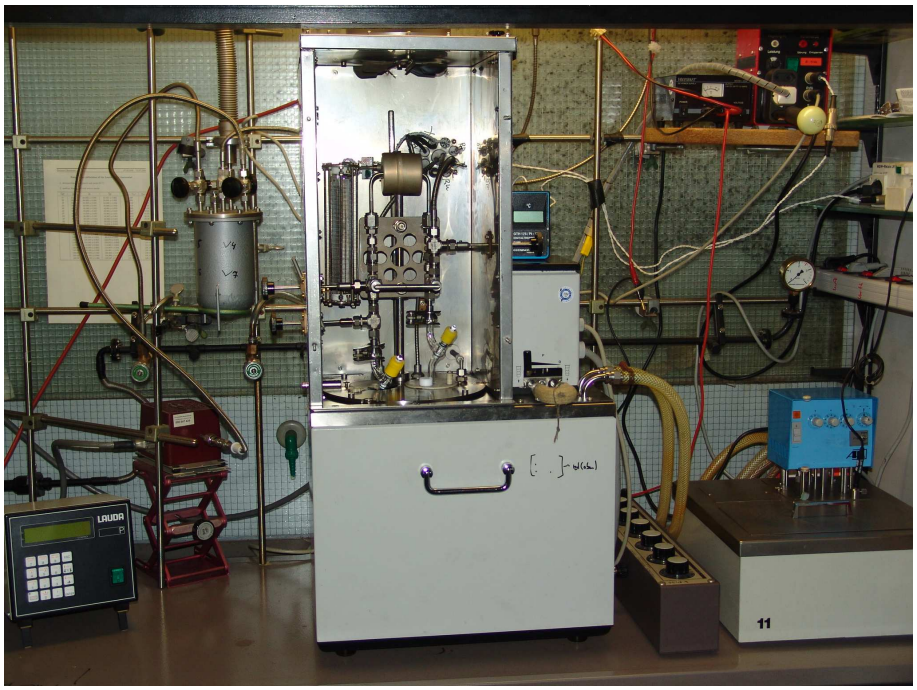

Figure 6.2.: Photograph of vapor pressure apparatus applied for high-temperature measurements

(Edwards, EXC 120). Specially designed adapters are attached to the valve handles to enable their control from outside the air thermostat. Stirring of the liquids is promoted throughout the measurements to ensure an even temperature distribution and to avoid retardation of boiling inside the sample flasks. Some modifications regarding the sampling flask have been made. The formerly used Ultra-Torr fittings of Swagelok® to connect the glass flask to the apparatus are replaced by lighter and leak-proofed Young® - stopcocks in conjunction with Rotulex® joints, allowing a higher accuracy of weighing the sample flask and the reduction of the overall leaking-rate by a factor of 2 in the system.
The vacuum system employed consists of a two Stage rotary vane pump (RV3) and a turbo pump (EXT 70) downstream. The pumping station is operated by a single controller unit (EXC 120) and responsible for the proper evacuation of the measuring device after each single vapor pressure measurement. New series of vapor pressure determinations follow a period of complete evacuation of more than 12 h. The final pressure achieved in this way is less than 10^{-5} Torr. Between the line of buffer vessel and vacuum pump a cryogenic trap ensures that no condensable vapor phase is entering the sensitive turbo pump.

Degassing The complete degassing of the pure PnP and the calibration liquids (water, ethanol) is essential for precise vapor pressure measurements. Otherwise, dissolved gases will give rise to an apparent higher total pressure of solvent or solution. The same is true for impurities, especially those with considerable higher volatility than the main component. The procedure is similar to that of Neueder [265] in a modified version by Kunz [270], both being based on the work of Dunlop [271]. A vacuum system, consisting of a rotary vane pump (LEYBOLD-HERAEUS, D16A) and a oil diffusion pump (LEYBOLD-HERAEUS, 22620), is attached to the degassing unit, which is shown in the picture. The system's final pressure is

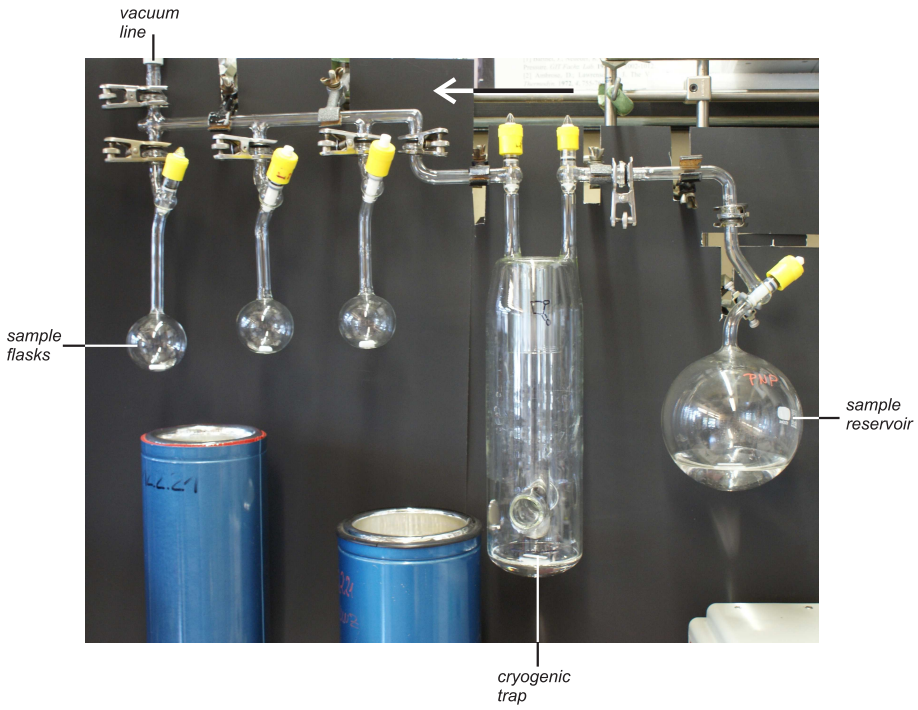

Figure 6.3.: Degassing unit; the arrow indicates the direction of gas flow

lower than 10^{-5} Torr with a cryogenic trap in line of the vacuum system capable of absorbing as much as 500 mL of condensable vapor.
In a first step most of the dissolved gases are carefully removed by applying weak vacuum to the rigorously stirred liquid (appr. 500 mL). This is done by gradually increasing temperature up to 80 °C (PnP, water) and 50 °C (Ethanol). Leaving the valve to the vacuum line slightly open the solvent is subsequently distilled under high vacuum into the cryogenic trap, from which it is distilled under vacuum into the sample flasks after thawing over night. Enhancement of the distillation is achieved by heating the solvent in the cryogenic trap as well. By adjusting the Young stopcocks a proper distillation equilibrium

is adjusted in order to dissipate the heat of condensation in the parts cooled by liquid nitrogen. An equal level of nitrogen is attended in the dewar to keep the whole amount of solvent frozen during the degassing process. A total volume of not more than 500 mL is recommended to be distilled at once into the cryogenic trap.
Permanent gases being efficiently removed during this degassing process, which takes approximately 3 days. Different charges of pure solvent obtained in this manner differ in vapor pressure by no more than 0.1 Torr ($T > 50\,°C$) and 0.01 Torr ($T \leq 30\,°C$), respectively. Due to the common way of degassing and its proven efficiency [262, 270], differences are supposed to be mainly because of experimental insufficiencies emerging from different leaking rates and measuring principle.

Preparation of electrolyte solutions or solvent mixtures The dried electrolytes are transferred into the sample flasks inside a glovebox on a balance with a resolution of 0.001 g. The flasks are subsequently attached to the degassing unit to evacuate it in a first step. Before distillation the mass of the flask under vacuum is determined to take into account the condition of pure solvent vapor of the solutions afterwards. The preparation of the frozen solution is done as quickly as possible under a steady application of vacuum. Approximately 1-5 mL of solvent is removed under stirring after thawing, ensuring the complete removal of residual gases of the salt crystals in the solution. The final amount of solvent is determined by weighing. Up to 3 different concentrations can be made per working step.
Working instructions for the preparation of fully degassed solvent mixtures are given in Sec. 4.14.1.

Method of operation Both the vessel with electrolyte solution (or solvent mixture) and the pure solvent are attached to the apparatus via Rotulex® junctions. The whole device is evacuated overnight. Prior to measurements some solvent vapor is released into the pipeline system and subsequently sucked off. Residual traces of gases on the tube walls are believed to be properly removed by this step.
The differential pressure sensor Δp has a maximum range of 1 Torr. If the pressure difference between solvent and solution (or solvent/solvent mixture and vacuum) is less than this maximum range, the differential pressure can directly be measured. In this case, flask 1 and 2 are opened after closing V4 and V3 and the signal is recorded in the usual way with sampling rate of 2 s.
To measure higher pressure differences or absolute vapor pressures exceeding 1 Torr, the pure solvent, electrolyte solution or solvent mixture is filled in flask 1, the vapor pressure of which applies on the left-hand side of the sensor. This pressure is compensated with nitrogen (via V6) on the right-hand side. The differential manometer then works as a null indicator and the total pressure is determined with the absolute pressure sensor p_{abs}. Flask 2 is not used in this case with V2 kept closed. The signal of both sensors have to be recorded in that case and corrected for the initial value of p^0_{abs} and Δp^∞, the actual values of Δp after pressure equalizing between both sides at the end of a measurement. Due to the installation of the differential pressure sensor, influencing the signals sign, the quoted vapor pressure p^* are given as corrected values according to the following equation:

$$p^* = \left[p_{\mathrm{abs}}(t) + \Delta p(t) - \left(p^0_{\mathrm{abs}} + \Delta p^\infty\right)\right] (t \to 0) \tag{6.26}$$

Δp^∞ is chosen for the correction because of the fact that both sides of the capacitance sensor are actually in contact with solvent vapor. This situation is equal to the sensor's environment during measurement and believed to resemble the influence of experimental conditions to the signal. This zero points are not very sensitive neither to the absolute pressure applied nor to the temperature, and do not change significantly during this work.
Fig. 6.4 and Fig. 6.5 show data points as typically recorded for absolut pressure measurements at elevated temperatures (left) and differential pressure measurements at room temperature (right). The extrapolation as a linear fit of data points in the range of $t > 15 - 20$ min gives the final value for the absolut pressure p^* (Eq. 6.26) and differential pressure Δp^* (Eq. 6.27). The linear range of this curve could also be verified at a prolonged time period. It is therefore regarded as being caused by different leaking rates on both sides of the differential pressure sensor [262]. Noteworthy to pronounce the increased leaking of the high-temperature apparatus compared to the measuring device at room temperature, mainly because

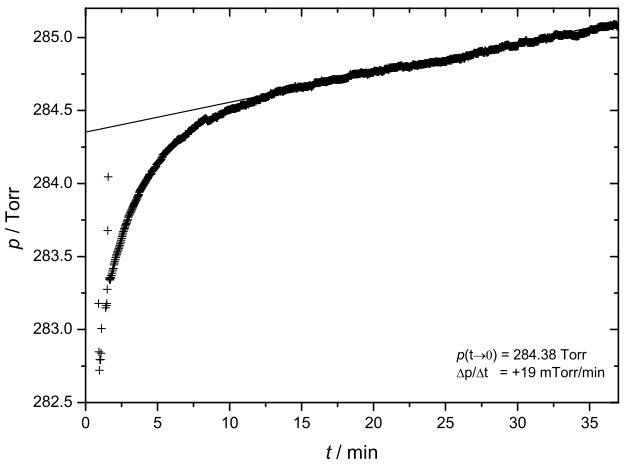

Figure 6.4.: Time dependent course of the signal obtained by Eq. (6.26) at 373.15 K (— extrapolation to $t \rightarrow 0$)

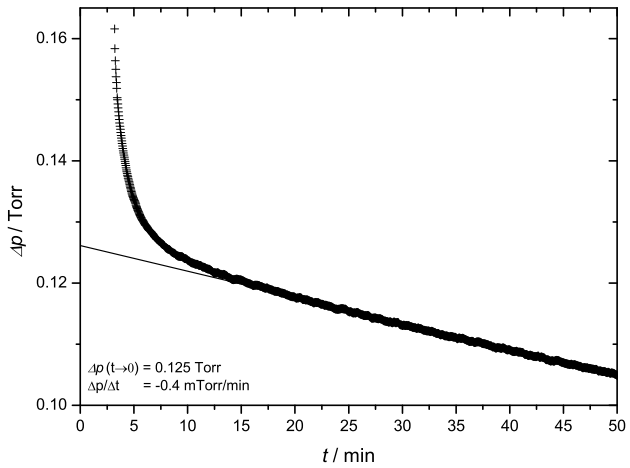

Figure 6.5.: Time dependent Δp signal at 298.15 K, Eq. 6.27

of the higher numbers of joints and valves and a presumably influence of temperature on the tightness of the Young stopcocks.

6.3.2. Measuring Device for Room Temperatures

The vapor pressure measurements for pure PnP at room temperature, aqueous solutions of ectoine and βpropiolactone at 298.15 K (the last two have been part of another project not included in this work) have been performed with the help of a new differential capacitance manometer (`MKS Baratron`, type 698A11TRA) operating in the high-precision apparatus at room temperature [265]. Technical difficulties require me to replace the formerly used pressure sensors and modify the pipeline system in accordance with the sensor's geometry and dimensions. The accuracy is given as $\pm 0.05\,\%$ of reading. An internal heater in the sensor package stabilizes the sensor thermally, resulting in a more stable signal. The capacitance manometer is calibrated with the help of aqueous solutions of sodium chloride. Reference data are taken from Gibbard et. al. [269]. Their concentration dependent osmotic coefficients are transformed into measurable vapor pressure depressions. The precision of this calibration is better than $0.2\,\%$ for $p^* < 4$ Torr.
The isothermal atmosphere of the air thermostat, the sensor is mounted within, guarantees for an improved thermal homogeneity on both sides of the capacitance membrane. A detailed description of the set-up, thermostat, vacuum line, experimental procedure as well as possible sources of errors is given in the work of Neueder [262]. Because of the long resting time of the machine without being used, the accuracy and precision of both, the liquid as well as air thermostat, have been re-evaluated by means of precise resistance thermometers. The liquid thermostat is calibrated with the same temperature sensor as used throughout the whole work, the accuracy of which was checked with the triple point of water. Uncertainty is less than 10^{-2} K with temperature fluctuations of less than 0.001 K. The long-time stability of the air thermostat is visualized in Fig. 6.6, recorded with a digital T-sensor. It reveals a constant temperature over a period of more than 8 h and a deviation from the mean temperature of less than 0.013 K.
The value for the differential pressure Δp is finally expressed by the extrapolation result to $t \rightarrow 0$ and is calculated according to

$$\Delta p = [\Delta p(t) - \Delta p^{\infty}]\,(t \rightarrow 0) \tag{6.27}$$

The apparatus being evacuated overnight and repeatedly exposed to solvent vapor prior to the measurements. The complete operation for precise vapor pressure measurements is very similar to that described before.

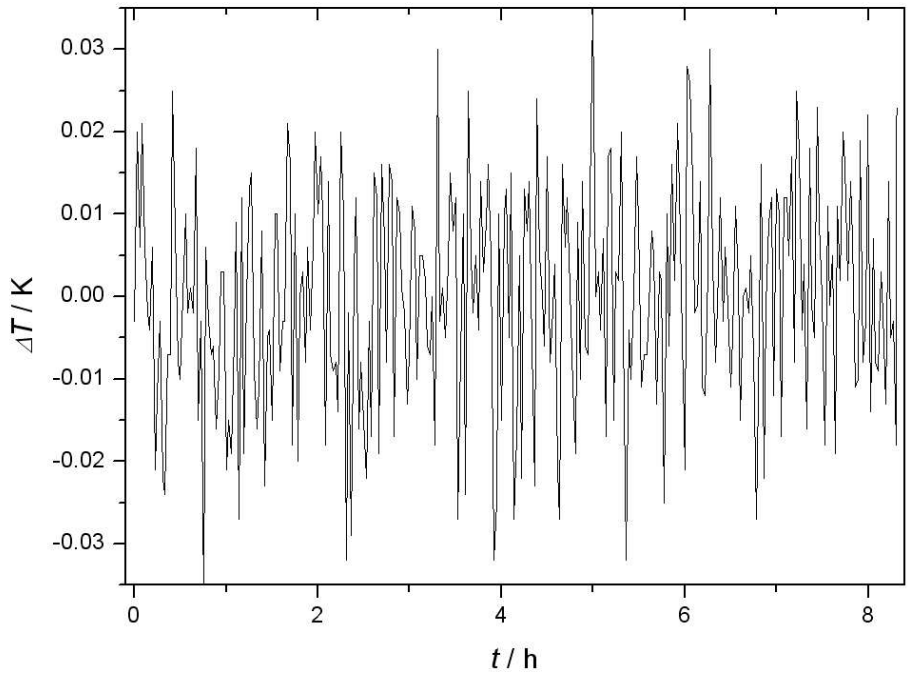

Figure 6.6.: Time-dependent temperature within the air thermostat, setpoint 40 °C

6.4. Results and Discussion

6.4.1. Vapor Pressure of Pure PnP

The vapor-liquid saturation line in a diagram of pressure versus temperature is the main characteristic of the vaporization equilibrium for a one-component system. The vapor pressure p^* is one of the most frequently measured thermodynamic properties for pure organic liquids, and the normal boiling temperature T_b is a basic physicochemical parameter for any substance. Vapor pressure data are needed for a variety of chemical engineering and thermodynamic calculations. Successful vapor-liquid equilibrium calculations, as explained in Chap. 4, are depending on the knowledge of precise vapor pressure data to a great extend. Different forms of vapor pressure equations are regularly used to correlate experimentally accessible quantities (e. g. temperature, phase-composition, system pressure) with each other.
The experimental determination of vapor pressure is relatively easy in the range between 1 and 200 kPa. Several compilations were published over the last decades [272–274]. At low pressure ($p^* < 1$ kPa) measurements become difficult. Direct static measurements, however, is proven to provide the most accurate data over a wide pressure range down to 1 Pa. Other methods are the

- thermogravimetry: after calibration using pure reference materials of known vapor pressure, the mass loss per unit area is detected and used to find the unknown p^* of a solid or liquid material (using the Langmuir equation for free evaporation) [275].
- saturation method using a carrier gas. The process comprises passing an inert gas over a sampled material at a controlled flow rate to create a vapor of the sampled materials that may be collected and analyzed [276].
- two techniques based on molecular effusion (weighing effusion and torsion effusion methods) [277].

Vapor pressures of 1-propoxy-2-propanol are determined in the temperature range between 298.15 K and 413.15 K in steps of 5 K. The experimental results are listed in Table F.1 together with the residuals $\Delta p = p(obs) - p(calc)$. The values of p(calc) have been obtained from the following equations, with coefficients given in Table 6.2. The present measurement extends the relatively small temperature range of previous investigations with the same apparatus [15].

The experimental vapor pressures have been fitted to the following three equations, used by Antoine,

$$\ln\left(\frac{p^{\mathrm{vap}}}{\mathrm{kPa}}\right) = A - \frac{B}{(\mathrm{T/K}) + C} \tag{6.28}$$

used by Wagner [278],

$$\begin{aligned} \ln\left(\frac{p^{\mathrm{vap}}}{\mathrm{p_c}}\right) &= \frac{\mathrm{T_c}}{\mathrm{T}} \cdot \left(A_1 \cdot \tau + A_2 \cdot \tau^{1.5} + A_3 \cdot \tau^3 + A_4 \cdot \tau^6\right) \\ \tau &= 1 - \frac{T}{\mathrm{T_c}} \end{aligned} \tag{6.29}$$

and used by Cox [279],

$$\ln\left(\frac{p^{\mathrm{vap}}}{\mathrm{p_0}}\right) = \left(1 - \frac{\mathrm{T_0}}{\mathrm{T}}\right) \cdot exp\left(\sum_{i=0}^{2} A_i \left(\frac{\mathrm{T}^i}{\mathrm{K}^i}\right)\right) \tag{6.30}$$

where A, B, C and A_i are adjustable coefficients, T is the thermodynamic temperature, p^{vap} the saturated vapor pressure and (T_0, p_0) an arbitrarily chosen reference point, here the critical vapor pressure p_c and temperature T_c, respectively [280]. The coefficients are obtained by fitting the vapor pressure data with the method of least squares. Although Antoine's equation is the most widespread equation

Table 6.2.: Coefficients of the different vapor-pressure equations for PnP

	A	B	C	
Antoine-Eq. (6.28)	14.2596	3243.215	-86.968	
	A_1	A_2	A_3	A_4
Wagner-Eq. (6.29)	-7.3359	-0.5368	-3.0893	-9.858
	A_0	A_1	A_2	
Cox-Eq. (6.30)	2.8044	-2.971×10^{-3}	2.9324×10^{-6}	

for representing temperature dependent vapor pressures, its poor performance and low flexibility, even in describing adequately the p^{vap} data in the medium-pressure region for compounds with specific interactions, is known [281]. Its use should be carefully questioned when the temperature interval of correlation becomes larger (i.e. 50 K). Due to an increasing number of experimental data, Wagner proposed another analytical expression for prediction of the vapor pressure saturation line up to the critical point. It is only applicable for substances with known critical properties. The number of adjustable coefficients in Eq. (6.29) is usually four; this four-parameter correlation is used as vapor-pressure equation in COSMOthermX for all substances under investigation.

Considered to be the most useful equation for extrapolations toward low pressures, the possibility of changing both the number of parameters and the reference condition $(\mathrm{T_0}, \mathrm{p_0})$ allows one to obtain different forms of the Cox equation suitable for particular applications. In this work a three-parameter form is applied, which describes sufficiently well the experimental data. According to the standard deviation (σ), defined as

$$\sigma = \sqrt{\Sigma\left[(p(obs) - p(calc))^2\right]/N} \tag{6.31}$$

with values of 0.029 (Eq.6.28) , 0.033 (Eq.6.29) and 0.023 (Eq.6.30), the equation of Cox is somewhat superior to that of Antoine or Wagner. Requiring the critical parameters there is no chance of applying Wagner's equation to a restricted temperature range, improving its accuracy and it is useless for high boiling chemicals that decompose below or near the normal boiling point [281].

If we compare our results of p^{vap} with that of Queste [15], a positive deviation compared to our values can be observed. This difference amounts to (14-50) Pa or (3-4.5) %. The published measurements were done some years ago using identical equipment, beside the technical improvements mentioned in the

experimental part herein. As the vapor pressure of the glycol ethers are generally lower in comparison to conventional organic solvents [81], their precise determination is often subject to larger systematic errors. The sensitivity of vapor pressure to sample impurities (especially to those being more volatile) and remaining dissolved gas is accounted for in the present paper by the distillation purification of the dried commercial product and the advanced method of degassing. Both improvements over the published methods should make the present values more reliable.
The temperature dependence of the vapor pressure can be represented by means of the enthalpy of vaporization also. It is obtained from the Clausius-Clapeyron equation (assuming gas-phase ideality and neglecting the liquid molar volume), representing the difference per mole of the enthalpy of the vapor and of the liquid at thermodynamic equilibrium:

$$\frac{d\ln p^{\mathrm{vap}}}{d\,(1/T)} = \frac{-\Delta_{\mathrm{vap}}H(\mathrm{T})}{\mathrm{R}} \tag{6.32}$$

$\Delta_{\mathrm{vap}}H(\mathrm{T})$ is directly linked to the cohesive energy inside the liquid and can easily be deduced from vapor pressure measurements. Based on the assumption that the enthalpy of vaporization linearly depends on the temperature, the integral form of Eq. (6.32) is expressed by:

$$\ln\frac{p^{\mathrm{vap}}}{\mathrm{kPa}} = a + b\cdot(\mathrm{T/K})^{-1} + c\cdot\ln(\mathrm{T/K}) \tag{6.33}$$

in agreement with following relation:

$$\frac{\Delta_{\mathrm{vap}}H(\mathrm{T})}{\mathrm{R}} = c\cdot\mathrm{T} - b \tag{6.34}$$

The parameters a, b, c have been evaluated by an unweighted least-squares method and are presented in Table **??**. The molar entropy of evaporation, $\Delta_{\mathrm{vap}}S$ is calculated from the thermodynamic relationship:

$$\Delta_{\mathrm{vap}}S = \frac{\Delta_{\mathrm{vap}}H}{\mathrm{T_b}} \tag{6.35}$$

A graphical representation of experimental vapor pressure values and the calculated values for $\Delta_{\mathrm{vap}}H/R$ are shown in Fig. 6.7.

According to Trouton's rule, the value for the entropy of vaporization at normal boiling point is constant and about (87-88) $\mathrm{J\,K^{-1}mol^{-1}}$ for various kinds of liquids, possessing no special intermolecular interactions. The value of 123.3 $\mathrm{J\,K^{-1}mol^{-1}}$ obtained here at 298.15 K shows a positive deviation from the rule and is similar to those of water and ethanol 118 and 120 $\mathrm{J\,K^{-1}\,mol^{-1}}$, molecules which are very well known to have additional cohesive intermolecular forces through hydrogen bonding.
Due to their chemical structure, glycol ethers are prone to form hydrogen bonds in solution (see Chap. 3), which is also an explanation for the existence of LCTS in aqueous systems with strong temperature-dependent solvation interactions [4]. The measured heat of evaporation is quite similar to that of short-chain alcohols [81], again an indication for equivalent kinds of interactions in the condensed liquid phase. It also holds for different glycol and glycerol-based solvo-surfactants [15].

6.4.2. Vapor Pressure Depression on Electrolyte Solutions

As outlined in Sec. 6.3 the experiments on vapor pressure depression of Bu_4NX (X = Br^-, NO_3^-, SCN^- and OAc^-) dissolved in 1-propoxy-2-propanol has been performed at temperatures between $323.15 \le T/\mathrm{K} \le 413.15$ in steps of 10 K. Values quoted are the results of extrapolation towards time $t = 0$ (see p. 144) and subsequently corrected for the calibration curve of the absolute as well as differential pressure sensor (see Sec. 6.3.1).
Electrolyte concentrations, covering a range of $0.1 < \mathrm{m/[mol\,kg^{-1}]} < 1.2$ (except Bu_4NBr with a maximum molality of about 0.6), are obtained from the weights of salts under vacuum and the completely degassed solvent. All weights are corrected for buoyancy. Differences in concentrations due to the minor

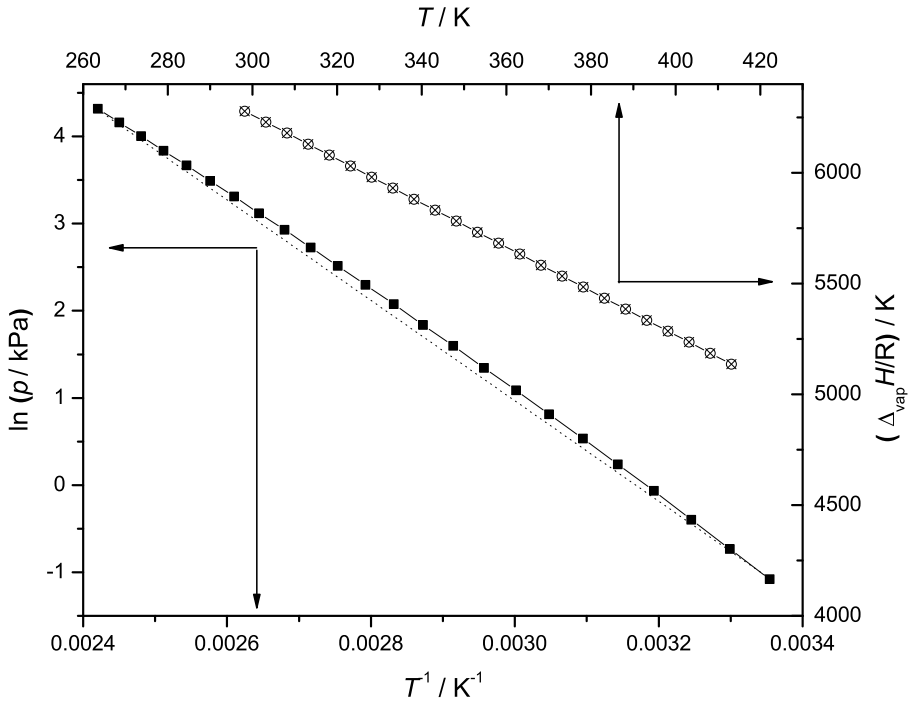

Figure 6.7.: Plot of $\ln(p)$ against T^{-1} for PnP (■) and values of the calculated heat of evaporation $\Delta_{\text{vap}}H/R$ (⊗)

amount of solvent evaporating into the apparatus can be neglected without hesitation and are not considered in this work therefore. Pure solvent's vapor pressure data over the given temperature range have been measured precisely owing to missing reference data in the literature.
Owing to uncertainties of the pressure sensor's zero settings, residual gases and leakage, an overall uncertainty of about 4 Pa $\simeq$ 0.03 Torr can be estimated for a single data point. At temperatures higher than 393.15 K, however, unacceptable leaking rates do not enable a reasonable extrapolation in several cases. Concentrations of electrolyte solutions are omitted in that case therefore.
The lowest possible concentration is limited by the deficiencies of temperature fluctuation, leaking rate, reproducibility, etc. and the maximum concentration is restricted by the solute's solubility and the increasing solution's viscosity. These disturbing effects are more pronounced at low molalities m, where Δp values are very small and uncertainties in Δp influence ϕ to a greater extend. A minimum temperature of 323.15 K is required because of the low vapor pressure of 1-propoxy-2-propanol and, as one may expect, small values for the vapor pressure depression.
The direct determination of Δp in a single acquisition run provides more accuracy than results obtained by differentiation of solvent and solution vapor pressure, since it eliminates the effects of small temperature variations. Furthermore, having identical relative accuracy of both vapor pressures (solvent/solution), the absolute accuracy in Δp is advanced. For example, an error in the experimental value of pressure of 0.03 Torr affect the uncertainty of the difference between two independent measurements (solvent/solution) in the following extent:

$$p^* = (10 \pm 0.03)\ \text{Torr}; p = (9.2 \pm 0.03)\ \text{Torr} \Rightarrow$$
$$\Delta p = (0.8 \pm 0.06)\ \text{Torr} = 0.8 \pm 7.5, \%$$

This error is unacceptable large when compared to a direct, single measurement of differential pressure: (0.8 ± 0.03) Torr $= 0.8 \pm 3.8\,\%$. For that reason an optimally designed measuring device would be capable of covering a broad range of accessible pressure differences in one single housing. The deficiency of limited pressure range and the increasing leaking rates at increased temperatures unfortunately reduces the accuracy and precision of the Δp results compared to those recorded at room temperature [262].
Being also dependent on the absolute value of p (increasing uncertainty because of increased leakage),

the error is shown to depend on Δp and reduces with increasing vapor pressure depression:

$$p^* = (10 \pm 0.03)\,\text{Torr}; p = (7.6 \pm 0.03)\,\text{Torr} \Rightarrow$$
$$\Delta p = (2.4 \pm 0.06)\ \text{Torr} = 2.4 \pm 2.5\,\%$$

Vapor pressure differences accounting for less than 1 Torr are always determined in a single measurement, therefore, making use of the lower uncertainty in determining Δp in one single run.

6.4.2.1. Experimental Osmotic Coefficients

The second virial coefficients are calculated by the method described by Xiang [83]. For clarity the second virial coefficient, the molar volume and the vapor pressure of pure PnP from 323.15 to 413.15 K at 10-K intervals are presented in Table 6.1.
The experimental vapor pressure data for all 4 electrolytes are given in Sec. F.2-Sec. F.5 together with osmotic coefficients obtained with the help of Eq. (6.25) at the end of this work.
The concentration dependence of the vapor pressure lowering of Bu_4NSCN in PnP solutions is given in Fig. 6.8 as a model example. All four salts show very similar and regular behavior of the measured vapor

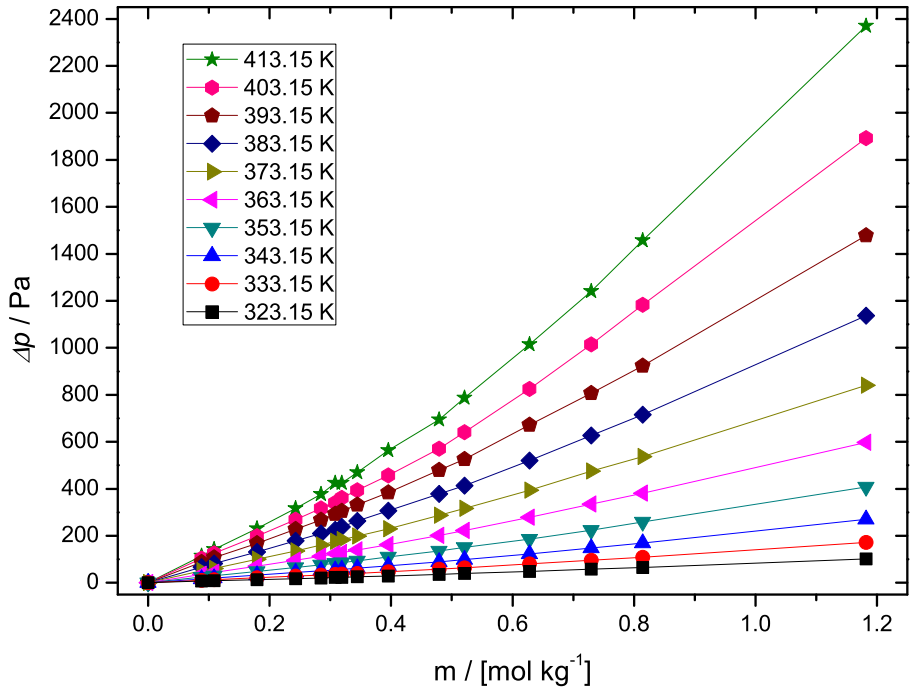

Figure 6.8.: The concentration dependence of the vapor pressure for Bu_4NSCN solutions at different temperatures.

pressure depression as function of molality and temperature. Unfortunately, the originality of this work does not allow for a thorough comparison with literature data in the same solvent.
Figures 6.9 - 6.12 show the osmotic coefficients of the tetrabutylammonium salts vs molality at selected temperatures. The osmotic coefficient at m = 0, e.g. pure solvent, is defined as unity. The curves reveal the typical pattern of the concentration dependence of the osmotic coefficients, namely, initially negative slopes (decrease of ϕ at increasing concentration) and approximately constant ϕ values or positive slopes at higher concentrations. According to Eq. (6.13) the osmotic coefficient is a measure of the solvent activity a_S. Generally speaking one can say that the smaller ϕ is, the smaller will be the interaction between electrolyte and solvent. Small interactions represent an electrolyte system of low ionic dissociation and hence a large solvent activity, and vice versa. The relation between ϕ and a_S then explains the resulting small values for osmotic coefficients. Noteworthy to emphasize the influence of the factor ν on the osmotic coefficient: strong ion association actually reduces ν down to a value between $1 < \nu < 2$. This

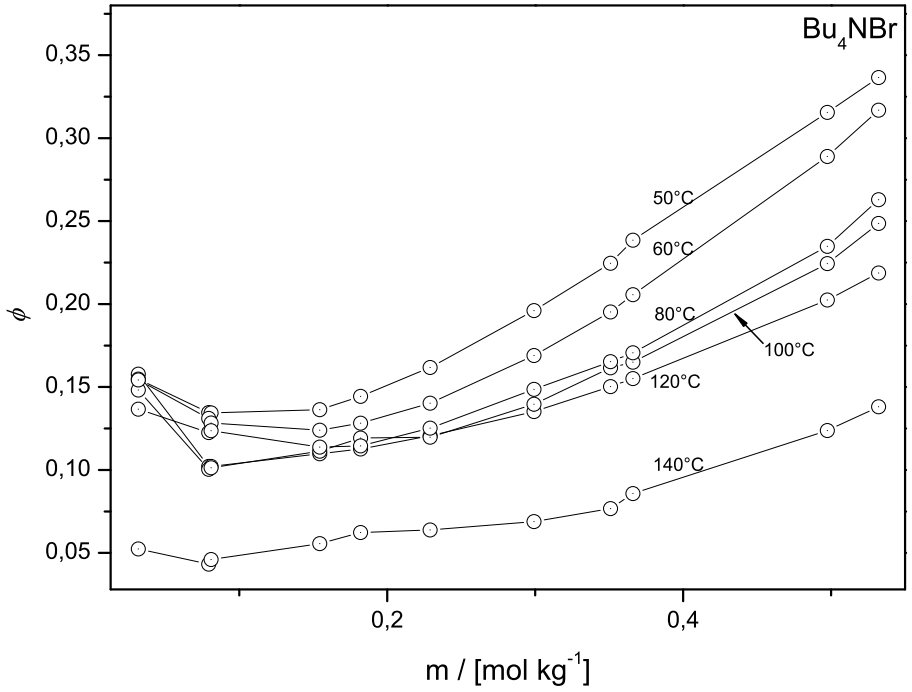

Figure 6.9.: The concentration dependence of osmotic coefficient for Bu_4NBr in 1-propoxy-2-propanol as function of molality at different temperatures

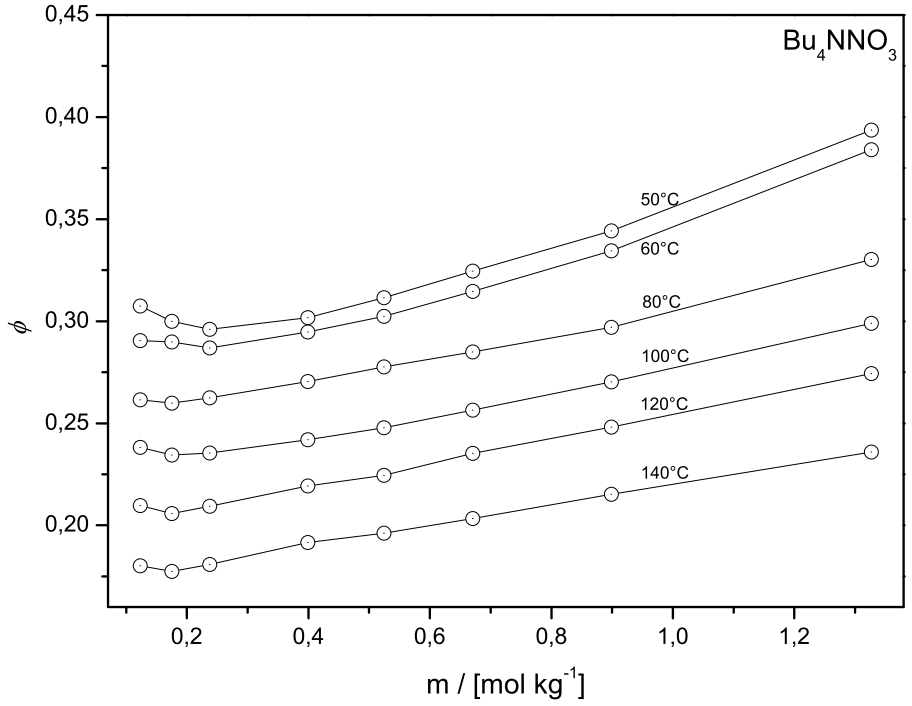

Figure 6.10.: The concentration dependence of osmotic coefficient for Bu_4NNO_3 in 1-propoxy-2-propanol as function of molality at different temperatures

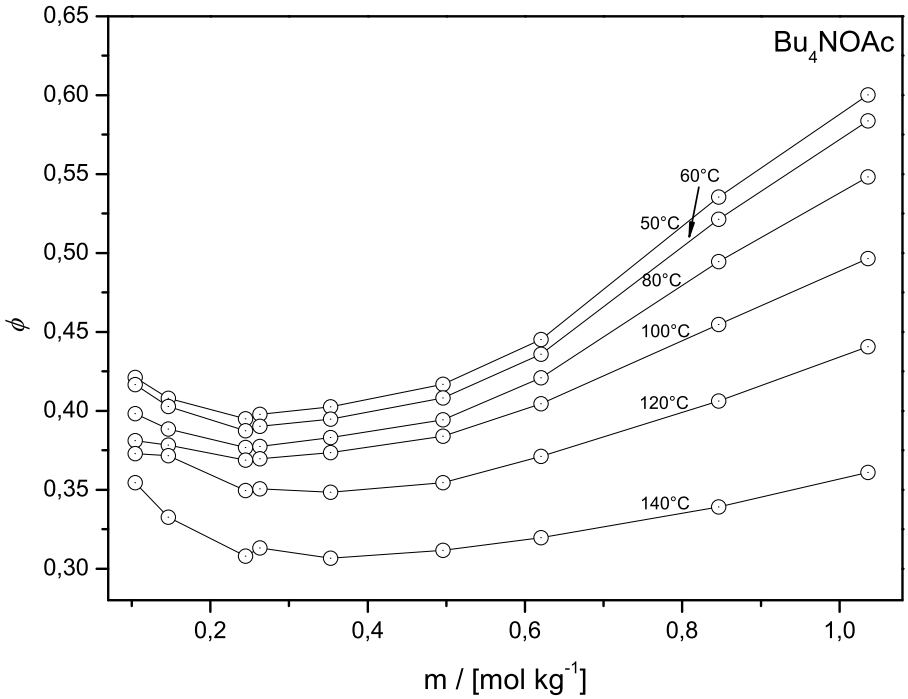

Figure 6.11.: The concentration dependence of osmotic coefficient for Bu_4NOAc in 1-propoxy-2-propanol as function of molality at different temperatures

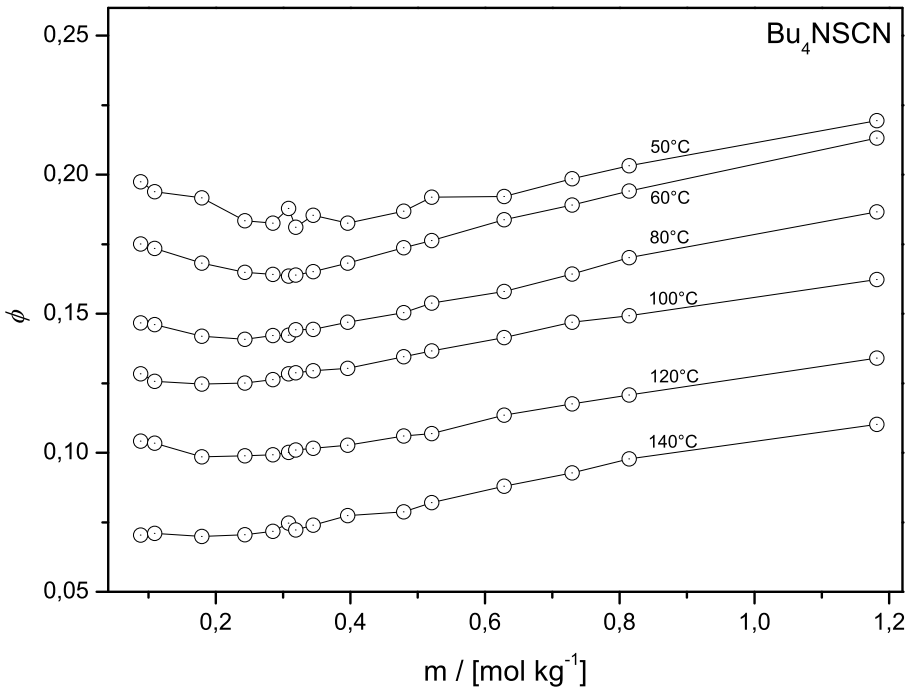

Figure 6.12.: The concentration dependence of osmotic coefficient for Bu_4NSCN in 1-propoxy-2-propanol as function of molality at different temperatures

fact, however, is not considered in the calculation according to Eq. (6.13). Consequently ϕ will also be reduced only because of insufficient knowledge of the actual value for ν.
Factors which are influencing the characteristics of $\phi = \phi(\mathrm{m})$ are considered to be primarily:

- the size of the ions
  With increasing ion radius the repulsion between the ions increases because of volumetric as well as structural effects [282]. Consequently the values of osmotic coefficients also increases. This electrostatic phenomenon can also be explained by the integral in Eq. (5.92), which decreases with increasing ion radius a.

- solvation of the ions
  The stronger the ion solvation, the higher the osmotic coefficient. An increase of Δp in a sequence of salts with one common ion comes along with an increase of solvation of the counterion. The more pronounced the interaction between solvent and ion, the larger is the effect of vapor pressure depression.

- ion association
  Reduction of the number of free ions by ion pairing is attended by a decrease of solvent-electrolyte interaction and hence by smaller values of osmotic coefficients. This is because of the much weaker non-coulombic interaction between solvent molecules and the neutral ion pairs.

These are qualitative and simple rules to interpret the osmotic coefficients as a function of concentration, however, they can not individually be accessed by experimental investigations.
Osmotic coefficients shown in this work clearly show very low values over the whole composition range at all temperatures. They follow the order of decreasing values with increasing temperature without exception as can be seen from the figures. According to the third rule, ion association increases in the order of increasing temperature for a given salt at constant concentration. There is, indeed, experimental evidence for strong ion pairing and increasing association constant with increasing temperature for solutions of Bu_4NX (X = Br^-, $NO_3{}^-$, SCN^- and OAc^-) in PnP from conductivity measurements at lower temperatures (refer to Sec. 5.6.6.2). Evaluations of osmotic coefficients with the help of different regression models will also show the necessity for an additional parameter β^2, which accounts for ion association, without which data correlation is loosing quality (see Sec. 6.4.2.2). This ion pairing is more pronounced for solvents of lower dielectric constants as is shown exemplarily for Bu_4NBr in different solvents in Fig. 6.13. Amongst solvents of the same class (aliphatic alcohols), the osmotic coefficients decrease with decreasing relative solvent permittivity ϵ in accordance with an increasing association, which is related to a lower ion solvation. Despite the fact that the lowest temperature accessible for Bu_4NBr in PnP is 323.15 K only, this trend is quite obvious in the series of solvents given. This argumentation, however, is only considering electrostatic interactions neglecting the occurrence of any non-coulombic forces. For instance, changing solvation power towards ions amongst different solvent classes (alcohols, AN, acetone) can have drastically non-coulombic effects on the cation and anion dependence of association (not shown in this work).
From osmotic coefficients alone it is difficult to estimate the temperature dependence of association constants and no comparable numerical values can be obtained without the application of a proper theoretical model. Based on the chemical model of Barthel, many electrolyte systems at different temperatures have been evaluated with respect to K_A allowing to obtain information on solution structures, non-coulombic contribution as well as thermodynamic functions of the association process [283–287]. Despite exhaustive attempts in order to correlate and interpret the data with the help of the lcCM, no reasonable agreement between the model and experiment can be found for all systems presented here. Although using the extended model with one additional parameter (next to K_A) [262], the iterative scheme does not converge, although advanced minimization procedures incorporated in *Maple* have been applied. This discrepancy can be explained by the following reasons:

- the low absolute values of Δp in combination with the very high association constant lead to very low osmotic coefficients without the possibility to measure the dilute range of increasing ϕ and

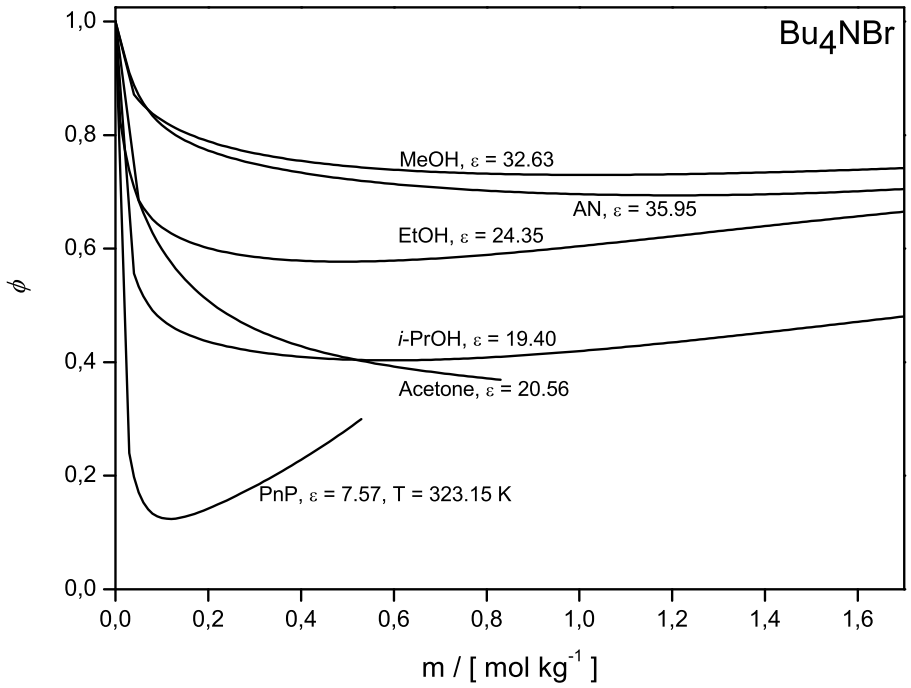

Figure 6.13.: Molality dependence of the osmotic coefficients for Bu_4NBr in methanol, ethanol, *i*-propanol, acetonitrile and acetone at 298.15 K and 1-propoxy-2-propanol at 323.15 K. Lines: Pitzer model

solvent activity. Naturally this is prone to cause bad parameter regression, as the correct curvature of the regression line can hardly be elucidated.

- experimental deficiencies and errors in the determination of osmotic coefficients
- inappropriate concentration range
  Originally developed the lcCM is capable for representing the osmotic coefficient up to concentrations of 0.2 mol L^{-1}. Extensions including the activity coefficient of the neutral ion pair extend the accessible concentration range. Not even this low concentration range, however, for which the theoretical assumption would be valid, is able to be measured in this work.
- very high association indicates strong ion-ion interactions beyond ion-pair formation (see Sec. 5.8). Association is believed to be the main reason for the the chemical model to fail.

Initial attempts to fit MSA-NRTL model parameters to the experimental osmotic coefficient data also failed within the given concentration range. This model turned out to be an accurate model for the description of the thermodynamics of electrolyte solutions [288], with parameters having a physical meaning. Again, reason for the discrepancy may originate from the insufficient range of dilute measurements and model inherent problems to describe properly the highly associated electrolyte system [289].
For that reason only qualitative argumentation about the association behavior of tetrabutylammonium salts in PnP can be given herein.
As already mentioned, all four systems can be regarded as highly associated with osmotic coefficients in the range of 0.5 and less. Similar low values of ϕ can also be found for 1:1 electrolytes in solvents with rather low relative permittivity, e.g. *i*-propanol [290], dimethoxyethane [291] and for 2:2 electrolytes in ethanol [292]. Comparison of the four electrolytic systems exhibits the following order of decreasing osmotic coefficients with regard of the anion: $OAc^{-1} > NO_3^{-1} > SCN^{-1} \geq Br^{-1}$. According to the first rule given above, this order also describes the sequence of increasing ion association for the electrolyte systems. From the point of view that a variation of the non-coulombic part of ΔG_A is not considered, the order of anions given resembles the order of decreasing anion radii. The higher the ion radii, the smaller the electrostatic interaction between oppositely charged ions. However, osmotic coefficients as well as

results from electrical conductance provide an indication for the presence of solvation effects, which accounts for the change of trends aside of the crystallographic dimensions of the anions (see Sec. 5.6.6.2). Unfortunately, no quantification of the contributions to the association process by model calculations are possible. Therefore and because of the very small and often unclear differences of ϕ among the anions Br^-, $NO_3{}^-$ and SCN^-, detailed interpretations on solvation, solvent structure or ion association should not be overemphasized.
Figures 6.9 - 6.12 show an important result: osmotic coefficients exhibit much less dependence on the anion in salts with Br^-, $NO_3{}^-$ and SCN^- when compared to the dependence on the acetate anion. The results means that there is no significant interaction of the Br^-, $NO_3{}^-$ and SCN^- anions with 1-propoxy-2-propanol. Only the significant differences in the results for OAc^{-1} hint at a more pronounced solvent-anion interaction, leading to higher values of ϕ. Measurements on the electrical conductivity support this observation. The solvation shell around acetate seems to be larger than for the remaining anions. Values for K_A are found to be lowest for Bu_4NOAc. At the same time the chemical model calculations shown in Fig. 5.21 on the conductance behavior do also exhibit very similar behavior amongst the anions Br^-, $NO_3{}^-$ and SCN^-. With respect to the sequence of ϕ as being regarded a measure for the ion association, both measuring techniques exhibit a similar association behavior over the whole temperature range between 248.15 and 413.15 K: similar association for Bu_4NX (X = Br^-, $NO_3{}^-$, SCN^-) and a smaller association constant for Bu_4NOAc. It is also known from the literature, that spherical tetrabutylammonium cations tend to be only very weakly solvated.
The different position of the nitrate anion ($NO_3{}^-$ exhibits the highest association constant according to the lcCM) between conductance and vapor pressure measurements can have the following reasons: from an experimental point of view, highly associated electrolyte systems may lead to larger errors in thermodynamic quantities derived from experimental data. This is certainly the case for Δp and calculated osmotic coefficients (see p. 149). Values of K_A obtained by even such accurate and precise methods like conductance measurements are known to be more uncertain than those obtained from systems with lower association. As pressure differences are not be measurable equally well as are electrolyte solution's resistances in this work, lower limits of the range of concentration are much higher. Thus, comparison between the results of both techniques suffers from the incompatibility of the concentration ranges; only tendencies reflected by the degree of association from vapor pressure and conductance methods can be addressed any physical interpretation. One should keep in mind also the different temperatures, each technique is applied to. Certainly, this will not fully explain the different results for $NO_3{}^-$. Furthermore, no separate information on the non-coulombic part of the association, known to be directly related to the solvation and a possible explanation, can be extracted.

6.4.2.2. Correlation of Activity and Osmotic Coefficients

Several models are available in the literature for the correlation of osmotic coefficients as a function of molalities. McMillan and Mayer (MM) proved the calculation of thermodynamic properties to be possible only with the knowledge of ion-ion interaction [293]. In this case solutes are regarded as being a real gas whilst the solvent is considered as a continuum. A virial equation connecting thermophysical properties with statistical mechanics can be established, which yields the osmotic pressure and osmotic coefficient at the MM level. Other approaches has been developed by Pitzer and Simonson [294], assuming the excess Gibbs energy to consist of two components: short-range force terms accounted for by a Margules expansion in concentration and a long-range force Debye-Hückel term that is a function only of the ionic strength of the solution (at constant temperature and pressure).
Alternative thermodynamic models of Chen [295] adopt the same Debye-Hückel term as used by Pitzer and Simonson but account for all short-range interactions by expressions based upon the „local composition" concept. It has been suggested that these local composition models are superior to those based on virial expansions or on the Margules series, but both the four linear parameters of virial or Margules models as well as the two nonlinear local composition parameters are easily optimized. Despite a great effort to evaluate values for interaction NRTL-parameters in the model equations of Chen, experimental osmotic coefficient data could not be correlated satisfactory within the concentration range given in this work. Computational problems with this model and less accurate data representation is also known from

literature and might be due to the nonlinearity in the parameters [296].

Pitzer Equations On basis of this equation Pitzer developed a most successful fitting equation for the osmotic coefficient, admitting the inclusion of three-particle interactions [297].

$$\phi - 1 = -A_\phi \frac{\sqrt{I}}{1 + b\sqrt{I}} + \mathrm{m} B^\phi + \mathrm{m}^2 C^\phi \tag{6.36a}$$

$$B^\phi = \beta^{(0)} + \beta^{(1)} \exp\left[-\alpha_1 \sqrt{I}\right] + \beta^{(2)} \exp\left[-\alpha_2 \sqrt{I}\right] \tag{6.36b}$$

$$A_\phi = \frac{\sqrt{2\pi N_A d_S^*}}{3} \cdot \left(\frac{e^2}{4\pi\epsilon_0 \epsilon kT}\right)^{3/2}; \qquad I = \frac{1}{2}\sum \mathrm{m}_i z_i^2 \tag{6.36c}$$

In these equations ($\beta^{(0)}$, $\beta^{(1)}$, $\beta^{(2)}$, $C^{(\phi)}$) are Pitzer's ion-interaction parameters that are dependent on temperature and pressure, (b, α_1, α_2) are adjustable parameters and A_ϕ is the Debye-Hückel constant for the osmotic coefficient on the molality scale. The parameters are adaptable to experimental data. The ionic strength I for a 1:1-electrolyte equals the molality m, where m_i is the molality of ith-ion and z_i is the absolute value for ith-ionic charge. A_ϕ is calculated from 323.15 K to 413.15 K at 10-K intervals and presented in Table 6.3. The values of density d^* and relative permittivity ϵ of pure PnP at different temperatures are taken as results from Eqs. (5.53),(5.59). Despite its non-linearity with respect to the adjustable parameters, adjustment and convergence of the correlation is readily performed.
The first term in Eq. (6.36a) describes the coulombic interactions. The B^ϕ-term takes into account the effect of short-range ion-ion interactions. Without a proper physical meaning it helps to produce appropriate fitting conditions [157]. Ion association in solvents of low permittivity or 2:2-electrolytes in all solvents is taken into account by the term $\beta^{(2)}$ [298]. The Pitzer equation may be understood as a type of virial development with β-parameters describing the short-range effects of the second virial coefficient, and C^ϕ represents the third virial coefficient. The high degree of association known for all four salt systems in this work requires the adjustment of $\beta^{(2)}$ in the process of data correlation.
The number of parameters may be reduced by summarizing (b, α_1, α_2) of groups of solutions, that have these parameters in common. Pitzer proposes $b = 1.2$, $\alpha_1 = 1.4$ and $\alpha_2 = 12.0$ for aqueous solutions and gives a collection of Pitzer parameters for a huge number of electrolytes and electrolyte systems [299].
From the analysis of the experimental osmotic coefficient data, values of $b = 20$, $\alpha_1 = 10$ and $\alpha_2 = 3.5$, found in this work, yield reliable fits for all temperatures, independent of the electrolyte system under investigation. The parameter set is chosen on basis of a comparative study of standard deviations for all four systems.

Table 6.3.: Density, d^*, relative permittivity, ϵ and Debye-Hückel constant for the osmotic coefficient in molality, A_ϕ, and mole fraction scale, A_x.

T	d^{*}[a]	ϵ[b]	A_ϕ[c]	A_x[d]	$\rho_{\mathrm{Br^-}}$[e]	$\rho_{\mathrm{NO_3^-}}$[e]	$\rho_{\mathrm{OAc^-}}$[e]	$\rho_{\mathrm{SCN^-}}$[e]
K	$\mathrm{kg\,m^{-3}}$		$\mathrm{kg^{1/2}\,mol^{-1/2}}$					
323.15	857.49	7.571	10.71714	31.17508	38.89033	39.54764	40.91701	42.75198
333.15	847.90	7.217	10.93980	31.82273	39.01131	39.67066	41.04429	42.88497
343.15	838.17	6.893	11.14759	32.42721	39.10606	39.76701	41.14398	42.98913
353.15	828.28	6.594	11.34246	32.99403	39.17731	39.83946	41.21894	43.06745
363.15	818.21	6.319	11.52632	33.52886	39.22760	39.89060	41.27185	43.12273
373.15	807.94	6.062	11.70116	34.03746	39.25930	39.92284	41.30521	43.15758
383.15	797.45	5.823	11.86897	34.52554	39.27457	39.93836	41.32127	43.17437
393.15	786.72	5.598	12.03165	34.99877	39.27539	39.93920	41.32214	43.17527
403.15	775.72	5.386	12.19116	35.46275	39.26356	39.92717	41.30969	43.16226
413.15	764.45	5.185	12.34935	35.92299	39.24067	39.90389	41.28561	43.13710

[a] Eq. (5.53)
[b] Eq. (5.59)
[c] Eq. (6.36c)
[d] Eq. (6.40b)
[e] Eq. (6.40c)

Ion-interaction parameters obtained from fitting of experimental osmotic coefficients of Bu_4NX (X = Br^-, NO_3^-, SCN^- and OAc^-) in PnP are shown in Table 6.4-6.7 along with the standard deviation between experimental and calculated values of ϕ.

Table 6.4.: The parameters for the Pitzer Model for PnP solutions of Bu_4NBr[a]

T	$\beta^{(0)}$	$\beta^{(1)}$	$\beta^{(2)}$	C^{ϕ}	$\sigma(\phi)$
K	kg mol^{-1}	kg mol^{-1}	kg mol^{-1}	kg^2 mol^{-2}	
323.15	0.163 443	−42.668 752	−7.495 240	0.275 095	0.002
333.15	−0.269 003	−43.961 377	−6.094 034	0.848 013	0.001
343.15	−0.595 935	−47.817 713	−4.561 617	1.196 183	0.002
353.15	−0.388 540	−44.331 135	−5.369 946	0.834 605	0.002
363.15	−0.462 683	−55.937 194	−4.220 250	0.750 029	0.003
373.15	−0.825 155	−55.440 279	−2.744 913	1.301 794	0.003
383.15	−1.011 925	−59.393 720	−1.944 282	1.373 840	0.002
393.15	−1.003 311	−58.704 355	−1.843 630	1.368 910	0.002
403.15	−1.250 922	−62.076 095	−0.840 633	1.656 796	0.003
413.15	−1.174 076	−63.864 984	−1.482 469	1.506 947	0.003

[a] $b = 20$, $\alpha_1 = 10$, $\alpha_2 = 3.5$. Units: kg$^{1/2}$ mol$^{-1/2}$

Table 6.5.: The parameters for the Pitzer Model for PnP solutions of Bu_4NNO_3[a]

T	$\beta^{(0)}$	$\beta^{(1)}$	$\beta^{(2)}$	C^{ϕ}	$\sigma(\phi)$
K	kg mol^{-1}	kg mol^{-1}	kg mol^{-1}	kg^2 mol^{-2}	
323.15	−0.059 933	−21.253 222	−3.857 858	0.044204	0.001
333.15	−0.082 735	−24.920 944	−3.575 088	0.058253	0.001
343.15	−0.086 936	−26.764 417	−3.500 722	0.050767	0.001
353.15	−0.092 302	−28.684 103	−3.510 307	0.044729	0.001
363.15	−0.068 055	−26.101 890	−3.942 807	0.028160	0.001
373.15	−0.083 184	−27.513 718	−3.857 923	0.034785	0.001
383.15	−0.067 871	−29.458 103	−4.135 767	0.023525	0.001
393.15	−0.071 790	−29.362 838	−4.087 819	0.024064	0.001
403.15	−0.082 700	−31.348 469	−4.217 903	0.025274	0.001
413.15	−0.095 136	−32.604 893	−4.134 564	0.029395	0.001

[a] $b = 20$, $\alpha_1 = 10$, $\alpha_2 = 3.5$. Units: kg$^{1/2}$ mol$^{-1/2}$

Extended Pitzer model of Archer The model of Pitzer and Mayorga with inclusion of Archer's ionic-strength dependence of the third virial coefficient C^{ϕ} was used for aqueous electrolyte systems [300, 301] and in a few cases for non-aqueous electrolyte solutions [302, 303, 290] with excellent capability.
The model extension, used for correlation of experimental osmotic coefficient data differs by one additional ion-interaction parameter $C^{(2)}$ and one adjustable parameter α_3 from Pitzer's equation (6.36).

$$\phi - 1 = -A_{\phi}\frac{\sqrt{I}}{1 + b\sqrt{I}} + \mathrm{m}B^{\phi} + \mathrm{m}^2 C^{\phi} \tag{6.37a}$$

$$C^{\phi} = C^{(1)} + C^{(2)} \exp\left[-\alpha_3\sqrt{I}\right] \tag{6.37b}$$

Investigations on the influence of the four adjustable parameters $\alpha_1, \alpha_2, \alpha_3$ and b on the quality of the correlation exhibit a similar set of parameters with $\alpha_1 = 10, \alpha_2 = 3.5, \alpha = 1.0$ and $b = 20$ (kg$^{1/2}$ mol$^{-1/2}$).

Table 6.6.: The parameters for the Pitzer Model for PnP solutions of Bu_4NOAc[a]

T	$\beta^{(0)}$	$\beta^{(1)}$	$\beta^{(2)}$	C^{ϕ}	$\sigma(\phi)$
K	$kg\,mol^{-1}$	$kg\,mol^{-1}$	$kg\,mol^{-1}$	$kg^2\,mol^{-2}$	
323.15	−0.055 368	−6.604 428	−2.464 664	0.228682	0.006
333.15	−0.041 577	−5.347 519	−2.497 647	0.210358	0.005
343.15	−0.062 929	−7.496 242	−2.225 004	0.216569	0.006
353.15	−0.033 590	−7.483 079	−2.265 128	0.180853	0.005
363.15	−0.021 058	−9.784 454	−2.077 810	0.146116	0.004
373.15	−0.034 562	−10.838 396	−1.860 060	0.137204	0.003
383.15	−0.066 849	−11.079 846	−1.636 619	0.143579	0.002
393.15	−0.051 233	−7.896 548	−1.920 757	0.116564	0.004
403.15	−0.006 400	−5.317 334	−2.463 149	0.055015	0.002
413.15	0.007 405	−3.925 463	−2.858 961	0.023729	0.002

[a] $b = 20$, $\alpha_1 = 10$, $\alpha_2 = 3.5$. Units: $kg^{1/2}\,mol^{-1/2}$

Table 6.7.: The parameters for the Pitzer Model for PnP solutions of Bu_4NSCN[a]

T	$\beta^{(0)}$	$\beta^{(1)}$	$\beta^{(2)}$	C^{ϕ}	$\sigma(\phi)$
K	$kg\,mol^{-1}$	$kg\,mol^{-1}$	$kg\,mol^{-1}$	$kg^2\,mol^{-2}$	
323.15	−0.177 113	−35.663 331	−5.251 384	0.057 582	0.003
333.15	−0.137 783	−36.196 124	−5.667 918	0.035 279	0.003
343.15	−0.166 538	−38.412 214	−5.488 921	0.053 462	0.003
353.15	−0.159 925	−39.192 532	−5.537 371	0.046 815	0.002
363.15	−0.158 883	−39.971 452	−5.470 751	0.042 418	0.002
373.15	−0.164 448	−40.887 406	−5.423 805	0.042 804	0.002
383.15	−0.174 889	−41.163 436	−5.533 337	0.049 535	0.002
393.15	−0.175 504	−41.153 493	−5.628 574	0.047 420	0.002
403.15	−0.166 938	−41.660 465	−5.868 755	0.041 884	0.003
413.15	−0.181 387	−44.331 094	−5.791 185	0.049 447	0.003

[a] $b = 20$, $\alpha_1 = 10$, $\alpha_2 = 3.5$. Units: $kg^{1/2}\,mol^{-1/2}$

The value $\alpha_3 = 1.0$, which is found to give good agreement in case of aqueous electrolyte systems [304], also maintain excellent results for electrolyte solutions in PnP.
Ion-interaction parameters obtained from fitting of experimental osmotic coefficients of Bu_4NX (X = Br^-, NO_3^-, SCN^- and OAc^-) in PnP are shown in Table G.1-G.4 along with the standard deviation between experimental and calculated values of ϕ.

Clegg-Pitzer Model The relations describing the osmotic coefficient in terms of the Clegg-Pitzer model are on a mole fraction scale. The mole fraction of the species, x, present in Bu_4NX(PnP), together with the ionic strength of the solution on mole fraction base, I_x, can be expressed in the following way for a 1:1 electrolyte:

$$x = x_{Bu_4N^+} = x_{X^-} = \frac{mM_S}{1 + 2mM_S} \tag{6.38a}$$

$$x_S = 1 - 2x_{Bu_4N^+} = 1 - 2x_{X^-} = \frac{1}{1 + 2mM_S} \tag{6.38b}$$

$$I = \frac{1}{2}\sum x_i z_i^2 = x \tag{6.38c}$$

In this model, like the NRTL model, the activity coefficients for a solvent γ_S (and hence the osmotic coefficient) can be written in terms of long-range (lr) and short-range (sr) contributions as given in Eq. (6.39)

$$\ln \gamma_S = \ln \gamma_S^{lr} + \ln \gamma_S^{sr} \tag{6.39}$$

In this model a three suffix Margules expansion is used for the short range contribution, and a modified Pitzer-Debye-Hückel (PDH) equation adapted by Clegg et al. [296] is used for the long range contribution. The modified PDH equation ($\ln \gamma_S^{PDH} = \frac{2A_x I_x^{3/2}}{1+\rho I_x^{1/2}}$) used in model of Clegg et. al. has the form

$$\ln \gamma_S^{PDH} = \frac{2A_x I_x^{3/2}}{1+\rho I_x^{1/2}} + 2x^2 \left[B_{ca} \exp\left(-\alpha_1 \sqrt{I_x}\right) + B_{ca}^1 \exp\left(-\alpha_2 \sqrt{I_x}\right) \right] \tag{6.40a}$$

$$A_x = \frac{\sqrt{2\pi N_A d_S^*}}{3M_S} \cdot \left(\frac{e^2}{4\pi\epsilon_0 \epsilon kT}\right)^{3/2} \tag{6.40b}$$

$$\rho = a \left(2e^2 N_A d_S^* / M_S \epsilon_0 \epsilon kT\right)^{1/2} \tag{6.40c}$$

Here, the first term in the right-hand side of Eq. (6.40a) is equal to the PDH equation, x is the mole fraction of the cation or anion, respectively; B_{ca} and B_{ca}^1 are long-range force parameters associated, respectively, with two adjustable parameters, α_1 and α_2. A_x is the Debye-Hückel constant for the osmotic coefficient in the mole fraction scale and ρ is a parameter depending on the distance parameter a. The parameter ρ is related to the hard-core collision diameter, or distance of closest approach, of ions in solution. It is calculated according to the method described by Barthel et. al. [152] with contributions from cation, anion and a solvent molecule (see 5.22). Values of ρ are tabulated in Table 6.3.
For most aqueous systems the α_1 value is set to 13. For aqueous unsymmetrical electrolyte systems, the model was basically developed for, the value $\alpha_2 = 2$ has been used. All systems under investigation reveal that the same values used for aqueous systems also give the best results in fitting experimental osmotic coefficient data of electrolyte solutions in PnP.
The equation of Clegg et. al. for the short-range contribution to the solvent activity coefficient, $\ln \gamma_S^{sr}$, of a symmetrical electrolyte system has the following form:

$$\ln \gamma_S^{sr} = 4x^2 \left[W_{1,ca} + (4x-1)\, U_{1,ca} - (1-2x)(1-6x) V_{1,ca} \right] \tag{6.41}$$

Here, $W_{1,ca}$ and $U_{1,ca}$ are model parameters describing short range interactions. The quaternary term $V_{1,ca}$ is used here also to effectively handle the osmotic coefficients at higher concentrations. Adding Eq. (6.40a) to Eq. (6.41), the necessary equation for the solvent activity coefficient is obtained. From this equation together with the relation $\ln a_S = \ln \gamma_S + \ln x_S$ and Eq. (6.13) the corresponding expression for the osmotic coefficient is derived. The obtained fit parameters together with standard deviation in osmotic coefficient are collected in Tables G.5-G.8.
From the inspection of the results, an equally well performance of all three models can be observed. The agreement between experimental and calculated osmotic coefficients is excellent with a group of common parameters, which may also be valid for this class of solvent.
Calculation of the mean molal activity coefficient $\gamma_\pm$ using each set of the model parameters is renounced, because the validity of $\gamma_\pm$ calculations depends on how well the model describes the osmotic coefficients in the dilute region. This concentration range, however, is insufficiently accessible within this work. Nevertheless, one might expect a rapid decrease of the activity coefficients with increasing concentration, as would be the case for systems with similar low permittivities like that of PnP [291].
Finally the following Fig. 6.14 is meant to present a comprehensive representation of the solvent's related physicochemical parameters in connection with vapor pressure experiments on electrolyte systems. It concludes the most important functions in an electrolyte system of molality m. The differences between a hypothetical ideal solution (x_{PnP} follows most obvious from its inspection compared to experimental values for the (nonideal) solvent activity $a = x\,f$. Most important of this presentation is the fact, that non-ideality is best accomplished by making use of the osmotic coefficient instead of solvent activity. The

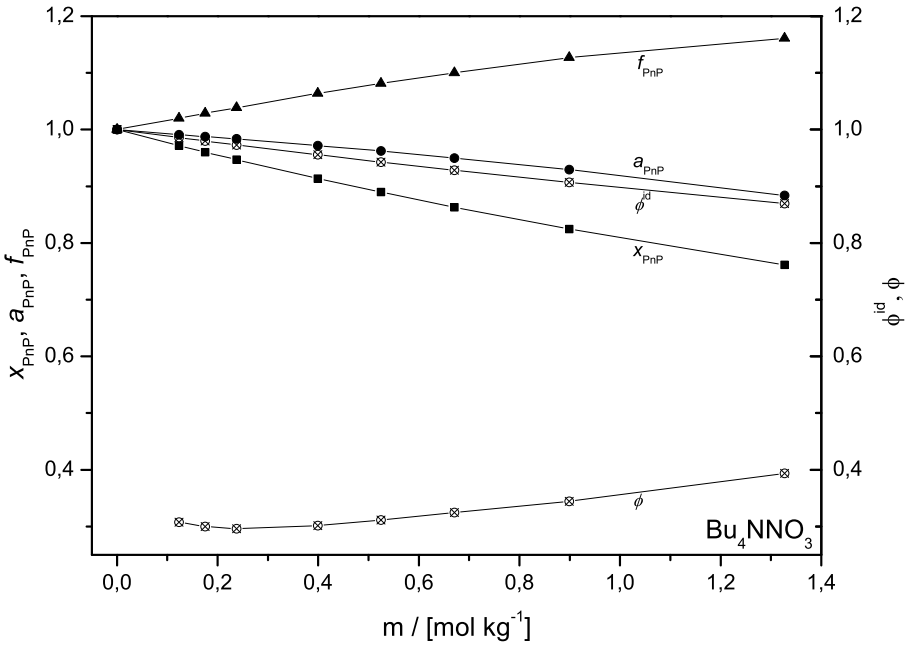

Figure 6.14.: Comparison between the ideal and real behavior at 323.15 K

last will only slightly differ from unity for many systems, although being quite apart from ideal behavior. Hence any conclusion with respect to association, solvation etc. would hardly be possible, because of very small differences in a. Whereas the definition of ϕ leads to a quantity, which clearly reflects the influence of the intermolecular interactions taking place in electrolyte solutions. It is very interesting to see, that the activity coefficient f for the solvent is always greater than one and increases with concentration. This indicates very weak solvent-ion interactions due to the low degree of dissociation in this solutions (low mean activity coefficients) and weakness of the solvent-ion-pair interaction.

7. Summary

This study presents an investigation of several thermodynamic as well as transport properties of chemical systems, all of which have 1-propoxy-2-propanol as common constituent. Different experimental techniques have been applied and can be split into two categories with respect to the composition: electrolyte-free, binary solvent mixtures of PnP with different alcohols, and water as well as electrolytic systems with four different salts of the same class: Bu_4NX (X = Br^-, $NO_3{}^-$, SCN^-, OAc^-). To our best knowledge, comparable studies are not known from the literature with respect to the application of those techniques on the chemical systems presented here. This work is intended to present a first original attempt to qualitatively and quantitatively describe the physico-chemical behavior of PnP in selected liquid systems, making use of very well developed laboratory machines and theoretically well-founded model calculations.

Binaries of PnP with a second liquid component have been used to study the isobaric as well as isothermal vapor-liquid equilibria (VLE) at different experimental conditions in order to obtain a qualitative and quantitative measure of the components intermolecular interactions. A commercial all-glass equilibration still with an electronic control unit in connection with a gas phase chromatograph (GC) allows for the exact determination of the phase variables: x, y, p and T.
Prior to measurements, the novelty of results with this equilibration still at the institute requires the acquisition of correct working methods including method calibration, sample preparation and handling of the various control parameters. Furthermore theoretical models have been required to be incorporated in an easy-to-use program for data processing for the first time, including the possibility to read-in, process and present graphically the VLE data in combination with quality related regression parameters.
Different activity coefficient models for binary mixtures are successfully applied to the measured VLE data. UNIQUAC model calculations, however, are found to show the highest deviations in most cases Further data processing with the help of two predictive models, the modified UNIFAC (Dortmund) and the COSMO-RS model, astonishingly gives good to very good agreement between measured and predicted phase diagrams. Noteworthy to emphasize on this occasion the fact, that COSMO-RS only requires a relatively small number of adjusted parameters, thus allowing the general prediction of various thermodynamic fluid properties in mixtures with multiple constituents.
Phase diagrams show both, positive and negative deviations from ideality (Raoult's law). Water + PnP/PM exhibit positive deviations due to decreasing H-bonding with increasing temperature. This increased hydrophobicity of the glycol ether is evident from large and positive values of γ_i, leading to partial miscibility in the case of water/PnP. Under conditions of lower thermal energy, strong intermolecular H-bonding lead to negative molar excess volumes. For non-aqueous systems, the deviations from ideality may be partially explained by the excess molar volumes of corresponding mixtures. Systems containing PnP with large negative V^{ex} (methanol, ethanol) form liquid mixtures with partially fitting of the components in void spaces of solvent structures with interaction potentials similar to the respective pure solvent ($\gamma_i \simeq 1$). PnP + 2-butanol/1-hexanol represent systems with much lower geometrical fitting, whilst dispersive interaction energies have a considerable amount ($\gamma_i < 1$).
Within the experimental uncertainties, a set of parameters for a given system obtained in the isobaric mode, can be used to calculate isothermal $p - x$ - diagrams with very good accuracy, proven exemplary for the binary PnP/EtOH. Finally, the effect of pressure on the overall behavior of the binary systems is shown to be only small, mainly determined by the different vapor pressure of the mixtures and not by relevant changes of interaction profiles.

Peculiarities of aqueous mixtures containing PnP in their phase behavior, investigated in a former work [5], have been motivation to prove these anomalies by further experimental evidence. It is well known that

several systems of glycol ethers, classified as hydrotropes, show a huge increase of solubility of water insoluble substances with increasing amount of the hydrotrope. Further results on the surface tension, molar volume as well as molar heat capacity of aqueous mixtures with increasing content of PnP reveal the effect of hydrotrope action: cooperative self-aggregation, often compared to the cooperative process such as micellization. Inferred from surface tension measurements, a minimum hydrotropic concentration (MHC) can be addressed to the structural changes. This value is in close agreement to the independently determined onset of solubilization, the minimum in the apparent molar volume as well as the maximum in the apparent molar heat capacity of PnP. These similarities are caused by the same phase transition and structural changes in the liquid state: microstructuring in the water rich region, accomplished by peak anomalies in the partial and apparent molar quantities. Assuming hydrophobic hydration of PnP in water at very low concentration, structuring of water around the organic compound is energetically favored, as the spatial network of water H-bonds is strengthen and will push nonelectrolyte molecules into their own microheterogenous phase. With increasing concentration of PnP, molar heat capacity will reach a maximum value, whilst occupation of the void spaces in the water structure by the organic substance gives rise to the minimum volumetric requirements of PnP. Beyond the MHC, at which the increasing number of network defects will cause the water structure to collapse around the solute molecules, existing microphases of PnP levels off the apparent molar quantities to values of the solute in its pure liquid state.

Electrolyte solutions in 1-propoxy-2-propanol have been the focus of precise conductivity experiments in combination with the results of theoretical models from infinite dilution up to high concentrations.
The experimental work can be subdivided into three independent parts, each of which gives the following results:

1. Determination of the pure solvents viscosity, density and relative permittivity within a temperature range of 248.15 and 313.15 K. Owing to the mathematical requirements of VLE - and vapor pressure - analysis for the molar volume of PnP, data of liquid density are extended up to a maximum temperature of 423.15 K. Viscosity and relative permittivity are shown to be solvent properties, which have a major influence on the conductance of dilute as well as concentrated electrolyte solutions. Both properties follow the order of decreasing value with increasing temperature. Most important is the low value of ϵ in the evaluation of experimental data.

2. Conductance studies at low concentration, with which one can obtain information of the association, mobility and solvation of ions in solution of PnP. Evaluation of the data results in the following conclusions:

   - because of the low value of the relative permittivity ϵ, all 4 salts show a high degree of association. The anions follow the sequence of increasing association in the order $OAc^- < Br^- \leq SCN^- < NO_3{}^-$. With respect to the minor impact of non-coulombic interactions, this trend can be rationalized in terms of electrostatic interactions: increasing radii of the solvated anions reduce the attractive interaction and hence the association of oppositely charged ions.
   - differences in K_A are smaller than in usual solvating type solvents.
   - the degree of association increases with increasing temperature in accordance with the decreasing value of ϵ. This provides another hint for the presence of only weak ion solvation, also reflected by the temperature-invariant entropy of association. Thermodynamics of the association process are marked by the major influence of coulombic interaction forces.
   - inspection of Walden's product reveal an opposite trend in the sequence of anions' radii when compared to the association constant. Again, this fact demonstrates the strong electrostatic interaction between the charged species.
   - Bu_4N^+ is believed to be, if at all, only weakly solvated in PnP, according to Krumgalz's anchor values for $\lambda^{\infty}_{Bu_4N^+}$ in several solvents of different classes.

3. Extensive results on the conductance behavior of the electrolyte solutions up to higher concentrations of more than 1 mol kg^{-1}. Important parameters obtained from those data are the maximum

conductivity κ_{m} and its position μ, as a result of applying the Casteel-Amis equation. Unfortunately, conductivity determining effects in concentrated solutions (viscosity, permittivity, association, solvation, ...) can not be separated due to their mutual interdependency. But for all systems under investigations the typical pattern of $\kappa = f(\mathrm{m})$ has been found, which is evident for the formation of charged species, namely triple-ions. The existence of those conducting aggregates explains the maximum in specific conductivity, the position of which is related to temperature and the the solvent's viscosity. Three-dimensional plots of $\kappa = f(\mathrm{m}, T)$ offers an accurate and easy access to predict specific conductivity arbitrarily within the range experimentally covered.

A concluding result between dilute and concentrated measurements is the increasing concentration of maximum specific conductance μ with decreasing Stoke's radii, as the ionic mobility is increasing in the same way. However, mobility of the anions alone can not account for the trend in κ_{max} and indicates the interplay of different effects, e.g. association.
A theoretical approach to the concept of triple-ion formation allows calculation of K_T to be made. Results reveal relatively small, but significant triple-ion formation constants with correct temperature dependency.

Determination of precise vapor pressure data of pure 1-propoxy-2-propanol over a large temperature range forms one important part of vapor-liquid equilibrium investigations of electrolytic solvent systems. Knowledge of p, as an important key parameter for many thermodynamic calculations, is crucial for data processing of the VLE experiments and correlation/prediction of phase diagrams. Its temperature dependence allows for the evaluation of the heat of evaporation of PnP. The value of $\Delta_{\mathrm{vap}}H$ is found to be quite large, comparable to those of simple alcohols, which are known to possess large intermolecular, adhesive interaction forces. This is in agreement with PnP's ability to form strong (temperature-dependent) hydrogen-bonds with water, observed through the existence of a lower critical solubility temperature.
Vapor pressure depressions of Bu_4NX ($X = Br^-$, $NO_3{}^-$, SCN^-, OAc^-) in PnP have also been determined between 323.15 and 413.15 K. Obtained values for the osmotic coefficient are subject to data analysis with the help of different model equations. It is found, that all four salts show very low ϕ-values, indicating strong ion-association in accordance to the results of conductance measurements. Unfortunately, due to the very high association constants of the electrolytes, Barthel's chemical model, applied on osmotic coefficients, could not be used successfully. Only quantitative evidence for similar association behavior between both experimental techniques (Λ and Δp) are given. Again, Bu_4NOAc shows the lowest amount of ion-pairs existing in solutions of PnP. The activity coefficient $\gamma_{\pm}$ is believed to decrease rapidly with concentration, with the solvent's activity being greater than unity.
The low permittivity as well as very low vapor pressure of 1-propoxy-2-propanol accounts for the problems with respect to required accuracy and precision of Λ and Δp values, which most probably gives the reason for the lcCM to fail in determining K_A as physically meaningful, quantitative parameter.

Appendix A: Binary Solution Data of PnP + Water

A.1. Apparent Molar Volumes at 298.15 K

x_{PnP}	d / $\frac{\mathrm{g}}{\mathrm{dm}^3}$	$v^{\mathrm{E}}_{\mathrm{PnP}}$ / $\frac{\mathrm{cm}^3}{\mathrm{mol}}$	$\Phi_{v,\mathrm{PnP}}$ / $\frac{\mathrm{cm}^3}{\mathrm{mol}}$	v_{PnP} / $\frac{\mathrm{cm}^3}{\mathrm{mol}}$	x_{PnP}	d / $\frac{\mathrm{g}}{\mathrm{dm}^3}$	$v^{\mathrm{E}}_{\mathrm{PnP}}$ / $\frac{\mathrm{cm}^3}{\mathrm{mol}}$	$\Phi_{v,\mathrm{PnP}}$ / $\frac{\mathrm{cm}^3}{\mathrm{mol}}$	v_{PnP} / $\frac{\mathrm{cm}^3}{\mathrm{mol}}$
0	997.04	0			0.1160	961.89	-0.723	127.90	127.90
0.0012	996.71	-0.015	123.88	123.88	0.1281	958.59	-0.756	128.22	128.23
0.0014	996.67	-0.016	123.93	123.93	0.1546	952.25	-0.830	128.75	128.76
0.0028	996.32	-0.032	123.49	123.49	0.1780	947.32	-0.888	129.13	129.13
0.0072	995.37	-0.083	122.97	122.97	0.2180	939.96	-0.970	129.67	129.67
0.0097	994.93	-0.112	122.77	122.77	0.2555	934.06	-1.032	130.08	130.08
0.0115	994.61	-0.134	122.65	122.65	0.2682	932.23	-1.050	130.20	130.20
0.0171	993.75	-0.202	122.41	122.41	0.3170	925.82	-1.100	130.65	130.65
0.0293	991.31	-0.336	122.70	122.70	0.3731	919.57	-1.133	131.08	131.08
0.0352	989.67	-0.388	123.12	123.12	0.4787	909.58	-1.097	131.82	131.82
0.0472	985.28	-0.465	124.31	124.31	0.5657	903.06	-1.019	132.31	132.31
0.0629	979.21	-0.537	125.60	125.60	0.7343	893.49	-0.797	133.03	133.03
0.0761	974.36	-0.589	126.40	126.40	0.8078	888.71	-0.490	133.50	133.50
0.0945	968.24	-0.653	127.21	127.22	1.0000	880.97	0	134.15	134.15
0.1091	963.68	-0.696	127.75	127.75					

density, d; molar excess volume, $v^{\mathrm{E}}_{\mathrm{PnP}}$; apparent molar volume, $\Phi_{v,\mathrm{PnP}}$; partial molar volume, v_{PnP}

A.2. Apparent Molar Heat Capacities

x_{PnP}	$\mathrm{m}_{\mathrm{PnP}}$ / $\mathrm{mol\,kg^{-1}}$	$c_{p,\mathrm{PnP}}$ / $\mathrm{J\,g^{-1}\,K^{-1}}$	$\Phi_{c,\mathrm{PnP}}$ / $\mathrm{J\,mol^{-1}\,K^{-1}}$	x_{PnP}	$\mathrm{m}_{\mathrm{PnP}}$ / $\mathrm{mol\,kg^{-1}}$	$c_{p,\mathrm{PnP}}$ / $\mathrm{J\,g^{-1}\,K^{-1}}$	$\Phi_{c,\mathrm{PnP}}$ / $\mathrm{J\,mol^{-1}\,K^{-1}}$
			278.15 K				
0	0	4.203		0.0326	1.8727	4.238	519.2
0.0031	0.1741	4.140	127.2	0.0330	1.8938	4.238	519.4
0.0091	0.5108	4.161	409.4	0.0388	2.2398	4.248	522.2
0.0115	0.6474	4.161	427.0	0.0450	2.6166	4.194	492.0
0.0146	0.8234	4.185	472.5	0.0612	3.6214	4.049	435.9
0.0165	0.9323	4.194	485.9	0.1323	8.4617	3.594	352.8
0.0188	1.0651	4.189	481.8	0.2215	15.7907	3.088	294.3
0.0251	1.4287	4.209	501.9	0.3656	31.9861	2.725	275.8
0.0286	1.6328	4.228	515.2	0.5502	67.9072	2.511	271.9
0.0317	1.8185	4.228	513.4	1.0000		2.257	266.8
			288.15 K				
0	0	4.187		0.0326	1.8727	4.241	529.8
0.0031	0.1741	4.128	149.1	0.0330	1.8938	4.238	527.7
0.0091	0.5108	4.148	414.4	0.0388	2.2398	4.230	519.3
0.0115	0.6474	4.163	454.7	0.0450	2.6166	4.179	490.8
0.0146	0.8234	4.176	480.1	0.0612	3.6214	4.035	435.0
0.0165	0.9323	4.177	482.5	0.1323	8.4617	3.626	362.1
0.0188	1.0651	4.186	493.7	0.2215	15.7907	3.149	306.4

Table A.1.: (continued)

x_{PnP}	m_{PnP} / mol kg^{-1}	$c_{\mathrm{p,PnP}}$ / J g^{-1} K^{-1}	$\Phi_{c,\mathrm{PnP}}$ / J mol^{-1} K^{-1}	x_{PnP}	m_{PnP} / mol kg^{-1}	$c_{\mathrm{p,PnP}}$ / J g^{-1} K^{-1}	$\Phi_{c,\mathrm{PnP}}$ / J mol^{-1} K^{-1}
0.0251	1.4287	4.206	510.1	0.3656	31.9861	2.793	286.5
0.0286	1.6328	4.221	519.8	0.5502	67.9072	2.578	280.9
0.0317	1.8185	4.239	529.4	1.0000		2.300	271.9
			298.15 K				
0	0	4.181		0.0326	1.8727	4.225	523.2
0.0031	0.1741	4.120	137.6	0.0330	1.8938	4.222	521.0
0.0091	0.5108	4.138	405.4	0.0388	2.2398	4.203	506.6
0.0115	0.6474	4.156	453.2	0.0450	2.6166	4.153	480.5
0.0146	0.8234	4.167	476.1	0.0612	3.6214	4.024	432.4
0.0165	0.9323	4.167	477.8	0.1323	8.4617	3.646	367.7
0.0188	1.0651	4.178	490.9	0.2215	15.7907	3.202	316.4
0.0251	1.4287	4.198	508.0	0.3656	31.9861	2.856	296.1
0.0286	1.6328	4.210	515.6	0.5502	67.9072	2.638	289.1
0.0317	1.8185	4.227	524.9	1.0000		2.341	276.7
			308.15 K				
0	0	4.179		0.0326	1.8727	4.191	501.7
0.0031	0.1741	4.115	118.9	0.0330	1.8938	4.191	501.6
0.0091	0.5108	4.130	391.4	0.0388	2.2398	4.165	485.9
0.0115	0.6474	4.140	429.4	0.0450	2.6166	4.116	462.5
0.0146	0.8234	4.158	466.2	0.0612	3.6214	4.015	429.3
0.0165	0.9323	4.165	476.7	0.1323	8.4617	3.655	370.0
0.0188	1.0651	4.164	477.7	0.2215	15.7907	3.247	324.7
0.0251	1.4287	4.185	498.8	0.3656	31.9861	2.913	304.7
0.0286	1.6328	4.195	505.3	0.5502	67.9072	2.694	296.5
0.0317	1.8185	4.191	502.2	1.0000		2.381	281.4

molality, m; specific heat capacity , $c_{p,\mathrm{PnP}}$; apparent molar heat capacity, $\Phi_{c,\mathrm{PnP}}$

Appendix B: GC Analysis of Binary Mixtures

Table B.1.: Experimental Data of GC for calibration with binary liquids over whole composition range

PnP + MeOH		PnP + EtOH		PnP + 2-BuOH		PnP + 1-HeOH		PnP + H_2O		PnP + PM		PM + H_2O	
ξ_{PnP}	x_{PnP}	ξ_{PnP}	x_{PnP}	ξ_{PnP}	x_{PnP}	ξ_{PnP}	x_{PnP}	ξ_{PnP}	x_{PnP}	ξ_{PnP}	x_{PnP}	ξ_{PnP}	x_{PnP}
1	1	1	1	1	1	1	1	0	0	0	0	0	0
0.986	0.938	0.930	0.830	0.955	0.936	0.936	0.949	0.021	0.010	0.050	0.028	0.089	0.023
0.984	0.928	0.856	0.686	0.918	0.888	0.905	0.924	0.041	0.184	0.130	0.077	0.221	0.081
0.960	0.837	0.843	0.665	0.880	0.838	0.861	0.884	0.061	0.256	0.170	0.102	0.338	0.135
0.937	0.762	0.747	0.522	0.842	0.789	0.819	0.852	0.081	0.318	0.210	0.130	0.468	0.204
0.912	0.691	0.679	0.441	0.803	0.746	0.773	0.813	0.097	0.373	0.280	0.182	0.534	0.247
0.890	0.637	0.645	0.405	0.755	0.690	0.701	0.752	0.118	0.421	0.350	0.238	0.562	0.272
0.872	0.597	0.517	0.286	0.722	0.653	0.577	0.642	0.136	0.463	0.390	0.268	0.666	0.361
0.806	0.475	0.404	0.203	0.685	0.613	0.541	0.601	0.154	0.501	0.440	0.306	0.716	0.413
0.787	0.445	0.292	0.134	0.647	0.572	0.472	0.538	0.195	0.571	0.460	0.326	0.755	0.459
0.738	0.382	0.226	0.099	0.594	0.518	0.388	0.454	0.258	0.668	0.500	0.363	0.789	0.512
0.601	0.253	0.147	0.065	0.539	0.463	0.339	0.400	0.382	0.769	0.590	0.447	0.810	0.541
0.547	0.213	0.091	0.038	0.501	0.428	0.238	0.289	0.495	0.836	0.630	0.488	0.849	0.599
0.471	0.168	0.075	0.031	0.424	0.362	0.173	0.212	0.563	0.868	0.660	0.518	0.877	0.652
0.396	0.128	0	0	0.395	0.328	0.152	0.184	0.738	0.930	0.720	0.584	0.911	0.722
0.345	0.108			0.346	0.283	0.070	0.086	0.899	0.973	0.760	0.633	0.930	0.765
0.246	0.071			0.286	0.227	0	0	1	1	0.810	0.699	0.952	0.821
0	0			0.227	0.177					0.870	0.783	0.958	0.840
				0.155	0.127					0.920	0.861	0.978	0.896
				0.094	0.080					0.950	0.910	0.989	0.935
				0.047	0.040					0.970	0.946	0.995	0.953
				0	0					1	1	1	1

area fraction, ξ; mole fraction, x

Appendix C: Experimental VLE Data

C.1. Measurements at 20.0 kPa

Table C.1.: Experimental VLE data for the binary mixtures of 1-Propoxy-2-propanol(1) with some aliphatic alcohols and water at 20.0 kPa

x_1	y_1	$\ln(\gamma_1/\gamma_2)$	T/K	x_1	y_1	$\ln(\gamma_1/\gamma_2)$	T/K
PnP(1) + MeOH(2)							
0	0		301.3	0.509	0.024	−0.188	314.6
0.006	0.0003	0.812	301.7	0.559	0.028	−0.246	317.0
0.013	0.001	0.437	301.8	0.575	0.030	−0.258	317.7
0.030	0.001	0.006	302.1	0.596	0.033	−0.259	318.9
0.055	0.001	−0.083	302.6	0.626	0.041	−0.168	320.3
0.089	0.002	−0.014	303.2	0.685	0.059	−0.114	324.3
0.122	0.003	−0.031	304.1	0.697	0.068	−0.034	325.0
0.162	0.004	−0.140	304.8	0.736	0.081	−0.069	328.1
0.197	0.005	−0.172	305.6	0.787	0.110	−0.088	333.0
0.241	0.007	−0.139	306.5	0.815	0.130	−0.096	334.7
0.284	0.009	−0.077	307.4	0.903	0.288	−0.008	347.9
0.354	0.012	−0.119	309.2	0.932	0.380	−0.045	353.8
0.413	0.017	−0.066	311.0	0.999	0.983	−0.112	374.4
0.461	0.020	−0.108	312.8	1	1		374.9
PnP(1) + EtOH(2)							
0	0		315.4	0.437	0.043	−0.029	324.1
0.032	0.002	0.167	315.8	0.509	0.057	−0.060	326.5
0.062	0.004	0.173	316.4	0.556	0.068	−0.067	328.2
0.094	0.007	0.131	317.0	0.621	0.087	−0.095	330.7
0.129	0.009	0.115	317.6	0.693	0.117	−0.119	334.4
0.154	0.011	0.114	317.9	0.768	0.164	−0.151	339.0
0.164	0.012	0.093	318.1	0.832	0.224	−0.209	344.3
0.194	0.015	0.078	318.8	0.900	0.351	0.230	351.9
0.317	0.028	0.045	321.2	0.979	0.744	−0.297	368.2
0.329	0.029	0.033	321.4	0.980	0.757	−0.272	369.1
0.370	0.034	−0.001	322.5	0.992	0.881	−0.326	372.1
0.372	0.035	0.032	322.7	1	1		374.8
PnP(1) + 2-BuOH(2)							
0	0		335.2	0.654	0.249	0.0003	352.3
0.007	0.001	−0.307	335.3	0.709	0.303	0.007	354.6
0.026	0.003	−0.277	335.6	0.754	0.355	0.015	356.6
0.064	0.009	−0.244	336.2	0.813	0.444	0.026	359.7
0.114	0.017	−0.206	337.1	0.880	0.578	0.026	364.4
0.174	0.029	−0.16	338.2	0.899	0.622	0.017	365.7
0.233	0.043	−0.136	339.4	0.925	0.699	0.032	367.9
0.284	0.057	−0.11	340.5	0.940	0.746	0.014	369.7

Table C.1.: (continued)

x_1	y_1	$\ln(\gamma_1/\gamma_2)$	T/K	x_1	y_1	$\ln(\gamma_1/\gamma_2)$	T/K
0.341	0.075	−0.082	341.8	0.975	0.871	−0.073	372.9
0.392	0.094	−0.066	343.4	0.991	0.948	−0.167	374.1
0.439	0.114	−0.046	344.4	0.998	0.991	0.095	374.8
0.480	0.133	−0.037	345.6	1	1		374.9
0.578	0.191	−0.01	349.6				
PnP(1) + 1-HeOH(2)							
0	0		386.1	0.499	0.619	0.0317	381.2
0.029	0.039	−0.112	386.0	0.554	0.673	0.046	380.5
0.058	0.078	−0.102	385.7	0.615	0.733	0.079	379.8
0.091	0.123	−0.107	385.5	0.685	0.794	0.098	378.8
0.138	0.186	−0.078	385.0	0.730	0.829	0.110	378.2
0.191	0.255	−0.062	384.5	0.779	0.866	0.129	377.6
0.241	0.318	−0.049	384.1	0.832	0.903	0.152	376.9
0.278	0.365	−0.039	383.7	0.884	0.936	0.170	376.3
0.316	0.412	−0.024	383.3	0.917	0.955	0.155	375.9
0.381	0.488	−0.006	382.6	0.945	0.974	0.29914	375.5
0.439	0.555	0.0137	381.9	1	1		374.9
PnP(1) + H_2O(2)							
0	0		333.3	0.449	0.135	0.253	331.7
0.009	0.087	4.227	332.4	0.525	0.136	-0.051	331.7
0.016	0.110	3.952	331.9	0.656	0.137	-0.599	332.9
0.022	0.123	3.718	331.8	0.769	0.165	-0.959	335.8
0.028	0.131	3.589	331.7	0.814	0.198	-1.031	339.0
0.035	0.133	3.355	331.7	0.897	0.252	-1.450	346.2
0.038	0.133	3.268	331.7	0.915	0.282	-1.524	349.6
0.039	0.133	3.243	331.7	0.940	0.334	-1.693	354.8
0.042	0.133	3.175	331.7	0.956	0.462	-1.496	360.3
0.042	0.134	3.167	331.7	1.000	1.000		374.9
0.072	0.134	2.599	331.7				

C.2. Measurements at 101.3 kPa

Table C.2.: Experimental VLE data for the binary mixtures of 1-Propoxy-2-propanol(1) with some aliphatic alcohols and water at 101.3 kPa

x_1	y_1	$\ln(\gamma_1/\gamma_2)$	T/K	x_1	y_1	$\ln(\gamma_1/\gamma_2)$	T/K
PnP(1) + MeOH(2)							
0	0		337.6	0.523	0.038	-0.324	354.3
0.024	0.001	0.220	338.1	0.633	0.061	-0.356	362.7
0.036	0.002	-0.022	338.4	0.669	0.079	-0.277	366.3
0.059	0.002	-0.266	338.6	0.779	0.137	-0.327	379.4
0.082	0.004	-0.045	339.7	0.854	0.215	-0.384	391.5
0.113	0.005	-0.065	340.4	0.910	0.330	-0.422	402.5
0.168	0.008	-0.105	341.7	0.956	0.483	-0.601	412.2
0.225	0.012	-0.039	343.0	0.962	0.589	-0.338	414.2
0.317	0.018	-0.150	345.5	0.973	0.639	-0.503	417.5
0.379	0.022	-0.240	347.3	0.983	0.787	-0.286	420.0
0.429	0.026	-0.286	349.3	0.997	0.984	0.683	423.0
0.461	0.029	-0.312	350.4	1	1		423.2
0.475	0.031	-0.300	351.1				
PnP(1) + EtOH(2)							
0	0		351.5	0.538	0.075	-0.226	365.4
0.107	0.010	0.012	352.0	0.551	0.084	-0.165	366.3
0.182	0.018	-0.017	353.5	0.665	0.127	-0.232	373.6
0.219	0.022	-0.030	354.5	0.740	0.173	-0.262	379.3
0.269	0.027	-0.074	355.9	0.810	0.240	-0.287	386.1
0.284	0.031	-0.045	356.3	0.853	0.302	-0.311	391.6
0.354	0.040	-0.093	358.4	0.904	0.440	-0.237	400.4
0.401	0.049	-0.102	360.2	0.988	0.900	-0.075	421.0
0.462	0.058	-0.187	362.5	1	1		423.4
0.482	0.063	-0.180	363.2				
PnP(1) + 2-BuOH(2)							
1	1		423.3	0.607	0.219	-0.125	392.7
0.978	0.902	-0.072	420.5	0.565	0.192	-0.110	390.9
0.954	0.823	0.018	418.3	0.483	0.130	-0.231	387.1
0.930	0.754	0.040	416.3	0.464	0.119	-0.253	386.5
0.915	0.698	-0.028	414.4	0.444	0.113	-0.237	385.8
0.895	0.643	-0.034	412.5	0.424	0.107	-0.212	385.2
0.876	0.601	-0.018	410.9	0.404	0.101	-0.193	384.7
0.862	0.557	-0.068	409.3	0.398	0.095	-0.230	384.1
0.844	0.524	-0.057	408.0	0.369	0.085	-0.230	383.1
0.828	0.492	-0.064	406.6	0.356	0.081	-0.226	382.6
0.805	0.454	-0.061	405.0	0.334	0.074	-0.222	381.9
0.783	0.422	-0.050	403.6	0.291	0.061	-0.224	380.6
0.767	0.395	-0.065	402.4	0.253	0.052	-0.202	379.5
0.752	0.362	-0.115	400.5	0.079	0.015	-0.074	374.6
0.714	0.321	-0.097	398.7	0.032	0.006	-0.045	373.6
0.685	0.292	-0.093	397.0	0.016	0.003	-0.050	373.2
0.651	0.256	-0.115	394.9	0	0		372.7

Table C.2.: (continued)

x_1	y_1	$\ln(\gamma_1/\gamma_2)$	T/K	x_1	y_1	$\ln(\gamma_1/\gamma_2)$	T/K
PnP(1) + 1-HeOH(2)							
0	0		430.7	0.995	0.996	-0.158	423.2
0.022	0.029	0.109	430.6	0.967	0.974	0.055	423.3
0.051	0.058	-0.036	430.4	0.926	0.944	0.093	423.7
0.081	0.090	-0.061	430.4	0.883	0.911	0.089	424.0
0.128	0.144	-0.047	430.2	0.831	0.871	0.113	424.5
0.183	0.211	-0.002	429.9	0.772	0.817	0.073	425.1
0.229	0.258	-0.021	429.7	0.719	0.769	0.065	425.4
0.283	0.324	0.013	429.3	0.644	0.700	0.058	426.3
0.327	0.374	0.023	429.0	0.592	0.651	0.056	426.8
0.428	0.474	0	428.3	0.507	0.565	0.044	427.6
0.509	0.567	0.045	427.5	0.453	0.500	0.001	428.2
0.573	0.630	0.040	426.6	1	1		423.2
PnP(1) + H_2O(2)							
0	0		373.2	0.713	0.180	-0.827	381.2
0.001	0.041	5.381	372.5	0.779	0.240	-0.823	385.8
0.003	0.058	4.646	372.2	0.807	0.270	-0.841	388.1
0.004	0.064	4.466	371.9	0.856	0.337	-0.888	392.8
0.005	0.088	4.590	371.7	0.873	0.373	-0.881	395.4
0.316	0.089	0.072	371.3	0.896	0.415	-0.938	398.8
0.355	0.088	-0.111	371.3	0.937	0.544	-0.977	405.7
0.401	0.088	-0.309	371.4	0.997	0.983	-0.229	423.2
0.492	0.090	-0.651	372.3	1	1		423.3
0.644	0.144	-0.764	377.6				
PnP(1) + PM(2)							
0	0		393.1	0.555	0.326	-0.093	406.0
0.018	0.008	0.041	393.2	0.604	0.371	-0.095	407.4
0.034	0.013	-0.084	393.5	0.657	0.431	-0.082	409.3
0.062	0.025	-0.030	394.0	0.693	0.467	-0.102	410.3
0.092	0.037	-0.052	394.6	0.734	0.512	-0.129	411.5
0.127	0.052	-0.073	395.3	0.771	0.566	-0.123	413.1
0.163	0.068	-0.084	396.0	0.796	0.604	-0.117	414.1
0.194	0.084	-0.068	396.8	0.827	0.648	-0.133	415.3
0.237	0.103	-0.108	397.6	0.857	0.700	-0.126	416.6
0.270	0.121	-0.095	398.5	0.889	0.756	-0.140	417.9
0.319	0.146	-0.121	399.5	0.923	0.823	-0.147	419.5
0.359	0.172	-0.110	400.6	0.947	0.881	-0.090	420.9
0.399	0.203	-0.081	401.7	0.976	0.943	-0.121	422.2
0.440	0.233	-0.077	402.9	0.985	0.971	0.093	422.8
0.496	0.269	-0.117	404.1	1	1		423.3
0.501	0.280	-0.088	404.4				
PM(1) + H_2O(2)							
0	0		373.5	0.691	0.373	-0.671	375.6
0.007	0.010	1.016	373.4	0.726	0.405	-0.707	376.6
0.010	0.028	1.667	372.5	0.769	0.447	-0.765	377.7

Table C.2.: (continued)

x_1	y_1	$\ln(\gamma_1/\gamma_2)$	T/K	x_1	y_1	$\ln(\gamma_1/\gamma_2)$	T/K
0.013	0.034	1.661	372.2	0.797	0.481	-0.793	378.6
0.015	0.050	1.867	372.0	0.828	0.525	-0.819	380.0
0.019	0.068	1.963	371.7	0.851	0.563	-0.834	381.3
0.027	0.096	2.004	371.3	0.879	0.600	-0.924	382.3
0.057	0.140	1.647	371.0	0.901	0.672	-0.835	384.5
0.110	0.171	1.165	370.8	0.909	0.697	-0.814	385.2
0.219	0.204	0.566	370.7	0.922	0.725	-0.844	385.9
0.262	0.227	0.462	370.8	0.930	0.752	-0.815	386.6
0.314	0.247	0.320	371.0	0.937	0.785	-0.746	387.4
0.358	0.258	0.175	371.3	0.937	0.782	-0.766	387.3
0.357	0.259	0.189	371.2	0.943	0.816	-0.657	388.2
0.400	0.265	0.039	371.6	0.951	0.852	-0.554	389.1
0.442	0.274	-0.090	372.0	0.950	0.861	-0.456	389.5
0.499	0.287	-0.255	372.5	0.958	0.870	-0.571	390.0
0.552	0.308	-0.366	373.2	0.960	0.889	-0.445	390.5
0.599	0.329	-0.461	374.0	0.965	0.908	-0.373	391.0
0.645	0.352	-0.556	374.7	1.000	1.000		393.2

C.3. Vapor Pressure of Binary System PnP(1) + EtOH(2)

Table C.3.: Values of the composition y_i, vapor pressure p, partial pressure p_1, and activity coefficients γ_i

313.15 K						333.15 K					
x_1	y_1 [a]	p [b]	p_1 [a]	γ_1 [a]	γ_2 [a]	x_1	y_1 [a]	p [b]	p_1 [a]	γ_1 [a]	γ_2 [a]
		kPa	kPa					kPa	kPa		
0	0	17.855	0	1.2185	1.0000	0	0	46.840	0	1.2001	1.0000
0.089	0.006	16.523	0.100	1.1722	1.0018	0.089	0.007	43.126	0.322	1.1598	1.0016
0.164	0.012	15.195	0.178	1.1391	1.0059	0.164	0.015	39.665	0.577	1.1304	1.0053
0.172	0.0124	15.043	0.187	1.1357	1.0065	0.172	0.016	39.283	0.605	1.1274	1.0058
0.274	0.021	13.456	0.287	1.0991	1.0160	0.274	0.026	35.354	0.928	1.0942	1.0145
0.508	0.051	9.758	0.500	1.0410	1.0517	0.508	0.063	25.736	1.613	1.0399	1.0479
0.509	0.052	9.567	0.501	1.0407	1.0520	0.509	0.064	25.240	1.616	1.0397	1.0482
0.637	0.081	7.550	0.613	1.0211	1.0792	0.637	0.099	19.997	1.972	1.0208	1.0743
0.697	0.101	6.558	0.665	1.0144	1.0936	0.697	0.123	17.409	2.137	1.0142	1.0883
0.949	0.455	1.942	0.884	1.0004	1.1653	0.949	0.508	5.553	2.821	1.0004	1.1592
1.0	1.0	0.937	0.930	1.0000	1.1822	1.0	1.0	2.967	2.962	1.0000	1.1762
353.15 K											
0	0	108.283	0	1.1671	1.0000						
0.089	0.009	99.341	0.881	1.1322	1.0014						
0.164	0.017	91.520	1.577	1.1071	1.0046						
0.172	0.018	90.760	1.654	1.1045	1.0051						
0.274	0.031	81.535	2.537	1.0765	1.0126						
0.508	0.074	59.414	4.403	1.0316	1.0403						
0.509	0.076	58.321	4.411	1.0314	1.0405						
0.637	0.116	46.307	5.371	1.0162	1.0614						
0.697	0.145	40.045	5.809	1.0110	1.0723						
0.949	0.556	13.664	7.605	1.0003	1.1258						
1.0	1.0	7.963	7.967	1.0000	1.1381						

[a] calculated [b] experiment

Appendix D: Properties of pure PnP

D.1. Experimental Densities

Table D.1.: Experimental densities d_{PnP} at different temperatures

T	d_{PnP}	T	d_{PnP}	T	d_{PnP}
K	$\mathrm{g\,cm^3}$	K	$\mathrm{g\,cm^3}$	K	$\mathrm{g\,cm^3}$
250.89	0.92476	318.24	0.86246	374.49	0.80662
253.55	0.92211	323.33	0.85764	379.36	0.80162
261.15	0.91429	328.40	0.85296	384.34	0.79651
266.00	0.91094	333.28	0.84820	384.52	0.79649
266.18	0.91035	337.96	0.84339	389.01	0.79180
278.56	0.89881	342.78	0.83826	393.73	0.78677
284.51	0.89336	348.48	0.83230	393.96	0.78627
290.97	0.88743	353.31	0.82732	398.51	0.78109
298.22	0.88113	358.30	0.82239	402.87	0.77582
303.05	0.87646	363.22	0.81758	407.88	0.76937
308.17	0.87185	368.28	0.81261		
313.15	0.86713	374.26	0.80672		

D.2. Experimental Dynamic Viscosities and Permittivities

Table D.2.: Experimental dynamic viscosities η_{PnP} at different temperatures

T	η_{PnP}	T	η_{PnP}
K	$10^{-3}\,\mathrm{Pa\,s}$	K	$10^{-3}\,\mathrm{Pa\,s}$
313.15	1.59	283.15	3.89
308.15	1.80	272.87	5.78
303.15	2.06	278.15	4.70
298.15	2.38	273.15	5.76
293.15	2.77	268.15	7.18
293.06	2.79	263.15	9.23
288.15	3.26	258.15	12.00
285.30	3.65	253.15	16.02

Table D.3.: Experimental relative permittivity ϵ_{PnP} at different temperatures

T	ϵ_{PnP}
K	
248.15	11.879
258.15	11.056
268.15	10.333
278.15	9.6913
288.15	9.1279
298.15	8.6235
308.15	8.1734
313.15	7.9580

Appendix E: Conductivity Measurements

E.1. Conductivity of Dilute Salt Solutions

$\tilde{m}$ x 10^3	Molar conductances, Λ/S·cm^2·mol^{-1}							
mol kg^{-1}	248.15 K	258.15 K	268.15 K	278.15 K	288.15 K	298.15 K	308.15 K	313.15 K
Bu_4NBr: $M_E = 322.37$; $d_E = 1.13$ [25]; $(a_+ + a_-) = 0.690$ [173]; $D = 54$								
0.4801	0.36133	0.58000	0.84203	1.15338	1.49642	1.84592	2.19167	2.36463
1.0852	0.26201	0.42045	0.61235	0.83416	1.07294	1.32430	1.57361	1.69790
1.7047	0.22098	0.35149	0.51565	0.70055	0.90283	1.11454	1.32450	1.42885
2.4060	0.19520	0.31119	0.45387	0.61891	0.79860	0.98604	1.17190	1.26459
3.1406	0.17722	0.28379	0.41405	0.56535	0.73020	0.90247	1.07317	1.15828
3.9287	0.16423	0.26340	0.38562	0.52733	0.68122	0.84280	1.00292	1.08297
5.0176	0.15312	0.24423	0.35905	0.49113	0.63628	0.78804	0.93901	1.01450
6.3808	0.14269	0.22868	0.33689	0.46249	0.59977	0.74411	0.88790	0.96013
Bu_4NNO_3: $M_E = 304.48$; $d_E = 0.909$ [26]; $(a_+ + a_-) = 0.714$ [173]; $D = 33$								
0.23994	0.60529	0.97600	1.43208	1.96383	2.52104	3.15034	3.74729	4.04153
0.70411	0.40078	0.63907	0.92656	1.26613	1.62612	2.00586	2.38386	2.57309
1.20543	0.32482	0.51574	0.75437	1.02312	1.31657	1.62325	1.92769	2.07998
1.85213	0.27743	0.44044	0.64061	0.87105	1.12187	1.38387	1.64280	1.77259
2.36208	0.25301	0.40389	0.58661	0.79936	1.02884	1.26941	1.50793	1.62736
3.20366	0.22791	0.36237	0.52921	0.72168	0.92983	1.14819	1.36504	1.47400
4.04881	0.21179	0.33602	0.49138	0.67063	0.86518	1.06950	1.27286	1.37493
4.99376	0.19728	0.31508	0.46150	0.63126	0.81557	1.00962	1.20320	1.30048
Bu_4NOAc: $M_E = 301.51$; $d_E = 1.0$; $(a_+ + a_-) = 0.764$ [173]; $D = 21$								
0.19859	0.69124	1.05870	1.55098	2.10876	2.71213	3.33023	3.89982	4.17488
0.53593	0.46558	0.74252	1.07435	1.45459	1.83944	2.22465	2.59040	2.77667
0.93149	0.38075	0.60353	0.87278	1.16763	1.47486	1.78206	2.06908	2.20535
1.53617	0.31855	0.50162	0.71864	0.96059	1.21168	1.46077	1.69235	1.80195
2.33541	0.27091	0.42788	0.61299	0.81975	1.03296	1.24348	1.43890	1.53106
3.11966	0.24632	0.38490	0.55225	0.73781	0.92889	1.11757	1.29215	1.37436
4.13647	0.22249	0.34891	0.50080	0.66873	0.84165	1.01212	1.17000	1.24422
5.09779	0.20701	0.32528	0.46676	0.62356	0.78549	0.94417	1.09127	1.16032
7.24842	0.18458	0.29094	0.41837	0.55919	0.70461	0.84778	0.98039	1.04259
Bu_4NSCN: $M_E = 300.55$; $d_E = 1.0$; $(a_+ + a_-) = 0.831$ [173]; $D = 21$								
0.37846	0.46851	0.77760	1.14738	1.58448	2.07488	2.58808	3.10643	3.37052
0.93323	0.30882	0.54729	0.80683	1.10456	1.43339	1.78632	2.14233	2.32326
1.65599	0.22983	0.43873	0.64332	0.88464	1.15156	1.43447	1.72044	1.86503
2.68444	0.17642	0.36688	0.54083	0.74538	0.97078	1.21057	1.45245	1.57559
3.40810	0.16448	0.33764	0.49915	0.68940	0.89881	1.12206	1.34762	1.46210
4.60528	0.14097	0.30738	0.45563	0.63031	0.82308	1.02890	1.23749	1.34372
5.62628	0.17940	0.29022	0.43112	0.59724	0.78091	0.97767	1.17739	1.27920
7.12563	0.16774	0.27251	0.40606	0.56421	0.73952	0.92783	1.11939	1.21744

Units: molar mass, M_E, g mol^{-1}; density, d_E, g cm^{-3}; distance parameter, a, nm; density gradient, D, kg^2 m^{-3} mol^{-1}

E.2. Specific Conductivity at High Concentrations

Bu_4NBr	$\kappa\,[\mathrm{S\,m^{-1}}]$ at $T\,[\mathrm{K}]$							
$m\,[\mathrm{mol\,kg^{-1}}]$	248.15	258.15	268.15	278.15	288.15	298.15	308.15	313.15
0.10039	9.87×10^{-4}	0.0015	0.0027	0.00397	0.00554	0.00724	0.00902	0.00991
0.10633	0.00104	0.00161	0.00283	0.00418	0.00584	0.00765	0.00957	0.01051
0.20619	0.00189	0.00305	0.00493	0.00745	0.01061	0.01434	0.01856	0.02086
0.20761	0.00192	0.00307	0.00496	0.00751	0.01069	0.01444	0.01872	0.02101
0.24694	0.00218	0.00358	0.00574	0.00872	0.01252	0.01701	0.02223	0.02507
0.38144	0.00284	0.00498	0.00816	0.01265	0.01837	0.02550	0.03381	0.03865
0.52149	0.00326	0.00597	0.01014	0.01598	0.02363	0.03313	0.04458	0.05111
0.53426	0.00329	0.00605	0.01030	0.01625	0.02406	0.03381	0.04551	0.05217
0.85125	0.00355	0.00697	0.01277	0.02086	0.03175	0.04571	0.06275	0.07263
1.11940	0.00347	0.00695	0.01302	0.02184	0.03401	0.04997	0.06969	0.08124
1.69949	0.00304	0.00595	0.01052	0.01864	0.03044	0.04672	0.06777	0.08048
2.65412		0.00409	0.00546	0.01046	0.01839	0.03022	0.04725	0.05807

Bu_4NNO_3	$\kappa\,[\mathrm{S\,m^{-1}}]$ at $T\,[\mathrm{K}]$							
$m\,[\mathrm{mol\,kg^{-1}}]$	248.15	258.15	268.15	278.15	288.15	298.15	308.15	313.15
0.06435	7.19×10^{-4}	0.00122	0.00186	0.00267	0.00362	0.00474	0.00576	0.00649
0.09418	0.00104	0.00179	0.00282	0.00408	0.00560	0.00746	0.00923	0.01037
0.16308	0.00173	0.00306	0.00491	0.00731	0.01023	0.01371	0.01756	0.01979
0.23086	0.00233	0.00418	0.00681	0.01031	0.01464	0.01972	0.02579	0.02898
0.35780	0.00324	0.00595	0.00993	0.01524	0.02200	0.03100	0.03979	0.04507
0.47361	0.00389	0.00722	0.01217	0.01895	0.02743	0.03801	0.05060	0.05781
0.57792	0.00431	0.00809	0.01375	0.02169	0.03185	0.04415	0.05922	0.06780
0.68256	0.00463	0.00881	0.01513	0.02396	0.03545	0.04940	0.06681	0.07654
0.80528	0.00488	0.00939	0.01628	0.02601	0.03877	0.05466	0.07434	0.08502
1.03095	0.00509	0.00999	0.01766	0.02866	0.04331	0.06196	0.08556	0.09774
1.30336	0.00505	0.01015	0.01831	0.03026	0.04644	0.06765	0.09462	0.10847
1.61811	0.00482	0.01001	0.01832	0.03076	0.04809	0.07124	0.10089	0.11672
2.43951	0.00383	0.00920	0.01748	0.03048	0.04880	0.07380	0.10622	0.12527

Bu_4NSCN	$\kappa\,[\mathrm{S\,m^{-1}}]$ at $T\,[\mathrm{K}]$							
$m\,[\mathrm{mol\,kg^{-1}}]$	248.15	258.15	268.15	278.15	288.15	298.15	308.15	313.15
0.05921	6.52×10^{-4}	0.00115	0.00182	0.00269	0.00374	0.00498	0.00637	0.0071
0.07464	8.11×10^{-4}	0.00143	0.00229	0.0034	0.00478	0.00635	0.00816	0.00913
0.22573	0.00218	0.00399	0.00661	0.01016	0.01461	0.01995	0.02625	0.02965
0.28857	0.00267	0.00493	0.00825	0.01277	0.01849	0.02547	0.03367	0.03815
0.59642	0.00439	0.00847	0.01473	0.02353	0.03502	0.04947	0.06676	0.07641
0.85360	0.00514	0.01022	0.01821	0.02971	0.04505	0.06468	0.08851	0.10105
1.18881	0.00547	0.01125	0.02062	0.03448	0.05341	0.07808	0.10857	0.12598
1.61022	0.00531	0.01128	0.02133	0.03666	0.05816	0.08671	0.12271	0.14355
2.54537	0.00420	0.00942	0.01883	0.03401	0.05632	0.08711	0.12738	0.15131
Bu_4NOAc	$\kappa\,[\mathrm{S\,m^{-1}}]$ at $T\,[\mathrm{K}]$							
$m\,[\mathrm{mol\,kg^{-1}}]$	248.15	258.15	268.15	278.15	288.15	298.15	308.15	313.15
0.09573	0.00110	0.00185	0.00285	0.00405	0.00541		0.00829	0.00901
0.13509	0.00157	0.00271	0.00425	0.00618	0.00842	0.01082	0.01352	0.01485
0.16327	0.00190	0.00331	0.00526	0.00773	0.01064	0.01386	0.01748	0.01934
0.19719	0.00227	0.00401	0.00644	0.00956	0.01332	0.01758	0.02234	0.02493
0.25295	0.00284	0.00511	0.00834	0.01257	0.01775	0.02385	0.03061	0.03428
0.33498	0.00356	0.00652	0.01082	0.01658	0.02379	0.03253	0.04237	0.04779
0.38257	0.00390	0.00723	0.01211	0.01864	0.02705	0.03720	0.04875	0.05480
0.55887	0.00476	0.00908	0.01564	0.02482	0.03669	0.05153	0.06887	0.07879
0.70216	0.00504	0.00979	0.01722	0.02776	0.04173	0.05942	0.08050	0.09266
0.86668	0.00500	0.00994	0.01782	0.02925	0.04479	0.06473	0.08902	0.10314
1.04514	0.00469	0.00956	0.01751	0.02928	0.04564	0.06699	0.09343	0.10895
1.27744	0.00408	0.00857	0.01611	0.02768	0.04408	0.06606	0.09376	0.11027
1.44477	0.00360	0.00773	0.01481	0.02593	0.0419	0.06371	0.09151	0.10828

Appendix F: Results on Vapor Pressure Measurements

F.1. Vapor Pressure of Pure PnP

Table F.1.: Experimental vapor pressure data of 1-propoxy-2-propanol, $\Delta p = (p(obs) - p(calc))/p(calc) \cdot 100\,\%$ where $p(calc)$ has been obtained from Eq. (6.28), Eq. (6.29) or Eq. (6.30) respectively.

T/K	p/kPa	Δp/% Eq. (6.28)	Δp/% Eq. (6.29)	Δp/% Eq. (6.30)
298.15	0.341	+2.03	+0.13	−0.14
303.15	0.481	+1.13	−0.33	−0.42
308.15	0.672	+0.63	−0.47	−0.43
313.15	0.937	+1.44	+0.65	+0.76
318.15	1.271	+0.85	+0.28	+0.43
323.15	1.707	+0.68	+0.28	+0.45
328.15	2.256	+0.12	−0.14	+0.01
333.15	2.967	+0.19	+0.04	+0.16
338.15	3.839	−0.26	−0.34	−0.25
343.15	4.951	−0.02	−0.04	+0.001
348.15	6.290	−0.32	−0.30	−0.30
353.15	7.963	−0.07	−0.02	−0.06
358.15	9.950	−0.26	−0.18	−0.27
363.15	12.385	−0.01	+0.07	−0.05
368.15	15.265	+0.01	+0.10	−0.04
373.15	18.697	+0.14	+0.22	+0.07
378.15	22.649	−0.14	−0.07	−0.22
383.15	27.424	+0.19	+0.24	+0.11
388.15	32.801	−0.09	−0.05	−0.15
393.15	39.182	+0.10	+0.13	+0.07
398.15	46.384	−0.04	−0.04	−0.04
403.15	54.753	+0.06	+0.04	+0.12
408.15	64.103	−0.14	−0.18	−0.02
413.15	74.983	+0.06	−0.01	−0.002

F.2. Solution's Vapor Pressure of Bu_4NBr

Table F.2.: Measured vapor pressure lowering, Δp, and osmotic coefficients, ϕ

m	Δp (Pa)	ϕ^{exp}	m	Δp (Pa)	ϕ^{exp}
	323.15 K			373.15 K	
0	0	1.000	0	0	1.000
0.0317	2.0	0.155	0.0317	21.1	0.148
0.0793	4.3	0.135	0.0793	35.7	0.100
0.0809	4.4	0.134	0.0809	36.8	0.101
0.1543	8.5	0.136	0.1543	76.9	0.111
0.1820	10.6	0.144	0.1820	97.1	0.119
0.2290	14.9	0.162	0.2290	122.6	0.120
0.2992	23.6	0.196	0.2992	186.5	0.140
0.3509	31.6	0.225	0.3509	252.6	0.162
0.3660	34.9	0.238	0.3660	269.0	0.165
0.4974	62.3	0.316	0.4974	494.2	0.224
0.5321	70.9	0.337	0.5321	584.2	0.249
	333.15 K			383.15 K	
0	0	1.000	0	0	1.000
0.0317	3.4	0.154	0.0317	30.2	0.144
0.0793	7.3	0.131	0.0793	45.5	0.087
0.0809	7.3	0.128	0.0809	44.8	0.084
0.1543	13.4	0.124	0.1543	94.1	0.092
0.1820	16.4	0.128	0.1820	116.6	0.097
0.2290	22.5	0.140	0.2290	165.9	0.110
0.2992	35.4	0.169	0.2992	226.5	0.115
0.3509	47.8	0.195	0.3509	292.3	0.127
0.3660	52.5	0.206	0.3660	308.3	0.128
0.4974	99.5	0.289	0.4974	558.9	0.172
0.5321	116.3	0.317	0.5321	680.1	0.196
	343.15 K			393.15 K	
0	0	1.000	0	0	1.000
0.0317	5.8	0.155	0.0317	47.6	0.158
0.0793	11.6	0.124	0.0793	77.0	0.102
0.0809	11.9	0.125	0.0809	78.6	0.102
0.1543	21.9	0.121	0.1543	160.7	0.110
0.1820	26.2	0.123	0.1820	194.5	0.113
0.2290	35.2	0.131	0.2290	261.8	0.121
0.2992	56.3	0.161	0.2992	382.9	0.135
0.3509	72.3	0.176	0.3509	498.3	0.150
0.3660	79.1	0.185	0.3660	536.2	0.155
0.4974	153.1	0.266	0.4974	945.7	0.202
0.5321	180.8	0.294	0.5321	1090.9	0.219
	353.15 K			403.15 K	
0	0	1.000	0	0	1.000
0.0317	8.2	0.137	0.0317	44.5	0.105
0.0793	18.4	0.123	0.0793	79.6	0.075

Table F.2.: (continued)

m	Δp (Pa)	ϕ^{exp}	m	Δp (Pa)	ϕ^{exp}
0.0809	19.0	0.124	0.0809	78.8	0.073
0.1543	33.3	0.114	0.1543	168.3	0.082
0.1820	39.4	0.115	0.1820	232.2	0.095
0.2290	54.2	0.125	0.2290	277.8	0.091
0.2992	83.9	0.149	0.2992	383.8	0.096
0.3509	109.3	0.165	0.3509	510.7	0.109
0.3660	117.6	0.171	0.3660	547.0	0.112
0.4974	218.5	0.235	0.4974	1036.8	0.157
0.5321	261.1	0.263	0.5321	1230.5	0.175
	363.15 K			413.15 K	
0	0	1.000	0	0	1.000
0.0317	11.4	0.121	0.0317	30.7	0.052
0.0793	20.3	0.087	0.0793	63.4	0.043
0.0809	21.5	0.090	0.0809	68.9	0.046
0.1543	46.2	0.101	0.1543	158.5	0.056
0.1820	58.4	0.109	0.1820	209.4	0.062
0.2290	81.7	0.121	0.2290	269.8	0.064
0.2992	131.2	0.149	0.2992	380.5	0.069
0.3509	166.7	0.162	0.3509	496.0	0.077
0.3660	172.5	0.160	0.3660	578.6	0.086
0.4974	312.0	0.215	0.4974	1129.7	0.124
0.5321	361.1	0.233	0.5321	1346.7	0.138

F.3. Solution's Vapor Pressure of Bu_4NNO_3

Table F.3.: Measured vapor pressure lowering, Δp, and osmotic coefficients, ϕ

m	Δp (Pa)	ϕ^{exp}	m	Δp (Pa)	ϕ^{exp}
	323.15 K			373.15 K	
0	0	1.000	0	0	1.000
0.1230	15.2	0.307	0.1230	131.1	0.238
0.1749	21.1	0.300	0.1749	183.2	0.234
0.2374	28.2	0.296	0.2374	249.4	0.235
0.3992	48.0	0.302	0.3992	428.8	0.242
0.5246	64.9	0.312	0.5246	575.0	0.248
0.6704	85.8	0.325	0.6704	756.3	0.256
0.8990	120.7	0.344	0.8990	1059.9	0.270
1.3270	198.7	0.394	1.3270	1698.5	0.299
	333.15 K			383.15 K	
0	0	1.000	0	0	1.000
0.1230	25.051	0.290	0.1230	175.8	0.216
0.1749	35.479	0.290	0.1749	243.6	0.211
0.2374	47.570	0.287	0.2374	336.2	0.215
0.3992	81.704	0.295	0.3992	591.1	0.226

Table F.3.: (continued)

m	Δp (Pa)	$\phi^{\exp}$	m	Δp (Pa)	$\phi^{\exp}$
0.5246	109.608	0.302	0.5246	795.1	0.232
0.6704	144.886	0.315	0.6704	1056.4	0.243
0.8990	204.388	0.335	0.8990	1487.2	0.257
1.3270	337.938	0.384	1.3270	2391.5	0.285
	343.15 K			393.15 K	
0	0	1.000	0	0	1.000
0.1230	40.0	0.277	0.1230	245.0	0.210
0.1749	56.4	0.276	0.1749	341.3	0.206
0.2374	76.8	0.277	0.2374	470.4	0.209
0.3992	131.7	0.284	0.3992	824.9	0.219
0.5246	177.0	0.292	0.5246	1105.3	0.224
0.6704	231.1	0.300	0.6704	1472.8	0.235
0.8990	325.2	0.318	0.8990	2066.9	0.248
1.3270	527.1	0.357	1.3270	3316.0	0.274
	353.15 K			403.15 K	
0	0	1.000	0	0	1.000
0.1230	60.8	0.261	0.1230	312.0	0.190
0.1749	85.8	0.260	0.1749	433.8	0.186
0.2374	117.4	0.262	0.2374	601.5	0.190
0.3992	202.3	0.270	0.3992	1060.3	0.200
0.5246	271.7	0.278	0.5246	1433.0	0.206
0.6704	354.5	0.285	0.6704	1894.9	0.215
0.8990	491.1	0.297	0.8990	2670.0	0.227
1.3270	789.8	0.330	1.3270	4288.1	0.251
	363.15 K			413.15 K	
0	0	1.000	0	0	1.000
0.1230	90.8	0.250	0.1230	409.7	0.180
0.1749	125.9	0.244	0.1749	573.1	0.177
0.2374	171.1	0.245	0.2374	791.9	0.181
0.3992	294.4	0.252	0.3992	1404.7	0.192
0.5246	397.4	0.260	0.5246	1883.0	0.196
0.6704	522.8	0.269	0.6704	2482.8	0.203
0.8990	731.6	0.283	0.8990	3500.1	0.215
1.3270	1174.2	0.314	1.3270	5575.1	0.236

F.4. Solution's Vapor Pressure of Bu_4NOAc

Table F.4.: Measured vapor pressure lowering, Δp, and osmotic coefficients, ϕ

m	Δp (Pa)	$\phi^{\exp}$	m	Δp (Pa)	$\phi^{\exp}$
	323.15 K			373.15 K	
0	0	1.000	0	0	1.000
0.1045	17.7	0.421	0.0317	177.8	0.381
0.1463	24.0	0.408	0.0793	246.7	0.378

Table F.4.: (continued)

m	Δp (Pa)	$\phi^{\exp}$	m	Δp (Pa)	$\phi^{\exp}$
0.2445	38.6	0.395	0.0809	400.4	0.369
0.2628	41.8	0.398	0.1543	430.7	0.370
0.3527	56.5	0.402	0.1820	581.8	0.373
0.4958	81.6	0.417	0.2290	834.7	0.384
0.6202	108.1	0.445	0.2992	1092.3	0.405
0.8462	173.8	0.536	0.3509	1648.8	0.455
1.0360	233.8	0.600	0.3660	2170.2	0.497
	333.15 K			383.15 K	
0	0	1.000	0	0	1.000
0.1045	30.5	0.417	0.0317	259.9	0.378
0.1463	41.2	0.403	0.0793	358.8	0.373
0.2445	65.9	0.387	0.0809	579.9	0.362
0.2628	71.3	0.390	0.1543	623.4	0.363
0.3527	96.4	0.395	0.1820	839.3	0.365
0.4958	139.1	0.408	0.2290	1194.4	0.372
0.6202	184.3	0.436	0.2992	1545.0	0.388
0.8462	294.8	0.521	0.3509	2302.3	0.430
1.0360	396.5	0.584	0.3660	3032.5	0.469
	343.15 K			393.15 K	
0	0	1.000	0	0	1.000
0.1045	49.6	0.405	0.0317	368.7	0.373
0.1463	67.4	0.394	0.0793	513.5	0.372
0.2445	108.9	0.383	0.0809	804.3	0.349
0.2628	117.3	0.384	0.1543	866.1	0.350
0.3527	158.3	0.388	0.1820	1151.0	0.348
0.4958	227.5	0.399	0.2290	1636.1	0.355
0.6202	301.3	0.426	0.2992	2128.3	0.371
0.8462	480.4	0.508	0.3509	3132.8	0.406
1.0360	643.9	0.566	0.3660	4103.8	0.441
	353.15 K			403.15 K	
0	0	1.000	0	0	1.000
0.1045	78.5	0.398	0.0317	507.9	0.365
0.1463	107.1	0.389	0.0793	687.6	0.353
0.2445	172.9	0.377	0.0809	1068.5	0.330
0.2628	185.9	0.377	0.1543	1157.8	0.333
0.3527	252.3	0.383	0.1820	1527.9	0.328
0.4958	362.4	0.394	0.2290	2170.4	0.334
0.6202	480.1	0.421	0.2992	2797.3	0.346
0.8462	755.6	0.495	0.3509	4066.8	0.373
1.0360	1007.4	0.548	0.3660	5244.5	0.398
	363.15 K			413.15 K	
0	0	1.000	0	0	1.000
0.1045	119.2	0.387	0.0317	681.8	0.355
0.1463	164.6	0.383	0.0793	894.6	0.333
0.2445	267.4	0.373	0.0809	1380.0	0.308

Table F.4.: (continued)

m	Δp (Pa)	$\phi^{\exp}$	m	Δp (Pa)	$\phi^{\exp}$
0.2628	287.3	0.374	0.1543	1505.8	0.313
0.3527	390.8	0.380	0.1820	1972.9	0.307
0.4958	561.2	0.391	0.2290	2801.3	0.312
0.6202	737.3	0.414	0.2992	3576.2	0.320
0.8462	1137.3	0.476	0.3509	5118.6	0.339
1.0360	1498.5	0.521	0.3660	6598.0	0.361

F.5. Solution's Vapor Pressure of Bu_4NSCN

Table F.5.: Measured vapor pressure lowering, Δp, and osmotic coefficients, ϕ

m	Δp (Pa)	$\phi^{\exp}$	m	Δp (Pa)	$\phi^{\exp}$
	323.15 K			373.15 K	
0	0	1.000	0	0	1.000
0.0880	7.0	0.197	0.0880	50.6	0.128
0.1088	8.5	0.194	0.1088	61.3	0.126
0.1790	13.8	0.192	0.1790	99.9	0.125
0.2430	17.9	0.183	0.2430	135.9	0.125
0.2844	20.9	0.183	0.2844	160.5	0.126
0.3082	23.3	0.188	0.3082	176.7	0.128
0.3188	23.2	0.181	0.3188	183.3	0.129
0.3446	25.7	0.185	0.3446	199.2	0.130
0.3957	29.0	0.183	0.3957	230.0	0.130
0.4789	35.8	0.187	0.4789	287.0	0.135
0.5208	40.0	0.192	0.5208	316.6	0.137
0.6280	48.1	0.192	0.6280	394.3	0.141
0.7294	57.6	0.199	0.7294	474.8	0.147
0.8141	65.6	0.203	0.8141	537.6	0.149
1.1821	101.8	0.219	1.1821	841.0	0.162
	333.15 K			383.15 K	
0	0	1.000	0	0	1.000
0.0880	10.8	0.175	0.0880	66.3	0.114
0.1088	13.3	0.173	0.1088	82.2	0.114
0.1790	21.1	0.168	0.1790	131.6	0.111
0.2430	28.1	0.165	0.2430	179.2	0.111
0.2844	32.7	0.164	0.2844	210.1	0.112
0.3082	35.3	0.164	0.3082	224.9	0.111
0.3188	36.5	0.164	0.3188	238.1	0.112
0.3446	39.8	0.165	0.3446	263.0	0.114
0.3957	46.5	0.168	0.3957	306.4	0.115
0.4789	58.0	0.174	0.4789	378.5	0.119
0.5208	63.9	0.176	0.5208	413.3	0.120
0.6280	80.1	0.184	0.6280	519.6	0.126
0.7294	95.5	0.189	0.7294	626.8	0.130
0.8141	109.2	0.194	0.8141	714.9	0.134

Table F.5.: (continued)

m	Δp (Pa)	$\phi^{\exp}$	m	Δp (Pa)	$\phi^{\exp}$
1.1821	172.2	0.213	1.1821	1136.2	0.148
	343.15 K			393.15 K	
0	0	1.000	0	0	1.000
0.0880	16.4	0.159	0.0880	87.1	0.104
0.1088	20.3	0.159	0.1088	107.0	0.104
0.1790	32.5	0.155	0.1790	167.5	0.099
0.2430	43.4	0.153	0.2430	227.9	0.099
0.2844	51.0	0.153	0.2844	267.6	0.099
0.3082	54.4	0.151	0.3082	292.3	0.100
0.3188	57.1	0.153	0.3188	305.0	0.101
0.3446	62.4	0.155	0.3446	331.5	0.102
0.3957	72.4	0.157	0.3957	384.5	0.103
0.4789	89.7	0.161	0.4789	479.7	0.106
0.5208	98.9	0.163	0.5208	526.0	0.107
0.6280	122.6	0.168	0.6280	671.8	0.113
0.7294	147.4	0.174	0.7294	807.4	0.118
0.8141	169.4	0.180	0.8141	924.0	0.121
1.1821	269.7	0.199	1.1821	1477.7	0.134
	353.15 K			403.15 K	
0	0	1.000	0	0	1.000
0.0880	24.5	0.147	0.0880	103.2	0.088
0.1088	30.1	0.146	0.1088	126.1	0.087
0.1790	48.1	0.142	0.1790	198.2	0.083
0.2430	64.7	0.141	0.2430	268.7	0.083
0.2844	76.4	0.142	0.2844	316.5	0.083
0.3082	82.8	0.142	0.3082	341.1	0.083
0.3188	86.8	0.144	0.3188	361.1	0.085
0.3446	93.9	0.144	0.3446	393.3	0.086
0.3957	109.6	0.147	0.3957	457.0	0.087
0.4789	135.5	0.150	0.4789	570.2	0.089
0.5208	150.6	0.154	0.5208	640.5	0.092
0.6280	186.1	0.158	0.6280	824.3	0.099
0.7294	224.2	0.164	0.7294	1014.0	0.105
0.8141	258.6	0.170	0.8141	1182.5	0.110
1.1821	407.6	0.187	1.1821	1892.2	0.122
	363.15 K			413.15 K	
0	0	1.000	0	0	1.000
0.0880	35.9	0.138	0.0880	114.4	0.070
0.1088	44.1	0.137	0.1088	142.8	0.071
0.1790	70.9	0.134	0.1790	231.2	0.070
0.2430	96.0	0.134	0.2430	316.5	0.071
0.2844	113.6	0.136	0.2844	376.4	0.072
0.3082	124.3	0.137	0.3082	424.3	0.075
0.3188	128.5	0.137	0.3188	425.0	0.072
0.3446	140.1	0.138	0.3446	470.1	0.074
0.3957	162.2	0.139	0.3957	564.4	0.077

Table F.5.: (continued)

m	Δp (Pa)	$\phi^{\exp}$	m	Δp (Pa)	$\phi^{\exp}$
0.4789	202.1	0.144	0.4789	694.0	0.079
0.5208	222.7	0.146	0.5208	786.7	0.082
0.6280	278.4	0.151	0.6280	1015.2	0.088
0.7294	334.3	0.157	0.7294	1240.3	0.093
0.8141	381.2	0.161	0.8141	1457.5	0.098
1.1821	596.8	0.175	1.1821	2370.1	0.110

Appendix G: Extended Correlation Results for Osmotic Coefficients

G.1. Extended Pitzer Model of Archer

Table G.1.: Parameters for PnP solutions of Bu_4NBr

T	$\beta^{(0)}$	$\beta^{(1)}$	$\beta^{(2)}$	$C^{(1)}$	$C^{(2)}$	$\sigma(\phi)$
K	$kg\,mol^{-1}$	$kg\,mol^{-1}$	$kg\,mol^{-1}$	$kg^2\,mol^{-2}$	$kg^2\,mol^{-2}$	
323.15	−3.688 86	−57.799 14	2.624 28	−5.495 48	23.940 48	0.001
333.15	−2.321 40	−52.022 43	−0.702 64	−2.226 39	12.754 82	0.001
343.15	−0.843 84	−48.791 38	−3.910 41	0.824 84	1.540 61	0.002
353.15	2.368 21	−33.503 69	−12.611 57	4.964 08	−17.132 03	0.002
363.15	1.630 01	−47.717 88	−9.717 50	3.884 79	−13.005 24	0.003
373.15	−5.500 83	−73.804 55	9.537 49	−5.702 15	29.057 37	0.003
383.15	3.423 96	−41.971 24	−13.596 80	8.018 60	−27.567 21	0.002
393.15	−3.586 72	−63.420 93	4.503 88	−3.474 12	18.381 54	0.001
403.15	−4.535 02	−74.974 77	7.786 27	−3.262 63	20.409 29	0.003
413.15	−5.482 98	−80.788 74	9.836 49	−4.947 60	26.778 08	0.002

[a] $b = 20$, $\alpha_1 = 10$, $\alpha_2 = 3.5$, $\alpha_3 = 1.0$. Units: $kg^{1/2}\,mol^{-1/2}$

Table G.2.: Parameters for PnP solutions of Bu_4NNO_3

T	$\beta^{(0)}$	$\beta^{(1)}$	$\beta^{(2)}$	$C^{(1)}$	$C^{(2)}$	$\sigma(\phi)$
K	$kg\,mol^{-1}$	$kg\,mol^{-1}$	$kg\,mol^{-1}$	$kg^2\,mol^{-2}$	$kg^2\,mol^{-2}$	
323.15	0.128 15	−18.593 26	−4.581 94	0.132 75	−0.697 61	0.001
333.15	−0.165 74	−26.094 84	−3.255 54	0.019 18	0.307 87	0.002
343.15	−0.129 78	−27.370 34	−3.335 78	0.030 60	0.158 91	0.001
353.15	0.065 84	−26.447 57	−4.119 13	0.119 18	−0.586 56	0.001
363.15	0.081 68	−23.984 36	−4.519 23	0.098 65	−0.555 35	0.004
373.15	−0.052 03	−27.641 89	−4.126 42	0.053 47	−0.137 01	0.002
383.15	0.055 64	−27.711 44	−4.611 24	0.081 67	−0.458 08	0.001
393.15	−0.016 01	−28.573 90	−4.302 58	0.050 33	−0.206 91	0.001
403.15	0.033 35	−29.707 26	−4.664 67	0.079 91	−0.430 43	0.001
413.15	−0.018 77	−31.524 89	−4.428 56	0.065 35	−0.283 24	0.001

[a] $b = 20$, $\alpha_1 = 10$, $\alpha_2 = 3.5$, $\alpha_3 = 1.0$. Units: $kg^{1/2}\,mol^{-1/2}$

Table G.3.: Parameters PnP solutions of Bu_4NOAc

T	$\beta^{(0)}$	$\beta^{(1)}$	$\beta^{(2)}$	$C^{(1)}$	$C^{(2)}$	$\sigma(\phi)$
K	$kg\,mol^{-1}$	$kg\,mol^{-1}$	$kg\,mol^{-1}$	$kg^2\,mol^{-2}$	$kg^2\,mol^{-2}$	
323.15	−1.509 74	−20.324 50	2.492 44	−0.739 24	6.180 78	0.004
333.15	−1.357 19	−17.758 62	1.986 52	−0.665 22	5.591 10	0.004
343.15	−1.575 06	−21.761 17	2.928 96	−0.789 80	6.426 23	0.004
353.15	−1.363 84	−20.032 24	2.268 92	−0.704 47	5.653 30	0.003
363.15	−1.210 64	−21.006 56	1.976 77	−0.645 58	5.055 47	0.003
373.15	−0.957 82	−19.548 15	1.286 80	−0.477 25	3.923 67	0.002
383.15	−0.595 77	−16.069 48	0.166 15	−0.208 43	2.247 79	0.002
393.15	−0.906 44	−15.964 28	0.994 14	−0.452 60	3.634 45	0.003
403.15	−0.423 31	−9.250 35	−1.042 14	−0.222 45	1.771 79	0.002
413.15	0.335 63	−0.829 07	−3.977 70	0.242 17	−1.394 90	0.002

[a] $b = 20$, $\alpha_1 = 10$, $\alpha_2 = 3.5$, $\alpha_3 = 1.0$. Units: $kg^{1/2}\,mol^{-1/2}$

Table G.4.: Parameters for PnP solutions of Bu_4NSCN

T	$\beta^{(0)}$	$\beta^{(1)}$	$\beta^{(2)}$	$C^{(1)}$	$C^{(2)}$	$\sigma(\phi)$
K	$kg\,mol^{-1}$	$kg\,mol^{-1}$	$kg\,mol^{-1}$	$kg^2\,mol^{-2}$	$kg^2\,mol^{-2}$	
323.15	−0.733 73	−41.055 64	−3.294 10	−0.267 06	2.248 18	0.003
333.15	−0.597 37	−40.648 48	−4.051 82	−0.232 78	1.856 29	0.002
343.15	−0.633 16	−42.932 75	−3.848 07	−0.218 70	1.884 72	0.002
353.15	−0.549 58	−42.967 41	−4.167 17	−0.180 45	1.573 84	0.002
363.15	−0.570 61	−43.960 11	−4.022 96	−0.197 72	1.662 97	0.001
373.15	−0.498 67	−44.125 21	−4.248 56	−0.152 13	1.349 92	0.001
383.15	−0.605 50	−45.335 03	−4.019 14	−0.201 62	1.739 24	0.002
393.15	−0.606 50	−45.328 87	−4.113 01	−0.203 96	1.740 81	0.002
403.15	−0.796 42	−47.758 70	−3.655 23	−0.325 26	2.542 50	0.001
413.15	−0.779 49	−50.125 31	−3.688 02	−0.299 40	2.415 75	0.002

[a] $b = 20$, $\alpha_1 = 10$, $\alpha_2 = 3.5$, $\alpha_3 = 1.0$. Units: $kg^{1/2}\,mol^{-1/2}$

G.2. Clegg-Pitzer Model

Table G.5.: Model of Clegg et al. parameters for PnP solutions of Bu_4NBr

T / K	B_{ca}	B'_{ca}	$W_{1,ca}$	$U_{1,ca}$	$V_{1,ca}$	$\sigma(\phi)$
323.15	−549.301 21	1342.71837	25.76463	1724.27750	−481.801 38	0.005
333.15	−533.138 42	1286.14955	41.14627	1539.67178	−444.511 19	0.012
343.15	−439.813 27	985.38718	61.84497	975.60669	−307.830 77	0.005
353.15	−556.079 19	1341.43597	49.96133	1564.03371	−455.854 16	0.007
363.15	−414.949 69	819.66674	71.77460	684.35821	−232.345 75	0.005
373.15	−278.689 10	414.50812	93.00088	−36.569 56	−56.151 75	0.006
383.15	−276.458 00	393.41437	93.42652	−64.729 39	−47.567 18	0.004
393.15	−327.133 18	606.15811	65.35913	423.30092	−158.815 58	0.002
403.15	−487.726 71	1009.01324	93.13124	812.32724	−281.999 46	0.004
413.15	−715.442 02	1658.03392	86.01681	1784.12066	−536.209 34	0.005

[a] $\alpha_1 = 13$, $\alpha_2 = 2.0$.

Table G.6.: Model of Clegg et al. parameters for PnP solutions of Bu_4NNO_3

T / K	B_{ca}	B'_{ca}	$W_{1,ca}$	$U_{1,ca}$	$V_{1,ca}$	$\sigma(\phi)$
323.15	−10.330 56	−2.559 51	1.18211	−12.742 76	2.38119	0.001
333.15	−28.125 85	16.29922	5.63018	−14.429 77	0.36897	0.010
343.15	−32.867 03	21.44532	6.54135	−12.651 48	−0.434 76	0.001
353.15	−24.565 23	−5.002 62	1.76608	−18.219 36	4.34300	0.001
363.15	−24.710 40	−4.105 64	1.09737	−12.586 16	2.95906	0.001
373.15	−47.048 21	29.32511	7.75905	−8.152 72	−2.271 69	0.001
383.15	−29.761 69	−15.551 99	−0.700 62	−16.277 72	5.31700	0.002
393.15	−65.900 84	48.22096	11.30660	−3.984 81	−5.518 95	0.001
403.15	−37.516 99	−15.429 58	−0.365 87	−17.323 49	5.59348	0.002
413.15	−65.640 95	29.19968	8.34515	−10.418 75	−1.585 68	0.001

[a] $\alpha_1 = 13$, $\alpha_2 = 2.0$.

Table G.7.: Model of Clegg et al. parameters for PnP solutions of Bu_4NOAc

T / K	B_{ca}	B'_{ca}	$W_{1,ca}$	$U_{1,ca}$	$V_{1,ca}$	$\sigma(\phi)$
323.15	23.131 48	6.188 49	2.611 38	−17.363 17	−0.259 81	0.004
333.15	20.700 96	−3.195 86	3.708 34	−36.511 92	4.751 27	0.011
343.15	13.435 54	15.579 62	5.489 63	−21.577 49	−0.386 30	0.004
353.15	27.705 28	3.585 43	−3.266 28	17.496 21	−5.903 37	0.007
363.15	14.012 20	5.733 48	1.169 91	−6.408 50	−1.248 46	0.004
373.15	10.622 49	0.424 27	1.989 14	−17.838 94	1.937 67	0.002
383.15	10.392 12	6.342 47	1.250 88	−4.134 66	−1.296 16	0.003
393.15	16.105 16	−4.380 08	−0.362 81	−7.897 74	0.816 06	0.003
403.15	9.154 92	2.485 06	0.640 27	−3.465 84	−0.730 49	0.001
413.15	10.133 45	0.697 74	−1.362 86	7.712 59	−2.548 88	0.002

[a] $\alpha_1 = 13$, $\alpha_2 = 2.0$.

Table G.8.: Model of Clegg et al. parameters for PnP solutions of Bu_4NSCN

T / K	B_{ca}	B'_{ca}	$W_{1,ca}$	$U_{1,ca}$	$V_{1,ca}$	$\sigma(\phi)$
323.15	−124.492 57	131.242 69	25.969 17	20.026 87	−21.370 20	0.003
333.15	−123.555 48	116.000 58	23.092 90	17.199 83	−18.814 70	0.010
343.15	−126.090 54	114.190 10	23.758 05	10.841 45	−17.249 53	0.002
353.15	−147.482 66	149.781 14	29.763 48	22.168 18	−24.131 86	0.002
363.15	−152.796 28	153.333 97	30.555 09	22.405 61	−24.544 80	0.002
373.15	−143.931 73	126.216 58	26.419 58	11.635 70	−18.748 43	0.002
383.15	−167.857 04	169.745 50	33.811 57	25.173 99	−27.254 19	0.002
393.15	−167.869 99	164.292 12	32.929 70	23.595 20	−26.224 04	0.002
403.15	−179.918 91	180.847 45	35.552 60	30.013 94	−29.719 47	0.002
413.15	−187.094 63	180.131 52	36.313 29	24.665 82	−28.456 36	0.002

[a] $\alpha_1 = 13$, $\alpha_2 = 2.0$.

Bibliography

[1] H. L. Cox, W. L. Nelson and L. H. Cretcher. Reciprocal Solubility of the Normal Propyl Ethers of 1,2-Propylene Glycol and Water. Closed Solubility Curves. II. *J. Am. Chem. Soc.* **49**(4), 1080–1083, **1927**.

[2] J. Etiemble. L'actualité chimique, **2003**. P. 145.

[3] P. J. Spencer. New toxicity data for the propylene glycol ethers – a commitment to public health and safety. *Toxicology Letters* **156**, 181–188, **2005**.

[4] P. Bauduin, L. Wattebled, S. Schroedle, D. Touraud and W. Kunz. Temperature dependence of industrial propylene glycol alkyl ether/water mixtures. *J. Mol. Liq.* **115**, 23–28, **2004**.

[5] P. Bauduin. Characterization of short polypropylene glycol monoalkylethers and design of enzymatic reaction media. Ph.D. thesis, University of Regensburg, **2005**.

[6] http://www.dow.com/glycolether/index.htm.

[7] H. J. Weltman and T. L. Phillips. Nonflammable mild odor solvent cleaner with (m)ethyl lactate and propylene glycol propyl ether. Patent No.: 5 604 196, Appl. No.: 456 778, Filed Jun. 1, 1995, Assignee: Lockheed Corporation, Del.

[8] D. E. Williams and O. L. Flaningam. Azeotropes of octamethyltrisiloxane and n-propoxypropanol. Patent No.: 5 454 972, Appl. No.: 08/306 293, Filed Sep. 15, 1994, Assignee: Dow Corning Corporation, Midland, MI.

[9] Patent No.: DE 197 40 965 A 1.

[10] T. C. Frank, F. A. Donate, J. E. Shields and J. R. Allen. Patent Application No. WO 2005/087791.

[11] T. C. Frank, F. A. Donate and B. J. Alstad. Patent Application No. WO2005/092915.

[12] T. C. Frank, F. A. Donate and T. C. Thyne. Patent Application No. WO 2005/087692.

[13] M. Moosavi and E. K. Goharshadi. Investigation of Volumetric Properties of Some Glycol Ethers Using a Simple Equation of State. *Int. J. Thermophys.* **27**(5), 1515–1526, **2006**.

[14] L. Lugo, E. R. Lopez, M. J. P. Comunas, J. Garcia and J. Fernandez. Measurements and EoS Predictions of Glycol Ethers from (283.15 to 353.15) K at Pressures up to 25 MPa. *J. Chem. Eng. Data* **49**, 1400–1405, **2004**.

[15] S. Queste, Y. Michina, A. Dewilde, R. Neueder, W. Kunz and J.-M. Aubry. Thermophysical and bionotox properties of solvo-surfactants based on ethylene oxide, propylene oxide and glycerol. *Green Chemistry* **9**, 491–499, **2007**.

[16] Y. Okauchi, R. Koike, Y. Yamazaki, S. Tamura and A. Wakisaka. Microscopic Structures in Water-propylene Glycol Monoalkyl Ether Binary Mixtures as Clarified by NMR and Mass Spectrometry. *J. Oleo Sci.* **55**, 647–652, **2006**.

[17] P. Bauduin, A. Renoncourt, A. Kopf, D. Touraud and W. Kunz. Unified concept of solubilization in water by hydrotropes and co-solvents. *Langmuir* **21**, 6769–6776, **2005**.

[18] K. Lunkenheimer, S. Schrödle and W. Kunz. Dowanol DPnB in water as an example of a solvo-surfactant system: adsorption and foam properties. *Progr. Colloid Polym. Sci.* **126**, 14–20, **2004**.

[19] T. C. Frank, F. A. Donate, A. S. Merenov, G. A. V. Wald, B. J. Alstad, C. W. Green and T. C. Thyne. Separation of Glycol Ethers and Similar LCST-Type Hydrogen-Bonding Organics from Aqueous Solution Using Distillation or Liquid-Liquid Extraction. *Ind. Eng. Chem. Res.* **46**(11), 3774–3786, **2007**.

[20] H. Krienke, G. Schmeer and A. Strasser. Thermodynamic properties of water from combined quantum and statistical mechanics in the temperature range from 273.15 to 423.15 K. *J. Mol. Liq.* **113**, 115–124, **2004**.

[21] P. Bauduin, L. Wattebled, D. Touraud and W. Kunz. Hofmeister ion effects on the phase diagrams of water-propylene glycol propyl ethers. *Z. Phys. Chem. (Muenchen, Germany)* **218**(6), 631–641, **2004**.

[22] R. R. Wolf. Leifähigkeitsmessungen an Lithium- und Tetrabutylammoniumelektrolyten in Butylencarbonat und Acetonitril. Ph.D. thesis, University of Regensburg, **1996**.

[23] P. Walden, H. Ulich and F. Laun. *Z. Phys. Chem.* **114**, 275, **1925**.

[24] D. R. Lide, editor. *Handbook of Chemistry and Physics*. CRC, **2002**. CD-ROM version.

[25] G. J. Janz and R. P. T. Tomkins. *Nonaqueous Electrolytes*, Vol 1. Academic Press, **1972**.

[26] C. J. James and R. M. Fuoss. Conductance in Isodielectric Mixtures. II. i-Butyronitrile with Benzene, Carbon Tetrachloride, Dioxane, and Tetrahydrofuran. *J. Solution Chem.* **4**(1), 91–104, **1975**.

[27] D. Balasubramanian, V. Srinivas, V. G. Gaikar and M. M. Sharma. Aggregation Behavior of Hydrotropic Compounds in Aqueous Solution. *J. Phys. Chem.* **93**, 3865–3870, **1989**.

[28] S. E. Friberg, T. D. Flain and D. W. Osborne. Diacid - a non-traditional hydrotrope. *Comum. J. Com. Esp. Deterg.* **16**, 57, **1985**.

[29] C. Neuberg. Hydrotropy. *Biochem. Z.* **76**, 107–176, **1916**.

[30] R. H. McKee. Use of Hydrotropic Solutions in Industry. *Ind. Eng. Chem. Ind. Ed.* **38**(4), 382–384, **1946**.

[31] G. Dempsey and P. Molyneux. Solubility of the Solutes 4-Hydroxybenzoic Acid and its Alkyl Esters ('Alkylparabens') in Aqueous Urea: Evidence for 1:1 Cosolute-Urea Association in Solution and Evaluation of the Methylene Group Contribution to the Free Energy of Association. *J. Chem. Soc., Faraday Trans.* **88**(7), 971–977, **1992**.

[32] R. E. Coffman and D. O. Kildsig. Self-association of nicotinamide in aqueous solution: light-scattering and vapor pressure osmometry studies. *J. Pharm. Sci.* **85**(8), 848–853, **1996**.

[33] M. Malmsten and B. Lindman. Self-assembly in aqueous block copolymer solutions. *Macromolecules* **25**(20), 5440–5445, **1992**.

[34] V. K. Jadhav, B. A. Dixit and N. S. Tavare. Solubilities of m- and p-Aminoacetophenones in Hydrotrope Solutions. *J. Chem. Eng. Data* **40**, 669–673, **1995**.

[35] S. E. Friberg and M. Chiu. Hydrotropes. *J. Dispersion Sci. Tech.* **9**(5 & 6), 443, **1988**.

[36] R. Breslow. *Structure and Reactivity in Aqueous Solutions – Characterization of Chemical and Biologicall Systems*, 291. ACS, **1994**.

[37] H. Rath. *Tenside* **2**, 1, **1965**.

[38] A. M. Saleh and L. K. El-Khordagui. Hydrotropic agents: a new definition. *Int. J. Pharm.* **24**(2-3), 231, **1985**.

[39] I. Danielsson and P. Stenius. Anion association and micelle formation in solutions of hydrotropic and short-chain carboxylates. *J. Colloid Interface Sci.* **37**, 264–280, **1971**.

[40] P. Firman, D. Haase, J. Jen, M. Kahlweit and R. Strey. On the effect of electrolytes on the mutual solubility between water and nonionic amphiphiles. *Langmuir* **1**, 718–724, **1985**.

[41] P. Makowski. Rapport de stage hydrotropes, **2006**. Unpublished results of the institute.

[42] S. H. Yalkowsky. *Solubility and Solubilization in Aqueous Media.* Oxford University Press, New York, **2000**.

[43] R. C. da Silva, M. Spitzer, L. H. M. da Silva and W. Loh. Investigatins on the mechanism of aqueous solubility increas caused by some hydrotropes. *Thermochim. Acta* **328**, 161–167, **1999**.

[44] S. I. Andersen and J. G. Speight. Observations on the critical micelle concentration of asphaltenes. *Fuel* **72**(9), 1343–1344, **1993**.

[45] R. Strey, Y. Viisanen, M. Aratono, J. P. Kratohvil, Q. Yin and S. E. Friberg. On the Necessity of Using Activites in the Gibbs Equation. *J. Phys. Chem. B* **103**, 9112–9116, **1999**.

[46] V. Srinivas, G. A. Rodley, K. Ravikumar, W. T. Robinson, M. M. Turnbull and D. Balasubramanian. Molecular Organization in Hydrotrope Assemblies. *Langmuir* **13**, 3235–3239, **1997**.

[47] G. Roux, G. Perron and J. E. Desnoyers. Model Systems for Hydrophobic Interactions: Volumes and Heat Capacities of *n*-Alkoxyethanols in Water. *J. Solution Chem.* **7**(9), 639–653, **1978**.

[48] M. D'Angelo and G. O. Santucci. Study of aggregation of *n*-butoxyethanol in water by compressibility and surface tension measurements. *Chem. Phys. Lett.* **220**, 59–63, **1994**.

[49] G. Onori. Structural properties of aqueous mixtures of monohydric alcohols from near-infrared absorption spectra. *Chem. Phys. Letters* **154**, 212–216, **1989**.

[50] M. D´Angelo, G. Onori and A. Santucci. Self-association of monohydric alcohols in water: Compressibility and infrared absorption measurements. *J. Chem. Phys.* **100**(4), 3107–3113, **1994**.

[51] D. Fioretto, A. Marini, G. Onori, L. Palmieri, A. Santucci, G. Socino and L. Verdini. Study of aggregation in water—n-butoxyethanol solutions by dielectric relaxation measurements. *Chem. Phys. Letters* **196**, 583–587, **1992**.

[52] Y. Koga. Vapor Pressures of Aqueous 2-Butoxyethanol Solutions at 25°C: Transitions in Mixing Scheme. *J. Phys. Chem.* **95**, 4119–4126, **1991**.

[53] Y. Koga. Transition of Mixing Scheme in the Water-Rich Region of Aqueous 2-Butoxyethanol: Partial Molar Volumes and Their Derivatives. *J. Phys. Chem.* **96**, 10466–10468, **1992**.

[54] P. Westh, A. Hvidt and Y. Koga. Transition of the mixing scheme in the water-rich region of aqueous 2-butoxyethanol: heat capacities and their temperature derivatives. *Chem. Phys. Lett.* **217**(3), 245–248, **1994**.

[55] C. de Visser, G. Perron and J. E. Desnoyers. Volumes and Heat Capacities of Ternary Aqueous Systems at 25°C. Mixtures of Urea, tert-Butyl Alcohol, Dimethylformamide, and Water. *J. Am. Chem. Soc.* **99**(18), 5894–5900, **1977**.

[56] J. E. Desnoyers, O. Kiyohara, G. Perron and L. Avedikian. Heat capacities and volumes of transfer from water to mixed aqueous solvents. *Adv. Chem. Ser.* **155**, 274–288, **1976**.

[57] K. Iwasaki and T. Fujiyama. Light-Scattering Study of Clathrate Hydrate Formation in Binary Mixtures of *tert*-Butyl Alcohol and Water. *J. Phys. Chem.* **81**, 1908–1912, **1977**.

[58] N. P. Rao and R. E. Verrall. Ultrasonic velocity, excess adiabatic compressibility, apparent molar volume, and apparent molar compressibility properties of binary liquid mixtures containing 2-butoxyethanol. *Can. J. Chem.* **65**, 810–816, **1987**.

[59] P. Bauduin, A. Basse, D. Touraud and W. Kunz. Effect of short non-ionic amphiphiles derived from ethylene and propylene glycol alkyl ethers on the CMC of SDS. *Colloids and Surfaces A* **270–271**, 8–12, **2004**.

[60] P. Bauduin, D. Touraud and W. Kunz. Design of low-toxic anionic temperature sensitive microemulsions using short propyleneglycol alkylethers as co-surfactants. *Langmuir* **21**(18), 8138–8145, **2005**.

[61] E. F. G. Herington. Recommended Reference Materials For Realization of Physiochemical Properties. Section: Density. *Pure & Appl. Chem.* **45**, 1–9, **1976**.

[62] S. M. Sarge, W. Hemminger, E. Gmelin, G. W. H. Höhne, H. K. Cammenga and W. Eysel. Metrologically Based Procedures for the Temperature, Heat and Heat Flow Rate Calibration of DSC. *J. Therm. Anal.* **49**, 1125–1134, **1997**.

[63] G. W. H. Höhne, W. Hemminger and H.-J. Flammersheim. *Differential Scanning Calorimetry*. Springer-Verlag, Berlin Heidelberg, **1996**.

[64] V. M. Shulga, F. G. Eldarov, Y. A. Atanov and A. A. Kuyumchev. Thermal Conductivity and Heat Capacity of Liquid Toluene at Temperatures Between 255 and 400 K and at Pressures up to 1000 MPa. *Int. J. Thermophys.* **7**(6), 1147–1161, **1986**.

[65] R. Páramo, M. Zouine and C. Casanova. New Batch Cells Adapted To Measure Saturated Heat Capacities of Liquids. *J. Chem. Eng. Data* **47**, 441–448, **2002**.

[66] F. Franks and D. J. Reid. *A Comprehensive Treatise*, Vol 2, chapter 5. Plenum Press, New York, **1973**.

[67] J.-P. E. Grolier, G. Roux-Desgranges and A. H. Roux. Thermodynamics of complex aqueous systems. *Fluid Phase Equil.* **30**, 157–172, **1986**.

[68] G. Roux, D. Roberts, G. Perron and J. E. Desnoyers. Microheterogeneity in Aqueous-Organic Solutions: Heat Capacities, Volumes and Expansibilities of Some Alcohols, Aminoalcohol and Tertiary Amines in Water. *J. Solution Chem.* **9**(9), 629–647, **1980**.

[69] J. L. Finney and A. K. Soper. Solvent structure and perturbations in solutions of chemical and biological importance. *Chem. Soc. Revs.* **23**, 1–10, **1994**.

[70] D. T. Bowron, J. L. Finney and A. K. Soper. Structural investigation of solute-solute interactions in aqueous solutions of tertiary butanol. *J. Phys. Chem.* **102**, 3551–3563, **1998**.

[71] V. Gaiduk and M. N. Rodnikova. The lifetime of a librational state as a measure of the elasticity of the spatial H-bond network. *J. Mol. Liq.* **82**, 47–55, **1999**.

[72] M. N. Rodnikova, T. M. Val'kovskaya, V. N. Kartzev and D. B. Kayumova. About Elasticity of Spatial H-Bond Network in Liquids. *J. Mol. Liq.* **106**(2-3), 219–222, **2003**.

[73] M. N. Rodnikova, T. M. Val'kovskaya, J. Barthel and D. B. Kayumova. On the Elasticity of the H-Bond Network in the Aqueous Solutions of Diamines, Diols, and Amino Alcohols. *Russ. J. Phys. Chem.* **80**(3), 483..485, **2005**.

[74] M. Kiselev, D. Ivlev, Y. Puhovski and T. Kerdcharoen. Preferential solvation and elasticity of the hydrogen bonds network in tertiary butyl alcohol-water mixture. *Chem. Phys. Lett.* **379**, 581–587, **2003**.

[75] I. A. Chaban and M. N. Rodnikova. Heat Capacity Close to the Unattainable Critical Layering Point. *Russ. J. Phys. Chem.* **82**(12), 2019–2024, **2007**.

[76] M. N. Rodnikova. The Relation Between Solvophobic Effects and Critical Phenomena in Solutions. *Acta Chim. Slov.* **56**, 215–217, **2009**.

[77] K. Menzel, A. Rupprecht and U. Kaatze. Broad-band Ultrasonic Spectrometry of CE/Water Mixtures. Precritical Behavior. *J. Phys. Chem. B* **101**(7), 1255–1263, **1997**.

[78] T. Boublik, V. Fried and E. Hála. *The Vapour Pressures of Pure Substances.* Elsevier, Amsterdam, **1973**.

[79] R. C. Reid, J. M. Prausnitz and B. E. Poling. *The Properties of Gases and Liquids.* McGraw-Hill, New York, 4th Ed, **1987**.

[80] R. M. Stephenson and S. Malanowski. *Handbook of the Thermodynamics of Organic Compounds.* Elsevier, New York, **1987**.

[81] Y. Marcus. *The Properties of Solvents*, Vol 4. Wiley, New York, **1999**.

[82] J. M. Smith, H. C. V. Ness and M. M. Abbott. *Introduction to Chemical Engineering Thermodynamics.* McGraw-Hill, New York, 5 Ed, **1996**.

[83] H. W. Xiang. The new simple extended corresponding-states principle: vapor pressure and second virial coefficient. *Chem. Eng. Sci.* **57**, 1439–1449, **2002**.

[84] G. M. Wilson. Vapor-Liquid Equilibrium. XI. A New Expression for the Excess Free Energy of Mixing. *J. Am. Chem. Soc.* **86**, 127–130, **1964**.

[85] C. A. Eckert, J. M. Prausnitz, R. V. Orye and J. P. O'Connell. Calculations of Multi-Component Vapour-Liquid Equilibria. *Ind. Chem. Eng. Symp. Ser.* **1**, 75, **1965**.

[86] R. V. Orye and J. M. Prausnitz. Multicomponent equilibrium with the Wilson equation. *Ind. Eng. Chem.* **57**(5), 18–26, **1965**.

[87] J. M. Prausnitz, C. A. Eckert, R. V. Orye and J. P. O'Connell. *Computer Calculations for Multicomponent Vapor-Liquid Equilibria.* Prentice Hall, New York, **1967**.

[88] J. Gmehling and U. Onken. Vapour-Liquid Equilibrium Data Collection. In D. Behrens and R. Eckermann, editors, *Chemistry Data Series*, Vol I, Part 2b. DECHEMA, Frankfurt/Main, **1982**.

[89] H. Renon and J. M. Prausnitz. Local Compositions in Thermodynamic Excess Functions for Liquid Mixtures. *AIChE* **14**(1), 135–144, **1968**.

[90] K. A. G. Schmidt, Y. Maham and A. E. Mather. Use of the NRTL equation for simultaneous correlation of vapour-liquid equilibria and excess enthalpy. *J. Therm. Anal. Calorim.* **89**, 61–72, **2007**.

[91] S. M. Walas. *Phase Equilibria in Chemical Engineering.* Butterworth, **1985**.

[92] F. A. Mato, R. B. Mato and F. Mato. A Simple Expression for the Nonrandomness Parameter α_{ij} in the NRTL Equation for Completely Miscible Systems. *Ind. Eng. Chem. Res.* **28**, 1441–1448, **1989**.

[93] D. Tassios. Limitations in Correlating Strongly Nonideal Binary Systems with the NRTL and LEMF Equations. *Ind. Eng. Chem. Proc. Des. Dev.* **15**, 574–578, **1976**.

[94] J. Rarey. Extended Flexibility for G^E Models and Simultaneous Description of Vapor-Liquid Equilibrium and Liquid-Liquid Equilibrium Using a Nonlinear Transformation of the Concentration Dependence. *Ind. Eng. Chem. Res.* **44**, 7600–7608, **2005**.

[95] A. Vetere. An improved method to predict VLE equilibria of subcritical mixtures. *Fluid Phase Equilib.* **124**, 15–29, **1996**.

[96] A. Vetere. A simple modification of the NRTL equation. *Fluid Phase Equilib.* **173**, 57–64, **2000**.

[97] A. Vetere. The NRTL equation as a predictive tool for vapor-liquid equilibria. *Fluid Phase Equilib.* **218**, 33–39, **2004**.

[98] S. R. M. Ellis and R. D. Garbett. A New Equilibrium Still for the Study of Partially Miscible Systems. *Ind. Eng. Chem.* **52**(5), 385–388, **1960**.

[99] D. S. Abrams and J. M. Prausnitz. Statistical Thermodynamics of Liquid Mixtures: A New P txpression for the Excess Gibbs Energy of Partly or Completely Miscible Systems. *AIChe J.* **21**(1), 116–128, **1975**.

[100] G. Maurer and J. M. Prausnitz. On the derivation and extension of the uniquac equation. *Fluid Phase Equilib.* **2**(2), 91–99, **1978**.

[101] T. F. Anderson and J. M. Prausnitz. Application of the UNIQUAC Equation to Calculation of Multicomponent Phase Equilibria. 1. Vapor-Liquid Equilibria. *Ind. Eng. Chem. Process Des. Dev.* **17**(4), 552–561, **1978**.

[102] S. Kemény and P. Rasmussen. A derivation of local composition expressions from partition functions. *Fluid Phase Equilib.* **7**(2), 197–203, **1981**.

[103] E. A. Guggenheim. *Mixtures*. Oxford University Press, Oxford, **1952**.

[104] R. T. Kuester and J. H. Mize. *Optimization Techniques with Fortran*. McGraw-Hil, New York, **1973**.

[105] E. F. G. Herington. A thermodynamic test for the internal consistency of experimental data on volatility ratios. *Nature (London)* **160**, 610–611, **1947**.

[106] O. Redlich and A. T. Kister. Thermodynamics of nonelectrolyte solutions, x-y-t relations in a binary system. *Ind. Eng. Chem.* **40**, 341–345, **1948**.

[107] H. C. V. Ness. Thermodynamics in the treatment of vapor/liquid equilibrium (VLE) data. *Pure Appl. Chem.* **67**, 859–872, **1995**.

[108] H. C. V. Ness. Exact forms of the unrestricted Gibbs-Duhem equation. *Chem. Eng. Sci.* **10**, 225–228, **1958**.

[109] H. C. V. Ness. Precise testing of binary vapour-liquid equilibrium data by the Gibbs-Duhem equation. *Chem. Eng. Sci.* **11**, 118–124, **1959**.

[110] S. Kemény and J. Manczinger. Treatment of Binary Vapour-Liquid Equilibrium Data. *Chem. Eng. Sci.* **33**, 71–76, **1978**.

[111] P. T. Eubank, B. G. Lamonte and J. F. J. Alvarado. Consistency Tests for Binary VLE Data. *J. Chem. Eng. Data* **45**, 1040–1048, **2000**.

[112] F. G. Cottrell. On the Determination of Boiling Points of Solutions. *J. Am. Chem. Soc.* **41**, 721–729, **1919**.

[113] W. Swietoslawski. *Ebulliometric Measurements*. Reinhold Publishing Corporation, New York, **1945**.

[114] J. Gmehling, J. Li and M. Schiller. A Modified UNIFAC Model. 2. Present Parameter Matrix and Results for Different Thermodynamic Properties. *Ind. Eng. Chem. Res.* **32**, 178–193, **1993**.

[115] A. Klamt and F. Eckert. COSMO-RS: a novel and efficient method for the a priori prediction of thermophysical data of liquids. *Fluid Phase Equilib.* **172**, 43–72, **2000**.

[116] Å. Fredenslund, R. L. Jones and J. M. Prausnitz. Group contribution estimation of activity coefficients in nonideal liquid mixtures. *AIChE* **21**, 1086–1099, **1975**.

[117] Å. Fredenslund, J. Gmehling, M. L. Michelsen, P. Rasmussen and J. M. Prausnitz. Computerized Design of Multicomponent Distillation Columns Using the UNIFAC Group Contribution Method for Calculation of Activity Coefficients. *Ind. Eng. Chem. Process Des. Dev* **16**, 450–462, **1977**.

[118] A. Jakob, H. Grensemann, J. Lohmann and J. Gmehling. Further Development of Modified UNIFAC (Dortmund): Revision and Extension 5. *Ind. Eng. Chem. Res.* **45**, 7924–7933, **2006**.

[119] J. Lohmann, R. Joh, B. Nienhaus and J. Gmehling. Revision and Extension of the Group Contribution Method Modified UNIFAC (Dortmund). *J. Chem. Technol.* **21**, 245–248, **1998**.

[120] S. Miertuš, E. Scrocco and J. Tomasi. Electrostatic Interaction of a Solute with a Continuum. A Direct Utilization of ab initio Molecular Potentials for the Prevision of Solvent Effects. *Chem. Phys.* **55**, 117–129, **1981**.

[121] A. R. Leach. *Molecular Modelling*. Prentice Hall, Harlow, 2nd Ed, **2001**.

[122] A. Klamt and G. Schüürmann. COSMO: A New Approach to Dielectric Screening in Solvents with Explicit Expressions for the Screening Energy and its Gradient. *J. Chem. Soc. Perkin Trans. II* **5**, 799–805, **1993**.

[123] F. Eckert and A. Klamt. Fast solvent screening via quantum chemistry: COSMO-RS approach. *AIChE J.* **48**(2), 369–385, **2002**.

[124] M. Neiman, H. Cheng, V. Parekh, B. Peterson and K. Klier. A critical assessment on two predictive models of binary vapor–liquid equilibrium. *Phys. Chem. Chem. Phys.* **6**, 3474, **2004**.

[125] A. Klamt. Conductor-like Screening Model for Real Solvents: A New Approach to the Quantitative Calculation of Solvation Phenomena. *J. Phys. Chem.* **99**, 2224–2235, **1995**.

[126] A. Klamt. *COSMO-RS: From Quantum Chemistry to Fluid Phase Thermodynamics and Drug Design*. Elsevier, **2005**.

[127] O. Spuhl and W. Arlt. COSMO-RS Predictions in Chemical Engineering - A Study of the Applicability to Binary VLE. *Ind. Eng. Chem. Res.* **43**, 852–861, **2004**.

[128] A. Klamt and F. Eckert. Prediction of vapor liquid equilibria using COSMOtherm. *Fluid Phase Equilib.* **217**, 53–57, **2004**.

[129] Y. Shimoyama, Y. Iwai, S. Takada, Y. Arai, T. Tsuji and T. Hiaki. Prediction of phase equilibria for mixtures containing water, hydrocarbons and alcohols at high temperatures and pressures by cubic equation of state with G^E type mixing rule based on COSMO-RS. *Fluid Phase Equilib.* **243**, 183–192, **2006**.

[130] C. Schürer and W. Peukert. Prediction of thermodynamic properties from pure compound information: Characterization of fullerenes. *Appl. Surf. Sci.* **252**, 512–518, **2005**.

[131] M. Pasanen, A. Zaytseva, P. Uusi-Kyyny, J.-P. Pokki, M. Pakkanen and J. Aittamaa. Vapor Liquid Equilibrium for Six Binary Systems of C_4-Hydrocarbons + 2-Propanoe. *J. Chem. Eng. Data* **51**, 554–561, **2006**.

[132] I. Clausen and W. Arlt. A priori Calculation of Phase Equilibria for Thermal Separation Processes Using COSMO-RS. *Chem. Eng. Technol.* **25**, 254–258, **2002**.

[133] S. Wang, J. M. Stubbs, J. I. Siepmann and S. I. Sandler. Effects of Conformational Distributions on Sigma Profiles in COSMO Theories. *J. Phys. Chem. A* **109**, 11285–11294, **2005**.

[134] A. Schäfer, A. Klamt, D. Sattel, J. C. W. Lohrenz and F. Eckert. COSMO Implementation in TURBOMOLE: Extension of an efficient quantum chemical code towards liquid systems. *Phys. Chem. Chem. Phys.* **2**, 2187–2193, **2000**.

[135] COSMOtherm program. Version C2.1, Release 01.07, COSMOlogic GmbH & Co KG, Leverkusen, Germany, **2007**.

[136] F. Eckert. COSMO*therm* Users Manual. Version C2.1, Release 01.07, COSMOlogic GmbH & Co KG, Leverkusen, Germany, **2007**.

[137] A. Pal and R. Gaba. Volumetric properties of (alkoxypropanol + *n*-alkanol) systems at 298.15 K. *J. Mol. Liq.* **135**, 146–152, **2007**.

[138] S.-C. Ku, I.-H. Peng and C.-H. Tu. Density and Viscosity of Mixtures of Alkoxypropanols with Ethanol at $T = (298.15, 308.15, \text{and } 318.15)$ K. *J. Chem. Eng. Data* **46**, 1392–1398, **2001**.

[139] A. Pal and R. Gaba. Excess Molar Volumes and Viscosities for Binary Mixtures of 1-Alkoxypropan-2-ols with 1-Butanol, and 2-Butanol at 298.15 K and Atmospheric Pressure. *Chin. J. Chem.* **25**, 1781–1789, **2007**.

[140] A. Krishnaiah, B. P. Gampper and D. S. Viswanath. Densities and Viscosities for Propylene Glycol Monomethyl Ether + Water. *J. Chem. Eng. Data* **38**, 401–403, **1993**.

[141] R. Riggio, H. E. Martinez, N. Z. de Salas, M. D. de Toigo and J. F. Ramos. Excess properties for cyclohexanone + butanols at 298.15 K. *Can. J. Chem.* **73**, 1274–1277, **1995**.

[142] S. P. Christensen, F. A. Donate, T. C. Frank, R. J. LaTulip and L. C. Wilson. Mutual Solubility and Lower Critical Solution Temperature for Water + Glycol Ether Systems. *J. Chem. Eng. Data* **50**, 869–877, **2005**.

[143] J. M. Prausnitz, R. N. Lichtenthaler and E. G. de Azevedo. *Molecular Thermodynamics of Fluid-Phase Equilibria*, chapter 6, 269–275. Prentice Hall, 3rd Ed, **1999**.

[144] O. Chiavone-Filho, P. Proust and P. Rasmussen. Vapor-Liquid Equilibria for Glycol Ether + Water Systems. *J. Chem. Eng. Data* **38**, 128, **1993**.

[145] C.-T. Hsieh, M.-J. Lee and H. mu Lin. Multiphase Equilibria for Mixtures Containing Acetic Acid, Water, Propylene Glycol Monomethyl Ether, and Propylene Glycol Methyl Ether Acetate. *Ind. Eng. Chem. Res.* **45**, 2123–2130, **2006**.

[146] P. M. V. Résibois. *Electrolyte Solutions.* Harper and Row, New York, **1968**.

[147] A. Münster. *Statistische Thermodynamik*. Springer-Verlag, Berlin, **1956**.

[148] J. Barthel. Ionengleichgewichte in nichtwäßrigen Elektrolytlösungen. *Chem. Ing. Techn.* **50**(4), 259–266, **1978**.

[149] H. Friedman. *Ionic Solution Theory*. Interscience Publisher, **1962**.

[150] J. Barthel. Electrolytes in Non-Aqueous Solvents. *Pure & Appl. Chem.* **51**, 2093–2124, **1979**.

[151] P. Debye and E. Hückel. Zur Theorie der Elektrolyte. *Phys. Z.* **24**, 185–206, **1923**.

[152] J. Barthel, H.-H. Gores, G. Schmeer and R. Wachter. *Topics in Current Chemistry*, Vol 111, 33–144. Springer, Heidelberg, **1983**.

[153] R. A. Robinson and R. H. Stokes. *Electrolyte Solutions*. Butterworths, London, 2nd Ed, **1970**.

[154] A. D. Mitchel and H. J. M. Bowen, editors. *Mixtures*. 11. Chemical Society, London, **1958**.

[155] J. Barthel, H.-J. Gores, G. Schmeer and R. Wachter. Non-Aqueous Electrolyte Solutions in Chemsitry and Modern Technology. *Top. Curr. Chem.* **111**, 33–144, **1983**.

[156] J. Barthel. *Ionen in nichtwäßrigen Lösungen*, Vol 10. Steinkopff Verlag, **1976**.

[157] J. M. G. Barthel, H. Krienke and W. Kunz. *Physical Chemistry of Electrolyte Solutions – Modern Aspects.*, Vol 5. Steinkopff/Darmstadt, Springer/New York, **1998**.

[158] H. Falkenhagen and W. Ebeling. *Ionic Interactions*, Vol 1. Academic Press, New York, **1970**.

[159] L. Onsager. Zur Theorie der Elektrolyte. *Phys. Z.* **28**, 277–298, **1927**.

[160] J. Barthel, W. Kunz, P. Turq and O. Bernard. *Encyclopedia of Physical Science and Technology*, Vol 5. Academic Press, San Diego, 3rd Ed, **2002**.

[161] J. F. Casteel and E. S. Amis. Specific Conductance of Concentrated Solutions of Magnesium Salts in Water-Ethanol System. *J. Chem. Eng. Data* **17**, 55–59, **1972**.

[162] V. M. Valyashko and A. A. Ivanov. *Zh. Neorg. Khim.* **19**, 2978, **1974**.

[163] M. A. Klochko. *Dokl. Akad. Nauk SSSR* **82**, 261, **1952**.

[164] R. Wachter and J. Barthel. Untersuchungen zur Temperaturabhängigkeit der Eigenschaft von Elektrolytlösungen. II. Bestimmung der Leitfähigkeit über einen großen Temperaturbereich. *Ber. Bunsen-Ges. Phys. Chem.* **83**, 634–642, **1979**.

[165] R. Wachter. Experimentelle Untersuchungen zur Bestimmung der Struktur nichtwässriger Elektrolytlösungen aus der Temperaturabhängigkeit ihrer elektrischen Leitfähigkeit. Teaching thesis, University of Regensburg, **1973**.

[166] R. N. Goldberg and R. D. Weir. Mixtures. *Pure & Appl. Chem.* **64**(10), 1545–1562, **1992**.

[167] Anton Paar KG, Graz, Austria. *Betriebsanleitung für digitale Dichtemeßeinrichtung für Flüssigkeiten und Gase (mit zusätzlichen Informationsblättern).*

[168] P. Fuchs. *Bedienungsanleitung für BCD-Datenlogger*. Elektronik/Chemie, University of Regensburg, Germany, **2002**.

[169] G. Schwitzgebel and J. Barthel. Dichte und partielles Volumen der Alkalimethylate in Methanol. *Z. Phys. Chem.* **68**, 79–90, **1969**.

[170] S. Weber. Kalorimetrische Bestimmung thermodynamischer Eigenschaften von 2:2-Elektrolyten in Wasser. Ph.D. thesis, University of Regensburg, **1990**.

[171] G. S. Kell. Thermal Expansivity and Compressibility of Liquid Water from 0°C to 150°C, Correlations and Tables for Atmospheric Pressure and Saturation Reviewed and Expressed on 1968 Temperature Scale. *J. Chem. Eng. Data* **20**(1), 97–105, **1975**.

[172] H. Roch. Elektrolyteigenschaften von 25°C bis 135°C. Die Lösungsmittel Dimethylsulfoxid, γ-Butyrolacton und S(-)-Propylencarbonat sowie LiBr in PC-DME und PC-AN-Mischungen. Ph.D. thesis, University of Regensburg, **1991**.

[173] J. Barthel, R. Neueder and P. Schröder. Electrolyte Data Collection. In G. Kreysa, editor, *Chemistry Data Series*, Vol XII, Part 1. DECHEMA, Frankfurt/Main, **1994**.

[174] R. Zana, J. E. Desnoyers, G. Perron, R. L. Kay and K. Lee. Ionic Volumes of Electrolytes in Propylene Carbonate from Densities, Ultrasonic Vibrations, Potentials and Transference Numbers at 25°C. *J. Phys. Chem.* **86**, 3996–4003, **1982**.

[175] H. M. Graml. Die Eigenschaften von 1.1-Elektrolyten in organischen Lösungsmitteln und Lösungsmitteleigenschaften von 25°C bis 135°C sowie theoretische Betrachtungen zum Leitfähigkeitsverhalten. Ph.D. thesis, University of Regensburg, **1994**.

[176] J. Barthel, R. Wachter and H.-J. Gores. *Modern Aspects of Electrochemistry*, chapter 1, 1–79. 13. Plenum Press, New York, **1979**.

[177] H. Utz. Bestimmung der statischen Dielektrizitätszahl von DME-, THF, γ-Butyrolacton, Methanol-Wasser, Ethanol-Wasser, Acetonitril-Wasser-Gemischen im Temperaturbereich von 30 bis -45°C. Diploma thesis, University of Regensburg, **1984**.

[178] F. Kohlrausch, V. Kose and S. Wagner. *Praktische Physik*. 1. Teubner Verlag, Stuttgart, **1996**.

[179] General Radio Company, Concord Massachusetts, USA. *Instruction Manual, Type 1621 Capacitance Measurement System*, **1971**.

[180] D. E. Gray. *American Institute of Physics Handbook*. McGraw-Hill Book Company, New York, 3. Ed, **1972**.

[181] R. H. Orcutt and R. H. Cole. Dielectric Constants and Pair Interactions in Argon, Carbon Dioxide and Ethylene. *Physica* **31**, 1779–1791, **1965**.

[182] R. H. Orcutt and R. H. Cole. Dielectric Constants of Imperfect Gases. *J. Chem. Phys.* **46**, 697–702, **1967**.

[183] T. K. Bose and R. H. Cole. Dielectric and Pressure Virial Coefficients of Imperfect Gases. *J. Chem. Phys.* **52**, 140–147, **1970**.

[184] H. T. French, M. Koshla and K. N. Marsh. Dielectric Constants and Apparent Moments of (butan-1-ol or butan-2-ol + cyclohexane) at 298.15 and 318.15 K and of (2-methyl-propane-2-ol + cyclohexane) at 298.15 and 318.15 K. *J. Chem. Thermodyn.* **20**, 1175–1182, **1988**.

[185] H. Umstätter. *Einführung in die Viskosimetrie und Rheometrie*. Springer-Verlag, Heidelberg, **1952**.

[186] Schott Instruments. *Operating Instructions: Ubbelohde Viscometer and Micro-Ubbelohde Viscometer*.

[187] L. Ubbelohde. *Zur Viskosimetrie*. S. Hirzel Verlag, Stuttgart, **1965**.

[188] G. Hagen. Über die Bewegung des Wassers in engen zylindrischen Röhren. *Pogg. Ann.* **46**, 423–442, **1839**.

[189] J. L. M. Poiseuille. Recheches expérimentales sur le mouvement des liquides dans les tubes de très-petit diamètres. *Comptes Rendus* **11**, 961–967, **1840**.

[190] E. Hagenbach. Über die Bestimmung der Zähigkeit einer Flüssigkeit durch den Ausfluss aus Röhren. *Pogg. Ann.* **109**, 385–4426, **1860**.

[191] M. Couette. Rotation verschiedener Flüssigkeiten zwischen Zylindern. *Ann. Chem. Phys.* **21**(6), 433, **1860**.

[192] M. R. Cannon, R. E. Manning and J. D. Bell. Viscosity Measurement The Kinetic Energy Correction and a New Viscometer. *Anal. Chem.* **32**, 355–358, **1960**.

[193] M. Kindler. Transporteigenschaften nicht-wässriger Elektrolytlösungen für Hochenergiebatterien mit Lithium als Anode. Ph.D. thesis, University of Regensburg, **1985**.

[194] T. Plebanski. RECOMMENDED REFERENCE MATERIALS FOR REALIZATION OF PHYSICOCHEMICAL PROPERTIES. SECTION: VISCOSITY. *Pure & Appl. Chem.* **52**, 2393–2404, **1980**.

[195] L. D. Eicher and B. J. Zwolinksi. High-Precision Viscosity of Supercooled Water and Analysis of the Extended Range Temperature Coefficient. *J. Phys. Chem.* **75**, 2016–2024, **1971**.

[196] W. Weber and W. Fritz. Über die Größe der Hagenbach-Couette-Korrektur und den Einfluß der Oberflächenspannung beim Ubbelohde-Viskosimeter. *Rheol. Acta* **3**, 34–43, **1963**.

[197] F. Kohlrausch. *Wied. Ann.* **60**, 315, **1897**.

[198] J. Barthel and J.-C. Justice. Méthodes électrochimiques, Conductimétrie. In *Techniques de l´Ingenieur*. **1985**.

[199] R. Gerber. Das Leitfähigkeitsverhalten von 1,2-Dimethoxyethan-Tetrahydrofuran-Mischungen vom Bereich hoher Verdünnung bis zur Sättigung. Ph.D. thesis, University of Regensburg, **1985**.

[200] G. Jones and R. C. Josephs. The Measurement of the Conductance of Electrolyte; 1. An Experimental and Theoretical Study of Design of the Wheat Stone Bridge for Use with Alternating Currents and an Improved Form of Direct Reading Alternating Current Bridge. *J. Amer. Chem. Soc.* **50**, 1049–1092, **1928**.

[201] G. Jones and G. M. Bollinger. The Measurement of the Conductance of Electrolytes, II. Improvements in the Oscillator and the Detector. *J. Amer. Chem. Soc.* **51**, 2407–2416, **1929**.

[202] T. Shedlovsky. A Screened Bridge for the Measurement of Electrolytic Conductance. I. Theory of Capacity Errors II. Description of the Bridge. *J. Amer. Chem. Soc.* **52**, 1793–1805, **1930**.

[203] K. W. Wagner. *Electrotechn. Z.* **32**, 1001–1002, **1911**.

[204] R. Wachter and J. Barthel. A Method for determining the precise dependence of conductivity data on temperature. *Electrochim. Acta* **16**, 713–721, **1971**.

[205] J. Barthel. Conductance of Electrolyte Solutions. *Angew. Chem. internat. Edit.* **7**(4), 1968, **1968**.

[206] H.-J. Gores. Leitfähigkeitsuntersuchungen an schwach assoziierenden Elektrolyten, insbesondere an Trägerelektrolyten für Batterien mit Lithium als Anode. Ph.D. thesis, University of Regensburg, **1974**.

[207] T. B. Hoover. The Frequency Extrapolation of Conductance Data for Aqueous Salt Solutions. *J. Phys. Chem.* **74**(13), 2667–2673, **1970**.

[208] G. Jones and S. M. Christian. The Measurement of the Conductance of Electrolytes, VI. Galvanic Polarization by Alternating Current. *J. Amer. Chem. Soc.* **57**, 272–280, **1935**.

[209] J. C. Nichol and R. M. Fuoss. A New Cell Design for Precision Conductimetry. *J. Phys. Chem.* **58**, 696–699, **1954**.

[210] J. Barthel, F. Feuerlein, R. Neueder and R. Wachter. Calibration of Conductance Cells at Various Temperatures. *J. Sol. Chem.* **9**, 209–219, **1980**.

[211] J. Barthel, J. C. Justice and R. Wachter. Electric Conductivity of Alcoholic Alkali Metal Alkoxide Solutions, VII. Discussion of the Distance Parameters Using the Extended Conductivity Equations. *J. Phys. Chem. N. F.* **84**, 100–113, **1973**.

[212] J. Barthel, H. Graml, R. Neueder, P. Turq and O. Bernard. Electrolyte conductivity from infinite dilution to saturation. *Current Topics in Sol. Chem.* **1**, 223–239, **1994**.

[213] J. Bartehl, H. Popp and G. Schmeer. *Software-Entwicklung in der Chemie 2, Die ELDAR-Methodenbank für Elektrolytlösungen.* Springer Verlag, Berlin, **1988**.

[214] L. Pauling. *Die Natur der chemischen Bindung.* Chemie Weinheim, **1968**. (Transl.).

[215] P. S. Ramanathan, C. V. Krishnan and H. L. Friedman. Models Having the Thermodynamic Properties of Aqueous Solutions of Tetraalkylammonium Halides. *J. Sol. Chem.* **1**, 237–262, **1972**.

[216] J. Barthel, U. Ströder, L. Iberl and H. Hammer. The temperature dependence of the properties of electrolyte solutions. IV. Determination of cationic transference numbers in methanol, ethanol, propanol, and acetonitrile at various temperatures. *Ber. Bunsen-Ges. Phys. Chem.* **86**, 636–645, **1982**.

[217] J. Barthel, L. Iberl, J. Rossmaier, H.-J. Gores and B. Kaukal. Conductance of 1,1-Electrolytes in Acetonitrile Solutions From -40°C to 35°C. *J. Solution Chem.* **19**(4), 321–337, **1990**.

[218] N. G. Tsierkezos. Conductivity Studies of *n*-Tetrabutylammonium Tetraphenylborate in Acetone and Acetonitrile in the Temperature Range from 283.15 to 303.15 K. *Z. Phys. Chem.* **222**, 63–79, **2008**.

[219] J. Barthel. The Temperature Dependence of the Properties of Electrolyte Solutions. I. A Semi-Phenomenological Approach to an Electroylte Theory Including Short Range Forces. *Ber. Bunsen-Ges. Phys. Chem.* **83**, 252–257, **1979**.

[220] S. B. Brummer and G. J. Hills. Kinetics of ionic conductance. Part 1.—Energies of activation and the constant volume principle. *Trans. Faraday Soc.* **57**, 1816–1822, **1961**.

[221] S. B. Brummer and G. J. Hills. Kinetics of ionic conductance. Part 2.—Temperature and pressure coefficients of conductance. *Trans. Faraday Soc.* **57**, 1823–1837, **1961**.

[222] B. E. Conway. The Evaluation and Use of Properties of Individual Ions in Solutions. *J. Solution Chem.* **7**, 721–770, **1978**.

[223] B. Krumgalz. Separation of Limiting Equivalent Conductances into Ionic Contributions in Non-aqueous Solutions by Indirect Methods. *J. Chem. Soc., Faraday Trans. I* **79**, 571–587, **1983**.

[224] R. N. Butler and M. C. R. Symons. Solvation Spectra Part 29. - Nuclear Magnetic Resonance Studies of Electrolyte Solutions: Ion-Solvent Interactions in Methanol. *Trans. Faraday Soc.* **65**, 2559–2566, **1969**.

[225] B. S. Krumgalz, V. M. Ryabikova, S. K. Akopyan and V. I. Borisova. Spectroscopic study of the solvation of some tetraalkylammonium ions. *Russ. J. Phys. Chem.* **48**, 2597–2598, **1974**.

[226] M.-H. Baron, J. Corset, C. de Loze and M.-L. Josien. Vibrational spectrometric study of the effect of salts on the structure of liquid N,N-dimethylacetamide. Dipole-dipole and ion-dipole interactions. *C. R. Acad. Sci., Ser. C* **274**, 1321–1324, **1972**.

[227] P. Walden, H. Ulich and G. Busch. Conductivity measurements in acetone. *Z. Phys. Chem.* **123**, –471, **1926**.

[228] B. S. Krumgalz. Separation of Limiting Equivalent Conductances into Ionic Contributions in Non-aqueous Solutions by Indirect Methods. *J. Chem. Soc. Faraday Trans. I* **79**, 571–587, **1983**.

[229] D. F. Evans and M. I. McElroy. The conductance of electrolytes in acetone-2-propanol and acetone-1,1,1,3,3,3-hexafluoro-2-propanol mixtures at 25°C. *J. Solution Chem.* **4**(5), 413–430, **1975**.

[230] D. F. Evans, J. Thomas, J. A. Nada and M. A. Matesich. Conductance of electrolytes in acetone and in 1-propanol-acetone mixtures at 25°C. *J. Phys. Chem.* **75**(11), 1714–1722, **1971**.

[231] U. Mayer. Solvent Effects on Ion-Pair Equilibria. *Coord. Chem. Rev.* **21**, 159–179, **1976**.

[232] J. Barthel, L. Iberl, J. Rossmaier, H. J. Gores and B. Kaukal. Conductance of 1,1-Electrolytes in Acetonitrile Solutions From -40°C to 35°C. *J. Solution Chem.* **19**(4), 321–337, **1990**.

[233] J. Barthel, M. Krell, L. Iberl and F. Feuerlein. Conductance of 1-1 Electrolytes in Methanol Solutions From -45°C to +25°C. *J. Electroanal. Chem.* **214**, 485–505, **1986**.

[234] D. F. Evans, C. Zawoyski and R. L. Kay. The Conductance of the Symmetrical Tetraalkylammonium Halides and Picrates in Acetonitrile at 25°C. *J. Phys. Chem.* **69**(11), 3878–3885, **1965**.

[235] J. Barthel, R. Wachter, G. Schmeer and H. Hilbinger. Conductance of electrolytes in 1-propanol solutions from -40 to 25°C. *J. Solution Chem.* **15**(7), 531–550, **1986**.

[236] R. I. Kay, C. Zawoyski and D. F. Evans. The Conductance of the Symmetrical Tetraalkylammonium Halides and Picrates in Methanol at 25 and 10°C. *J. Phys. Chem.* **69**(18), 4208–4215, **1965**.

[237] I. Svorstøl, H. Høiland and J. Songstad. Solvent properties of dichloromethane. III. Conductivity studies of some tetraalkylammonium-, tetraphenylarsonium- and bis(triphenylphosphine)iminium salts in dichlroromethane. *Acta Chem. Scand. B* **38**, 885–893, **1984**.

[238] J. Barthel, R. Gerber and H.-J. Gores. The Temperature Dependence of the Properties of Electrolyte Solutions. VI. Triple Ion Formation in Solvents of Low Permittivity Exemplified by $LiBF_4$ Solutions in Dimethoxyethane. *Ber. Bunsenges. Phys. Chem.* **88**, 616–622, **1984**.

[239] J. Barthel. Transport properties of electrolytes from infinite dilution to saturation. *Pure & Appl. Chem.* **57**(2), 355–367, **1985**.

[240] J. Barthel, M. Krell, L. Iberl and F. Feuerlein. Conductance of 1-1 Electrolytes in Methanol Solutions from -45 to +25°C. *J. Electroanal. Chem.* **214**, 485–505, **1986**.

[241] J. Barthel, R. Neueder, F. Feuerlein, F. Strasser and L. Iberl. Conductance of Electrolytes in Ethanol Solutions from -45 to 25°C. *J. Solution Chem.* **12**(7), 449–471, **1983**.

[242] J. Barthel, R. Wachter, G. Schmeer and H. Hilbinger. Conductance of Electrolytes in 1-Propanol Solutions from -40 to 25°C. *J. Solution Chem.* **15**, 531–550, **1986**.

[243] J. Barthel, R. Wachter and H.-J. Gores. Contribution on Non Coulombic Forces to Ion-pair Formation in some Non-aqueous Polar Solvents. *Faraday Disc. Chem. Soc.* **64**, 285–294, **1977**.

[244] R. Meier. Neue nichtwässrige Elektrolyte für technische Anwendungen. Ph.D. thesis, University of Regensburg, **1998**.

[245] J. Barthel, H.-J. Gores and G. Schmeer. The Temperature Dependence of the Properties of Electrolyte Solutions. III. Conductance of Various Salts at High Concentrations in Propylene Carbonate at Temperatures from -45 °C to -25 °C. *Ber. Bunsen-Ges. Phys. Chem.* **83**, 911–920, **1979**.

[246] J. Barthel, R. Buestrich, E. Carl and H.-J. Gores. A New Class of Electrochemically and Thermally Stable Lithium Salts for Lithium Battery Electrolytes II. Conductivity of Lithium Organoborates in Dimethoxyethane and Propylene Carbonate. *J. Electrochem. Soc.* **143**(11), 3565–3571, **1996**.

[247] Y. Matsuda, M. Morita and T. Yamashita. Conductivity of the $LiBF_4$/Mixed Ether Electrolytes for Secondary Lithium Cells. *J. Electrochem. Soc.* **131**(12), 2821–2827, **1984**.

[248] J. Barthel and H.-J. Gores. *Nonaqueous Electrolyte Solutions. Current Process.* VCH, New York, **1994**.

[249] H.-J. Gores and J. Barthel. Conductance of Salts at Moderate and High Concentrations in Propylene Carbonate-Dimethoxyethane Mixtures at Temperatures from -45°C to 25°C. *J. Solution Chem.* **9**(12), 939–954, **1980**.

[250] J. Barthel and H.-J. Gores. Data on transport properties of electrolyte solutions for applied research and technology. *Pure & Appl. Chem.* **57**(8), 1071–1082, **1985**.

[251] R. M. Fuoss and C. A. Kraus. Properties of Electrolytic Solutions. IV. The Conductance Minimum and the Formation of Triple Ions Due to the Action of Coulomb Forces. *J. Am. Chem. Soc.* **55**(6), 2387–2399, **1933**.

[252] E. C. Baughan. Note on the Fuoss-Kraus Equation for the Conductance of Solutions Containing Ion-Triplets. *J. Phys. Chem.* **64**(12), 1951–1951, **1960**.

[253] R. M. Fuoss and F. Accascina. *Electrolytic Conductance.* Interscience, New York, **1959**. P. 258.

[254] S. Boileau and P. Hemery. Conductance of some Tetraphenylboron and Fluorenyl Salts in Tetrahydrofuran. *Electrochim. Acta* **21**, 647–655, **1976**. P. 258.

[255] Y. Marcus and G. Hefter. Ion Pairing. *Chem. Rev.* **106**(11), 4585–4621, **2006**.

[256] H. Weingartner. Corresponding states for electrolyte solutions. *Pure Appl. Chem.* **73**, 1733–1748, **2001**.

[257] A. M. Sukhotin and Z. N. Timofeeva. Ion association in solution. III. Potentiometric ion activity determination in solutions of low dielectric constants. *Zh. Fiz. Khim.* **33**, 1739–1743, **1959**.

[258] E. A. S. Cavell and P. C. Knight. Effect of concentration changes on permittivity of electrolyte solutions. *Z. Phys. Chem.* **57**, 331–334, **1968**.

[259] S. Petrucci and E. M. Eyring. Multibody interaction theory of triple ions and dimerion pairs. *J. Phys. Chem.* **95**, 1731–1736, **1991**.

[260] M. Grigo. Remarks on Triple Ion Formation. Interpretation of Conductance Data. *J. Solution Chem.* **11**(8), 529–537, **1982**.

[261] S. Petrucci and E. M. Eyring. Microwave dielectric relaxation, electrical conductance and ultrasonic relaxation of $LiClO_4$ in polyethylene oxide dimethyl ether-500 (PEO-500). *Phys. Chem. Chem. Phys.* **4**, 6043–6046, **2002**.

[262] R. Neueder. Dampfdruckuntersuchungen an methanolischen Lösungen schwach assoziierter Elektrolyte. Ph.D. thesis, University of Regensburg, **1982**.

[263] J. A. Rard, A. Habenschuss and F. H. Spedding. A review of the osmotic coefficients of aqueous calcium chloride at 25°C. *J. Chem. Eng. Data* **22**(2), 180–186, **1977**.

[264] A. P. Kudchadker, D. Ambrose and C. Tsonopoulos. Vapor-Liquid Critical Properties of Elements and Compounds. Oxygen Compounds Other Than Alcohols and Cycloalcohols. *J. Chem. Eng. Data* **46**, 457–479, **2001**.

[265] J. Barthel and R. Neueder. Präzisionsmeßanlage zur statischen Bestimmung des Dampfdruckes von Lösungen. *GIT Fachz. Lab.* **28**, 1002–1012, **1984**.

[266] D. Ambrose and I. J. Lawrenson. The vapour pressure of water. *J. Chem. Thermodynamics* **4**, 755–761, **1972**.

[267] H. F. Stimson. Some Precise Measurements of the Vapor Pressure of Water in the Range From 25 to 100°C. *J. Research of the National Bureau of Standards A. Physics and Chemistry* **73A**, 493–496, **1969**.

[268] D. Ambrose and C. H. S. Sprake. Thermodynamic properties of organic oxygen compounds XXV. Vapour pressures and normal boiling temperatures of aliphatic alcohols. *J. Chem. Thermodynamics* **2**, 1970, **1970**.

[269] H. F. Gibbard, G. Scatchard, R. A. Rousseau and J. L. Creek. Liquid-Vapor Equilibrium of Aqueous Sodium Chloride, from 298 to 373K and from 1.0 to 6 mol kg^{-1}, and Related Properties. *J. Chem. Eng. Data* **19**(3), 281–288, **1974**.

[270] W. Kunz. Vapour Pressure Measurements and Statistical-Mechanical Theories for the Determination of Thermodynamic and Structural Properties of Electrolytes in Acetonitrile and Methanol. Ph.D. thesis, University of Regensburg, **1988**.

[271] T. N. Bell, E. L. Cussler, K. R. Harris, C. N. Pepela and P. J. Dunlop. An Apparatus for Degassing Liquids by Vacuum Sublimation. *J. Phys. Chem.* **13**, 4693–4695, **1968**.

[272] T. Boublik, V. Fried and E. Hala. *The Vapour Pressures of Pure Substances.* Elsevier, Amsterdam, 2 Ed, **1984**.

[273] T. E. Daubert and R. P. Danner. *Physical and Thermodynamics Properties of Pure Chemicals: Data Compilation.* Hemisphere Publishing Corp., Bristol, Pennsylvania, **1992**.

[274] B. E. Poling, J. M. Prausnitz and J. M. O'Connell. *The Properties of Gases and Liquids.* McGraw-Hill, Boston, 5 Ed, **2001**.

[275] North American Thermal Analysis Society. *Vapor Pressure Determination by Thermogravimetry*, **1999**.

[276] J. P. D. Silva and A. M. D. Silva. Vapor Pressure of Triadimefon by the Gas Saturation Method. *J. Chem. Eng. Data* **42**(3), 538–540, **1997**.

[277] J. Tomiska. A new technique for the determination of vapour pressures by the Knudsen effusion method. *J. Phys. E: Sci. Instrum.* **14**, 420–424, **1981**.

[278] W. Wagner. New vapor pressure measurements for argon and nitrogen and a new method for establishing rational vapor pressure equations. *Cryogenics* **13**(8), 470–482, **1973**.

[279] E. R. Cox. Hydrocarbon Vapor Pressures. *Ind. Eng. Chem.* **28**, 613–616, **1936**.

[280] D. M. VonNiederhausern, L. C. Wilson, N. F. Giles and G. M. Wilson. Critical-Point Measurements for Nine Compounds by a Flow Method. *J. Chem. Eng. Data* **45**, 154–156, **2000**.

[281] K. Ruzicka and V. Majer. Simple and controlled extrapolation of vapor pressures toward the triple point. *AIChE J.* **42**(6), 1723, **1996**.

[282] G. Lauermann. Dampfdruckmessungen an nichtwässrigen Elektrolytlösungen und ihre statistisch thermodynamische Beschreibung über einen weiten Konzentrationsbereich. Ph.D. thesis, University of Regensburg, **1985**.

[283] J. Barthel, R. Neueder and G. Lauermann. Vapor Pressure on Non-Aqueous Electrolyte Solutions. Part 1. Alkali Metal Salts in Methanol. *J. Solution Chem.* **14**(9), 621–633, **1985**.

[284] J. Barthel, G. Lauermann and R. Neueder. Vapor Pressure Measurements on Non-Aqueous Electrolyte Solutions. Part 2. Tetraalkylammonium Salts in Methanol. Activity Coefficients of Various 1-1 Electrolytes at High Conentrations. *J. Solution Chem.* **15**(10), 851–867, **1986**.

[285] J. Barthel and G. Lauermann. Vapor Pressure Measurements on Non-Aqueous Electrolyte Solutions. Part 3: Solutions of Sodium Iodide in Ethanol, 2-Propanol, and Acetonitrile. *J. Solution Chem.* **15**(10), 869–877, **1986**.

[286] J. Barthel and W. Kunz. Vapor Pressure Data for Non-Aqueous Electrolyte Solutions. Part 5. Tetraalkylammonium Salts in Acetonitrile. *J. Solution Chem.* **17**(5), 399–415, **1988**.

[287] J. Barthel, R. Neueder, H. Poepke and H. Wittmann. Osmotic Coefficients and Activity Coefficients of Nonaqueous Electrolyte Solutions. Part 4. Lithium Bromide, Tetrabutylammonium Bromide, and Tetrabutylammonium Perchlorate in Acetone. *J. Solution Chem.* **28**(12), 1277, **1999**.

[288] N. Papiconomou, J.-P. Simonin, O. Bernard and W. Kunz. MSA-NRTL model for the description of the thermodynamic properties of electrolyte solutions. *Phys. Chem. Chem. Phys.* **4**(18), 4435–4443, **2002**.

[289] L. Blum. *Primitive Electrolytes in the Mean Spherical Approximation*, Vol 5, 1–63. Academic Press, **1980**.

[290] K. Nasirzadeh, R. Neueder and W. Kunz. Vapor Pressures, Osmotic and Activity Coefficients of Electrolytes in Protic Solvents at Different Temperatures. 3. Lithium Bromide in 2-Propanol. *J. Solution Chem.* **34**(1), 9–24, **2005**.

[291] J. Barthel, R. Neueder, H. Poepke and H. Wittmann. Osmotic Coefficients and Activity Coefficients of Nonaqueous Electrolyte Solutins. Part 2. Lithium Perchlorate in the Aprotic Solvents Acetone, Acetonitrile, Dimethoxyethane, and Dimethylcarbonate. *J. Solution Chem.* **28**(5), 489–503, **1999**.

[292] M. T. Zafarani-Moattar and J. Jahanbin-Sardroodi. Measurement and correlation of osmotic coefficients and evaluation of vapor pressures for solutions of $CaCl_2$ and $Ca(NO_3)_2$ in ethanol at 298 K. *Fluid Phase Equil.* **172**, 221–235, **2000**.

[293] W. G. M. Jr. and J. E. Mayer. The Statistical Thermodynamics of Multicomponent Systems. *J. Chem. Phys.* **13**(7), 276–305, **1945**.

[294] K. S. Pitzer and J. M. Simonson. Thermodynamics of Multicomponent, Miscible, Ionic systems: Theory and Equations. *J. Phys. Chem.* **90**, 3005–3009, **1986**.

[295] C.-C. Chen, H. I. Britt and J. F. Boston. Local composition model for excess Gibbs energy of electrolyte systems. Part I: Single solvent, single completely dissociated electrolyte systems. *AIChE J.* **28**(4), 588–596, **1982**.

[296] S. L. Clegg and K. S. Pitzer. Thermodynamics of Multicomponent, Miscible, Ionic Solutions: Generalized Equations for Symmetrical Electrolytes. *J. Phys. Chem.* **96**, 3513–3520, **1992**.

[297] K. S. Pitzer. Thermodynamics of electrolytes. I. Theoretical basis and general equations. *J. Phys. Chem.* **77**, 268–277, **1973**.

[298] K. S. Pitzer and G. Mayorga. Thermodynamics of electrolytes. III. Activity and osmotic coefficients for 2-2 electrolytes. *J. Solution Chem.* **3**, 539–546, **1974**.

[299] K. S. Pitzer. *Activity coefficients in electrolyte solutions.* CRC Press, Boca Raton, 2nd Ed, **1991**.

[300] D. G. Archer. Thermodynamic properties of the sodium bromide + water system. *J. Phys. Chem. Ref. Data* **20**(3), 509–555, **1991**.

[301] D. G. Archer. Thermodynamic properties of the sodium chloride + water system. II. Thermodynamic properties of $NaCl_{(aq)}$, $NaCl{\cdot}2\,H_2O_{(cr)}$, and phase equilibria. *J. Phys. Chem. Ref. Data* **21**(4), 793–829, **1992**.

[302] K. Nasirzadeh, N. Papaiconomou, R. Neueder and W. Kunz. Vapor Pressures, Osmotic and Activity Coefficients of Electrolytes in Protic Solvents at Different Temperatures. 1. Lithium Bromide in Methanol. *J. Solution Chem.* **33**(3), 227–245, **2004**.

[303] K. Nasirzadeh, R. Neueder and W. Kunz. Vapor Pressures and Osmotic Coefficients of Aqueous LiOH Solutions at Temperatures Ranging from 298.15 to 363.15 K. *Ind. Eng. Chem. Res.* **44**, 3807–3814, **2005**.

[304] D. G. Archer and J. A. Rard. Isopiestic Investigation of the Osmotic and Activity Coefficients of Aqueous $MgSO_4$ and the Solubility of $MgSO_4{\cdot}7\,H_2O_{(cr)}$ at 298.15 K: Thermodynamic Properties of the $MgSO_4$ + H_2O System to 440 K. *J. Chem. Eng. Data* **43**, 791, **1998**.